eman ta zabal zazu

Universidad del País Vasco
Euskal Herriko Unibertsitatea

Doctoral thesis

Validation of ^{31}P-NMR spectroscopy as analytical method for assessing metabolic landscape of mouse liver

Presented by:

Jon

Bilbao

Supervised by:

José María Mato de la Paz

Faculty of Science and Technology

Department of Biochemistry and Molecular Biology

Doctoral Programme in Molecular Biology and Biomedicine

Leioa, 2023

AGRADECIMIENTOS

En primer lugar, me gustaría mostrar mi agradecimiento a **José M. Mató** por darme la oportunidad de poder realizar este trabajo en el CIC bioGUNE durante estos últimos cinco años además de ayudarme a poder entender mejor la interpretación biológica de los resultados que he obtenido a lo largo de la misma.

Este agradecimiento es extensible a **Óscar Millet**, que ha sido clave para el desarrollo y la gestión de este proyecto del cual se han obtenido unos resultados fructíferos. Además, me siento agradecido por darme la posibilidad de formar parte de multitud proyectos ambiciosos que me han ayudado a crecer profesionalmente y que han ayudado a que pueda conseguir los objetivos propuestos inicialmente además de inculcarme su ambición y sus ganas de superarse en todo lo que hace.

Por otra parte, no podría olvidarme de **Ganeko Bernardo**. El ha sido una referencia, un guía e incluso un psicólogo para mi durante estos años. Gracias por toda la ayuda en cualquier momento, por escucharme, por aconsejarme, por creer en mí siempre, por convertir la experiencia del doctorado en algo del cual tendré un bonito recuerdo en el futuro. También por tu paciencia y por tu generosidad así como por tener el placer de poder aprender de alguien como tú tanto a nivel profesional y personal. Gracias de corazón, Ganeko.

A **Tammo** también por su apoyo durante el proyecto, siempre ha estado disponible, sea la hora que sea, para cualquier imprevisto de última hora, que los ha habido y muchos. También por su sentido del humor, sobre todo en cualquier problema relacionado con Bruker.

Tampoco me podría olvidar de **Ruben**. Agradecerle su paciencia ante mis insistentes preguntas sobre R así como por inculcarme su interés en la bioinformática.

Asimismo, tengo que agradecerles a **Sara** y **Karen** su apoyo incondicional. **Sara**, aunque no hemos coincidido mucho, durante este poco tiempo me has demostrado que eres una chica que puede hacer frente a cualquier proyecto y que me siento muy orgulloso de que continues este proyecto. Mucho ánimo, no te rindas porque vales mucho, puedes con la fosforómica y con todo lo que te propongas. **Karen**, nos conocemos desde hace 7 años, somos amigos desde entonces, pero no tengo palabras para agradecer todo el apoyo que me has dado incluso en algunos momentos no tan buenos que he atravesado a lo largo de este último año. Ahora mismo, estas iniciando una etapa que te llevará hasta donde tú te propongas, porque vales mucho y aunque

haya a veces dificultades, piensa que para conseguir el objetivo hay que tropezarse, pero hay que levantarse y seguir luchando. Te quiero mucho compi.

Igualmente, me gustaría agradecer a todos los **compañeros** del laboratorio de **Medicina de Precisión y Metabolismo** por su apoyo ya que han contribuido a que esta experiencia sea positiva y enriquecedora. Ha sido un placer conoceros a todos, mucho ánimo y espero que consigáis todo lo que os propongáis.

De igual manera, siento un profundo agradecimiento por todo el apoyo que todos los miembros del laboratorio de Exosomas así como de la plataforma de Metabolómica, ambos dirigidos por Juan Manuel Falcón, me han dado a lo largo de estos años, especialmente el primer año de doctorado. Mención especial a **Diana, Sebastiaan** y el propio **JuanMa**, gracias por enseñarme y ayudarme tanto en el procesamiento y tratamiento de datos en espectrometría de masas, así como todo el apoyo recibido además de adoptarme en la plataforma durante todo este tiempo.

También, me gustaría agradecer a todos mis amigos por todo el apoyo que me han brindado todos estos años. Gracias a **Maider**, mis compis **Kathe C.** y **Kathe T.** (y su **bebe Derek**), **Heidy**, **Sofia, Eli, Amaya, Teresa, Esthefanie** (y su **bebe Izaro**). Gracias por apoyarme, darme consejos, y sobretodo nunca soltarme de la mano. Me siento muy orgulloso de teneros en mi vida, gracias a todas, os quiero mucho. También agradecer a **Will** y **Óscar**, aunque haya pasado poco tiempo, hemos disfrutado de grandes momentos que me han venido muy bien para afrontar el doctorado. Gracias por todo chicos. Tampoco podría olvidarme de mis chicas de inglés (**Ane, Arrate, Alba** y **Ainara**), gracias por todas las conversaciones que hemos tenido, sois geniales e increíbles.

También me gustaría agradecer a todas las personas que durante estos años he podido conocer gracias a los viajes de voluntariado que he podido hacer, en los que he descubierto que es necesario salir a veces del laboratorio para conocer la realidad que tenemos e intentar poner un granito de arena. Gracias a mi compañera de viajes **Amaia, a Claudia, Silvia, Ana, Elisa, Paula, Andrea, Jaime, Maca, Paula, Joan** y muchos más.

Asimismo, me gustaría agradecer todo el apoyo a **Enrique**. Gracias por ser como eres, tener la paciencia que tienes conmigo, a veces no ha sido fácil y sobre todo por haber hecho que estos dos años y medio a tu lado hayan sido maravillosos y especiales. Te quiero muchísimo.

Por último, agradecer a **mis padres, a mi hermano Xiker** y **al resto de mi familia**, sus ánimos infinitos, sin ellos, sin duda, no habría conseguido lo que he conseguido. Gracias por como sois y por estar siempre a mi lado, en las buenas y en las malas, os quiero.

TABLE OF CONTENTS

ABBREVIATIONS

3OH-But: 3-hydroxybutyrate

Ace: Acetate

AKP: Alkaline phosphatase

Ala: Alanine

ALA: Aminolevulinate

ALT: Alanine aminotransferase

AQ: Acquisition time of the FID

ARA: Arachidonic acid

AST: Aspartate aminotransferase

ATP: Adenosine 5´-TriPhosphate

AUC: Area Under the Curve

BML: Birmingham Metabolite Library

BMRB: Biological Magnetic Resonance Bank

CDAA: Choline and L-amino acid defined diet

CDAHFD: Choline-deficient, L-amino acid defined, high-fat diet

CDD: Choline-Deficient Diet

CDHF: Choline-Deficient High-Fat Diet

CEP: Congenital Erythropoietic Porphyria

CHO: Choline

COPROI: Coproporphyrin I

CPX: Ciclopirox

Cre: Creatine

D_1: Relaxation delay

D_6-DMSO: Dimethyl sulfoxide d_6

DHA: Docohexenoic acid

EDTA: Ethylenediaminetetracetic acid

Eth: Ethanol

EWAT: Epididymal white adipose tissue

FA: Fatty Acids

FID: Free Induction Decay

For: Formate

FT: Fourier Transform

G3P: Glyceraldehyde 3-Phosphate

GC-MS: Gas Chromatography Coupled to Mass Spectrometry

Gdbut: Gadobutrol

Gdter: Gadoteridol

Glc: Glucose

Gln: Glutamine

GPC: GlyceroPhosphoCholine

GPE: GlyceroPhosphoEthanolamine

GSH: Glutathion

GSSG: Glutathione oxidized

HCC: HepatoCellular Carcinoma

HFD: High-Fat Diet

HMB: HydroxyMethylBilane

HMBC: Heteronuclear Multiple Bond Correlation

HMDB: Human Metabolome Database

HSQC: Heteronuclear Single Quantum Correlation

Ile: Isoleucine

Ino: Inosine

InvRec: Inversion Recovery

KEGG: Kyoto Encyclopaedia of Genes and Genomes

LAC: Lactate

Leu: Leucine

LPC: LysoPhosphatidylCholine

MAT1A-KO: Methionine Adenosyltransferase 1A Knockout

MDB: Mallorty-Denk Body

Met: Methionine

MS: Mass Spectrometry

MUFA: MonoUnsaturated Fatty Acids

NADH: Nicotinamide Adenine Dinucleotide

NADPH: Nicotinamide Adenine Dinucleotide Phosphate

NAFLD: Non-Alcoholic Fatty Liver Disease

NASH: Non-Alcoholic SteatoHepatitis

NFA: Non-esterified Fatty Acids

Nia: Niacinamide

NMR: Nuclear Magnetic Resonance

NOE: Nuclear Overhauser Effect

NS: Number of Scans

OPLS-DA: Orthogonal Partial Least Squares for Discriminant Analysis

PAA: PhosphoAcetic Acid

PC: PhosphatidylCholine

PCA: Principal Component Analysis

PDE: PhosphoDiEsters

PDGF: Platelet-Derived Growth Factor

PE: PhosphatidylEthanolamine

PEMT: PhosphatidylEthanolamine *N*-MethylTransferase

Phe: Phenylalanine

PL: PhosphoLipids

PLS-DA: Partial Least Squares Projection Discriminant Analysis

PME: PhosphoMonoEsters

PPARα: Proliferator-Activated Receptor α

PPP: Pentose Phosphate Pathway

PUFA: PolyUnsaturated Fatty Acids

PYR: Pyruvate

RBC: Red Blood Cells

RP: Radiofrequency Pulse

RG: Receiver Gain

ROC: Receiving Operating Characteristic

S/N: Signal-to-noise *ratio*

SAMe: S-AdenosylMethionine

SFA: Saturated Fatty Acids

SMPDB: Small MoleculePathway Data Base

SOP: Standard Operating Procedures

Succ: Succinate

SW: Spectral Window

T2D: Type 2 diabetes mellitus

TC: Total Cholesterol

TCA: TriCarboxylic Acid

TG: TriGlycerides

TGF-β: Transforming Growth Factor-β

TMP^+: TetraMethylPhosphonium chloride

TNF-α: Tumor Necrosis Factor-α

TOCCATA: TOCSY Customized Carbon Trace Archive

Tyr: Tyrosine

UDPG: Uridine DiPhospho Glucose

UFA: Unsaturated Fatty Acids

Uri: Uridine

URO I: Uroporphyrinogen I

URO IIIS: Uroporphyrinogen III synthase

UV: Ultraviolet radiation

VIP: Variable Importance in Projection

VLDL: Very Low Density Lipoproteins

WT: Wild Type

α-SAM: α-Smooth muscle actin

CHAPTER 1

GENERAL INTRODUCTION

1.1 Introduction to metabolomics

Advances in high throughput technologies have revolutionized biomedical research, leading to a substantial rise in investigations in the field. The isolated study of genes, mRNA, proteins, and metabolites have been displaced using omics sciences[1], which encompass genomics, transcriptomics, proteomics and metabolomics[2] respectively. The basic principle of omics sciences is based on studying biological systems, acquiring the data to define a subsequent hypothesis[3]. These omics sciences take a holistic view, and the information obtained through the omics sciences, from genes to metabolites, passing through transcripts and proteins, gives rise to numerous connections called networks. Nowadays, there are numerous software to obtain networks that allow to integration and visualization of all the omics data (Cytoscape[4], OmicsNet[5], mixOmics[6], MultiDataSet[7], among others) as well as to correlate all the information to determine the biological pathways involved and altered in a certain organism under specific physiological and pathological conditions[8].

Likewise, alterations in the metabolome reflect the *status quo* in the living organism and the current manifestation of previously described omics. Thus, any change detected in the metabolome or in the levels of the metabolites that form it, represents an alteration in the dynamic state of the organism and directly reflects the biochemical activity at that precise moment. These alterations, which are reflected in the metabolome, can occur due to changes induced by diseases, drug treatments, life habits, environment, or diets[9] (**Figure 1.1**).

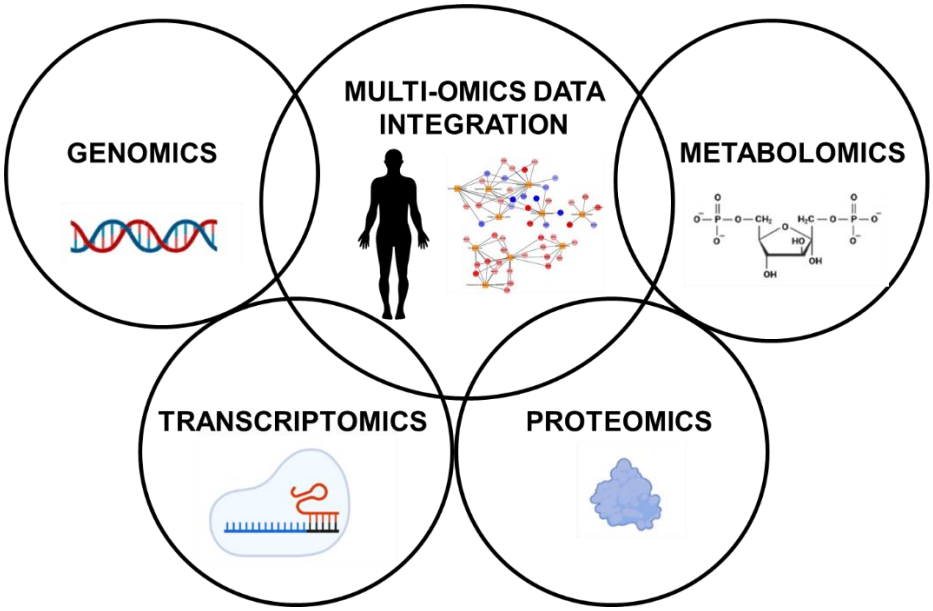

Figure 1.1. Representation of the cascade of omics sciences, from genes to metabolites, passing through transcripts and proteins.

The metabolome is a set of low molecular weight molecules or metabolites (< 1500 Da) produced by the cells of an organism[10,11]. These metabolites, defined as the final product of a metabolic process essential for maintenance, growth, and cellular functionality, constitute the final response of a biological system to genetic or environmental changes[12]. The metabolites that make up the metabolome can be classified into (1) *endogenous compounds*, originated mostly from enzymes encoded in the genome, and include precursors, intermediates, and final products of metabolic pathways, as well as hormones; (2) *exogenous compounds*, from ingestion or contact with external factors and (3) *microbiota compounds*, the chemical compounds that can alter gut microbiota diversity. Consequently, the metabolome is a group of metabolites of a diverse nature (amino acids, fatty acids, lipids, alkaloids, among others) with high structural heterogeneity, differences in physicochemical properties (polarity, charge, solubility, volatility, stability) ,and concentration levels[13]. All these qualities make the determination and identification of metabolites an analytical challenge[11] (**Figure 1.2**).

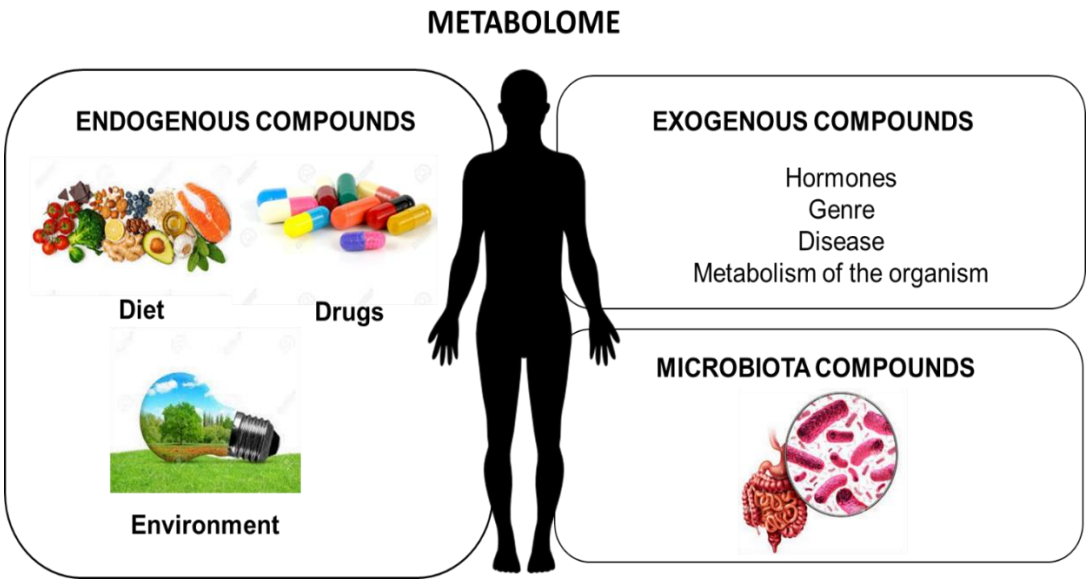

Figure 1.2. Composition and factors that influence the metabolome, such as exogenous compounds (diet or drugs), environment, endogenous compounds (hormones, genre, disease, or metabolism of the organism) and microbiota compounds.

Considering the concepts of metabolome and metabolite, metabolomics is defined as the study of the entire set of metabolites of a certain organism under certain conditions[14,15]. However, different definitions and terms are been found in the literature that refer to the study of the metabolome and that vary depending on the field of application (**Table 1.1**).

Nevertheless, in biomedical research, metabolomics has been extensively employed due to the advantages that it presents over other omics sciences. In this sense, one of

its main advantages is its proximity to the phenotype. In addition, it is the result of what happens in the organism at previous molecular levels (genes, transcripts, and proteins)[2] but with a decrease in the complexity of the information to be processed[16].

Table 1.1. Definitions and concepts associated with the study of the metabolome and its metabolites.

Term	Definition
Metabolomics	It evaluates the changes that occur in the levels of metabolites of tissues and biofluids because of a disease, a stimulus, or a pharmacological treatment[17–19].
Metabonomics	It measures the dynamic metabolic response of living systems to biological stimuli, focusing on understanding systemic change through time in complex multicellular systems[20].
Metabolic profiling	Analysis focused on the identification and quantification of a certain group of pre-established metabolites. Normally, they are related to a specific metabolic pathway or certain group of compounds, for example, carbohydrates, amino acids, etc[17,18].
Metabolic fingerprinting	Global analysis of samples to classify them according to their origin or their biological relevance. Metabolic quantification or identification is not carried out[17,18].
Metabolic footprinting	Strategy for determining the properties of a cell or tissue by analyzing excreted or incorporated metabolites from its environment, as in the case of a culture medium[21,22].

Besides the concepts outlined in **Table 1.1**, metabolomics can be categorized into two distinct approaches: untargeted metabolomics and targeted metabolomics. On one hand, *untargeted metabolomics* aims to analyze simultaneously the largest possible number of metabolites, often unknown, in a matrix to generate a new hypothesis, discover new biochemical interactions or find new biomarkers of the biological state of the organism (**Table 1.2**). On the other hand, *targeted metabolomics* focuses on analyzing specific metabolites, previously defined or with an stablished hypothesis, which are associated with a specific metabolic pathway, an enzymatic system, or a certain class of metabolites[23].

Table 1.2. BIOMARKER definition[24]
The Food and Drug Administration (FDA) defines a biomarker as[25] "*A defined characteristic that is measured as an indicator of normal biological processes, pathogenic processes or responses to an exposure or intervention, including therapeutic intervention".* In metabolomics, a biomarker is the significant metabolite, identified and confirmed with standards, in addition to meeting what is defined by the FDA. Likewise, biomarkers can be subdivided into classes depending on their application (diagnostic biomarkers, monitoring biomarkers, pharmacodynamics response biomarkers, predictive biomarkers, risk biomarkers, etc.).

1.2 Metabolomics workflow

During this chapter, the different stages of the workflow used in metabolomics will be explained (**Figure 1.3**).

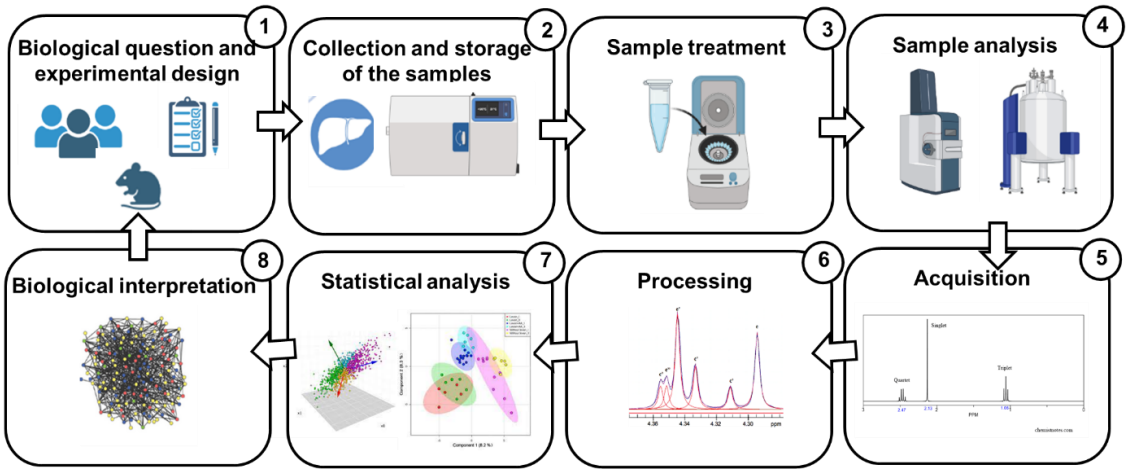

Figure 1.3. Diagram of the workflow in metabolomics.

1.2.1 Biological question and experimental design

In any metabolomics study, it is crucial to first establish the biological question being addressed. With that determined, a well-designed experiment is essential, defined as "the data collection design of the study that assesses all possible sources of variation, and which is used to obtain reliable results"[26]. In fact, a poor experimental design can lead to not very robust results, lack of reproducibility and an economic and time loss. On the other hand, a good experimental design involves selecting and use of samples effectively to answer the biological question of the study. Ideally, all sources of variation should be controlled except for those of interest, although this is not always feasible.

When controlling sources of variation is challenging, maintaining representativeness between samples from different groups is critical. Finally, there are extrinsic sources of variation that are very difficult to control (for instance, diet or life habits); in these cases, it is vital to collect this information as it could be critical for the outgoing research purpose.

One of the most critical aspects of an experimental design is the suitable sample size for the study. The number of samples and the group sizes depend on the biological variability associated with the system being studied. If the samples come from controlled environments, such as cell cultures, few samples are needed per group (3-5 samples). Nevertheless, in less controlled environments, like animal models that are more complex, it requires a larger sample size (between 5 and 12 samples)[26] although it is important to be conscientious when deciding on the number of samples, as animal sacrifice is often necessary). In the literature, it is possible to find many approximations to calculate the minimum number of samples that provide good statistical power[27,28] and normally the justification of the number of the samples is an essential requirement for overcoming the Ethics Committees associated with biological sample studies.

1.2.2 Collection and storage of the simples

Sample handling, either collection or storage, can significantly affect the results of a metabolomics study. For that reason, it is essential to carry out specific protocols and standard operating procedures. The process includes all the steps prior to the measurement of the samples such as the collection, storage, treatment, and extraction of metabolites. In this section, it will discuss the collection processes and sample storage.

The collection of biological samples is usually carried out by personal specializes, normally, outside of the laboratory. The choice of the type of sample, the moment of sample collection and the sampling method must be specified.

Given that metabolomics is an accurate picture of the metabolite levels at a given time, and the biological samples consist of a dynamic metabolic process, it is necessary to establish a guideline to prevent changes related to the undesired enzymatic activity, sample degradation or ischemia. Per se, the composition of the metabolome obtained in the analysis represents the exact metabolome at the time of metabolic extraction and could not necessarily correspond to the sample collection. Thus, fast handling of the samples and the possible freezing of them is highly recommended.

In this doctoral thesis, the liver has been extensively used as the primary tissue; therefore, the collection and storage of this specific sample be discussed.

The liver, like other tissues, should be collected in a fast way to avoid changes in metabolites by enzymatic activity. One of the most common ways to inhibit enzymatic activity is to drastically reduce the temperature immersing the tissue directly in liquid nitrogen[29–31].

The liver samples in this study have been stored at -80°C, a condition widely employed in metabolomics research for preserving this type of samples[30].

1.2.3 Sample treatment

Sample preparation is a crucial stage in the metabolomics workflow, prone to introducing variability and error[32]. For this reason, it is vitally important to use a protocol that ensures reproducible sample preparation.

Biological samples are inherently complex, normally composed of low molecular weight molecules, both organic and inorganic that include lipids, salts or hormones, and high-weight molecules such as proteins[33]. The choice of sample treatment will depend on several factors including the type of metabolites of interest, the sample or biological matrix and the analysis technique employed. Obtaining the largest possible number of metabolites from the liver requires treatment of a sample that modifies the original sample as little as possible as well as it would be fast and reproducible.

In the case of the liver, a homogenization process is necessary prior to the extraction of the metabolites and various studies evaluating different extraction solvents and conditions have been found in the literature[34,35].

1.2.4 Sample analysis

As it has been previously commented, metabolites are part of different molecular families which have very different physicochemical properties. This makes it impossible to measure all metabolites present in a biological sample by a single analytical technique. Therefore, it is essential to combine different techniques to fully capture the complexity of the metabolome[36].

Overall, the metabolic profiling is primarily conducted using two analytical platforms, nuclear magnetic resonance (NMR)[37,38] and mass spectrometry (MS)[39,40], each with its own set of advantages and disadvantages (**Table 1.3**).

Table 1.3. Summary of the most important advantages and limitations of NMR spectroscopy compared to MS in metabolomics studies[41].

	NMR	MS
Reproducibility	High reproducibility	If it is compared with NMR, it is less reproducible
Sensitivity	Lower sensitivity although it can enhance by using multiple scans (time), higher magnet field strength and cryo-cooled probes	Higher sensitivity, in fact, metabolites with nanomolar concentrations can be identified
Sample measurement	All metabolites which have detectable concentration values can be detected in one measurement	Different ionization methods are needed to detect as much metabolites as possible
Sample preparation	It involves minimal sample preparation, which sometimes can be automated	It is more complex because it requires chromatography as well as derivatization processes for gas chromatography (GC)-MS
Sample recovery	Non-destructive	Destructive

Given the advantages, during this thesis NMR will be used as analytical technique. Subsequently, a brief explanation of its technical principles will be provided.

1.2.4.1 Basic principles of NMR

NMR is considered as a spectroscopy approach through the detection of energy states transitions (FID) of some nuclear spin state once have been applied an electromagnetic pulse under the influence of a magnetic field.

The NMR phenomenon depends on a quantum mechanical property of atomic nuclei known as nuclear spin (I). Nuclei have positively charged particles and they create a magnetic field consequently as any particle which has the capability to gyrate. The orientation and magnitude of magnetic angular (μ) are determined by its spin, in the case of a single nucleus. Likewise, the angular momentum that a nucleus with a spin quantum number other than zero assumes when it is introduced into a stronger magnetic field

depends on the magnetic quantum number (m). As a result of having an unpaired proton, all these odd mass number nuclei, including ^{1}H, ^{13}C, ^{15}N or ^{31}P (I = ½), produce magnetic dipoles. Under these circumstances, the Zeeman effect predicts that nuclei will only divide into two energy states in the presence of the magnetic field: m = -½ (higher energetic level), m = +½ (lower energetic level).

Under the influence of a magnetic field B_0, these dipolar nuclei split into two different energetic states (Zeeman effect): one where the magnetic momentum is aligned to the magnetic field (m = +½; higher energy state), and the other one with opposite orientation (m = -½; lower energy state) (**Figure 1.4**). μ is dependent on the constant gyromagnetic ratio γ, spin number (I) and $\hbar = h/2\pi$ in which h is the Planck´s Constant ($6.626.10^{-34}$. J.s).

$$\mu = \gamma . I . \hbar$$

Energy levels, previously discussed, are quantized and the difference between the two levels will depend on the constant gyromagnetic ratio γ and the magnetic field (B_0), as it has been defined in **Equation 1.1**.

$$\Delta E = h . v = \hbar . \gamma . B_0$$

Equation 1.1. Nuclear energetic transitions where are equivalent to Larmor frequency (v) and Planck´s constant (h = $6.626.10^{-34}$. J.s)

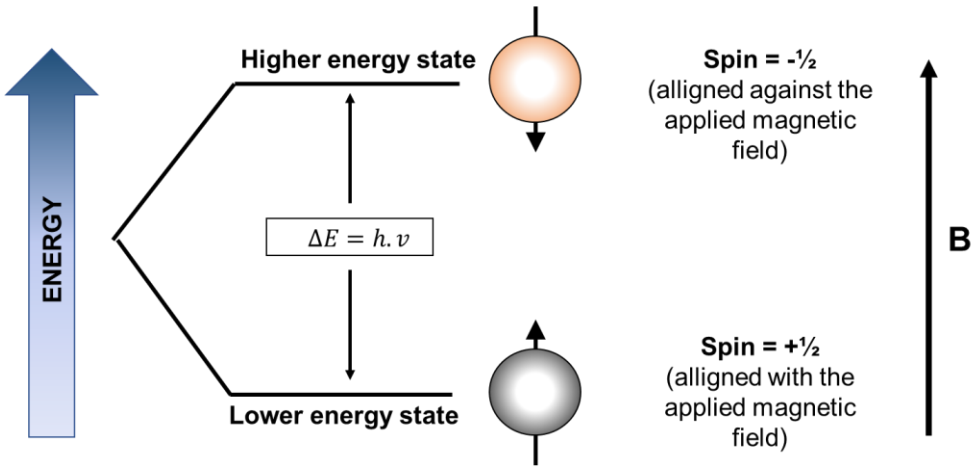

Figure 1.4. Spin precession and energetic diagram.

The frequency range and resolution increase in direct proportional to the size of the magnetic field. Even though there have been many progresses made to generate stronger magnets, the population differences between the two energetic levels are still relatively small. Therefore, NMR is a low-sensitivity technology, that needs to perform the same experiment many times to raise the signal-to-noise *ratio*. Other alternatives for

improving its sensitivity could be to increase the nucleus concentration or sample volume.

According to quantum physics, when measuring the z component, it is unable to measure the spin rotation components in the x and y axes. Depending on the resonance frequency, the magnetic moments oscillate about the z-axis. Spin-precession is the term of this phenomenon. As previously discussed, when we apply a radiofrequency pulse (RP), populations of the various energy levels are changed, and as a result, the orientation of the net magnetic moment also changes.

Net longitudinal magnetization along the z-axis changes into transversal magnetization on the xy plane when the oscillation precession of the spin-precession equals the Larmor frequency. The magnetization then oscillates with an offset to the nuclei´s resonating frequency and Larmor frequency. The sample´s magnetization stays in the xy plane and continues to process regarding the static field after the RP has finished. This precession continues until the spin system achieves thermal equilibrium along the z-axis, at which point Free Induction Decay (FID)), is produced (**Figure 1.5**). However, the FID displays a time-domain signal that includes contributions from several nuclei. The FID is Fourier-transformed to transform this into a frequency-domain spectrum, or the more well-known NMR spectrum.

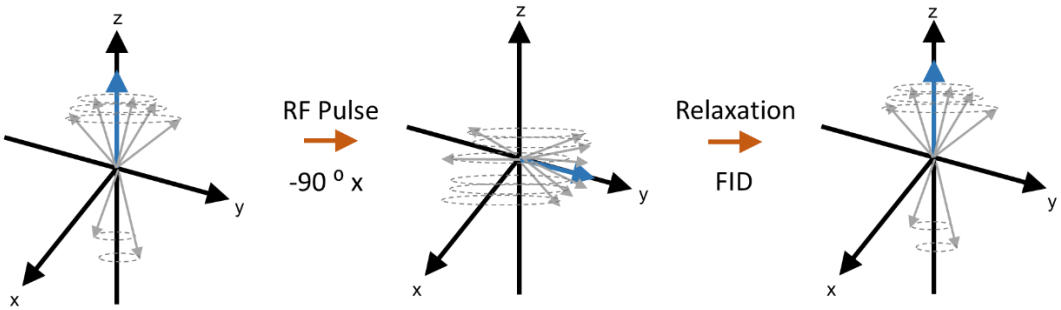

Figure 1.5. Magnetic moment perturbation and relaxation. At Larmor frequency, each magnetic moment (shown by a grey arrow) precession oscillates around the z-axis. Net magnetization is parallel to the field (blue arrow). Individual magnetic moments' z and y components are shifted to the y axis after a radiofrequency pulse at Larmor frequency along the x axis, where they continue to process around the z axis at Larmor frequency. The spin system emits radiofrequency signals (FID) after the RF pulse to regain thermal equilibrium in the z plane, which are then recorded and analyzed.

Steric and electronic effects are very sensitive to resonance frequencies (v). Thus, they are dependent on the magnetic fields surrounding the observed nuclei (B_{local}) as well as their exposure to the solvent (B_0), and the local magnetic field that is influenced by the external magnetic field (B_0). As a result, it would anticipate that the observed magnetic field would be ($B_{local} = B_0 + B_{induced}$) and each of the nuclei under study has a unique

distinctive resonating frequency (v). Because of this, nuclei in various chemical shift settings will resonate at various frequencies, which are more commonly referred to as chemical shifts (δ) (**Equation 1.2**).

Chemical shifts are measured in MHz and depend on the magnetic field. However, MHz is given as parts per million (ppm) to facilitate a homogeneous comparison.

$$\text{Chemical shift}, \delta(ppm) = \frac{v_0 - v_{REF}}{Spectrometer\ frequency\ (MHz)} . 10^6$$

Equation 1.2. Chemical shifts in ppm. Derived by subtracting the resonance frequency from a reference molecule (such as tetrametylsilane (TMS) or a comparable compound) and normalizing the result by the spectrometer's frequency.

1.2.4.2 ^{1}H-NMR

^{1}H-NMR spectroscopy is widely used in most NMR-based metabolomics studies. Indeed, ^{1}H atoms are found in many metabolites, especially in those which are organic compounds. **Figures 1.6 and 1.7** illustrate an example of a one-dimensional 1D ^{1}H-NMR spectrum collected from mouse liver that contain 29 aqueous metabolites and 8 lipid classes[42].

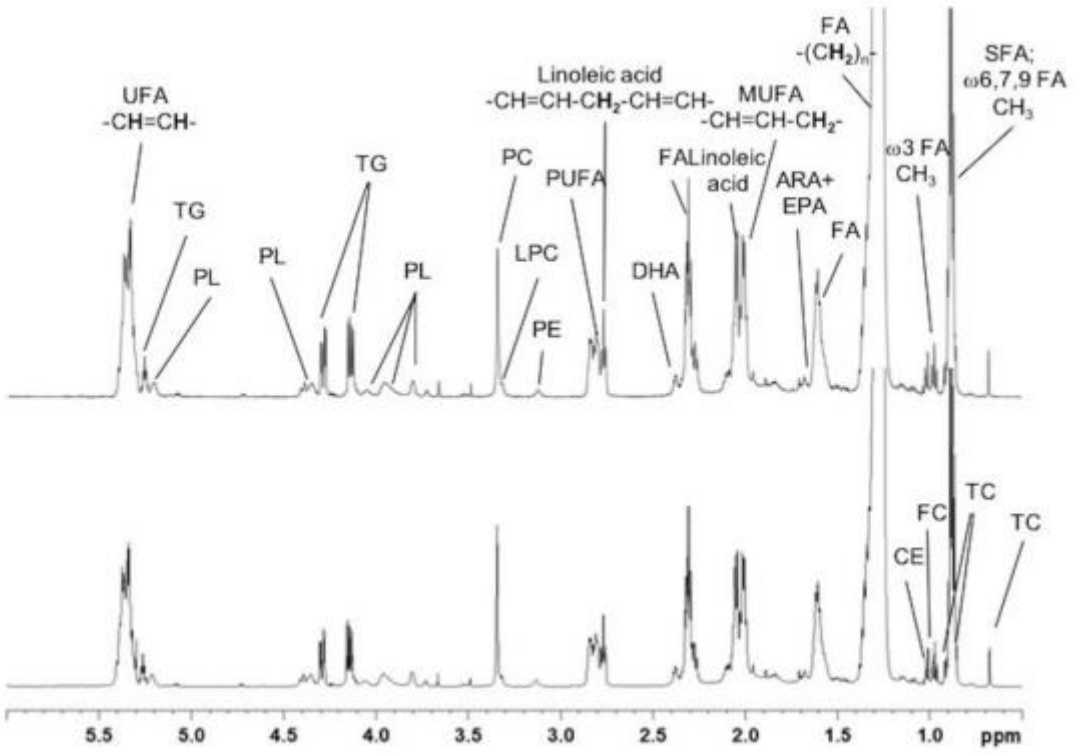

Figure 1.6. ^{1}H spectra of lipophilic extract from mouse liver samples. The peaks were assigned as follows: FC, free cholesterol; CE, cholesterol ester; TC, total cholesterol; FA, fatty acids; SFA, saturated fatty acids; ARA, arachidonic acid; EPA, eicosapenenoic acid; MUFA, monounsaturated fatty acids; DHA,

docosahexenoic acid; PUFA, polyunsaturated fatty acids; PE, phosphatidylethanolamine; LPC, lysophosphatidylcholine; PC, phosphatidylcholine; PL, phospholipids; TG, triglycerides; UFA, unsaturated fatty acids[42].

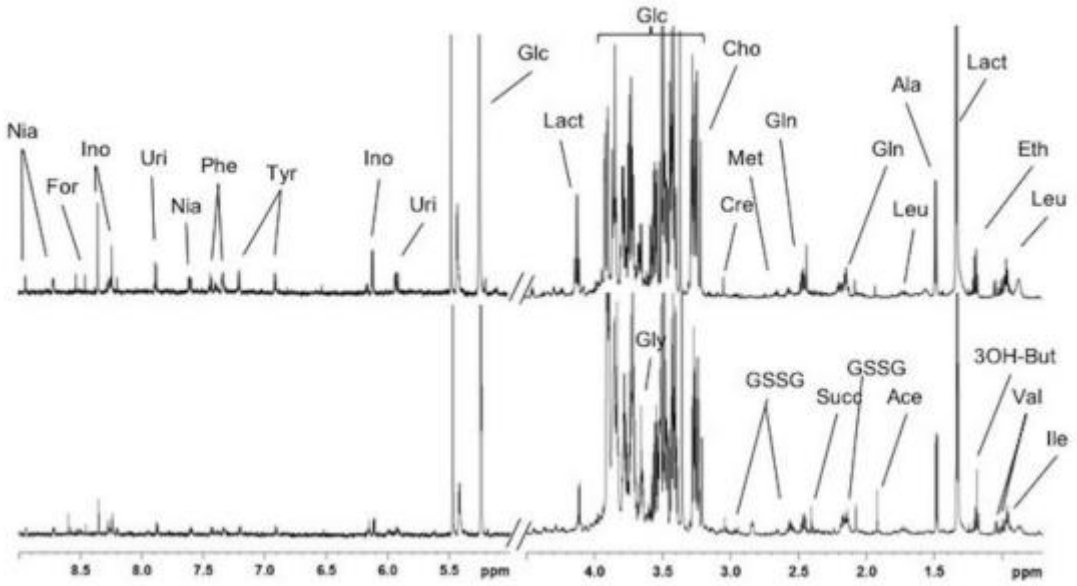

Figure 1.7. ^{1}H-NMR spectra of aqueous extracts from mouse liver samples. The peaks were assigned as follows: Ile, isoleucine; Val, valine; 3OH-But, 3-hydroxybutyrate; Ace, acetate; GSSG, glutathione oxidized; Succ, succinate; Gly, glycine; Leu, leucine; Eth, ethanol; Lact, lactate; Ala, alanine; Gln, glutamine; Met, methioninie; Cre, creatine, Cho, choline; Glc, glucose; Uri, uridine; Ino, inosine; Tyr, tyrosine; Phen, phenylalanine; Nia, niacinamide; For, formate[43].

As it can be observed in these spectra each distinct signal corresponds to one or more hydrogen atoms within their chemical structures. Likewise, there are some advantages of using ^{1}H-NMR spectroscopy, such as the signal intensity, its high isotopic natural abundance (about 99%) and its narrow line widths (often below 1Hz). The identification of the metabolites is aided by the fact that chemical shifts of standard compounds ^{1}H-NMR spectra from a vast collection of known metabolites have been already stored and purged in a large number of public databases[42]. In addition, numerous software tools exist for automated or semi-automated processing and analysis of 1D ^{1}H-NMR spectra, which allows the identification and quantification of metabolites[43,44].

Considering that a significant portion of spectra acquired for metabolomics studies are in aqueous solutions, solvent suppression is an important consideration. To overcome this, depending on the nature of the metabolites under study, different approaches can be employed[45,46].For instance the use of deuterated solvents (D_2O instead of H_2O) can be adopted when interested only in non-exchanging protons in a sample.). Additionally,

a variety of NMR pulse sequence techniques are available to further address this issue.[45,46].

Although it is more common to conduct fast 1D-^{1}H experiments without taking time to reanalyze the sample using 2D correlation experiments, 2D correlation experiments offer substantially more resolving power[47]. This includes pulse sequences such as 2D ^{1}H,^{13}C-heteronuclear single quantum correlation spectroscopy (HSQC), heteronuclear multiple bond correlation (HMBC), correlation spectroscopy (COSY), total correlation spectroscopy (TOCSY)[47–49], among others. One of the greatest strengths of these experiments is that it is possible to characterize novel compounds, positively identify known compounds or uncover previously undetected compounds.

1.2.4.3 ^{31}P-NMR

Although there are many advantages of ^{1}H-NMR spectroscopy, certain limitations should be acknowledged. One major drawback is the narrow chemical shift window, leading to a high possibility of overlapping peaks. This overlap can induce significant uncertainty in both identification and quantification of the chemical compounds.

On the other hand, ^{31}P-NMR is a particularly interesting nucleus to be studied by NMR. It has a natural abundance of 100% and has a relatively large gyromagnetic constant, approximately 40.4% with respect to ^{1}H, which makes it highly receptive to radio-frequency energy. Because of its electronic density, it has a greater range of chemical shift values, which allows a greater dispersion in the signals, avoiding overlapping. Its nuclear spin is ½, which simplifies spectral interpretation. As each ^{31}P nucleus responds independently to the NMR experiment, it provides a direct, quantifiable readout of its local molecular environment. This makes ^{31}P-NMR particularly well-suited for studying biochemical and organic systems, as phosphorus is a key constituent in many biological compounds such as DNA, RNA, and ATP.

However, one disadvantage is that the relative sensitivity of ^{31}P is less than ^{1}H. Therefore, to ensure sufficient signal intensity, it is recommended to use concentrated samples and a specific NMR probe tailored for the detection of this nucleus. During this thesis, the focus will be on the ^{31}P nucleus and its significant role in our studies.

1.2.4.3.1 ^{31}P-NMR in the liver

The liver is of particular interest due to its high content of phosphorylated compounds. More than a century ago, Lean and Williams in 1909 concluded that phospholipids made up 84% of the total lipids in the liver[50]. In the 1980s, the lipid and nucleoside composition of the liver was analyzed by resonance imaging for the first time[51,52]. Since then, a great

commitment has been made to the implementation of this technique in the diagnosis of different liver diseases, both *in vivo* and *in vitro* (**Figure 1.8**).

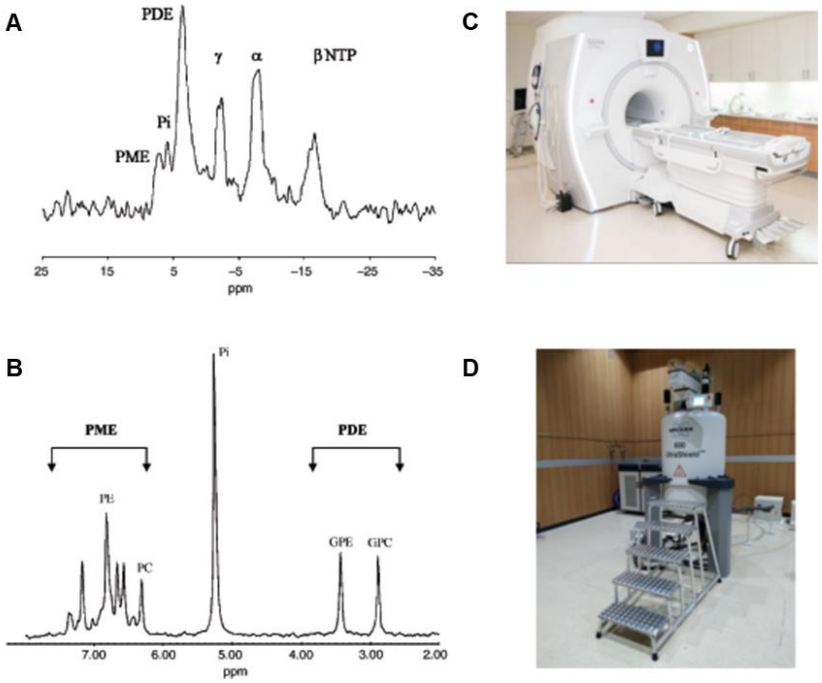

Figure 1.8. A, B) Examples of phosphorus spectra acquired *in vivo* and *in vitro* respectively. C) The *in vivo* spectrum was acquired using a 1.5 tesla magnetic field. D) The *in vitro* spectrum was acquired in a field of 11.7 tesla. *In vitro* experimentation allows reaching a higher resolution and sensitivity. Abbreviations: phosphomonoesters (PME); phosphodiesters (PDE); phosphoethanolamine (PE); phosphocholine (PC); inorganic phosphate (P_i); glycerophosphoethanolamine (GPE); glycerophosphocholine (GPC). Figure adapted[53].

Non-alcoholic fatty liver disease (NAFLD) is a high prevalent chronic liver disease which is extended from a simple non-alcoholic fatty liver (NAFL), non-alcoholic steatohepatitis (NASH) with different degrees of fibrosis to cirrhosis, which is the major risk factor for hepatocellular carcinoma (HCC). According to different studies, 25% of the population develops NAFL. About 25% of individuals with NAFL can progress to NASH, and 25% of them evolve to cirrhosis. Finally, only 1-2% of these patients develop HCC[54,55]. The main factors that are involved are obesity, type 2 diabetes mellitus (T2D) and dyslipidemia. Currently, liver biopsy is necessary for differentiating simple steatosis from NASH. Although several biomarkers have shown a relative utility for the differentiation in different stages of the disease[56] none of them have been validated yet. Thus, there is an urgent need to provide new biomarkers that could easily report the stage in which a NAFLD patient is developing. At the moment, there are no approved therapies for NASH[57], being only lifestyle changes the therapeutic approach that can stop the progression of NAFLD[58].

Some investigators[59] compared the absolute concentration of phosphorylated metabolites (Phosphomonoesters (PME), Inorganic phosphate (Pi), Phosphodiesters (PDE), Adenosine 5´-triphosphate (ATP)) of human liver biopsies in three groups; 1) steatosis without severe inflammation (NAFLD); 2) severe fibrosis and cirrhosis; and 3) the control groups. In addition, anabolic charge parameter, AC = (PME)/(PME)+(PDE) was calculated. When they compared cirrhosis and control samples, they found lower levels of PDE and higher levels of CA in cirrhotic samples. At the same time, when they compared NAFLD group with a cirrhotic group it was shown the same outcome whereas there were not any differences between the controls and NAFLD [60]. Thus, PDE and AC could be used as a biomarker to differentiate mild fibrosis from advanced.

Sevastianova *et.al*[60] tried to differentiate between stages of NAFLD by using ^{31}P-NMR *in vivo* spectroscopy. The PME/ (PME + PDE), PME/PDE and PE/ (PME + PDE) *ratios* were higher and GPC/(PME + PDE) *ratio* was lower in patients with cirrhosis than the rest of the groups studied. Meanwhile, the NADPH/ (PME + PDE) *ratio* was higher in patients with NASH and cirrhotic group than in control subjects. Therefore, they concluded that NADPH, a biomarker of inflammation, was increased in patients with NASH and those with cirrhosis being ^{31}P-NMR *in vivo* a promise spectroscopy technique to differentiate NAFLD stages (**Figure 1.9**).

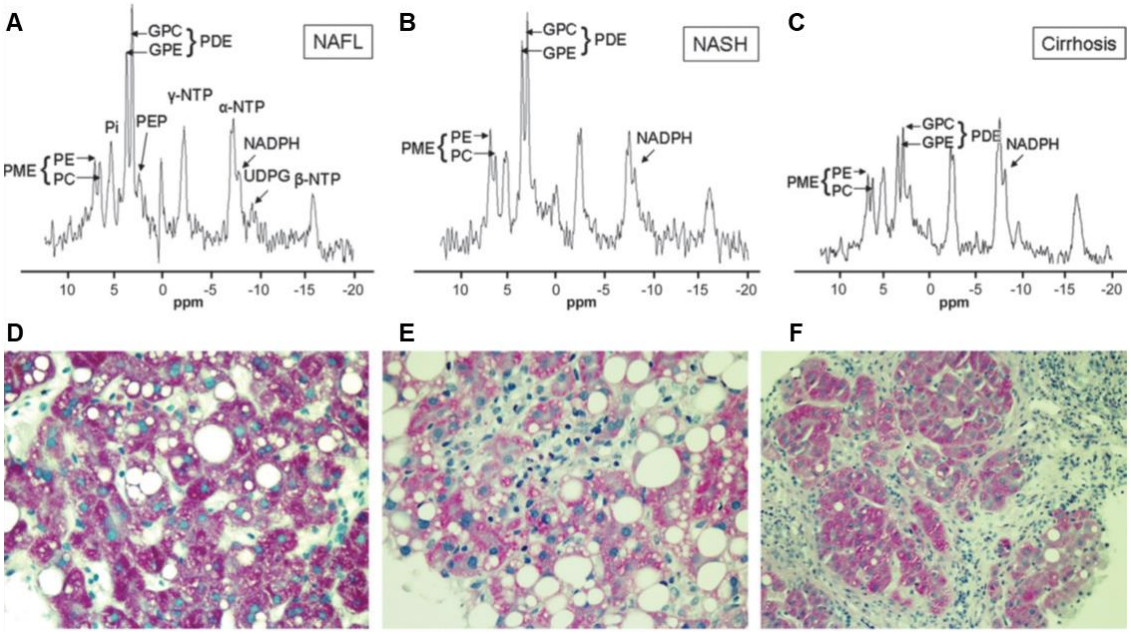

Figure 1.9. A-C) *In vivo* phosphorus spectrum of a patient with NAFLD, NASH and cirrhosis respectively. D) Histology corresponding to the NAFLD patient, where fatty accumulations can be observed. E) NASH with pericellular fibrosis, inflamed hepatocytes, and inflammatory cells. F) Cirrhosis with extensive fibrosis. Abbreviations: phosphomonoesters phosphoenolpyruvate (PEP); γ-nucleoside triphosphate (γ-NTP); α-nucleoside triphosphate (α-NTP); nicotinamide adenine dinucleotide phosphate (NADPH); uridine

diphosphoglucose (UDPG); β-nucleoside triphosphate (β-NTP); non-alcoholic fatty liver (NAFL); non-alcoholic steatohepatitis (NASH). Figure adapted[60].

Traussningg *et al.*[61] explored ^{31}P-NMR *in vivo* to know alterations of hepatic lipid, cell membrane and energy metabolism in the spectrum of NAFLD. They used biopsies of patients with NAFL or NASH and measured their levels of PME (PE) and PDE (GPC, PCr, NADPH, P_i, Υ-ATP and total phosphorus (TP). They observed an increase of PE/TP *ratio,* a marker of cell membrane turnover, with advanced fibrosis. The GPC/PME + PDE *ratio*, a marker of cell membrane breakdown products, decreased compared to no/mild fibrosis. The Υ-ATP/TP *ratio* was lower in advanced fibrosis and NADPH/TP *ratio* increased with high grades of ballooning. Both *ratios* are biomarkers of hepatic energy metabolism (**Figure 1.10**).

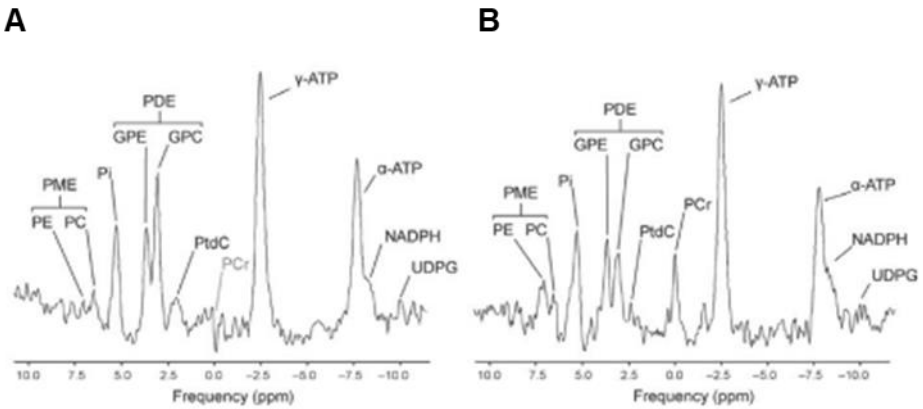

Figure 1.10. ^{31}P-NMR spectra from patients with A) NAFL (no/mild fibrosis) and B) NASH (advanced fibrosis). Figure adapted[61].

Likewise, the phosphorome has not only been analyzed *in vitro* and *in vivo* in the liver, but also it has been analyzed in other tissues such as the brain[62], kidney[63], heart[64], stomach[65] or breast[66].

In Chapter 4, we will apply ^{31}P-NMR methodology with the aim of analyzing the liver phosphorome of two dietary models of NASH to better understand the metabolic state of this liver disease over time.

1.2.4.4 Standard Operating Procedure (SOP)

Standard Operating Procedures (SOPs) are specific procedures that describe the necessary protocols to minimize both random and systematic variation in metabolic profiles[67]. Moreover, standardized reporting is vital to enable researchers to compare and merge results from numerous studies[68]. Therefore, SOPs are a hallmark of metabolomics pipelines, with the objective of ensuring statistically significant detection of experimental differences.

Significant advances have been made in the development of SOPs for ^{31}P-NMR[69]. However, challenges remain, especially in relation to the quantitative ^{31}P-NMR methodology. This is since ^{31}P-NMR signals shift and broaden according to diverse parameters that need to be controlled, such as solvent, pH, type and concentration of salt, or temperature.

In Chapter 5, it will delve into these challenges and explore the latest advancements and improvements in ^{31}P-NMR methodology. It will discuss new techniques and strategies to control these variables effectively and how these developments are enabling more accurate, repeatable, and reliable analysis of phosphorus-containing compounds.

1.2.5 NMR acquisition

To effectively compare NMR data, experimental conditions during acquisition must be standardized. The main parameters that dictate the nature and quality of a spectrum are outlined in **Table 1.4**.

Table 1.4. Definitions and concepts associated with NMR acquisition.

Term	Definition
Spectral Window (SW)	It establishes the range of frequencies to be observed.
Acquisition time of the FID (AQ)	It must be enough to maximize the amount of signal that is contained in the FID and ensures good resolution.
Relaxation delay (d1)	It corresponds to the return to equilibrium of the magnetization vector before each new sequence of pulses. It is strongly recommended to wait 3 times the value of the highest T_1 to obtain the complete return of the magnetization vector after a 90 ºC pulse.
Number of scans accumulation (NS)	With the aim of improving the sensitivity, a series of n pulses can be applied after the recording of the first signal allowing the recording of n signals which will accumulate before obtaining the spectrum. The signal-to-noise *ratio* (S/N) will be proportional to √n, many accumulations will correspond to a better S/N.
Receiver gain (RG)	It controls the amplitude of the FID which itself depends on the concentration of the sample. The optimum gain determined corresponds to the maximum value obtained for the intensity of the strongest signal.

Pulse width	It defines the time required to fully switch the magnetization vector of the Z axis in the XY plane for a 90 ºC. This duration depends on the intensity of the irradiation.

After the sample is placed into the NMR spectrometer, prior to the spectra acquisition, the “lock” and the “shimming” are vital to perform with the aim of generating good quality spectra.

To take a high-resolution spectrum, the magnetic field must be stable and homogenous because whether the magnetic field strength changes during acquisition, the signals will appear broadened, and the spectrum will have poor resolution. To keep the field stable, the spectrometer uses a mechanism which corrects the field´s drift which is called “the lock system”. Thus, the drift is measured through the absorption frequency of the solvents resonance (the lock signal). Due to the frequency changes because of a change in the field, an electric current is applied to a coil in the magnet that increases or decreases the field´s strength to keep the signal in the same position and the field constant.

Another key factor to get a good quality NMR spectrum is shimming. NMR demands a homogenous magnetic field over the whole of the sample volume placed within the probe´s detection coil. If the field is not homogenous, the resulting spectra could suffer a distorted line shape, resulting a poor resolution and sensitivity spectra. Therefore, the field must be optimized to every sample introduced in the magnet, calling the process of adjusting the field´s homogeneity “shimming”. Hence, applying different electrical currents to these coils it is necessary to compensate for deficiencies in the field homogeneity.

Typically, the conventional pulse sequence is used to acquire 1D ^{1}H-NMR spectra. This simple pulse sequence consists of a RD, followed by a radiofrequency 90º pulse, and the acquisition time. This pulse sequence is repeated several times (or scans) and added together to magnify the intensity of the measurements and to improve the signal-to-noise ratio. Concurrently, ^{31}P-NMR measurements are carried out using a standard 90º pulse program, as discussed previously, but with inverse-gate decoupling (*zgig*). With it, the decoupling is only during the acquisition period, which minimizes Nuclear Overhauser Effect (NOE) (**Table 1.5**) enhancements and obtains more quantitative results.

Table 1.5. Nuclear Overhauser Effect (NOE).
It is the cross-relaxation between the z-magnetization of two spins, strongly contributing to relaxation being a very important tool for obtaining structural information because the magnitude of cross-relaxation and magnetization transfer heavily depends on the distance.

Two-dimensional (2D) NMR experiments have also been carried out to improve the characterization of the detected metabolites. 2D ^{31}P,^{1}H-HSQMBC-TOCSY spectrum is the NMR experiment which correlates protons and phosphorus within a given spin system, extending beyond geminal or vicinal nuclei. Magnetization is transferred successively over up to 5 or 6 bonds if protons and phosphorous are coupled. This type of magnetization transfer, also known as scalar coupling or *J-coupling*, occurs through bond or electron cloud interactions between proton and phosphorous, both being nuclei with non-zero spin. This type of heteronuclear coupling (^{1}H-^{31}P) is very useful in the assignment of phosphometabolites. Consequently, this experiment provides a high-resolution “fingerprint” of the sample, proving invaluable in detailed phosphometabolomics analysis.

Regardless of the pulse sequence used, the detected data is always an FID function, which depends on time. By application of the Fourier Transform (FT), the time domain domain data (FID) into a frequency domain NMR spectrum. This is a critical step in NMR spectroscopy, as the NMR signal is initially detected in the time domain, while the spectra that chemists are familiar with are in the frequency domain. The Fourier Transform helps to translate the raw, time-domain NMR data into a usable, interpretable NMR spectrum.

Likewise, according to the Nyquist sampling theorem states, FID must be sampled at a rate at least twice the highest frequency in the FID to faithfully reproduce the correct frequencies in an NMR spectrum. Thus, in the FID, the highest frequency is ± ½ the spectral width. If a resonance falls within ± ½ the spectral width, it will be correctly represented in the spectrum. In the absence of digital filters, if a resonance is outside of the spectral width but within the filter bandwidth of the spectrometer, it will still appear in the spectrum but at the wrong frequency.

1.2.6.1 NMR preprocessing

One of the main goals of NMR metabolomics is to analyze the abundance of phosphometabolites from NMR data and to interpret variations in these abundances as alterations in metabolism. To achieve this aim, the acquired data needs to be accurate. The quality of the data does not only depend on the experimental design, instrumentation

and on pulse, sequences used, but it can also be enhanced by applying data pretreatments. There are many NMR preprocessing methods used to enhance spectral resolution and peak shapes, sensitivity and align shifted resonances. These tools can be applied either in the time domain (in the FID spectrum) or in the frequency domain (in the NMR spectrum).

1.2.6.1.1 Apodization

Apodization or Weighting Function is the mathematical function that the FID is multiplied by before FT. It has the effect of altering the shape of the FID signal before it is transformed into the frequency domain, thereby enhancing the resolution and the signal-to-noise *ratio* of the resulting spectrum.

Thus, once it has passed an acquired time, all spin nuclear have been impaired and total data points are representative of noise, having contributed to noise in the spectrum the presence of noise in these last data points in the FID. Consequently, it reduces the signal-to-noise *ratio* of the measured resonances. Exchanging these noise values by zero would introduce a sharp discontinuity in the FID, introducing artifacts into the spectrum. Alternately, the FID can be multiplied by a negative exponential function that emphasizes the early data in the FID and deemphasizes the latter, in this way, increasing the signal-to-noise *ratio* (**Figure 1.11**), even though final resonances are broader and smaller in their peak height. After FT, peaks are sharper, resulting in an enhancement of resonance resolution.

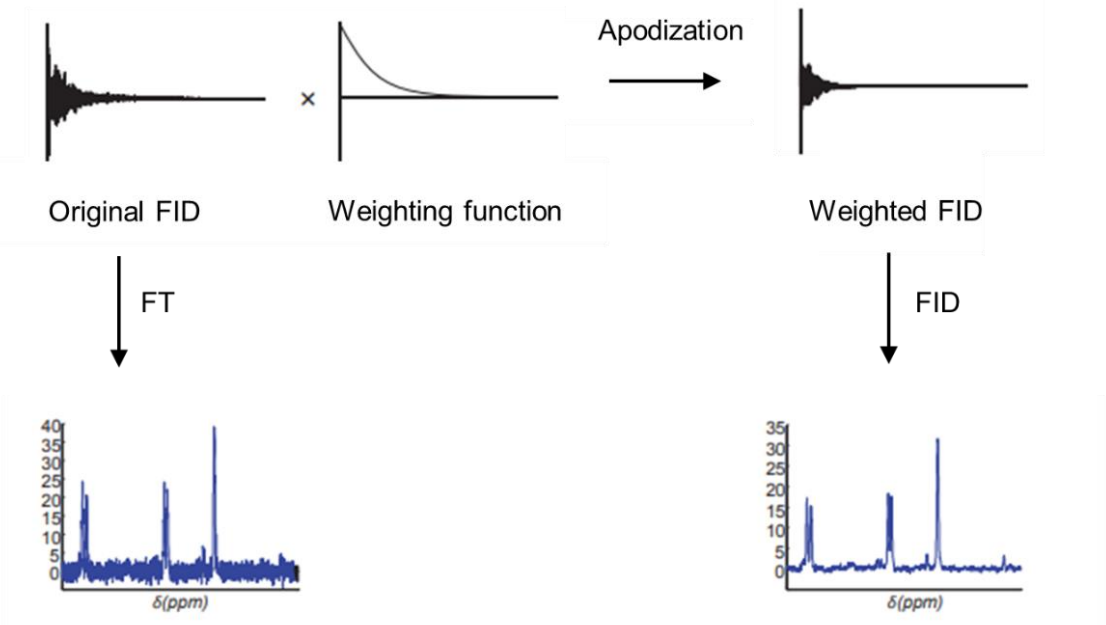

Figure 1.11. Apodization with an exponential negative weighting function.

1.2.6.1.2 Zeros filling

This step consists of adding zeros to the end of the FID. Nevertheless, considering that all nuclei complete their decay before finishing the acquisition of the FID, the added zero values would correspond to the expected measured values if the acquisition time had been longer, and consequently, this procedure does not affect peak positions, intensities, or linewidths of the spectrum. Instead, it allows for more data points in the frequency domain, which can lead to smoother line shapes and an overall better-looking spectrum after the application of FT (**Figure 1.12**). Habitually, the number of added zeros is the same as the number of real points in the original FID and, because of this operation, the spectral resolution could be doubled.

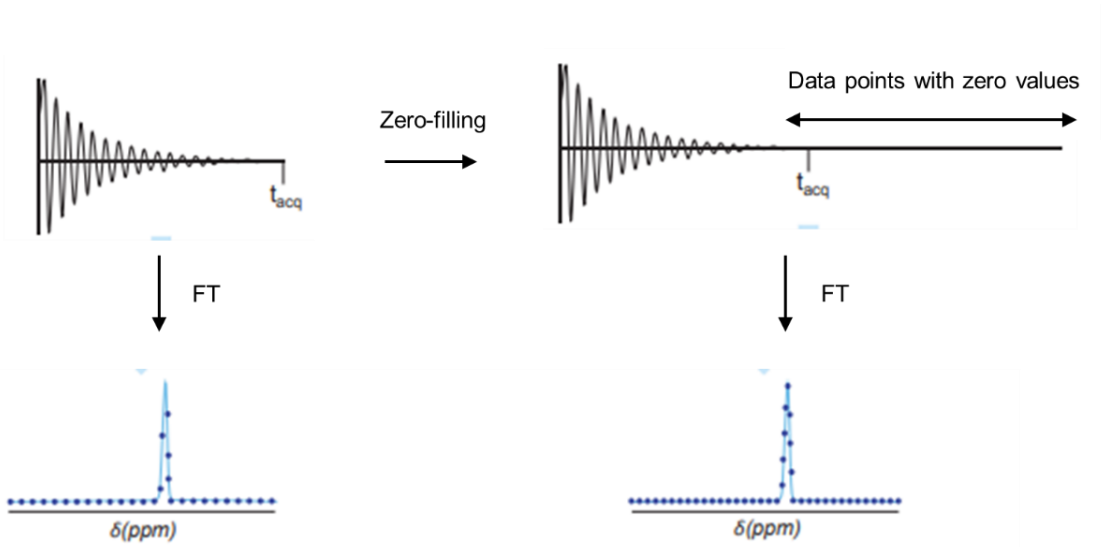

Figure 1.12. Zero-filling.

1.2.6.1.3 Phase correction

Once have converted FID into the frequency domain NMR spectrum, some peaks cannot have the peak shape expected (some of them may be half up-half down or in dispersive mode) because of issues in phase. These phase obstacles often come from maladjustment of the phase corrector, from delays between the initial RF pulse and the start of data acquisition, as well as from the electronic filtering of the NMR signal. Therefore, phase correction is needed to correct phase errors (**Figure 1.13**). It is applied 0 phase correction to the whole spectrum and its aim is to account for any phase shift which occurs independently of the signal frequency.

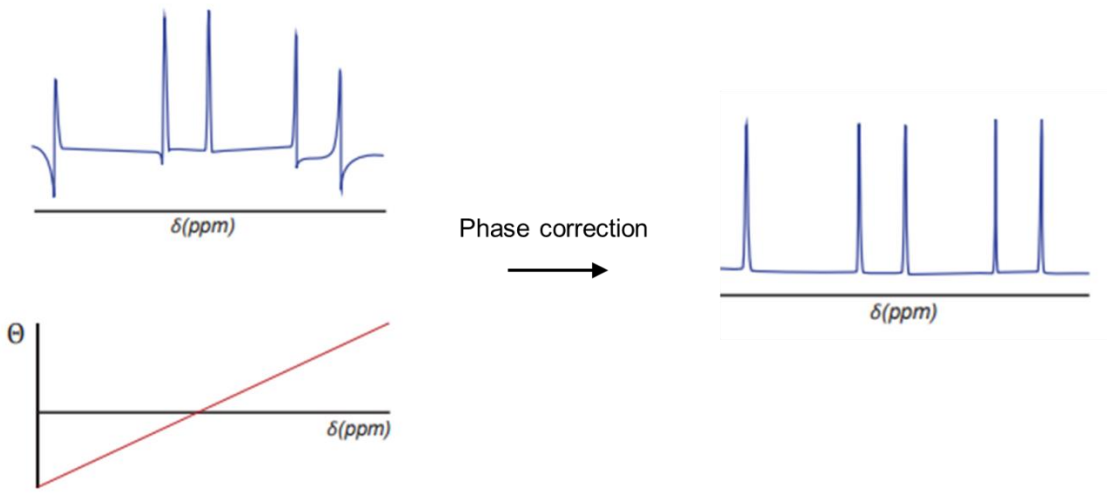

Figure 1.13 Phase correction.

1.2.6.1.4 Baseline correction

Not only baseline distortions can come from the misrepresentation of the first few data points in the FID, but, they can also be caused due to the presence of macromolecules that decay faster than the other low molecular weight metabolites or by instabilities. In order to solve it, a smooth function, which represents the offset between the original and ideal spectrum, is performed, being subsequently subtracted from the original spectrum. Just in case the baseline correction is accurately applied, the noise values of the corrected spectrum will have centered to zero (**Figure 14**).

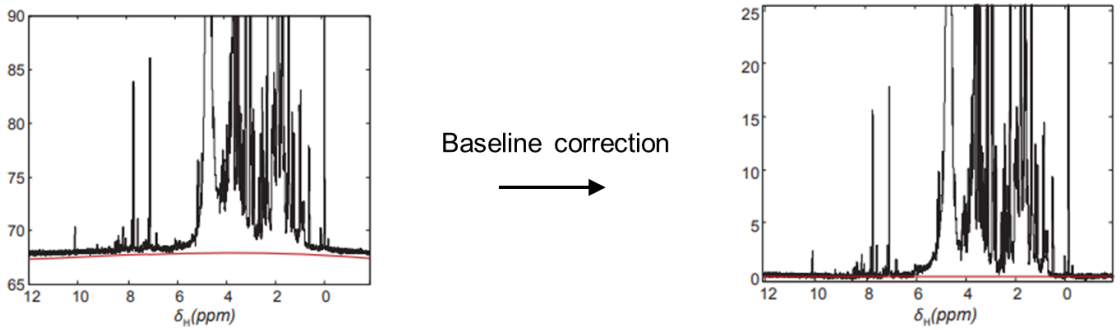

Figure 1.14. Baseline correction.

1.2.6.1.5 Setting the reference

The final step involves setting the reference peak that the sample must contain. This peak is used as a reference point for all other peaks in the spectrum to compare the chemical shift of different compounds in different spectra. It's important to select a reference peak that has a known chemical shift.

Alternatively, the solvent peak could be used as a chemical shift reference although this can only be used in dilute solutions where there is only one solvent with known resonance chemical shifts.

Likewise, the position of NMR signals can be affected by several chemical and physical factors, such as the magnetic field, buffer composition, changes in pH, temperature, a different salt concentration or different relative concentrations of specific ions. Relaxation delay (D_1) and longitudinal relaxation times (T_1) (**Table 1.6**) for the metabolite of interest also play roles in this process. It's crucial to control these factors as much as possible for accurate, reproducible results.

Table 1.6. T_1 relaxation
T_1 relaxation, also known as *spin-lattice* relaxation or longitudinal relaxation[70], is the process by which the net magnetization vector returns to its equilibrium state aligned parallel to B_0 after being disturbed by an RF pulse. During this recovery process, the excited spins return to their original state by transferring their excess energy to the surrounding lattice[70]. The time it takes for the net magnetization vector to grow back to approximately 63% of its maximum value is defined as the T_1 relaxation time. In order to ensure the full relaxation between each pulse, the D_1 is thus defined as 3 times T_1. From a theoretical perspective, T_1 relaxation is a stochastic (random) process that is highly dependent on various factors such as 1) the chemical nature of the metabolites, 2) the magnetic field strength, 3) the temperature, 4) the presence of paramagnetic ions or molecules, or 5) the viscosity of the sample.

1.2.6.1.6 Resonance alignment

Although standardized protocols are widely used in metabolomics, spectral misalignments can occur because of several issues such as pH changes or molecular interactions between the metabolites present in biological complex samples. However, the vast majority of the robust NMR integration tools can manage these chemical shifts.

1.2.6.1.7 Binning or bucketing

Once have divided NMR spectra into a certain number of bins, all intensity values inside each bucket are summed with uniform area width (typically 0.04 ppm). Binning is commonly used to reduce the data dimensionality. Nevertheless, the resolution is simultaneously reduced, losing information, and causing undesired artifacts.

With the aim of avoiding a source of mistakes that come from bucketing, bucketing algorithms have been proposed, capturing single metabolite resonances into single

buckets in addition to adapting the width to each bucketed resonance. It is simple and rapid; therefore, several NMR metabolomics studies obtain biological interpretations analyzing this type of bucket. Although this approach results faster, it does not have to be assumed that each bucket is totally correct resonance integral.

1.2.6.1.8 Assignment of the metabolites

Each NMR spectrum is, consequently, perceptible from other compounds in an NMR spectrum of a complex mixture. Despite its uniqueness, the assignment of metabolites in a NMR spectrum is not trivial, being extracted from it a large amount of information that can be analyzed together. Hence, there are several spectroscopic parameters that can be used to identify unequivocally a chemical compound such as chemical shifts, the *spin-spin* splitting pattern or multiplicity, the coupling constants, and the resonance integrals.

1.2.6.1.8.1 Chemical shift

When a sample is under the influence of a magnetic field, B_0, the electronic cloud surrounding a nucleus begins to circulate, creating an induced current that generates a magnetic field opposed to the B_0 field, reducing the effective magnetic field felt by this nucleus. This reduction (also called deshielding) is measured in the order of ppm, and it varies from nuclei to nuclei, depending on the electron density in the neighboring environment.

1.2.6.1.8.2 Coupling constant

Indirect *spin-spin* coupling (*J*-coupling or indirect dipole-dipole) indicates the magnetic interaction between individual nuclear spins transmitted by the bonding electrons through which the nuclear spins are indirectly connected.

This coupling depends on the hybridization of the atoms involved in the coupling, the dihedral angles, the bond angles, and the bond length as well as the effect from the substituent atoms, such as neighboring π-bonds or electronegativity.

In the NMR spectrum, this coupling is shown as a splitting of the resonance in a structured pattern with a defined spacing between splits that coincides with the *J*-coupling measured in Hertz (Hz).

1.2.6.1.8.3 *Spin-spin* splitting pattern

In case the resonances from all nuclei that are coupled to a given resonance are distant in the spectrum from this resonance, the coupling is weak and the splitting pattern relatively simple. On the other hand, if resonances are coupled to nearby peaks, more

complex patterns are observed. Because the order of the splitting pattern depends on the proton distance measured in Hz, a signal observed of non-first order splitting patterns may become of the first order in a higher magnetic field.

Splitting patterns depend on the chemical structure, using as example L-lactic acid (2S)-2-hydroxypropanoic acid (**Figure 1.15**). Hence, for this chemical compound, two proton resonances are expected (one for the CH_3 group and another for the CH group). Three protons from CH_3 group are magnetically equivalent, therefore, they resonate at the same frequency. On the contrary, the proton resonance from the hydroxyl group cannot be detected with exchangeable deuterium from the medium because the equilibrium rate of the proton is fast.

Next, the two proton resonances detected are coupled because the nuclear spins of the protons from both groups interact. The two resonances are very far from each other, and consequently, the splitting pattern that defines these couplings is of first order. In this kind of coupling, each of the protons from the CH_3 group (which can be either α or β) interacts with the proton in the CH group (also at α or β), and vice versa. From all the possible spin combinations, the proton from the CH group, which can be found at two different spin states, couples to the wight spin state combinations possible in the CH_3 group. These eight spin states combinations are found in four energetic states because of the spin degeneration, therefore, the resonance from the CH is detected as a quadruplet resonance with an intensity *ratio* that coincides with the degeneration pattern (1:3:3:1). Meanwhile, using the same explanation, the protons from the CH_3 group are detected as a doublet resonance with the same intensity.

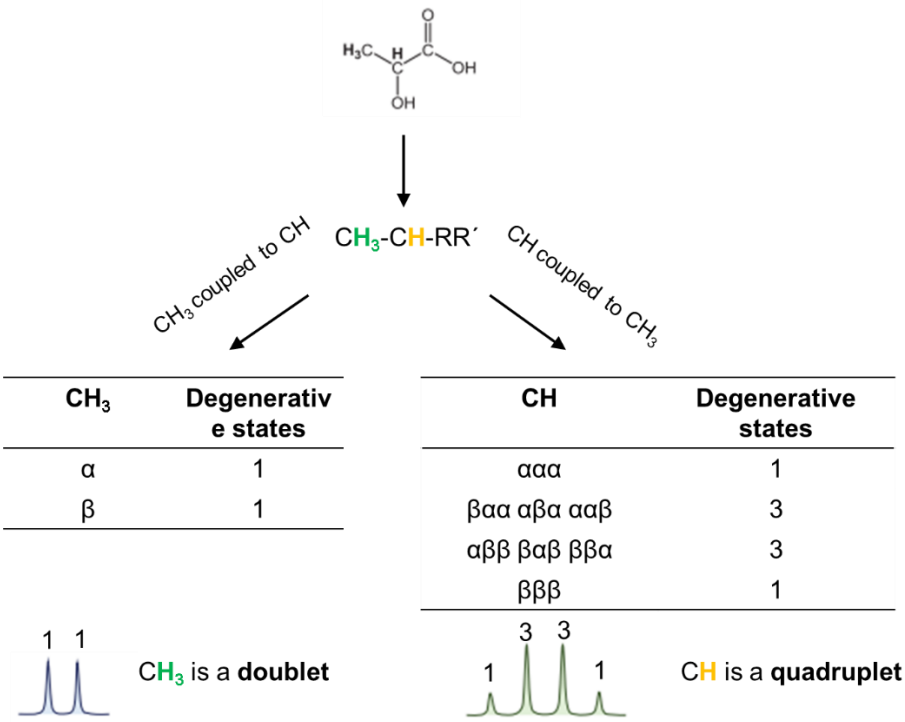

Figure 1.15. Proton nuclear spin states combinations for the inequivalent protons in L-lactic acid.

1.2.6.1.8.4 Resonances integral

Nuclei measured can achieve full relaxation after each successive scan if enough D1 time is left, in this way, being resonance integrals quantitative. It means that the areas of the different resonances are comparable. Thus, for instance, the integral relative to the resonance associated with three magnetically equivalent protons (CH_3) will be three times larger than the area of a resonance relative to one proton (CH).

1.2.6.1.8.5 NMR databases

NMR assignment is very laborious especially for metabolomics analysis because their samples are complex. In an NMR spectrum hundreds of peaks can be detected but only a small fraction of them is finally assigned.

To bear with this severe issue, sophisticated NMR metabolite spectral databases have been developed to aid in the identification and quantification of metabolites for metabolic purposes. The most well-known among these are the Biological Magnetic Resonance Bank (BMRB)[71], the Human Metabolome Database (HMDB)[72],the Birmingham Metabolite Library (BML-NMR)[73], and the TOCSY Customized Carbon Trace Archive (TOCCATA)[74].

Even though there are several databases, sometimes it is not easy to confirm the NMR assignment of a chemical compound in a metabolomics sample. In these cases,

acquiring complementary 2D NMR experiments on the same sample or spiking the sample with the candidate compound are strongly recommended.

1.2.6.2 Processing

The last purpose of acquiring and processing the NMR spectra is to apply data analysis strategies on the set of NMR spectra. Sometimes, several detected resonances are overlapped, being misleading the obtained results. Due to this, it is preferable to apply data analysis on the peaks integrals (obtained by separation or deconvolution approaches) of the detected metabolites relative to the same samples than directly in the raw NMR spectra. Next, the different integration approaches are going to be explained below.

1.2.6.2.1 Integration of non-overlapped signals

Habitually, resonance integrals might have been calculated by summing the intensity values within the range of each resonance, being these integral values proportional to their height. For a simple NMR spectrum, the calculated integrals are proportional to the atom concentration of the measured compounds. Hence, for an individual compound, all resonances must be of the same height, except those which have magnetically equivalent atoms, being the area proportional to the number of magnetically equivalent atoms.

However, NMR analysis is much more complex, therefore several situations can be considered. In an NMR spectra from metabolomics samples, sometimes atom resonances can appear overlapped. Consequently, to calculate the integrals for each of the resonances in the overlapped region, it is vital to be separated using computer-derived approaches such as spectral deconvolution methods.

1.2.6.2.2 Spectral deconvolution

An NMR spectrum can be considered as a linear combination of resonances from a defined group of metabolites in the presence of some residual noise. Once spectroscopic parameters such as δ, multiplicity or *J* that define the resonances from these metabolites are known, it is possible to deconvolute the real NMR spectrum into a set of line functions (**Figure 1.16**). Then, the corresponding integrals can be calculated by estimating the area under the curve of these line functions.

Thus, any existent resonance splitting pattern can be described as the sum of the line-shape functions representing each of the *spin-spin* splitting transitions. For instance, a doublet can be defined as the sum of two line-shape functions of equal intensity.

Therefore, each *spin-spin* splitting transition is detected at a distribution of frequencies that can be approximated by a Gaussian function, being a line shape a convolution of Lorentzian peaks with a Gaussian distribution that jointly follows the Lorentzian-Gaussian (or Voigt) line shape.

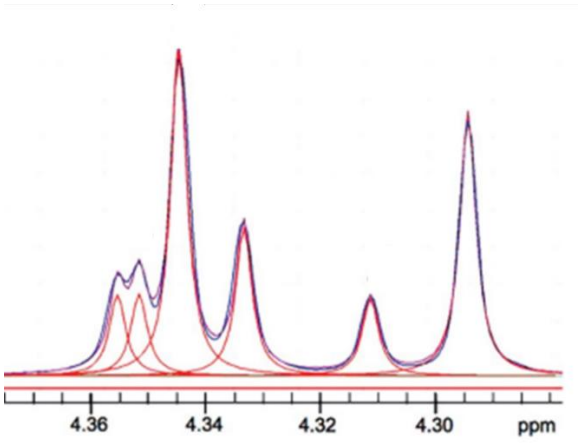

Figure 1.16. Deconvolution of the ^{1}H NMR spectrum zone.

1.2.6.2.3 Generating absolute concentrations from resonance integrals

Since NMR is inherently quantitative, absolute concentration can be directly estimated for all the metabolites contained in the measured samples. In other words, there is no need to use calibration standards for every metabolite. To obtain this, a metabolite of known concentration has to be measured simultaneously with the sample. Thus, after establishing the relationship between the measured intensity (integral) and the concentration for the NMR standard, the absolute concentration for the rest of the metabolites can be calculated.

1.2.6.2.4 Normalization

The objective of normalization is to make samples comparable to each other taking into consideration metabolite dilution, being this step extremely important for the analysis of liver samples[75]. There are many different normalization approaches, one of which normalises to total amount of liver weighted[75].

1.2.6.2.5 Scaling

Prior to multivariate analysis, a scaling step is vital to consider the fact that metabolites can range over many orders of magnitude[75]. Consequently, with the aim of avoiding this issue, the scaling step is crucial[75]. Several scaling approaches exist, such as auto scaling, mean entering and range scaling, among others. Auto-scaling implies scaling all data to unit variance[75]. Likewise, mean entering, adjusts all values to vary around zero

instead of the mean[75]. Meanwhile, in pareto scaling the square root of the standard desviation is used as a scaling factor[75].

1.2.7 Statistical analysis

1.2.7.1 Univariate analysis

The student´s *t-test* is commonly used to compare two sample groups. It requires that each sample have a normal distribution, that the variances of the two populations are equal, and that the data are independently sampled. When comparing more than two groups, a one-way analysis of variance (ANOVA) is employed with the aim of differentiating between group means of each variable.

1.2.7.2 Multivariate analysis

When it is necessary to examine the impact of multiple variables or study many variables at a single time, multivariate analysis becomes essential. Several multivariate analysis methods have been proposed in the literature, although Principal Component Analysis (PCA) and Partial Least Squares Projection to Latent Structures (PLS) are the most used ones.

1.2.7.2.1 Principal Component Analysis (PCA)

PCA is a method that transforms original variables, which are correlated with each other, into new uncorrelated variables. These new variables are constructed as linear combinations of the originals, being these new variables called PCAs. **Figure 1.17** illustrates a schematic of the construction of a PCA model. The first principal component (PC1) captures the direction of maximum variance in the data, and the second principal component (PC2) captures the direction of maximum variance orthogonal to PC1, thus generating a new set of coordinates (PC1 vs. PC2).

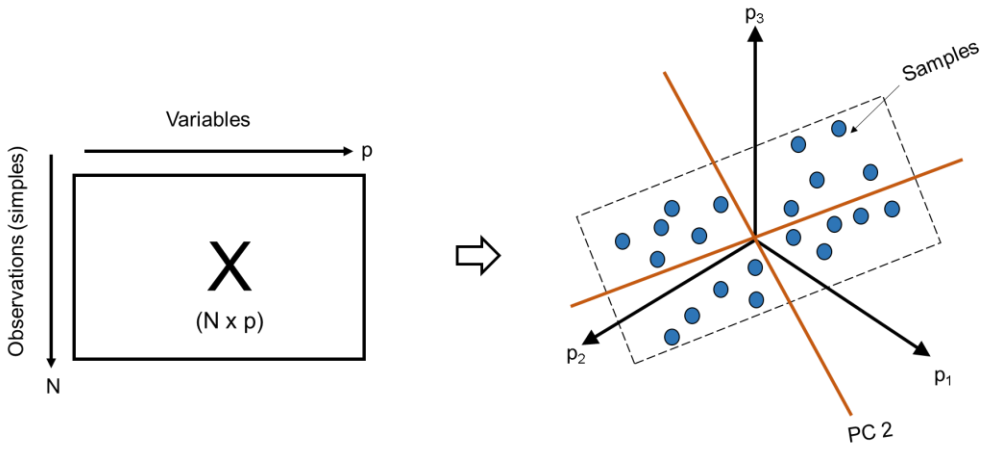

Figure 1.17. Graphical representation of the construction of PCA model with three variables.

The projections of the observations or samples in the new axes (PC1 and PC2) are called scores, obtaining scores plot. Conversely, if one considers the coefficients of the vectors of each feature on the coordinate axis defined by PC1 and PC2, this will result in the loading plot.

1.2.7.2.2 Partial Least Squares Projection to Latent Structures (PLS)

PLS-Discriminant Analysis (PLS-DA) is a chemometric regression tool that is used to optimize the separation between the different groups. It considers the data matrix X and the qualitative matrix Y, which contains information about the class or group to which each sample belongs. This method is particularly useful when the variability within groups is greater than the variability between groups[76]. It maximizes the covariance between the variables of the matrix X and the corresponding dependent variables of matrix Y by simultaneous rotation of the PCs generated for each matrix X and Y[77].

1.2.8 Biological interpretation

After identifying the important variables or metabolites of interest, the last step is to integrate these metabolites into the biological network. It is vital to study and establish the biological role or metabolic pathway associated with this metabolite, to determine whether it is relevant for the biological question initially proposed. But what it is the most significant is to integrate the whole data of the metabolites to elucidate changes in the metabolite behavior within a specific biological network during disease, physiological processes, or external stimuli. Likewise, the enzymes which regulate the metabolite levels can be investigated to seek a deeper understanding of the biological mechanisms associated with a particular disease or condition. Among the most used biological databases for this purpose are the Kyoto Encyclopaedia of Genes and Genomes (KEGG)[78] ,Small Molecule Pathway Database (SMPDB)[79], MetaCyc[80] or WikiPathways[81], among others.

CHAPTER 2

HYPOTHESIS AND OBJECTIVES

2.1 Hypothesis

Although phosphoromics is not a new methodology, a small set of phosphometabolites have been possible to analyze by ^{31}P-NMR until now due to several issues in erroneous peaks assignment, quantification errors of the phosphometabolites, the lack of internal references for quantitative analysis as well as the lack of resolution spectral and sensitivity, among others. Hence, the hypothesis of this study was that by overcoming these aforementioned issues a promising analytical method could be used to quantify a larger set of phosphorylated metabolites in live samples.

2.2 Objectives

The main objective of this study was to develop and standardize phosphoromics as an analytical method in the liver. For the implementation of this method in the metabolomics field, the following were carried out:

- The development of ^{31}P NMR-based method to study liver "phosphorome" through the simultaneous identification and quantification of multiple hydrophilic and hydrophobic phosphorylated metabolites. The main objectives of that were:

    - Optimization of biphasic extraction protocol.
    - Correct assignment of the phosphometabolites.
    - A robust and reproducible quantification protocol of the metabolites.
    - As proof of concept, this method could be applied in murine models of two well-known liver diseases (CEP and NASH) to determine metabolic phenotypes of liver injury as well the mechanism of a drug action with CPX.

- The extension of the application of phosphoromics to a longitudinal study with the sole purpose of observing hepatic metabolic phenotypes and distinguishing metabolic profiles from mice fed with two well-known diets (HFD and CDHF) that can progress to NASH. The main objectives of this study were:

    - Distinguish a unique liver phosphoromics signature from mice fed different NASH-developed diets.
    - Verify if aging was a crucial variable at the metabolic level in the progression of NASH.
    - Develop a mathematical model to distinguish different hepatic phosphoromics profiles from mice fed different diets that can cause NASH.

- The enhancement of ^{31}P-NMR protocol with the aim of standardizing a quantitative ^{31}P-NMR analysis under SOPs for either hydrophilic or hydrophobic fraction, verifying the suitable:

- Chelating agent at optimal concentration (only for hydrophilic fraction)
- Buffer and pH
- Solvent
- PRE effect type at optimal concentration and temperature
- D_1 or relaxation delay
- Temperature at 2D correlation NMR experiments

CHAPTER 3

DEVELOPMENT OF ^{31}P-NMR METHOD AND ITS APPLICATION IN LIVER DISEASES

3.1 Introduction

The human metabolome represents a set of small compounds found in the human organism including peptides, lipids, amino acids, nucleic acids, carbohydrates, organic acids, vitamins, minerals, drugs, contaminants, and other chemical compounds that humans can ingest, metabolize or be into contact with[82]. In order to generate a valuable resource for researchers studying human metabolism and related diseases, the HMDB (www.hmdb.ca) was created in 2007 and contains a standard metabolomic resource for human metabolic studies which contains information about human metabolites relative to their biological roles, concentrations, disease associations, chemical reactions, metabolic pathways and reference spectra[83].

The first version of HMDB 1.0 provided a small amount of data on 2180 metabolites, taking part in the Human Metabolome Project[84]. Two years later, HMDB 2.0 added much more reference spectral and biological information up to 6408 metabolites[85]. Meanwhile, HMDB 3.0, described in 2013, added more lipid information data in addition to expanding the spectral reference library and introducing more metabolic pathways, among other improvements, containing 40153 metabolites[86].

Fundamentally, this expansion has been motivated because only < 10% of known human metabolites have been experimentally collected by NMR, GC-MS or MS/MS spectra[82]. The solution to this problem has meant a great economic investment[87]. Furthermore, the most viable solution found has been to use *in silico* approaches to predict NMR, GC-MS or MS/MS spectra of predicted metabolite structures[88–90]. Therefore, based on these *in silico* approaches with the combination of more conventional ones gave rise to the most significant expansion of its history[78], called HMDB 4.0.

Thus, according to the HMDB 4.0, there are more than 114000 metabolites, of which nearly 20000 metabolites can be identified and quantified[78]. Furthermore, there are about 3271 metabolites identified but not quantified, 7552 compounds with concentration data, more than 5000 compounds with disease links, 18192 metabolic reactions, 25570 metabolic pathways and 3840 experimental NMR spectra[78].

Consequently, the map that configures the human metabolism is intriguingly complex. Therefore, to have a global view of metabolism, it is vital to reduce this complexity to the minimum information available. In consequence, it has been proposed in this thesis that the majority of the metabolism may be explained by focusing on a set of small chemical compounds whose structures enable a diverse group of transfer reactions such as ATP, NADH, acetyl-CoA and UDPG glucose[91]. The first three molecules are mainly

accumulated in degradative metabolism (catabolism) and then they are used to power anabolic small molecules and macromolecules, including proteins, nucleic acid metabolism and oligosaccharides. Likewise, ATP, NADH and acetyl-CoA are the end products of cellular energy metabolism[92–94]. They are pretty versatile because they can work as phosphoryl or nucleotidyl donors (ATP)[95], acyl donors for building up biosynthetic carbon scaffolds (acetyl-CoA) and electron donors (NADH, NADPH) most notably to the components of the respiratory chain[94].

Meanwhile, UDP-glucose is an entry point metabolite through which thousands of metabolites can be incorporated into oligosaccharides, for defense (bacterial lipopolysaccharide), structural (cellulose) and energy storage (glycogen) purposes[96].

In **Table 3.1** indicates the main metabolic pathways in which these four metabolites are activated in order to transfer a group which power the following steps of each metabolic pathway[87].

Table 3.1. The metabolic pathways that are involved ATP, NADPH, NADH, acetyl-CoA and UDP-glucose[87].

Metabolic pathways	Key substrates
Glycolysis	ATP, NADH
Pentose phosphate pathways	NADPH
Glycogen assembly	UDPG
Glycoproteins	UDPG
Trycarboxylate cycle	Acetyl-CoA, NADH
Fatty acid biosynthesis	ATP, acetyl-CoA, NADPH
Fatty acid β-oxidation	Acetyl-CoA, NADH
Purine and pyrimidine biosynthesis	ATP
Urea cycle	ATP
Nitrogen metabolism	NADH

By this way, it has proposed that metabolism can be quantitatively described by focusing on the phosphorylated fraction of the metabolism, called “phosphorome”, because these metabolites are involved in all catabolic (degradative) and anabolic (synthetic) pathways, such as glycolysis, gluconeogenesis, the TCA cycle, oxidative phosphorylation, the PPP, the urea cycle, glycogenesis or the synthesis of phospholipids, TG, and TC[97].

For another hand, it is vital to bear in mind that metabolomics studies in humans are limited due to the intrinsic necessity of monitorization of the subjects for long periods,

even decades. In addition, there are several ethical limitations in giving drugs to patients or collecting samples from patients. Therefore, animal models are used instead in the medical research field[98]. The most widely used animals are rodents because they have a short reproduction period, and the distribution of their organs is quite similar to that of humans[99]. Likewise, it allows controlled experimental conditions, low cost compared with large animal models, and experimental time periods that are affordable for researchers (3-6 months). Whereas human studies are confined to a single time point, rodent studies allow sufficient tissue without sampling error and physiological, molecular, and cellular dynamics can be studied[100]. All mice experimental models should follow the Animal Research: Reporting In Vivo Experiments (ARRIVE) criteria[101]. ARRIVE recommends reporting strain of the animals, use of littermate controls, a list of diet and nutrient details and other elements of healthy animal husbandry as well as the minimization of animal experimental in case of ineffective use[102,103].

The success of rodent experimentation has been translated to a large number of mouse models (either dietary[104] or genetic[105]) available to investigate diverse pathogenic mechanisms, metabolic features, histopathology and disease progression[106] as well as the therapeutic effect of drugs on these diseases[107]. Nevertheless, there are some limitations such as their behavior, nutrient requirements, control of metabolic regulation, microbiome, etc. Despite these limitations, many studies have validated the metabolic similarity, and most of the extracted conclusions can be applied to human beings as well.

The identification and quantification of the metabolites from the liver have several instrumental limitations such as a) the range of the concentration levels in which metabolites appear in the liver (from millimolar to picomolar concentration), b) the complexity of the sample, c) the chemical nature of the metabolites (nonpolar, polar, etc.). Phosphorylated metabolites can be measured through different analytical techniques including MS[108] and NMR spectroscopy[109]. ^{1}H-NMR has some advantages like its sensitivity. Nevertheless, it is quite difficult to quantify the metabolites because of their widespread signal in addition to the strong background signal from water.

However, ^{31}P-NMR has many advantages. Firstly, this nucleus has a natural abundance of 100%. Furthermore, it has a wide signal dispersion and a relatively high sensitivity[110]. As it has mentioned in the introductory chapter, phosphorylated metabolites from liver extracts have been identified through *in vitro* studies[111,112]and *in vivo* using magnetic resonance imaging (MRI)[113]. Nevertheless, these studies are normally not quantitative by focusing on a small number of phosphorous compounds such as phospholipids and

phosphorylated metabolites of nucleoside metabolism involved in energy metabolism[114,115], being vital to do more ^{31}P-NMR quantitative studies.

Thus, it presents a method to characterize and quantify phosphorylated metabolites from mouse liver samples. For this purpose, several problems and technical and methodological limitations will be considered that must be overcome:

1. Lack of standardization in the extraction method. Extractions have been reported in perchloric acid, chloroform-methanol-water, in dichloromethane/methanol, methanol-water-acetonitrile, or in detergents such as cholate. The metabolic profile of the same sample may change depending on the extraction method or even introduce artifacts as in the case of perchloric acid.

2. Lack of internal references to standardize chemical shifts. A simple way to deal with the problem is to add a phosphorylated compound as a reference whose chemical shift is known and it is in a clean area of the spectrum, free of any possible overlap. Nowadays, there are three compounds that are used as references for quantitative ^{31}P NMR analysis. Firstly, Orthophosphoric acid (KH_2PO_4), reference at 0 ppm, masks the intrinsic inorganic phosphate signal of the sample in addition to being soluble in water. Secondly, Phosphonoacetic acid (PAA), referenced at 16 ppm, is soluble in water as well as in organic solvents. The counterpart that it has is that the organism can produce the compound, which would lead to errors. Thirdly, triphenyl phosphate (TPP), reference to 17 ppm, is only soluble in organic solvents.

3. Lack of spectral resolution and sensitivity. While only about ten metabolites are roughly studied *in vivo* using magnetic fields up to 7 tesla, more phosphometabolites could be extracted and concentrated for analysis *in vitro* in stronger magnetic fields (>14 tesla) with probes direct detection of phosphorous.

4. Erroneous assignment of metabolites. In the literature, it has been observed that using low magnetic fields has sometimes led to an erroneous assignment of the peaks. Sometimes, there are regions of the spectrum that have been assigned as “Phosphomonoesters (PME)” or “Phosphodiesters (PDE)” although it has subsequently been shown that these signals are composed of other metabolites, thus, compromising the conclusions reached. Likewise, very few groups have measured patterns of phosphorylated compounds and they have adopted an

erroneous signal assignment by direct comparison with other spectra previously assigned under different conditions.

5. Quantification of metabolites. NMR is an intrinsically quantitative technique where the intensity of the signals is directly proportional to the number of atoms present in the sample. The data acquisition process requires a high number of repetitions in order to improve the signal-to-noise *ratio*. During the acquisitions, a minimum amount of time must be allowed so that the spins of the sample can fully recover their magnetization. This time is defined mainly by the size of the molecules, with a shorter time the larger the molecule. When it measures a complex sample, this time must be long enough to enable even the smallest molecules to recover their magnetization, otherwise, it will not be quantifiable.

Likewise, as a proof of concept, it is going to elucidate the liver phosphorome from a mouse model of the autosomal recessive disorder congenital erythropoietic porphyria (CEP)[116], also known as Günther´s disease. CEP is a metabolic disorder resulting from a deficiency of uroporphyrinogen III synthase (URO IIIS), the fourth enzyme in the heme biosynthetic pathway[117,118]. As a consequence as the deficiency of this enzyme, there is an accumulation of uroporphyrin I (URO I) and coproporphyrin I (COPRO I) in the whole body, especially in the skin, leading to hemolysis, severe anemia and cutaneous photosensitivity[111,112]. The phosphoromic method is going to analyze quantitatively the liver metabolic landscape of CEP with the aim of determining alterations in the phosphorylated metabolites of glycolysis, glycogenesis, pentose phosphate pathway, oxidative phosphorylation, phospholipid metabolism and apoptosis.

Likewise, it is going to be measured phosphoromics profile of CEP mice after treatment with the off-patent synthetic antimicrobial ciclopirox (CPX). It has been demonstrated *in vivo* and *in vitro* that CPX acts as an URO IIIS pharmacological chaperone, in other words, it acts as an allosteric chemical stabilizer of UROSIIIS, regulating heme group metabolism and reverting most of the symptomatology[119].

By the way, the phosphoromic patterns of two murine models of NASH are going to be analyzed. One of them, is genetic, methionine adenosyltransferase 1A knockout (MAT1A-KO) mice[120]. This murine model of NASH exhibits a deficiency in MAT1A, an enzyme which is responsible for S-adenosylmethionine (SAMe) synthesis in the liver[121]. SAMe donates a methyl group to different molecules such as DNA, RNA, phospholipids and proteins as well it donates its sulfur atom to cellular antioxidants and its propylamine group to polyamine synthesis, having an important role in processes such as gene

expression, proliferation, differentiation and apoptosis. It has shown that MAT1A-KO has a decrease in hepatic SAMe levels and this fact can cause liver disease[114].

The second murine model of NASH is dietary, mice fed a choline-deficient high-fat (CDHF) diet[122]. It has been demonstrated that after 8-12 weeks of feeding a choline-deficient high-fat diet (CDHFD; 45% of kcal fat), male mice can develop NASH and mild fibrosis. In addition, they can develop obesity and insulin resistance, more rapidly than a choline-deficient diet[116]. The serum profile shows an increase in leptin, triglycerides, cholesterol, AST and ALT levels[116]. Moreover, it can induce oxidative stress and mitochondrial damage and after 12 months of treatment, 25% of mice can develop liver tumors that resemble HCC in humans[123].

3.2 Methods

3.2.1 Animals and diets

Transgenic CEP female mice (n = 14, of which 7 were treated with CPX and wild type (WT) littermates (n = 6) were generated as reported previously[114,116]. Ten-month old male MAT1A-KO mice (n = 9) and WT littermates (n = 6) were generated as shown elsewhere[115,116]. CDHF male mice (n = 9; C57B1/6 background control mice n = 6) were generated as previously indicated[116,124,125]. All experiments were approved by CIC bioGUNE's Biosafety and Bioethics Committee and the Country Council of Bizkaia[116]. At the end of the animal experiments livers were collected (always in the morning with all the animals belonging to the same experiment sacrificed at the same time), cryogen zed in liquid nitrogen and stored at -80 C until further use[116]. All experiments were repeated between six and nine times to ensure statistical significance[116].

3.2.2 Histological procedures

Every staining was done in mouse liver tissue. Liver tissues were fixed in neutral buffered 10% Formalin solution (Sigma-Aldrich, HT501128-4L), embedded in paraffin, and cut into 5 mm sections with HistoCore MULTICUT microtome (Leica)[116]. Liver sections were deparaffinised with Histo-Clear I solution (Electron Microscopy Sciences, 64110-01) and hydrated through decreasing concentration of alcohol solutions[116]. For the Hematoxylin/Eosin staining, samples were stained with Harris Hematoxylin (Sigma-Aldrich, Merck, HHS128-4L), washed in running tap water for 5 minutes, and after 1 second in 0.5% HCl the sections were stained with aqueous Eosin solution (Sigma Aldrich, Merck, HT1102128-4L) for 15 minutes[116]. Finally, the samples were washed in running tap water for 3 minutes, dehydrated in increasing concentrations of alcohol solutions until 100% and mounted with DPX mounting medium (Sigma Aldrich, Merck 06522)[116]. For the Prussian Blue stain (Polysciences, 24199) tissue sections were stained two times with 4% hydrochloric acid and 4% potassium ferrocyanide, 10 minutes each[116]. The slides were counterstained with 1% nuclear fast red solution and rinsed twice[116]. Finally, the samples were dehydrated in ethanol, cleared in Histo-Clear I solution and mounted with DPX[116]. For the Cleaved Caspase III, sections were unmasked 5 minutes at 600W in a microwave followed by 15 minutes at 800W with EDTA 1mM pH 8.0[116]. Then, samples were blocked for unspecific binding with 3% H_2O_2 for 10 minutes followed by 30 minutes of incubation with 2,5% normal goat serum. Sections were then incubated 1 h at 37 ºC with the primary antibodies (Cleaved Caspase III ref: 9661S; Cleaved PARP, 94885, Cell Signaling) followed by 30 minutes of incubation with ImmPRESS® Goat anti-Rabbit IgG (Vector Laboratories, MP-7451)[116]. Samples were

developed with Vector Vip purple substrate (SK-4600) and sections were counterstained 1 minute with Mayer´s Hematoxylin, dehydrated, cleared and mounted with DPX[116]. For the Masson's trichromic staining, slides were deparaffinized and hydrated, preheated in Bouin's Solution at 56°C for 15 minutes and cooled in water. After the stain with Working Weigert's Iron Hematoxylin Solution (5 minutes), slides were washed and stained with Biebrich Scarlet-Acid Fucshin (5 minutes)[116]. Samples were stained with Working Phosphotungstic/Phosphomolybdic Acid Solution and Aniline Blue Solution (5 minutes each). Finally, slides were placed in Acetic Acid, 1%, for 2 minutes, rinsed, dehydrated with alcohol, cleared in Histo-Clear I and mounted with DPX. For the Oil Red O staining, frozen sections were cut at 4 µm, fixed in 10% Formalin solution and washed during 5 mins[116]. After the incubation with 60% isopropanol, tissues were stained with Oil red O (Sigma-Aldrich, O0625-25G) for 15 minutes and washed with 60% isopropanol, lightly stained with Mayer´s Hematoxylin and mounted[116]. All images were captured using a Leica DM750 optical microscopy with a Leica ICC50W digital color camera[116].

3.2.3 NASH Score

Total, NAS score (NAFLD Activity Score), which represents the sum of scores for steatosis, lobular inflammation, and ballooning, ranging from 0-8, was calculated for WT, CEP and CEP+CPX mice based on the analysis of the Masson trichrome staining and according to the criteria Publisher y Klein *et al*[116,126].

3.2.4 Extraction method

For each set of experiments 3 different mice were used to ensure robustness and statistical significance[116]. We used the following weighted livers (**Table 2.2**)[116].

Table 3.2. Liver weights are used for extraction for the different animals employed[116].

Target	Porphyria			NASH			
Mice models	Control CEP (6 mice)	CEP (7 mice)	CEP+CPX (7 mice)	Control MAT1A-KO (6 mice)	MAT1A-KO (9 mice)	Control CDHF (6 mice)	CDHF (9 mice)
Weighted liver (mg)	302	308	301	303	362	309	107
	329	312	279	340	319	304	103
	308	283	294	322	319	317	111
	315.5	196	299	309.5	311	307	129
	318	292	313	302	331.6	318	99
	317	251	298	317	313	301	104
		301	321		306		98
					314.4		100
					303		101

The metabolic extraction procedure was done according to the protocol described in **Figure 3.1**[116].

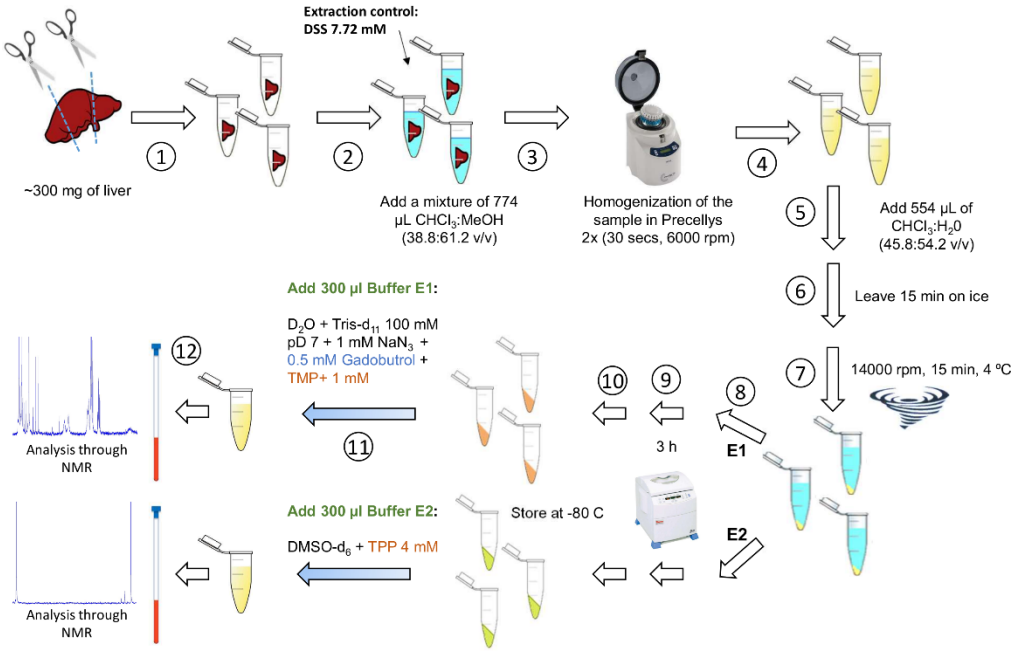

Figure 3.1. Extraction procedure. The protocol details how the metabolic extraction was performed for each liver[116].

1) An aliquot of about ~300 mg of mouse liver was weighted[116].
2) This amount of liver tissue was divided into 100 mg pieces and placed into 3 different Eppendorf's[116].
3) The extraction was carried out considering previously reported ternary mixtures of chloroform:methanol:water (Treatment 1[127] and Treatment 2[128], **Figure 3.1**). During liver extraction it is assumed that 90% of liver's weight will contribute to the water phase (indicated as a shift to darker spheres)[116]. Thus, 55:25:20 w/w/w chloroform:methanol:water mixture ensures an equilibrated extraction with a marked biphasic extraction of chloroform:methanol:water (indicated as a solid red line)[116]. Dashed green line indicates the maximum estimated chloroform "tie-line"[116]. Thus, for every 100 mgs of liver 774 µL of chloroform:methanol (38.8:61.2 v/v**) was added[116]. During this step 7.72 mM of DSS was added for the determination of yield extraction[116].
   ** For the sake of clarity, we transform weights to volumes[116].

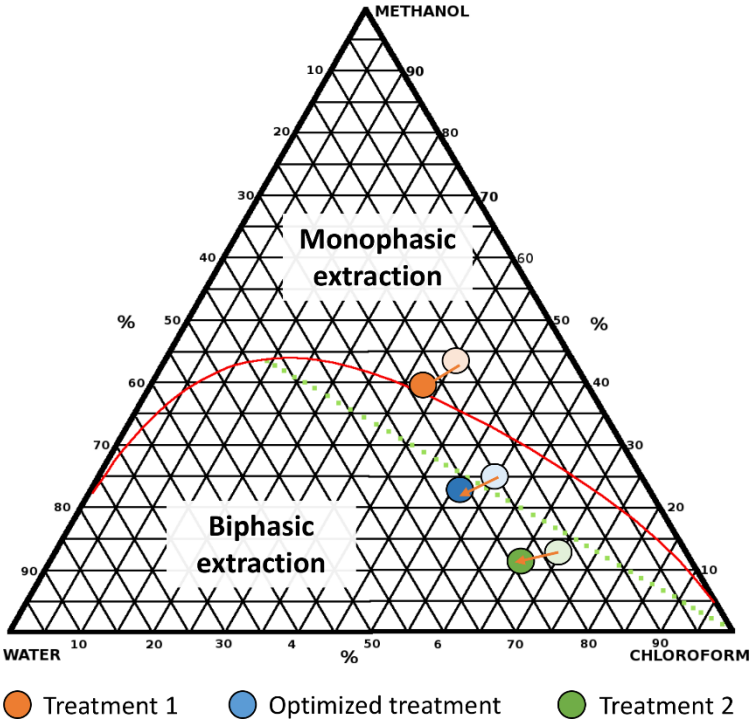

Figure 3.2. Ternary phase diagram of chloroform:methanol:water[116]. *Treatment 1* (orange sphere) corresponds to an extraction at 40:44:16[121], *Treatment 2* (green sphere) corresponds to mixture of 70:13:17[122], and *Optimized treatment* corresponds to a proportion of 55:25:20 w/w/w of chloroform:methanol:water[116]. Dashed green line indicates the maximum estimated chloroform "tie-line". Red line indicated the biphasic separation region[116]. During liver extraction, it was considered that 90% of liver's weight will contribute to the water phase (indicated as a shift to darker spheres)[116].

4) Tissue was homogenized using two cycles of Precellys for 30 minutes at 6000 rpms[116].
5) Afterwards 554 µL of chloroform:methanol (45.8:54.2 v/v) were added to each Eppendorf[116].
6) Samples were vortexed and leaved for 15 minutes on ice[116].
7) Tubes were centrifuged at 14000 rpms for 15 minutes at 4 ºC[116].
8) Phases were carefully divided into different Eppendorfs as hydrophilic and hydrophobic material[116].
9) Samples were dried using Speedvac for at least 3 h[116].
10) The remaining powder was stored at -80 ºC until further use[116].
11) For NMR measurements of the hydrophilic extraction of the liver (hydrophilic phase) the extracted material from the three dried Eppendorfs was combined and resuspended using 300 uL of hydrophilic buffer (100 mM Tris-d_{11} at pD 7 + 1 mM NaN_3 + 0.5 mM Gdbut + 1 mM TMP^+ (internal reference) in D_2O). Lipophilic extraction was resuspended in 300 µL of buffer hydrophobic (d_6-DMSO + TPPO 4 mM) following the same procedure[116].
12) The resuspended extracts (300 µL) were filled into 5 mm Shigemi NMR tubes and NMR experiments were recorded[116].

3.2.5 NMR Spectroscopy

3.2.5.1 NMR data acquisition and spectra processing

All NMR experiments were recorded at 298 K on a Bruker 600 MHz (12 T) Avance III spectrometer equipped with a QXI (^{1}H,^{13}C,^{15}N,^{31}P) or a BBO (BB,^{1}H) probehead[116]. For each sample three different experiments were collected: (i) a 1D ^{31}P *zgip* spectrum with inverse gated ^{1}H decoupling (3-11.5 h), (ii) a 1D ^{1}H *p3919gp* with water signals suppression using a binomial 3-9-19 pulse with echo gradient pair (7 min), and (iii) a 2D ^{31}P,^{1}H *COLOC* spectrum with coherence selection by gradients (5-13.5 h)[116]. The 1D ^{31}P experiment was recorded with long interscan delays $D_1 > 3 \cdot T_{1,max}(^{31}P)$ for quantification, where the paramagnetic relaxation enhancer () added only to the hydrophilic fraction allowed to use a short D_1 = 1 s while the hydrophobic fraction required D_1 = 5 s[116].

Altogether, considering all the experimental set-up we obtained a detection limit of ~200 pmol of ^{31}P-compound per mg of liver with a signal-to-noise *ratio* of 4[116]. At this configuration we concluded that a minimum of 100 mg and an optimal value of 300 mg of liver tissue are required for a reliable metabolite quantification by this method[116]. Yet, we reckon that an optimized NMR hardware set (i. e. direct observation for heteronuclei) would result in a 5-fold increase in sensitivity, equivalent to a demand of only 20 mg of liver tissue (**Figure 3.3**)[116].

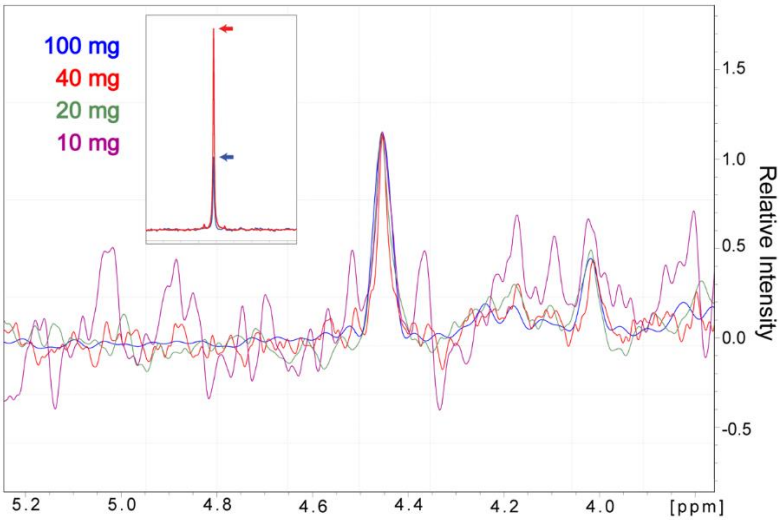

Figure 3.3. Signal-to-noise *ratio* as a function of the amount of tissue initially used. The spectrum can be quantified using 20 mg of tissue or more. Inset: comparison of the same signal with two different NMR probes.

3.2.5.2 NMR peak assignment

The same set of spectra were recorded for some 100 pure phosphorylated standard compounds (listed in **Table 3.3**) to facilitate the identification of phosphorylated liver

metabolites[116]. Each of ^{31}P standards was prepared at increased 5 mM concentration, in the appropriate solution corresponding to either hydrophilic or hydrophobic extract (see above), to allow faster NMR data acquisition[116].

The phosphorylated liver metabolites were identified by comparison with the ^{31}P chemical shifts of the pure standard compounds compiled in **Table 3.3**.

Table 3.3. Phosphorilated metabolites tested.

Compound	Company	Reference
1-(9Z-octadecenoyl)-sn-glycero-3-phospho-L-serine	Avanti	858143P
1,2-diheptadecanoyl-sn-glycero-3-phosphate (sodium salt)	Avanti	830856P
1,2-dimirystoyl-sn-glycero-3-phospho-1´-rac-glycerol	Avanti	840445
1,2-dimirystoyl-sn-glycero-3-phosphocholine	Avanti	850345
1-hexanoyl-2-hydroxy-sn-glycero-3-phosphate (ammonium salt)	Avanti	857119C
1-oleyl-2-hydroxy-sn-glycero-3-phosphocholine	Avanti	845875
1-oleyl-2-hydroxy-sn-glycero-3-phosphoethanolamine	Avanti	846725
1-palmitoyl-2-hydroxy-sn-glycero-3-phosphoethanolamine	Avanti	856705P
1-palmitoyl-2-oleyl-sn-glycero-3-phosphocholine	Avanti	850457
1-palmitoyl-2-oleyl-sn-glycero-3-phosphoethanolamine	Avanti	850757
2,3-Diphospho-D-glyceric acid pentasodium salt	Sigma	D5764
3-Deoxy-2-keto-6-phosphogluconic acid lithium salt	Sigma	79156
6-Phosphogluconic acid trisodium salt	Sigma	P7877
Adenosine 3´,5´-cyclic monophosphate sodium salt	Sigma	A6885
Adenosine 5´diphosphate sodium salt	Sigma	A2754
Adenosine 5´-diphosphoglucose disodium salt	Sigma	A0627
Adenosine 5´-diphosphoribose sodium salt	Sigma	A0752
Adenosine 5´-monophosphate sodium salt	Sigma	A1752
Adenosine 5´-triphosphate disodium salt	Sigma	A2383
Cardiolipine (Heart,Bovine) (sodium salt)	Avanti	840012
CDP-ethanolamine sodium salt hydrate	Sigma	90756
Cytidine 5´-diphosphate sodium salt	Sigma	C9755
Cytidine 5´-diphosphocholine sodium salt	Sigma	C0256
Cytidine 5´-monophosphate disodium salt	Sigma	C1006
Cytidine 5´-triphosphate disodium salt	Sigma	C1506
D-(-)-3-phosphoglyceric acid disodium salt	Sigma	79473
D-(+)-2-phosphoglyceric acid disodium salt	Sigma	79470
D-Erythrose 4-phosphate sodium salt	Sigma	E0377
D-Fructose 1,6-bisphosphate trisodium salt	Sigma	F6803
D-Fructose 6-phosphate disodium salt	Sigma	F3627
D-Glucose 6-phosphate disodium salt	Sigma	G7879
Dihydroxiacetone phosphate lithium salt / Glyceraldehyde 3-phosphate	Sigma	37442
D-Ribose 5-phosphate disodium salt	Sigma	R7750
D-Ribulose 5´-phosphate disodium salt	Sigma	83899
D-Sedoheptulose 7-phosphate lithium salt	Sigma	78832
D-Xylulose 5´-phosphate lithium salt	Sigma	15732
Farnesyl pyrophosphate	Sigma	F6892
Flavin adenine dinucleotide disodium salt	Sigma	F6625
Geranyl pyrophosphate	Sigma	G6772
Guanosine 5´-diphosphate sodium salt	Sigma	G7127
Guanosine 5´-diphosphoglucose sodium salt	Sigma	G7502
Guanosine 5´-monophosphate disodium salt	Sigma	G8377
Guanosine 5´-triphosphate sodium salt	Sigma	G8877

Lithium 6-phospho-D-galactonate	Sigma	55962
Lithium carbamoylphosphate dibasic hydrate	Sigma	C5625
Lithium potassium acetyl phosphate	Sigma	A0262
L-α-Glycerophosphocholine	Sigma	G5291
L-α-Phosphatidylcholine	Avanti	840054
L-α-Phosphatidylglycerol (Egg,Chicken) (sodium salt)	Avanti	841138
L-α-Phosphatidylinositol(Liver,Bovine) (sodium salt)	Avanti	840042
L-α-Phosphatidylserine(Brain,Porcine) (sodium salt)	Avanti	840032
O-Phosphorylethanolamine	Sigma	P0503
Phospho(enol)pyruvic acid monopotassium salt	Sigma	860077
Phosphocholine chloride calcium salt tetrahydrate	Sigma	P0378
Phosphocreatine disodium salt hydrate	Sigma	P6502
Riboflavin 5´-monophosphate sodium salt	Sigma	F2253
sn-Glycerol 1-phosphate lithium salt	Sigma	92034
sn-Glycerol 3-phosphate bis(cyclohexylammonium) salt	Sigma	G4631
Sodium phosphate	Sigma	342483
Sodium pyrophosphate tetrabasic	Sigma	322466
Spingomyelin (Egg,Chicken)	Avanti	860061
Tetramethylphosphonium chloride	Sigma	288276
Thymidine 5´-diphosphate disodium salt	Sigma	T7004
Thymidine 5´-monophosphate disodium salt	Sigma	T7004
Thymidine 5´-triphosphate sodium salt	Sigma	T0251
Triphenylphosphine oxide	Sigma	T84603
Uridine 5´-diphosphate disodium salt	Sigma	94330
Uridine 5´-diphosphogalactose disodium salt	Sigma	U4500
Uridine 5´-diphosphoglucose disodium salt	Sigma	94335
Uridine 5´-diphosphoglucuronic acid trisodium salt	Sigma	U6751
Uridine 5´-monophosphate disodium salt	Sigma	U6375
Uridine 5´-triphosphate trisodium salt hydrate	Sigma	94370
α-D-Glucose 1-phosphate disodium salt	Sigma	G7000
β- Nicotinamide adenine dinucleotide	Sigma	N0632
β-Glycerophosphate disodium salt	Sigma	G9422
β-Nicotinamide adenine dinucleotide 2´-phosphate reduced tetrasodium salt	Sigma	N7505

In some cases, spiking experiments with selected pure standard compounds were performed to confirm the metabolite assignment[116]. **Figure 3.4** shows the use of the ^{1}H-^{31}P-COLOC experiment in the assignment of phosphorylated metabolites[116]. In a complex mixture of phosphorylated compounds from a CEP UROIII$S^{P248Q/P248Q}$ mouse liver extraction we overlay 3 different ^{1}H-^{31}P-COLOCs from S7P, PEA and UDPG standards[116]. The peaks overlap and automatically identify the compounds in the hydrophilic extract[116].

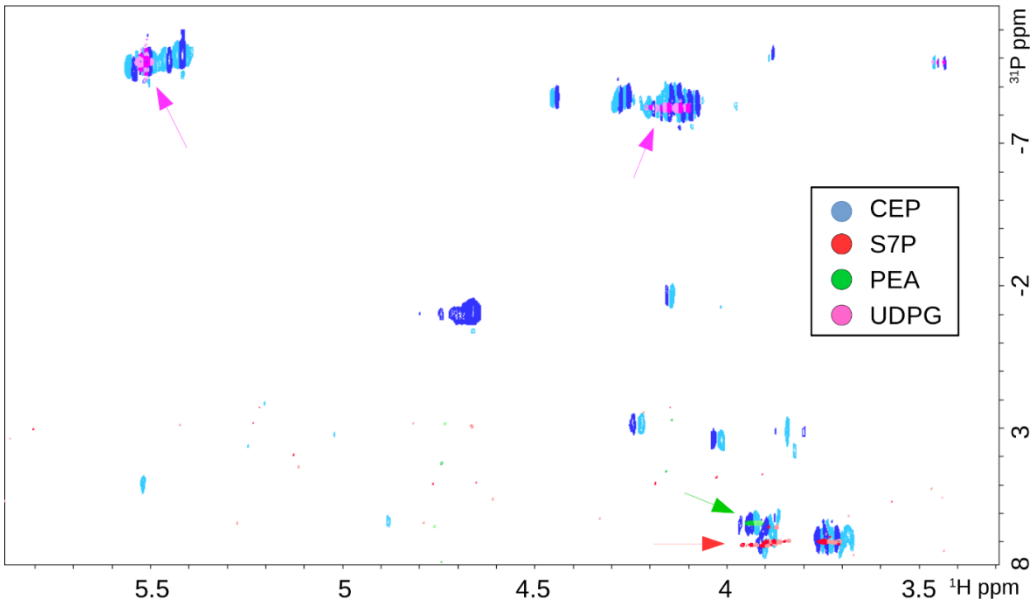

Figure 3.4. ^{1}H-^{31}P-COLOC spectrum CEP UROIII$S^{P248Q/P248Q}$ hydrophilic extraction[116]. Correlation spectroscopy *via* Long-range Coupling (^{1}H-^{31}P-COLOC) is a 2D heteronuclear experiment that correlates ^{31}P and ^{1}H nuclei[116]. The addition of a second dimension facilitated the assignment of overlapping signals. In blue ^{1}H-^{31}P-COLOC spectrum CEP mouse liver E1 extraction. S7P (red), PEA (green) and UDPG (pink) ^{1}H-^{31}P-COLOC spectra were overlaid as an example of chemical shift assignment[116].

3.2.5.3 NMR peak integration, deconvolution, and quantification

All NMR data processing and analysis was done using TopSpin 4.0.7 (Bruker Biospin GmbH) and in-house MatLab scripts[116]. Assigned ^{31}P-metabolites are ten quantified by referencing their ^{31}P peak integral against the added internal reference compound as shown in **Figure 3.5**[116] In case of signal overlap, it is applied peak deconvolution (command LDCON) to assign corresponding peak areas and thus determine the final concentration[116]. For instance, in the lipophilic phase of a Chow mouse liver PE and CL are overlapping[116]. After peak deconvolution it can determine the area for each compound within the overlapping signal, finally determining the concentration of each. In the phosphorous spectra it can easily find our internal reference on the left which will be integrated and calibrated to a determined concentration value (1 mM for tetramethylphosphonium chloride (TMP^{+}) and 4 mM for triphenylphosphine oxide (TPPO))[116]. Considering this, metabolic quantification is done by peak integration and comparison with the reference considering the spin system of the peak[116].

For the ^{1}H-spectra we identify, integrate, and calibrate the reference's peak and it is performed the same operation as for phosphorous metabolites but in this case for the lactate and choline quantification in the hydrophilic phase and triglycerides (TG) and total cholesterol (TC) determination in the lipophilic phase[116].

The extraction yield was calculated through the comparison of the remaining peak observed at 0 ppms that corresponds to the extraction reference (Sodium trimethylsilylpropanesulfonate (DSS)) that integrates 9 H and the absolute integral of the peak that integrates 12 H of the reference compound of the hydrophilic fraction (TMP^+)[116].

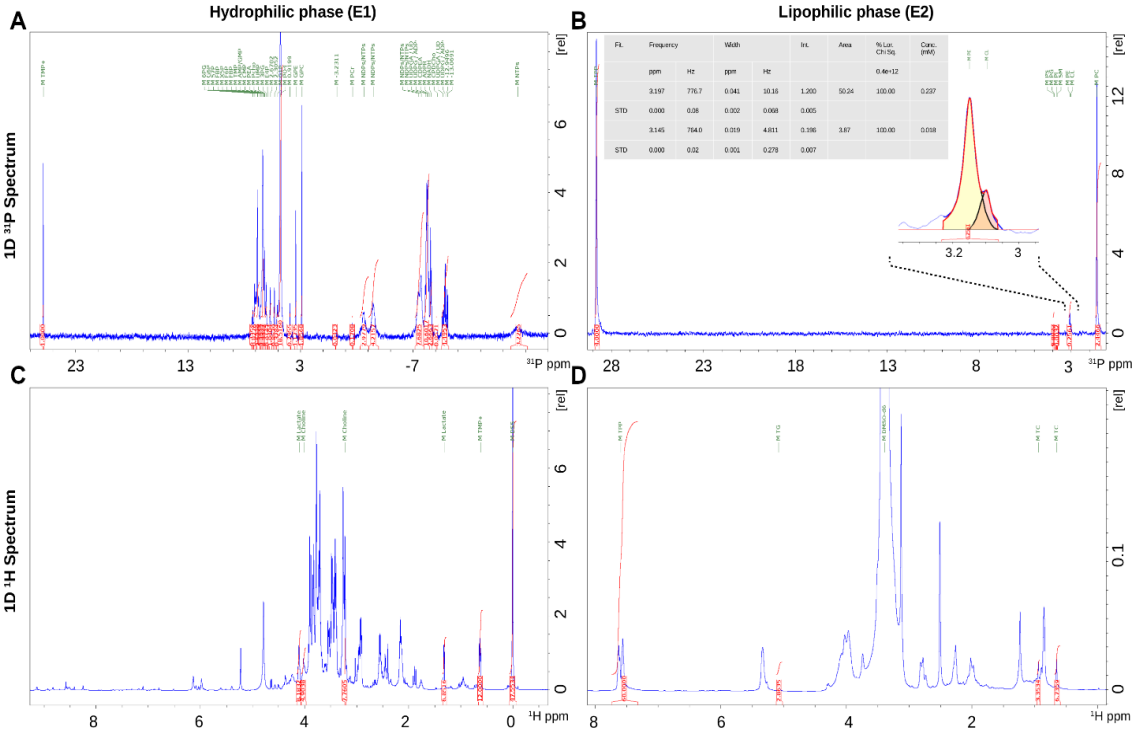

Figure 3.5. Peak quantification. ^{31}P-NMR *zgig* spectra (first row) and ^{1}H-NMR *p3919gp* spectra (second row) of the hydrophilic (first column) and the lipophilic (second column) of a WT mouse liver extraction. Peak assignment, deconvolution and quantification were performed as mentioned above[116].

3.3 Results and discussion

3.3.1 Phosphoromics analysis of mice liver extract

The main goal was to analyze phosphorylated metabolites in the liver based on the direct observation and quantification of the phosphorous signal.

Likewise, it was determined that the detection limit is around 30 pmol of phosphorylated metabolite per milligram of the liver, having a signal-to-noise *ratio* of 4, after the analysis of the phosphorome (**Figure 3.3**). Therefore, a mínimum of 20 mg and optimal value of 100 mg of the liver extract was required to quantify. Considering that the average of liver weight is about 1 g, the sample amount resulting could be divided into different liver fractions for different phosphoromic analyses, as it happened with tumor resection, or complementary histological, transcriptomics, and proteomic analyses[116].

The processing of mouse liver includes the metabolic extraction from the tissue and subsequent fractionation into the hydrophilic and the hydrophobic extracts (**Figure 3.6**)[116]. First, the first objective was to find which of various mixtures of chloroform: methanol: water. In the literature, Bligh[122] *et al.* developed a method for the extraction and purification of lipids by measuring the amount of lipid content in chloroform layer and they concluded that the best optimal condition was 40:44:16 (w/w/w of chloroform: methanol: water). They claimed that it is imperative to maintain this *ratio*, including the water present in the sample. They applied that 100 g of sample contained 80 g water. However, if the extraction material did not contain 80% water, it was necessary to adjust the volume of chloroform and methanol to obtain the correct proportions of the ternary mixture or adjust the size of the material to get 80 g water. Thus, the water molecules, which liver homogenization releases, often compromise phase separation.

To improve it, the ternary phase diagram was analyzed, as illustrated in **Figure 3.2**, identifying an optimal stoichiometry at 55:25:20 (w/w/w of chloroform: methanol: water). This extraction protocol provided excellent reproducibility and good yields (69% ± 5%) determining with an added reference compound (DSS).

Regarding quantitative analysis, the ^{31}P-NMR signal intensity is proportional to its concentration for each metabolite. For that purpose, a commercially paramagnetic relaxation enhancer, called Gadobutrol[129], was added over hydrophilic fraction. It induces fast relaxation of the signal without increasing line broadening[123]. This approach has not been applied to the hydrophobic extract because of its insolubility, and instead, longer recovery times were used. Internal reference to each fraction had to be added to quantify phosphorylated metabolites. ^{31}P-NMR required a reference compound yielding a sharp,

separated with minimal shift dependence on solvent, pH, cations, temperature, etc. For hydrophilic fraction, TMP^+ was chosen that produced sharp, largely invariant ^{31}P (22.86 ppm) and ^{1}H (1.79 ppm) singlet signals, both well separated from most of the metabolites. Likewise, for the hydrophobic fraction, TPPO was chosen because it generated a defined signal of either ^{31}P (25.58 ppm) or ^{1}H (7.60 ppm) and separated from the rest of the small compounds present in the sample. Reproducibility and statistical significance were established with a series of between six and nine repetitions.

An illustrative ^{31}P-spectrum of mouse liver hydrophilic and hydrophobic extracts is presented in **Figure 3.6** and **Table 3.4**, and as it can be seen, there is an excellent peak dispersion. Peaks were assigned by comparison with a database of ^{31}P chemical shifts for more than 80 metabolites (**Table 3.4**). Phosphorylated standards were collected at the same experimental conditions. In order to confirm the assignment, it is used heteronuclear 2D ^{1}H, ^{31}P-COLOC, which correlates $^{31}P(-O-C-)^{1}H_n$ moieties present in a wide majority of the metabolites. Moreover, in some cases, it was necessary to spike the sample with an uncertain phosphorylated compound to corroborate the assignment.

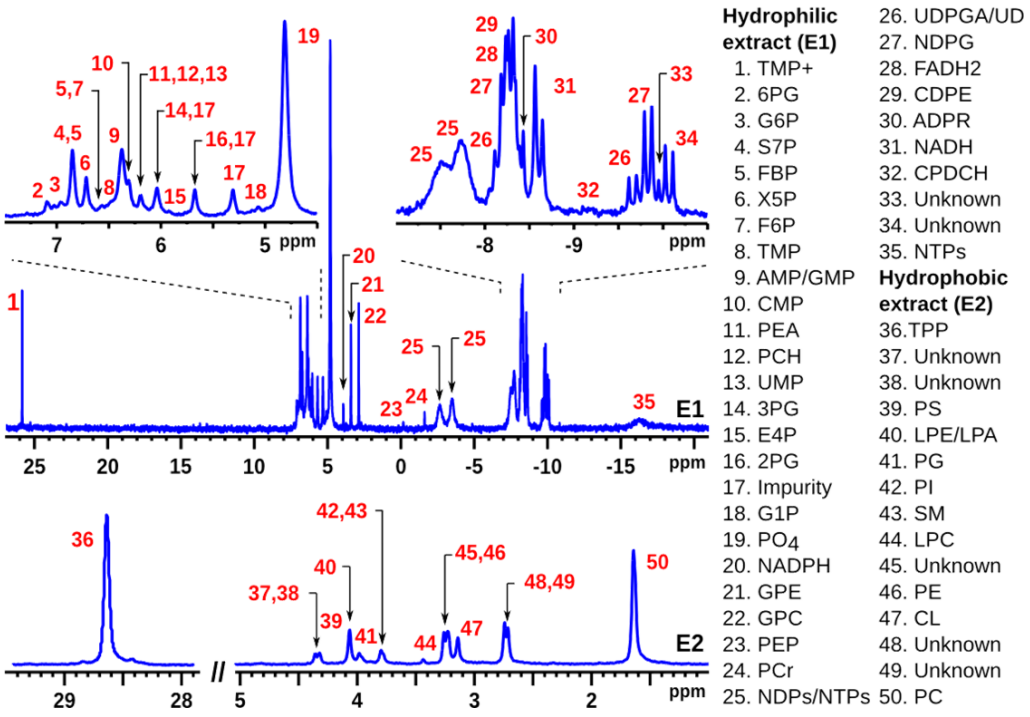

Figure 3.6. ^{31}P-NMR spectrum of mouse liver extracts in which a total of 50 different peaks were identified in two extracts.

Table 3.4. ^{31}P Chemical shifts of assigned metabolites in the hydrophilic and hydrophobic phase.

E1 (Hydrophilic)	^{31}P (ppm)	STDV
TMP+ (REF)	25.83	0.01
6PG	6.86	0.36
G6P	6.79	0.28
S7P	6.66	0.25
FBP	6.65 6.39	0.25 0.21
X5P	6.51	0.23
F6P	6.39	0.22
TMP	6.22	0.28
AMP/GMP	6.14	0.26
CMP	6.13	0.22
PEA	5.97	0.24
PCHO	5.96	0.23
UMP	5.95	0.22
3PG	5.77	0.24
E4P	5.60	0.24
2PG	5.40	0.25
G1P	4.71	0.37
PO4	4.45	0.41
NADPH	3.90	0.05
GPE	3.41	0.01
GPC	2.87	0.01
PEP	-0.23	0.06
PCr	-1.62	0.00
NDPs/NTPs	-2.86 -3.94 -7.17 -7.68	0.29 0.49 0.27 0.04
UDPGA / UDPgal	-8.20 -9.65	0.05 0.02
UDPG / ADPG / GDPG / FADH2	-8.24 -9.83	0.01 0.01
CDPE	-8.26	0.02
ADPR	-8.34	0.11
NADH	-8.61	0.05
CDPCH	-9.07	0.09
NTPs	-16.72	0.37

E2 (Hydrophobic)	^{31}P (ppm)	STDV
TPP (REF)	28.60	0.09
PS	4.05	0.08
LPA/LPE	4.02	0.06
PG	3.99	0.07
PI	3.84	0.10
SM	3.80	0.10
LPC	3.46	0.04
PE	3.15	0.07
CL	3.19	0.10
PC	1.67	0.09

^{31}P chemical shifts are very sensitive to different parameters that are vital to take into consideration such as temperature, pH, solvent, and metabolite concentrations[116]. Chemical shift fluctuation was estimated for each metabolite from a comparison of a set of mouse liver samples, as shown in **Figure 3.7**[116].

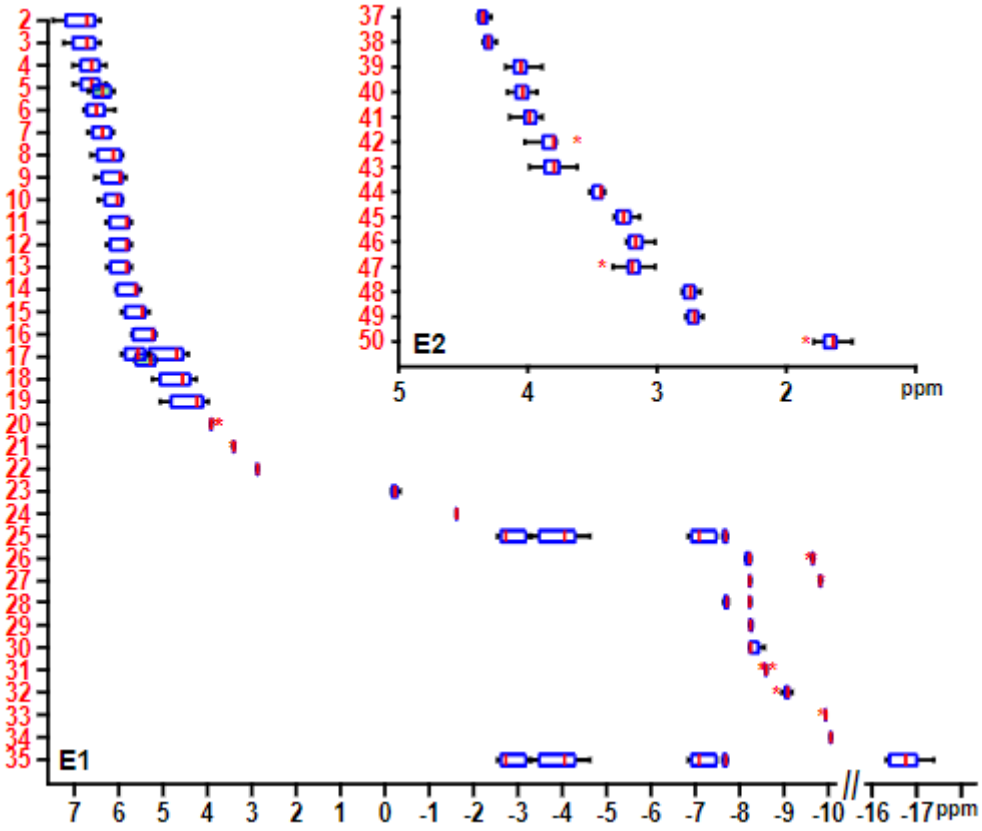

Figure 2.7. Chemical shift fluctuation was estimated by a comparison of more than 50 spectrum from liver samples.

Most of the metabolites were monophosphorylated, therefore, it appeared one ^{31}P-NMR signal in the spectrum. However, pyrophosphorylated metabolites habitually exhibit ^{31}P-NMR signals with doublet (terminal phosphate groups) or triplet (central phosphate groups) structure[116].

Nucleoside diphosphates (NDPs) and nucleoside triphosphates (NTPs) could not discriminate due to their nucleobase, and they appeared as broad ^{31}P signals with overlap[116]. Thus, according to **Figure 3.6**, peak 25 corresponded to the terminal α and β-phosphates in NDPs and α and γ-phosphates in NTPs. Meanwhile, signal 35 corresponded to a broad but well-separated central β-phosphate in NTPs.

In relation to hydrophobic extract, as shown in **Figure 3.6**, phosphatidylcholine (PC; peak 50 at 1.67 ppm) dominated lipophilic fraction, followed by phosphatidylethanolamine (PE; peak 46 at 3.15 ppm). Some samples, including CEP mouse liver samples, contained minority phospholipids such as lyso-PC (LPC; peak 44 at 3.46), lyso-PE (LPE; peak 40 at 4.02 ppm), phosphatidylserine (PS; peak 39 at 4.05 ppm), sphingomyelin (SM, peak 43 at 3.80 ppm) and phosphatidylinositol (PI; peak 42 at 3.84 ppm).

In addition to being validated this method in liver tissue from mouse models, this methodology has also been validated with the corresponding analysis of human samples. **Figure 3.8** shows a ^{31}P-NMR spectrum of a biopsy of a patient with hepatocellular carcinoma, being identified and assigned all the metabolites.

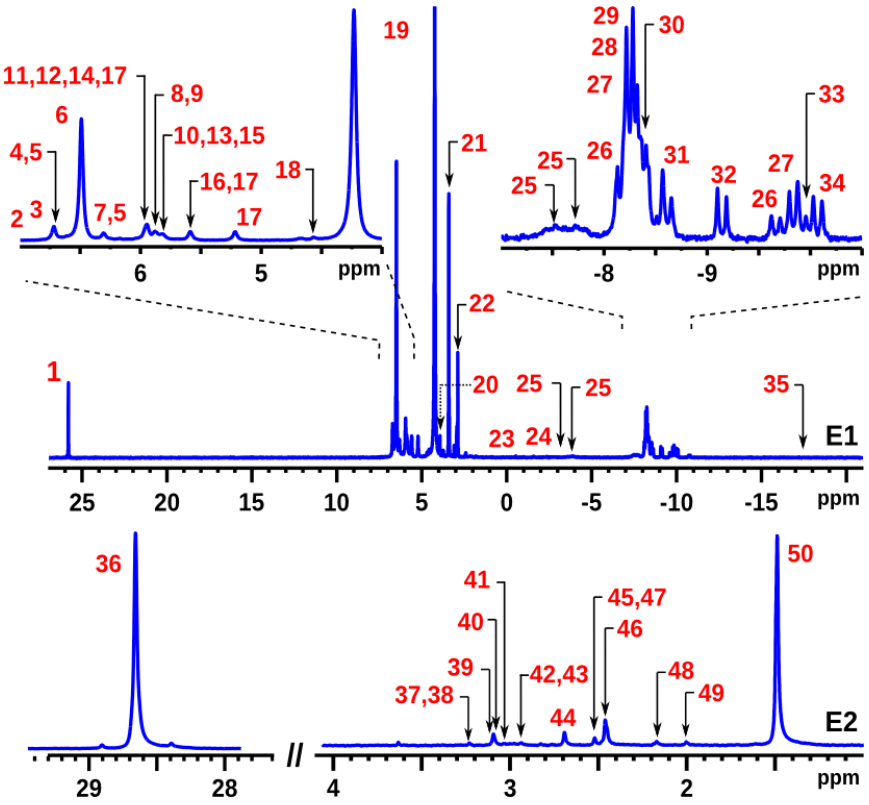

Figure 3.8. ^{31}P-NMR spectrum of a sample of human liver tissue (hepatocellular carcinoma) obtained from biopsy. A total of 50 different peaks were identified within the two extracts.

2.3.2 Metabolic signature of the phosphorome

54 phosphorylated metabolites have been identified and quantified in this ^{31}P-NMR methodology, covering the main metabolic pathways like central metabolism (glycolysis, PPP, and the TCA cycle), glycogenesis, phospholipids, nucleotides and nicotinamide metabolism as well as 4 non-phosphorylated metabolites (Lactate (LAC), choline (CHO), triglycerides (TG) and total cholesterol (TC)) (**Figure 3.9**).

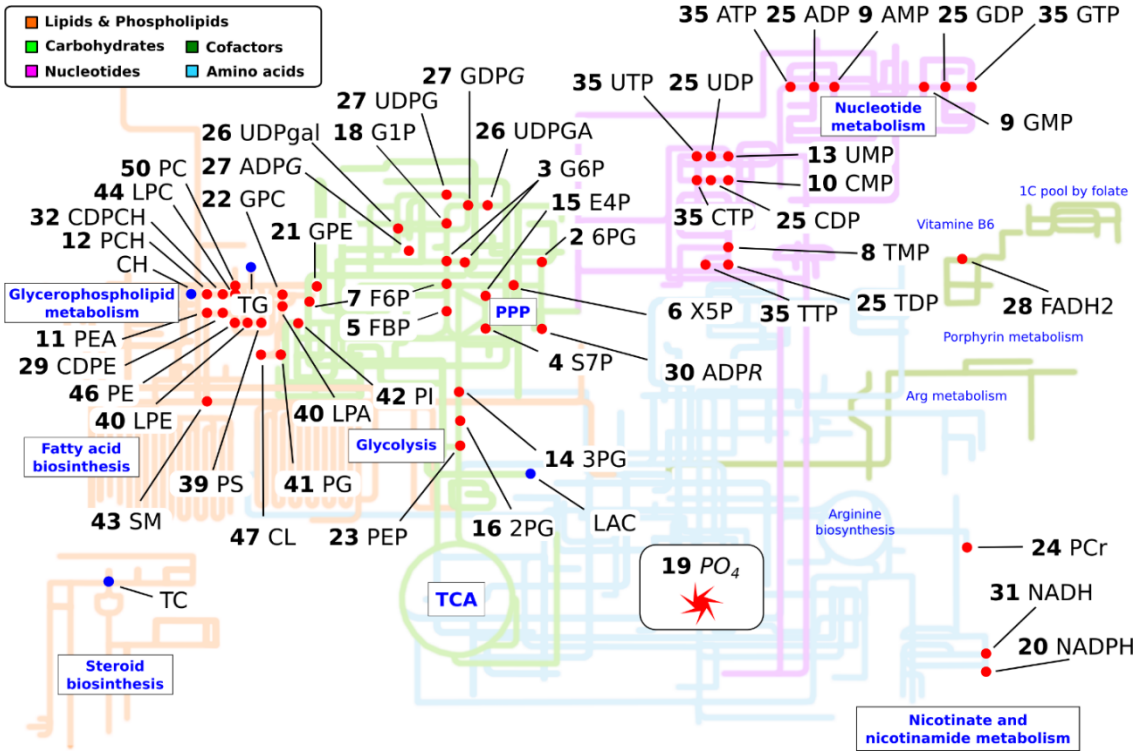

Figure 3.9. Map of the phosphorome, in which the metabolites measured by ^{31}P-NMR were represented as red circles whereas the metabolites assigned by ^{1}H-NMR exhibited blue circles.

As it is represented in **Figure 3.9**, metabolites identified and quantified are marked by red circles. The remaining phosphorylated compounds were tested but not detected, perhaps, because their concentration values were below the detection limit (nearly 20 µM in this ^{31}P-NMR methodology).

In global terms, the phosphorome gives us information on the entire liver metabolism. Hydrophilic extract reports on the central carbon metabolism, whereas hydrophobic fraction yields information on the phospholipid composition[116].

Thus, this method provided quantitative information about the level of glucose 6-phosphate (G6P), the first intermediate of glucose catabolic metabolism which lies at the start of two major metabolic pathways: glycolysis and the pentose phosphate pathway (PPP) and consequently its catabolic products, fructose 6-phosphate (F6P) and 6-phosphogluconate (6PG). In addition to these two metabolic pathways, G6P is also produced during glycogenesis from glucose 1-phosphate (G1P), the first product of the breakdown of glycogen. Next, G1P reacts with uridine-5-triphosphate (UTP) to form uridine diphosphoglucose (UDPG), a nucleotide sugar metabolite that in addition to being precursor of glycogen, can convert into uridine diphospho-galactose (UDPgal) and uridine diphospho-glucuronic acid (UDPGA), which can then be used as substrates by

the enzymes that make polysaccharides containing galactose and glucuronic acid as well as a precursor of sucrose, lipopolysaccharides and glycosphingolipids.

One thing that is vital to the liver is the quantification of phosphorylated metabolites involved in glycolysis such as fructose 1,6-bisphosphate (FBP), 3-phosphoglycerate (3PG), 2-phosphoglycerate (2PG) and phosphoenolpyruvate (PEP), being PEP the last phosphorylated metabolite involved in the conversion of glucose to pyruvate.

Likewise, the activity of the non-oxidative phase of the PPP in the liver was measured by the quantification of xylulose 5-phosphate (X5P), sedoheptulose 7-phosphate (S7P) and erythrose 4-phosphate (E4P).

The concentration values of NTPs, NADH, NADPH and flavin adenine dinucleotide ($FADH_2$) indicated the level of phosphoryl and electron-transfer potential in anabolic pathways because they are involved in redox reactions, carrying electrons from one reaction to another by the release of energy. Phosphocreatine (PCr), a phosphorylated form of creatine that serves as a mobilizable reserve of high-energy phosphates in muscle, was measured.

Also, it was necessary to obtain information about the levels of nucleosides triphosphates, diphosphates and monophosphates (NTPs, NDPs and NMPs) that were crucial because the liver is one of the main sites of nucleotide synthesis that is used to flow energy in hepatocytes.

The content of adenosine 5´-diphosphoribose (ADPR), a product of the activity of PARPs, also known poly(ADP-ribose) polymerases, which plays an important role in the cellular response to stress, including DNA damage repair[130], was also measured.

Phosphatidylcholine (PC) is the most abundant phospholipid of all mammalian cell types. PC comprises 40-50% of total cellular phospholipids. PC has a crucial role as a direct or indirect source of structural building blocks for cellular membranes[131]. In addition, the levels of the precursors of the biosynthesis of phosphatidylcholine, also known Kennedy pathways or CDP-choline pathways, such as glycerophosphocholine (GPC), lyso-phosphatidylcholine (LPC), phosphocholine (PCHO), choline (CH) and cytidine diphosphocholine (CDPCH) were determined. However, in hepatocytes, PC is also synthesized by the sequential methylation of phosphatidylethanolamine (PE), a reaction catalyzed by the enzyme PE *N*-methyltransferase (PEMT), consuming three molecules of SAMe for each molecule of PC formed. Specifically, in the liver, 70% of PC is biosynthesized from choline via CDPcho pathway, whereas 30% of PC is derived from PE via PEMT pathway[116,132]. PC can also be secreted as an important component of very

low-density lipoproteins (VLDL)[116]. What is more, PC provides choline for sphingomyelin (SPM) synthesis, and it is a precursor of phosphatidylserine (PS), being both compounds identified and quantified by this platform.

PE is the second most abundant phospholipid in mammalian membranes, being 15-25% of total phospholipids. PE is synthesized by two separate biosynthetic pathways. One of them, via CDP-ethanolamine pathway, which parallels the CDP-choline pathway for PC synthesis, phosphoethanolamine (PEA), cytidine diphosphoethanolamine (CDPEA), glycerophosphoethanolamine (GPE), lyso-PE are the responsible for the production of PE, thus, these phosphorylated metabolites were measured by this ^{31}P-NMR method. Likewise, abnormality PC/PE molar *ratios* in different tissues can influence energy metabolism and it is correlated to disease progression. In fact, in the liver, PC/PE *ratio* is a key regulator of cell membrane integrity, and it plays an important role in the progression of steatosis into steatohepatitis[116,133].

Cardiolipin (CL), a phospholipid mostly localized in mitochondrial membranes, was measured in addition to its precursors such as lyso-phosphatidic acid (LPA) or phosphatidylglycerol (PG). CL has been involved in the formation of enzyme complexes of the respiratory chain and in the mitochondrial apoptotic pathway, being a potential target for therapeutical intervention in diseases in which cell death is dysregulated, such as cancer[134,135].

Moreover, phosphatidylinositol (PI), a low-abundance membrane phospholipid, was determined.

2.3.3 Liver damage caused by CEP

In this proof, the value of the phosphoromic approach by studying a metabolic disease and the therapeutic effect of a new drug for CEP treatment, called CPX was evaluated.

CEP is a rare autosomal recessive disease, resulting from a deficiency in the activity of the fourth enzyme of the heme biosynthetic pathway (UROS). Consequently, there is an accumulation of the porphyrinogen I isomers (uroporphyrinogen I and coproporphyrinogen I) in bone marrow erythroid precursors and erythrocytes [34,35,136,137]. Then, these isomers are auto-oxidized resulting in the corresponding porphyrins, that are photo-activated, damaging erythrocytes and finally, depositing in tissues and bones. Because of their photocatalytic properties, different sources of long-wave ultraviolet light like sunlight can cause a skin reaction[138,139].

It is one of the less common porphyria, whose prevalence has been estimated at about 1 or less in 1000000, with approximately 300 cases reported in the world[140]. This

metabolic disorder is always characterized by skin photosensitivity and hemolytic anemia. It is considered as a multi-system disease because of the wide range of signs and symptoms that patients suffer, such as hematological, cutaneous, ocular, and skeletal pathologies. The severity of the clinical manifestation's changes among CEP patients and it is likely independent of the amount of porphyrin accumulated in the tissues[141].

The molecular basis of CEP is related to the alteration of the biosynthesis of the heme group. As defined above, a deficiency of UROSIIIS enzyme. The heme groups are needed for a variety of hemoproteins, such as hemoglobin, myoglobin, respiratory cytochromes required for mitochondrial electron transport and cytochrome P450 enzyme. In humans, the heme group is produced in all cells. However, it is mainly synthesized by erythrocytes in the bone marrow and most of the rest takes place in hepatocytes cells[142] . Heme biosynthesis is a chemical process, in which subsequent reactions are carried by eight different intracellular enzymes located between the mitochondria and the cytosol.

As observed in many diseases, CEP also generates hepatic damage[143]. Histological analysis revealed that the liver from CEP animals showed steatosis with fibrosis confirmed by the NASH score (**Table 2.5**), in which their values showed moderate steatosis and fibrosis. Likewise, they exhibited porphyrin deposits and an elevated content of erythroid cells clustering around sinusoids[144,145], being the erythroid abnormalities attributed to ineffective erythropoiesis, active erythropoiesis with the premature death of red blood cells (RBC), with the most probable cause is the porphyrin accumulation from marrow erythroid precursors[146–148]. This erythropoiesis is stimulated in response to the severity of hemolytic anemia, the main hematological feature found in CEP.

Table 2.5. NAS score for CEP. Reference values for NAS scores: 0-2 considered as not diagnostic of NASH, 3-4 borderline diagnosis of NASH, 5-8 positive diagnostic of NASH.

Mice	Control CEP (n = 6)	CEP (n = 6)	CEP+CPX (n = 6)
NAS score	**0** (100%)	**2** (66%); **3** (33%)	**0** (100%)
Fibrosis stage	**0** (100%)	**1** (66%); **0** (33%)	**0** (66%); **1** (33%)

The phosphorome approach was used in order to compare liver samples from CEP mice with liver samples from WT mice to have more knowledge about the metabolic alterations

of the CEP condition (**Figure 3.10**, **Table 3.6**). From E1 liver ^{31}P-NMR fraction, it provided a reduction of G6P in addition to its catabolic (6PG, PPP) and anabolic product (G1P, glycogenesis) (**Figure 3.10 A**). Consequently, in relation to decreased levels of G1P, UDPG/ADPG, GDPG (glycogenesis) concentration values were reduced (**Figure 3.10 A/B**). Likewise, with respect to decreased values of 6PG, NADPH (**Figure 3.10D/E**), one of the products of the oxidative phase of PPP, was reduced as well as the content of X5P and S7P (**Figure 3.10 D**), two of the major metabolites involved in a non-oxidative phase of PPP.

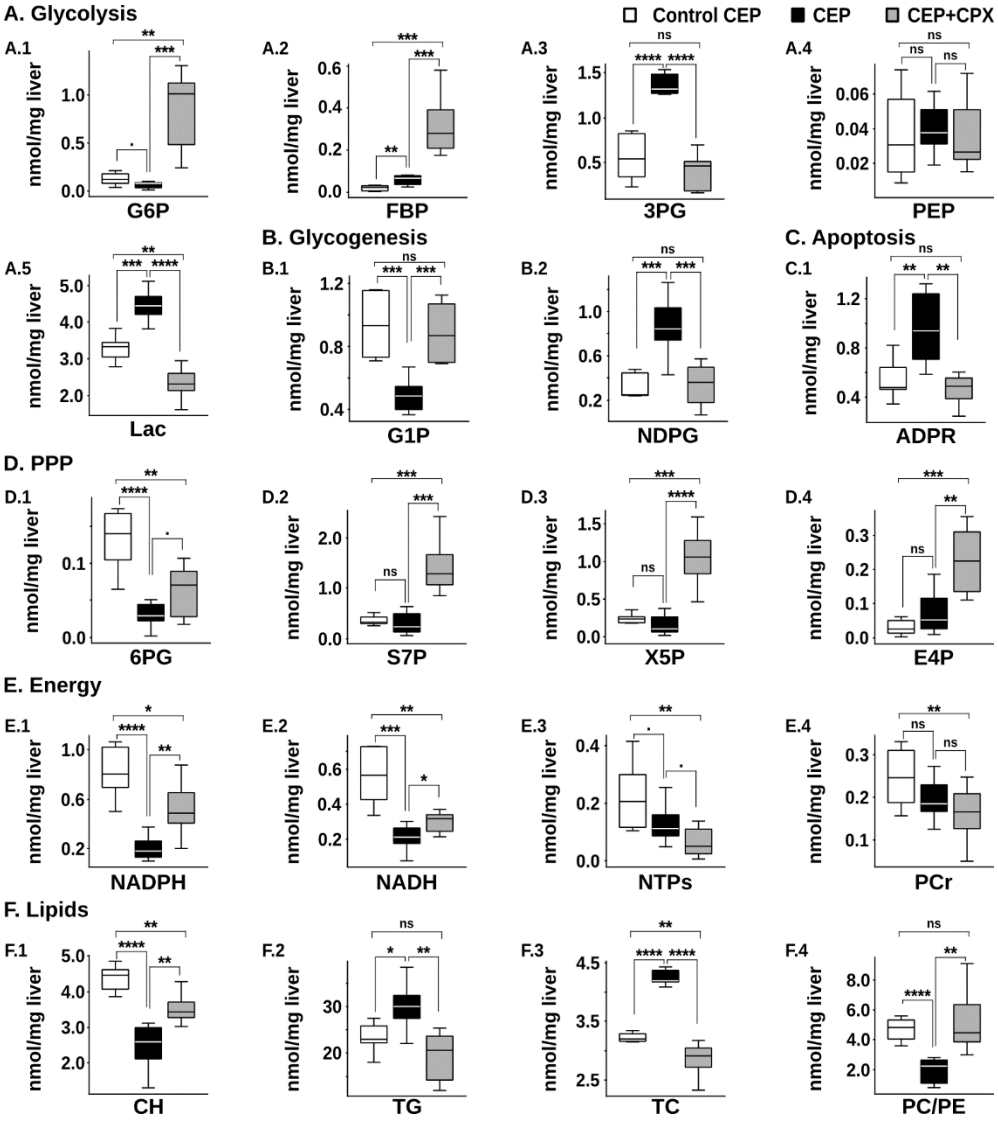

Figure 3.10. Metabolite quantification for the CEP model. Comparison of the concentration values of phosphorylated metabolites (nmol/mg liver) between control CEP (white bars; n = 6), CEP (black bars; n = 7) and CEP treated with CPX (grey bars, n = 7). A) Glycolysis, B) Glycogenesis, C) Apoptosis, D) Pentose phosphate (PPP), E) Energy, F) Lipids[116]. P values of < 0.1, 0.05, 0.01, 0.001 and 0.0001 are represented by, *, **, *** and ****, respectively[116].

Table 3.6. Quantification of the metabolites and standard deviations (STDV) for the different compounds and mouse models under consideration. The following number of mice were used in each experiment: Control CEP, n=6; CEP, n=7; CEP+CPX, n=7.

Peak	Compound	Extract	Control CEP	STDV	UROS	STDV	UROS + CPX	STDV
16	2PG	E1	0.44	0.06	0.38	0.06	0.43	0.08
14	3PG	E1	0.56	0.10	1.37	0.04	0.39	0.08
2	6PG	E1	0.13	0.02	0.03	0.01	0.06	0.01
30	ADPR	E1	0.54	0.07	0.97	0.11	0.46	0.05
9	AMP/GMP	E1	1.44	0.18	1.21	0.14	1.84	0.10
32	CDPCH	E1	0.15	0.02	0.31	0.04	0.14	0.01
29	CDPE	E1	1.14	0.12	0.93	0.18	0.86	0.08
	Cho	E1 (1H)	4.38	0.15	2.45	0.24	3.52	0.15
47	CL	E2	0.40	0.07	0.62	0.10	0.41	0.07
10	CMP	E1	1.06	0.14	0.80	0.10	1.33	0.08
15	E4P	E1	0.03	0.01	0.07	0.02	0.22	0.04
7	F6P	E1	0.02	0.01	0.10	0.04	0.32	0.05
28	$FADH_2$	E1	0.78	0.13	0.37	0.03	1.17	0.24
5	FBP	E1	0.02	0.01	0.06	0.01	0.32	0.05
18	G1P	E1	0.94	0.09	0.49	0.04	0.88	0.07
3	G6P	E1	0.12	0.03	0.06	0.01	0.82	0.15
22	GPC	E1	5.58	1.03	3.22	0.49	2.29	0.76
21	GPE	E1	3.23	0.38	1.65	0.41	1.40	0.47
17	Impurity	E1	1.27	0.06	1.38	0.11	1.38	0.13
	LAC	E1 (1H)	3.30	0.15	4.45	0.16	2.36	0.16
40	LPA/LPE	E2	0.02	0.00	0.01	0.00	0.01	0.00
44	LPC	E2	0.07	0.01	0.12	0.01	0.06	0.01
31	NADH	E1	0.56	0.07	0.21	0.03	0.30	0.02
20	NADPH	E1	0.81	0.09	0.20	0.04	0.52	0.08
25	NDPs	E1	1.81	0.08	1.31	0.05	2.07	0.15
35	NTPs	E1	0.23	0.05	0.13	0.03	0.07	0.02
50	PC	E2	2.78	0.18	1.53	0.26	3.00	0.28
12	PCHO	E1	0.15	0.01	0.11	0.01	0.67	0.10
24	PCr	E1	0.25	0.03	0.19	0.02	0.16	0.02
46	PE	E2	0.62	0.08	0.84	0.10	0.64	0.10
11	PEA	E1	0.13	0.02	0.11	0.01	0.54	0.09
23	PEP	E1	0.04	0.01	0.04	0.01	0.04	0.01
41	PG	E2	0.10	0.01	0.18	0.07	0.11	0.05

42	PI	E2	0.07	0.02	0.05	0.01	0.06	0.02
19	PO_4^{3-}	E1	63.00	1.74	52.82	4.45	84.80	6.20
39	PS	E2	0.36	0.06	0.25	0.06	0.27	0.07
4	S7P	E1	0.35	0.04	0.28	0.09	1.44	0.20
43	SM	E2	0.07	0.01	0.05	0.01	0.10	0.04
	TC	E2 (1H)	3.23	0.03	4.25	0.05	2.85	0.11
	TG	E2 (1H)	23.14	1.31	29.88	1.89	18.98	1.96
8	TMP	E1	0.18	0.03	0.28	0.05	0.52	0.06
1	TMP+	E1	0.99	0.01	1.00	0.01	1.01	0.02
36	TPPO	E2	3.79	0.06	4.46	0.32	4.00	0.06
27	NDPG	E1	0.32	0.05	0.87	0.10	0.33	0.07
26	UDPGA / UDPgal	E1	0.14	0.01	0.57	0.03	0.17	0.05
13	UMP	E1	0.07	0.01	0.06	0.01	0.42	0.09
6	X5P	E1	0.24	0.03	0.15	0.05	1.05	0.14
33	Unknown	E1	0.09	0.01	0.13	0.03	0.07	0.01
34	Unknown	E1	0.44	0.07	0.67	0.10	0.36	0.07
37	Unknown	E2	0.06	0.01	0.17	0.08	0.07	0.03
38	Unknown	E2	0.12	0.03	0.31	0.08	0.19	0.05
45	Unknown	E2	0.16	0.05	0.21	0.07	0.21	0.08
48	Unknown	E2	0.12	0.03	0.54	0.16	0.25	0.09
49	Unknown	E2	0.15	0.04	0.65	0.13	0.30	0.09

On another hand, one of the first metabolites involved in glycolysis, fructose 1,6-bisphosphate (FBP), was increased (**Figure 3.10A**), which means, that glycogenesis and PPP were slowed down whereas the flow of glucose through glycolysis was favored. This idea was corroborated by the content of 3PG and LAC (**Figure 3.10A**), the end products of glycolysis, which were increased in CEP mice compared with WT animals. The phenomenon that took place was Warburg effect[149] (**Figure 3.11**), which is mainly

observed in cells that ferment glucose to lactic acid through the glycolytic pathway even in the presence of oxygen. It is one of the main fundamental causes of cancer.

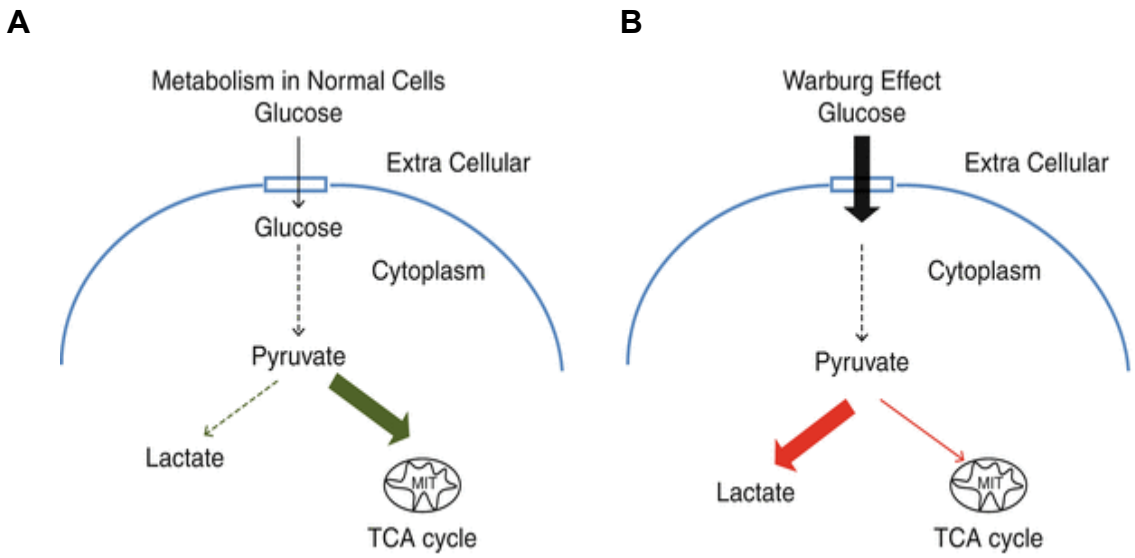

Figure 3.11. Schematic representation of Warburg effect in which in A) normal cells, most of the flux which comes from glucose goes to TCA cycle. However, in cancer cells, it goes to lactate (LAC). Figure adapted[66].

In the presence of a normal cell (**Figure 3.11A**), glucose is transformed into pyruvate and then it is incorporated into TCA cycle in mitochondria through oxidative phosphorylation in which oxygen acts as an electron acceptor making it possible to recycle NADH to NAD^+. Therefore, it is an efficient energetic process in which one mole of glucose generates 36 moles of ATP.

In the absence of oxygen (**Figure 3.11B**), cells transform the pyruvate into lactate. It occurs typically in muscle during heavy exercise when the oxygen is limited, and it is called anaerobic glycolysis. Nevertheless, in the presence of oxygen, Warburg observed that cancer cells convert glucose into LAC, preferring cancer cells energy inefficient process even under aerobic conditions and he claimed that mitochondrial dysfunction was the primary reason for the cancer[150].

In CEP mice, Warburg effect could be explained by heme deficit, which is present in porphyria and the main consequence of that causes mitochondrial respiration damage. In previous literature, it was suggested that the existence of mitochondrial dysfunction can be used as a potential non-invasive biomarker for the activity of this disease, having been reported a reduction in the respiratory cytochromes in cells isolated from peripheral blood of patients of different porphyries[151].

In relation to Warburg effect, it is associated in CEP liver with a decrease in NTPs, NADH and $FADH_2$ (**Figure 2.10E**), where NADH and $FADH_2$ are used as a redox cofactor in

TCA cycle and then, they are used in oxidative phosphorylation (electron transport) pathway to produce usable chemical energy in the form of ATP, therefore, having deficient cellular respiration.

Likewise, iron is an essential nutrient that is used for oxygen transport, DNA synthesis and cell proliferation[152,153]. In CEP mice, there is a rise in iron accumulation, which comes from heme degradation, that leads to a Fenton reaction with hydrogen peroxide to generate highly hydroxyl radicals in hepatocytes that are associated with DNA damage and lipid peroxidation[154,155].

What is more, in CEP animals, ADPR concentration values (**Figure 3.10C**), a molecular biomarker associated with cell injury and apoptosis[116,156,157], were decreased.

Regarding the phospholipids analysis in the hydrophobic fraction (**Figure 3.12**), it showed an accumulation of lipids in CEP liver as compared with WT mice although PC, the major component of total phospholipids, was decreased. Likewise, in relation to a decrease in PC levels, there was a decrease in the content of CDPCH, a phosphorylated intermediate in the synthesis of PC from CH *via* CDPCH pathway in addition to a marked reduction in liver CH levels. Moreover, there was an increase in lyso-PC concentration values, a phospholipid mediator in hepatic lipotoxicity[158]. In fact, it has been demonstrated that hepatic tissue concentrations of LPC are greater in the liver of NASH patients than in healthy controls[153]. Furthermore, increased levels of TG and TC were observed which are biomarkers of NASH[159] (**Figure 3.10F**). Because of a reduction of PC levels, the major phospholipid present in VLDL, causes an impaired VLDL biosynthesis and a reduction in the capacity to export VLDL into extrahepatic tissues. In summary, all the features mentioned have been correlated with the human phenotype of NASH.

Equivalently, an accumulation of PG, PE and CL has also been associated with mitochondrial disease playing an important role in defects of mitochondrial phospholipid metabolism[160]. PI, PS and SM levels were unchangeable whereas PC/PE and PC(PE + SM) *ratios* (**Figure 3.10F**) were significantly reduced in CEP mice liver, which are biomarkers of impaired membrane integrity, liver failure and steatohepatitis[133,161]. One interesting result was the reduction in liver CH levels observed in CEP mice (**Figure 3.10F**) causing an impaired VLDL biosynthesis and export with an increase in intrahepatic TG (**Figure 3.10F**). In agreement with this conclusion, liver histology of CEP mice also exhibited steatosis, inflammation, and fibrosis (**Figure 3.12**)[116].

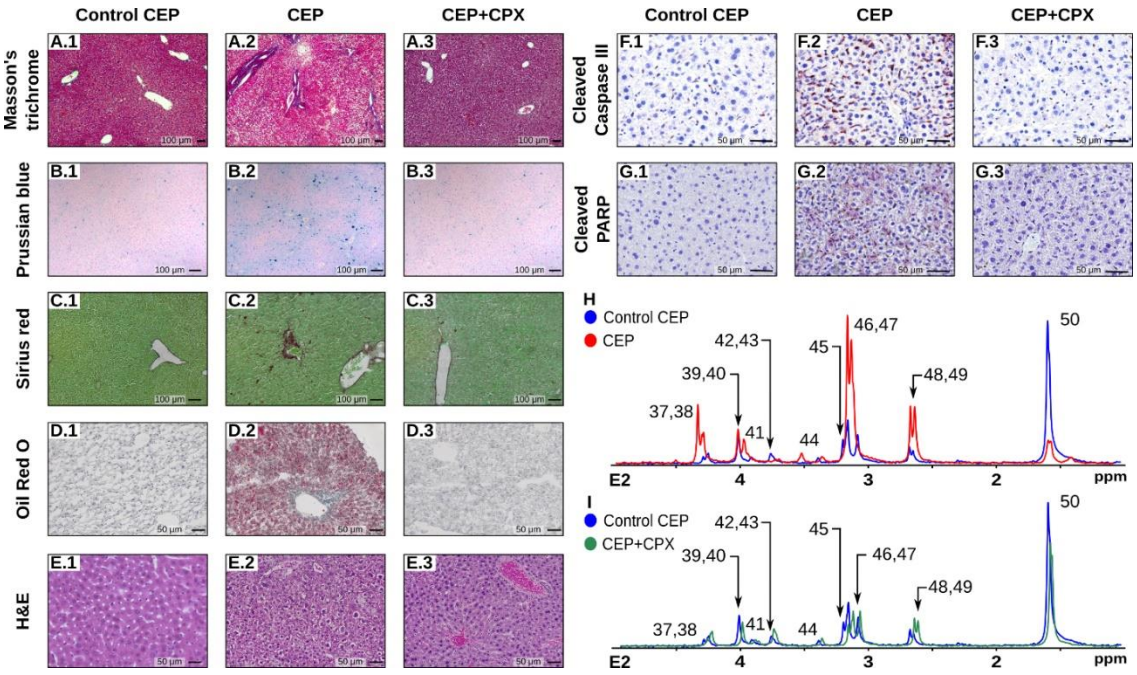

Figure 3.12. Impact of CEP condition in ^{31}P signature of mice liver and metabolic improvements by CPX[116]. A-G) Histology performed by A) hematoxylin/eosin, B) Prussian blue, C) sirius red, D) Oil Red O, E) Masson´s trichrome, F) caspase-3, or G) PARP staining of control CEP (1) and CEP mice (2) with the latter also treated with CPX (3). CEP murine models (n = 7) exhibited steatosis with fibrosis, phosphryrin deposits, and accumulation of erythroid cells clustering around sinusoids as well as compared with WT mice (n = 6)[116]. All these pathogenic features decreased after the administration of CPX (n = 7)[116]. H,I) ^{31}P spectra of lipophilic fraction by comparison of WT (blue) peaks *versus* CEP liver (red) and CEP liver treated with CPX (green)[116]. Abbreviations: hematoxylin and eosin (H&E)[116].

Overall, it was possible to conclude that mitochondrial malfunction was the origin of anaerobic glycolysis and consequently, a lactate accumulation (Warburg effect) in CEP animals[116]. Thus, in this scenario, the increased glucose consumption was used as a carbon source for anabolic processes in which the excess carbon was diverted into multiple pathways (for instance, *de novo* lipogenesis[162]) that come from glycolysis to generate nucleotides, lipids and proteins. This together with the decrease of PC, which is vital for VLDL synthesis and export, as well as increase in iron deposition, which generates reactive oxidative compounds could explain the development of NASH in CEP liver mice (**Figure 3.13**).

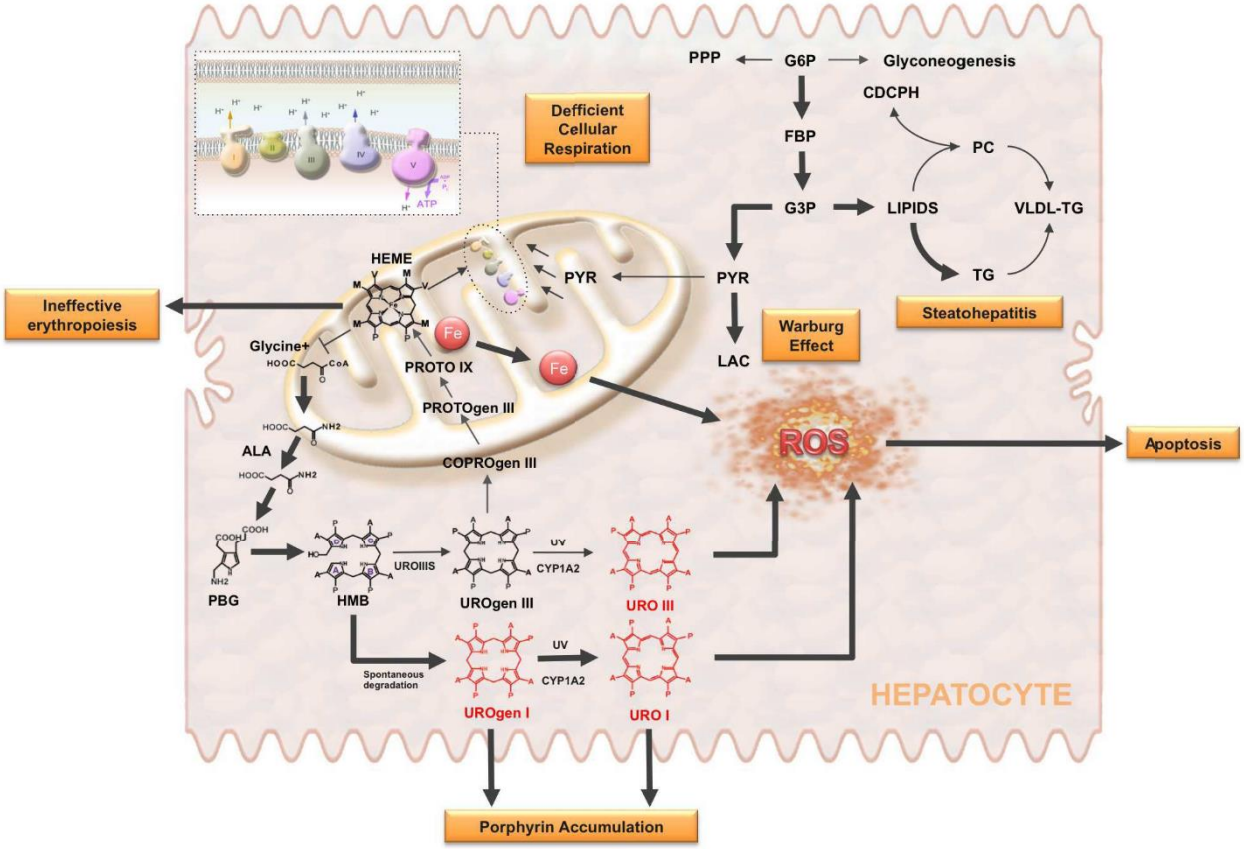

Figure 3.13. Porphyrin accumulation and oxidative stress in CEP. CEP is a metabolic disorder of heme biosynthesis in which UROSIIS activity is reduced and nonphysiologic porphyrins (UROgen I and URO I). This disease can cause iron deposition, ineffective erythropoiesis, mitochondrial impairment and production of reactive oxygen species (ROS). The illustration also shows the activation of glycolysis produced by mitochondrial dysfunction (Warburg effect). This effect, with the decrease of phosphatidylcholine (PC), which is vital for the VLDL biosynthesis and export, and elevated production of ROS can explain the development of steatohepatitis in CEP animals. Abbreviations: aminolevulinate (ALA); coproporphyrinogen (COPROgen); cytochrome P450 1A2 (CYP1A2); glyceraldehyde 3-phosphate (G3P); heme group (HEME); hydroxymethylbilane (HMB); porphobilinogen (FGB); protoporphyrin (PROTO); protoporphyrinogen (PROTOgen); pyruvate (PYR); uroporphyrin (URO); uroporphyrinogen (UROgen); ultraviolet radiation (UV).

2.3.4 Therapeutic effect of CPX as investigated by phosphoromic analysis of liver extracts

The conformation of UROSIIIS enzyme is not stable thermodynamically, however, its lifetime is long enough to apply its function[116,163]. Nevertheless, most of the inherited mutations in the UROSIII genes (C73R and P248Q) can accelerate protein aggregation and impair its homeostasis in the cell[116,164,165].

Recently, it has been discovered that antifungal CPX has been identified as a chaperone allosteric active drug against CEP. It has shown that treatment with CPX at different doses can modulate homeostasis of UROSIIIS as well as C73R or P248Q mutations

without apparently other cellular systems being affected. Thus, CPX binds to UROSIIS and kinetically stabilizes this enzyme[36]. In addition, it has been reported that CPX enhances the pathogenic phenotype of CEP at sub-toxic concentrations in which it is capable to revert most of pathological effects reducing significantly hemolysis, steatosis and porphyrin deposition[36].

According to ^{31}P-NMR spectrum from hydrophilic and hydrophobic extracts (**Figure 3.12, Table 2.5**), the abnormal ^{31}P liver profile of mice was restored to normal on CPX administration. Therefore, the hepatic G6P level (Figure 10A), which was dramatically reduced in CEP mice liver, recovered its normal levels even though it is above the level of WT mice. Consequently, G6P´s anabolic products (glycogenesis) such as G1P and UDPG/ADPG/GDPG (**Figure 3.10B**) were increased as well as the content of 6PG, X5P and S7P (**Figure 3.10D**), which are catabolic products of G6P. Likewise, the concentration values of lactate (**Figure 3.10A**), which was increased in CEP mice liver, decreased significantly after CPX treatment, reaching normal liver values.

For another hand, energy-related metabolites, AMP/GMP, CMP/UMP, and NADPH (**Figure 3.10E**) also reached normal values after CPX treatment. Meanwhile, ADPR values (Figure 10 C) were decreased in CEP mice liver treated with CPX.

In conclusion, from hydrophilic fraction, all findings lead to an improvement in central carbon metabolism in addition to enhanced mitochondrial function in response to CPX treatment in CEP mice (Table S2).

Relative to phospholipidic hydrophobic liver extract (**Figure 3.12**), the vast majority of the phospholipids quantified as well as the PC/(PE + SM) and PC/PE molar *ratios* (**Figure 3.10F**) were restored to healthy normal values, indicating these outcomes a stabilization of the UROSIIIS and restoration to normal values of heme level production. In addition, CPX could correct alterations in cell membranes and reverse liver injury, as it is observed in the histological analysis (**Figure 3.12**).

2.3.5 Phosphoromics analysis of two murine models of two murine models of NASH

^{31}P-NMR analysis revealed that steatohepatitis was induced by CEP liver mice, therefore, it could be useful to compare the ^{31}P fingerprint of two well-known murine models of NASH: one genetic, MAT1A-KO mice[114], and other dietary, mice fed a CDHF diet[116] (**Table 3.7**).

Genetic murine models of NAFLD are generally based on knocking down enzymes involved in lipid and carbohydrate metabolism, for example, MAT1A-KO mice[115].

Methionine adenosyltransferase (MAT) is an essential enzyme to catalyze the formation of SAMe, which is used for the donation of methyl groups in transmethylation reactions, a process in which SAMe is transformed to S-adenosylhomocysteine (SAH). Mammals express three MAT isoenzymes (MATIA, MATII and MATIII), whose genes are MAT1A and MAT2A[166]. MAT1A is mainly expressed in adults and in differentiated liver[167,168], however, MAT2A is expressed in fetal liver and extrahepatic tissues and it is associated with rapid growth or differentiation[160].

MAT1A-KO mice lack MAT1A gene and therefore, it shows a deficiency in MATI and MATIII enzymes. This genetic model of NASH is characterized by having reduced SAMe levels compared to WT, plasmatic hypermethioninemia and hyperglycemia with normal insulin levels, decreased levels of glutathione (GSH), accumulation of TG but the content in hepatic SAMe and plasma total homocysteine are not changed[169,120]. Likewise, there is an increase in liver weight. At three months MAT1A-KO mice when fed a choline-deficient diet than control animals, they prone to develop NAFLD, and at 8 months of age, NASH, whereas at 18 months they can progress to HCC[114] being an animal model of NASH less aggressive.

There is a large number of dietary models that can monitor the progression of NAFLD. One of them, a methionine and choline deficiency high fat diet[116] which can cause an increase of serum parameters (alanine aminotransferases) of liver injury from 1 week after feeding being the accumulation of hepatic lipids prominent from 1 week and it was accompanied by significant inflammatory and fibrogenic responses at 6 weeks[170]. Characteristics are very similar to the general clinical features of human NASH (obesity, dyslipidemia, insulin resistance or increased hepatic TG) and it can be a very useful murine model in order to analyze the main risk factors and the oxidative stress damage related to human NASH[171,172].

Thus, with respect to the E1 extract (**Figure 3.14**), MAT1A-KO mice showed an increase in hexose-phosphates and triosephosphates such as G6P, FBP, G1P and 3PG (**Figure 3.15A**) as well as a reduction in PEP (**Figure 3.15A**), whereas lactic acid (**Figure 3.15A**) and UDPG/ADPG/GDPG (**Figure 3.15B**) remained without changes. The content of ADPR (**Figure 3.15C**) was elevated, indicating cellular damage in the liver caused by the deletion of MAT1A. Likewise, the levels of 6PG and X5P (PPP) (**Figure 3.15D**) in addition to energy-related metabolites (NADPH, NADH and NTPs) (**Figure 3.15E**) were significantly increased showing the last ones an alteration in mitochondrial function.

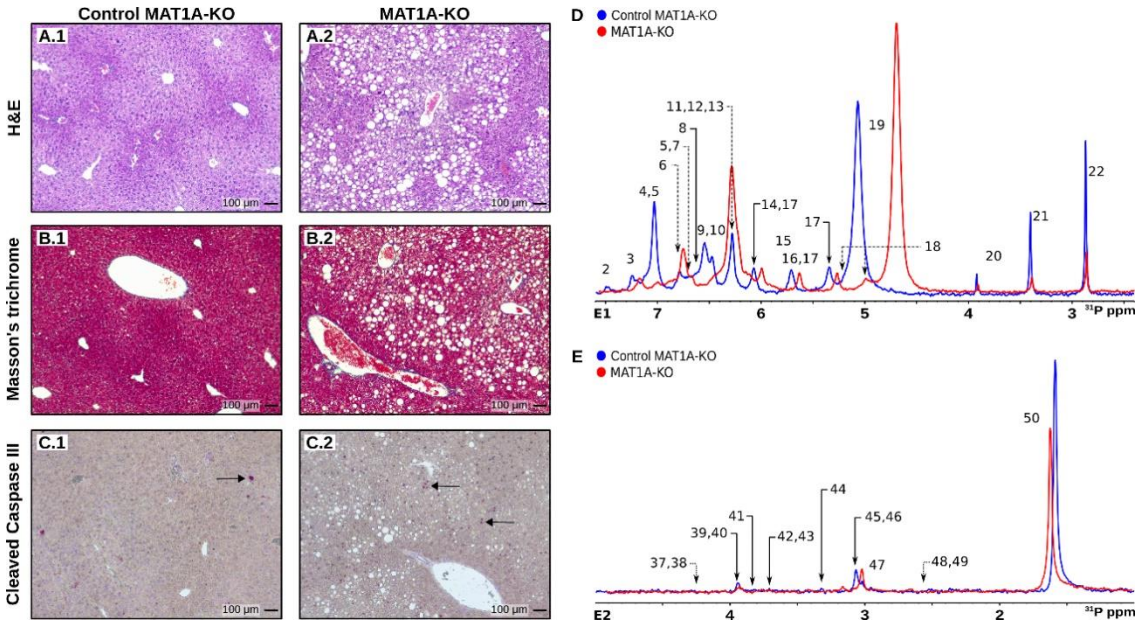

Figure 3.14. Characterization of the MAT1A-KO mice. A-C) Histology performed by Hematoxylin/Eosin (A.#) Masson's trichrome (B.#) and Cleaved Caspase III staining (C.#) of Control MAT1A-KO (#.1) and MAT1A-KO (#.2) mice models. MAT1A-KO mice were compatible with a steatotic liver with fibrosis. Arrows point to cells with Caspase III activity. D-E) ^{31}P-NMR spectra of hydrophilic (D) and lipophilic (E) phase for WT (blue) and MAT1A-KO (red) mice models.

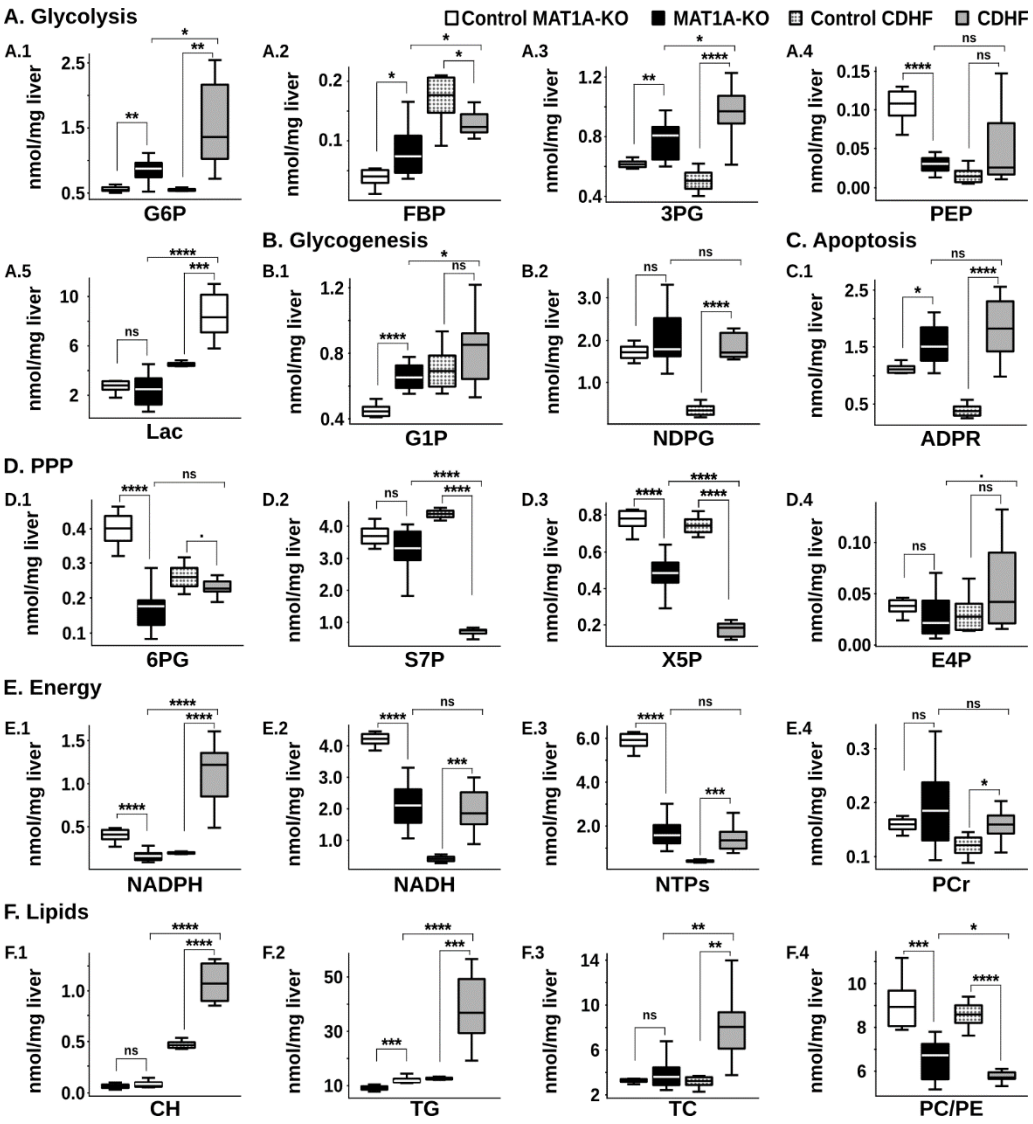

Figure 3.15. Metabolite quantification for validated NASH models. Comparison of quantified metabolites (nmol/mg liver) between control MAT1A-KO (white bars; n = 6), MAT1A-KO (black bars; n = 9), control CDHF (dotted gray bas; n = 6), and CDHF (grey bars; n = 9). A) Glycolysis, B) Glycogenesis, C) Apoptosis, D) Pentose phosphate pathway (PPP), E) Energy, F) Lipids[116]. P values of < 0.1, 0.05, 0.01, 0.001 and 0.0001 are represented by, *, **, *** and ****, respectively[116]

Table 3.7. Quantification of the metabolites and standard deviations (STDV) for the different compounds and mouse models under consideration. The following number of mice were used in each experiment: Control MAT1A-KO, n=6; MAT1A-KO, n=9; Control MAT1A-KO, n=6; CDHF, n=9.

Peak	Compound	Extract	Control MAT1A-KO	STDV	MAT1A-KO	STDV	Control CDHF	STDV	CDHF	STDV
16	2PG	E1	0.28	0.00	0.24	0.02	0.17	0.01	0.54	0.03
14	3PG	E1	0.62	0.01	0.78	0.04	0.51	0.03	0.96	0.06
2	6PG	E1	0.40	0.02	0.17	0.02	0.26	0.02	0.23	0.01
30	ADPR	E1	1.12	0.04	1.55	0.13	0.39	0.05	1.81	0.19
9	AMP/GMP	E1	3.59	0.27	6.97	0.59	3.80	0.04	9.08	0.65
32	CDPCH	E1	0.39	0.02	0.17	0.02	0.27	0.00	0.04	0.01
29	CDPE	E1	3.53	0.08	1.57	0.35	1.48	0.07	1.36	0.12
	Cho	E1 (1H)	0.07	0.01	0.09	0.01	0.47	0.02	1.08	0.06
47	CL	E2	0.05	0.01	0.06	0.01	0.18	0.01	0.13	0.01
10	CMP	E1	1.26	0.10	1.58	0.16	1.46	0.07	1.17	0.07
15	E4P	E1	0.04	0.00	0.03	0.01	0.03	0.01	0.06	0.01
7	F6P	E1	0.04	0.01	0.11	0.02	0.05	0.00	0.16	0.02
28	FADH2	E1	2.74	0.39	0.60	0.21	1.76	0.36	0.80	0.16
5	FBP	E1	0.04	0.01	0.08	0.01	0.17	0.02	0.13	0.01
18	G1P	E1	0.46	0.02	0.66	0.03	0.71	0.06	0.83	0.07
3	G6P	E1	0.56	0.02	0.85	0.06	0.55	0.01	1.52	0.23
22	GPC	E1	2.74	0.12	0.79	0.09	1.53	0.15	2.16	0.18
21	GPE	E1	1.57	0.13	0.39	0.06	0.65	0.07	0.68	0.04
17	Impurity	E1	1.21	0.05	1.01	0.10	1.27	0.03	3.16	0.20
	LAC	E1 (1H)	2.73	0.22	2.41	0.43	4.57	0.08	8.53	0.63
40	LPA/LPE	E2	0.01	0.00	0.01	0.00	0.00	0.00	0.01	1.00
44	LPC	E2	0.00	0.00	0.01	0.00	0.00	0.00	0.02	0.00
31	NADH	E1	4.21	0.09	2.10	0.23	0.43	0.04	1.96	0.24
20	NADPH	E1	0.39	0.03	0.16	0.02	0.19	0.00	1.09	0.12
25	NDPs	E1	3.08	0.14	2.89	0.25	1.27	0.06	3.39	0.24
35	NTPs	E1	5.86	0.17	1.69	0.23	0.42	0.02	1.43	0.19
50	PC	E2	2.25	0.17	2.58	0.26	2.64	0.11	5.61	0.68

12	PCHO	E1	0.53	0.11	0.43	0.06	0.95	0.07	0.17	0.01
24	PCr	E1	0.16	0.01	0.19	0.03	0.12	0.01	0.16	0.01
46	PE	E2	0.25	0.01	0.40	0.03	0.31	0.01	0.97	0.12
11	PEA	E1	0.67	0.11	0.27	0.05	0.89	0.04	0.37	0.03
23	PEP	E1	0.11	0.01	0.03	0.00	0.02	0.00	0.05	0.02
41	PG	E2	0.01	0.00	0.01	0.00	0.02	0.01	0.06	0.01
42	PI	E2	0.00	0.00	0.01	0.00	0.02	0.00	0.04	0.00
19	PO_4	E1	21.54	2.07	29.49	2.28	47.68	0.16	23.62	1.26
39	PS	E2	0.13	0.01	0.13	0.02	0.03	0.01	0.18	0.04
4	S7P	E1	3.71	0.14	3.28	0.24	4.38	0.06	0.69	0.04
43	SM	E2	0.00	0.00	0.01	0.00	0.05	0.01	0.02	0.00
	TC	E2 (1H)	3.28	0.08	3.91	0.47	3.17	0.22	8.23	0.98
	TG	E2 (1H)	9.10	0.38	12.02	0.40	12.62	0.18	38.89	4.31
8	TMP	E1	0.51	0.07	0.64	0.07	0.53	0.00	0.43	0.10
1	TMP+	E1	0.93	0.05	1.06	0.06	1.00	0.00	1.00	0.00
36	TPP	E2	3.54	0.15	3.84	0.04	3.87	0.02	4.00	0.00
27	NDPG	E1	1.73	0.08	2.09	0.24	0.36	0.06	1.87	0.10
26	UDPGA / UDPgal	E1	0.95	0.07	0.47	0.06	0.28	0.01	0.72	0.03
13	UMP	E1	0.59	0.08	0.39	0.05	0.87	0.05	0.14	0.01
6	X5P	E1	0.77	0.03	0.48	0.04	0.75	0.02	0.17	0.01
33	Unknown	E1	0.27	0.01	0.07	0.01	0.07	0.00	0.16	0.02
34	Unknown	E1	1.69	0.05	0.65	0.08	0.54	0.01	0.95	0.03
37	Unknown	E2	0.00	0.00	0.01	0.00	0.00	0.00	0.02	0.00
38	Unknown	E2	0.00	0.00	0.01	0.00	0.00	0.00	0.02	0.00
45	Unknown	E2	0.00	0.00	0.01	0.00	0.03	0.01	0.12	0.01
48	Unknown	E2	0.00	0.00	0.02	0.00	0.00	0.00	0.06	0.01
49	Unknown	E2	0.00	0.00	0.01	0.00	0.00	0.00	0.05	0.01

The phosphoromic profile of mice fed a CDHF[116] was different from those in MAT1A-KO[117]. Although G6P, 3PG and lactic acid were increased in CDHF mice liver, FBP concentration values were significantly lower as compared to WT mice liver. PEP remained inalterable as well as G1P. Nevertheless, there was a significant increase of

UDPG/ADPG/GDPG in CDHF animals whereas the content of S7P and X5P were drastically reduced. Moreover, NTPs, NADH, NADPH and PCr were significantly higher in CDHF mice livers.

Regarding hydrophobic extract (**Figure 3.16**), it is remarkable to reveal a general alteration in lipid metabolism in either MAT1A-KO or CDHF mice, having a TG accumulation and a decrease in PC/PE and PC/(PE + SM) molar *ratios* (**Figure 3.15F**), as illustrated in the CEP animal model. However, PC/PE and PC/(PE + SM) *ratios* were much lower in CDHF mice, and in this way, this tendency could be correlated with a more rapid development of NASH[127]. Moreover, ^{31}P signature of CDHF showed an elevation of CH (**Figure 3.15F**), together with a small reduction in its transformation into CDPCH (**Table 3.6**) and an increase of PC (**Figure 3.16**), whose increase could be explained by an adaptive mechanism carried out with the aim of compensating the deficiency of CH[173].

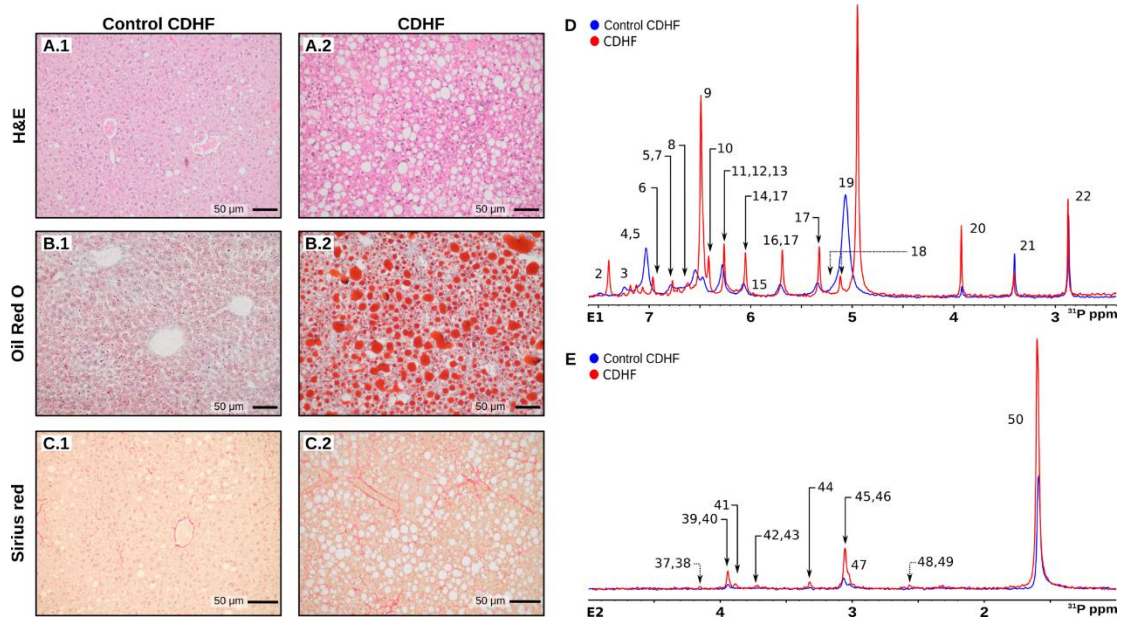

Figure 3.16. Characterization of the CDHF mice. A-C) Histology performed by Hematoxylin/Eosin (A.#), Oil Red-O (B.#) and Cleaved Caspase III staining (C.#) of Control CDHF (#.1) and CDHF (#.2) mice models. CDHF mice were compatible with a steatotic liver with fibrosis. Arrows point to cells with Caspase III activity. D-E) ^{31}P-NMR spectra of hydrophilic (D) and lipophilic (E) phase for WT (blue) and CDHF (red) mice models.

In summary, this ^{31}P-NMR-based platform provides the absolute concentration of up to 54 phosphorylated metabolites separated into two phases[116]. The hydrophilic phase covers a wide array of pathways from glycolysis, glycogenesis, the PPP, TCA, and the phosphoryl- and electron-transfer pathways that power much of the anabolic processes[116]. Likewise, the lipophilic phase provides information on the phospholipid metabolism that can be rationalized in terms of membrane integrity and composition[116].

In addition, the platform gives quantitative information on four key non-phosphorylated metabolites[116]. On the whole, it provides a snapshot of the organ´s metabolism in health, disease and response to treatment, which correlates with liver histology and provides mechanistic information[116].

CHAPTER 4

AN EXTENSION OF PHOSPHOROMICS: A LONGITUDINAL STUDY OF TWO DIETARY MODELS OF NASH

4.1 Introduction

4.1.1 Definition, risk factors and treatment of NAFLD and NASH

NAFLD is a set of spectrums of diseases, which occur in the absence of excessive alcohol consumption that covers from isolated hepatic TG accumulation (steatosis, NAFL), through hepatic TG accumulation plus inflammation (non-alcoholic steatohepatitis, NASH), and finally, it can advance to fibrosis, cirrhosis, and potentially hepatocellular carcinoma[174]. It is associated with metabolic syndrome[175], a cluster of conditions including obesity[176], type 2 diabetes mellitus (T2DM)[177] and dyslipidemia[178]. The global prevalence in adults is estimated at 25-30%,[179] although the prevalence rates vary by country[180]. The highest NAFLD prevalence has been found in South America (31.31%), followed by Europe (30.11%), Asia (29.92%), North America (24.28%) and Africa (8.10%)[181]. NAFLD has become more prevalent during the last ten years[8], therefore, this liver disease represents an emerging global health threat[182,183].

The pathogenesis of NASH has not been elucidated yet, being the only treatment available is lifestyle modification by diet and exercise[184,185]. NAFLD/NASH studies in humans are somewhat restricted due to the long-term duration required for observation - often several decades – as well as ethical considerations associated with drug administration or liver sample collection frompatients[186]. Instead, NAFLD/NASH mice models are widely used as the experimental interventions are easy to control and the experimental duration is relatively short in addition to obtaining sufficient tissue without sampling error.

4.1.1 Diet-induced Models of NAFLD

4.1.1.1 High-fat diet

A high-fat diet (HFD) is routinely used to produce hepatic steatosis and NASH in mice[187]. The term “HFD” encompasses a wide array of diet formulas and fat types as well as their relative levels (30-60% of the kcal intake in fat form) in addition to other compositional additives such as low or high sucrose, low or high fructose and low or high cholesterol[188].

HFD are often employed in biomedical research for leading obesity[189]. This diet provokes steatosis (mainly macrovesicular) without necrosis inflammation after 8 weeks of feeding, showing a significant increase in body weight, liver and plasma free fatty acid, TG levels, plasma alanine aminotransferase activities and total TC as well as insulin

levels[190]. Despite these findings, a small amount of research has been reported based on the sequence of events over time in this diet-induced NASH model, which will be summarized below.

Thus, when C57BL/6J male mice were fed this diet for 16 weeks, they exhibited steatosis accompanied by mild inflammation and fibrosis[191]. Furthermore, SREBP-1c, the major transcriptional regulator of the enzymes involved in *de novo* lipogenesis[192], was often up-regulated. Moreover, body weight, liver TG and serum aspartate aminotransferase (AST) levels were increased[184]. Peroxisome proliferator-activated receptor α (PPARα) mRNA expression also increased[184] as this protein is the main regulator of lipid metabolism through regulation of many genes involved in fatty acid uptake and activation, mitochondrial and peroxisomal fatty acid oxidation, ketogenesis, triglyceride turnover, gluconeogenesis and bile synthesis and secretion in the liver[193]. Moreover, α-smooth muscle actin (α-SAM) expression, an actin isoform that predominates in vascular smooth muscle cells and plays an important role in liver fibrogenesis[194], was slightly increased[184], indicative of mild liver fibrosis. A separate study using a HFD with a different nutritional composition (71% kcal fat, 11% kcal carbohydrate and 18% kcal protein) carried out in C57BL/6J mice showed that these mice exhibited steatosis with the presence of ballooned hepatocytes without fibrosis and inflammation. This observation was verified biochemically by an increase of liver TG present in HFD[195]. Likewise, serum levels of the anti-inflammatory cytokine adiponectin were significantly decreased in HFD group whereas fasting levels of serum glucose were significantly increased[188]. Likewise, another study in C57BL/6 male mice induced NASH-like pathology accompanied by an increase of liver TG and hepatic expression of cytochrome P450 2E1 (CYP2E1), which carries out omega hydroxylation of fatty acids and it has been reported in human NASH by promoting oxidative stress, protein modifications, inflammation, and insulin resistance[196].

After 20 weeks of HDF feeding, distinct responses between mouse strains (A/J and C57BL/6J) and sexes became evident. In fact, hyperleptinemia and weight gain were similar in both strain and sexes along with observable glucose tolerance, hyperinsulinemia, and hypercholesterolemia[197]. Nevertheless, A/J males developed alterations in glucose tolerance and insulin resistance whereas in C57BL/6J mice, they promoted type 2 diabetes remaining normoglycemic in A/J mice[190]. In another study carried out over the same period, C57BL/6J mice fed HFD induced histopathological features of human NASH such as hepatic steatosis, ballooning, inflammation, and fibrosis accompanied by elevated enzymes ALT, AST, alkaline phosphatase (AKP),

hyperglycemia, hyperinsulinemia and hypoadiponectinemia[198]. Inflammatory cytokines, such as hepatic tumor necrosis factor-α (TNF-α), transforming growth factor (TGF)-β and platelet-derived growth factor (PDGF) were significantly increased in HFD group than in the control group[190]. The development of fibrosis in the HFD group also was confirmed by an elevation of collagen (Collagen I, III and IV) expressions (protein and mRNA)[191].

At 24 weeks of feeding HFD in C57BL/C mice, severe steatosis, ballooning, liver inflammation and fibrosis were observed accompanied by elevated body weight, serum ALT, serum TC, fasting serum blood glucose, TNF-α and α-SAM expression[199]. Likewise, differences between strains were found to be more severe NAFLD in HF C57BL/6J than BALB/C mice confirmed by an elevated steatosis score, necro inflammatory score, hepatocyte ballooning, serum ALT, body weight, blood glucose and serum TC[200].

For another hand, at the end of 40 weeks an elevation in the NAFLD activity score, inflammation and hepatocytes ballooning in HFD groups as compared to the 24-week HFD group[201] was observed. HFD was associated with insulin resistance either 24 or 40 weeks after the start of the diet in mice, confirmed by an increase in the levels of fasted insulin and homeostatic assessment of insulin resistance (HOMA-IR), a biomarker of insulin resistance[202]. The chemokine monocyte chemoattractant protein 1 (MCP-1), a macrophage biomarker in the liver that plays an important role in the progression of hepatic inflammation and fibrosis[203], was significantly increased in HFD cohort at 40 weeks compared to 24 weeks one. In addition, body weight gradually increased until 40 weeks[194].

After 52 weeks of HFD, histopathological analysis of liver fractions exhibited an increase in steatosis grade, suggesting a progressive accumulation of liver lipids over time although hepatic ballooning, TG, NASH score and body weight remained unchangeable as compared to 40 weeks cohort[194]. Moreover, anti-inflammatory cytokines (TNF-α) and hepatic macrophage biomarker (MCP-1) significantly decreased as compared to the 40-week HFD group[194].

In summary, HFD can replicate the principal histological features observed in human NAFLD although the grade of hepatic pathology is not severe in a short-mid-term study. Therefore, it becomes necessary to combine HFD with other dietary components to investigate hepatic steatosis and NASH.

4.1.1.2 Choline-deficient diet

One of the main clinical observations is the lack of choline in NASH patients[204]. Choline is an essential amino acid that plays different functions in cell membrane integrity, phosphatidylcholine synthesis, neurotransmission, and trans-methylation metabolism[198]. In humans, choline deficiency is associated with liver dysfunction and the progression of NAFLD including liver lipoprotein exportation, oxidative stress provoked by mitochondrial impairment and endoplasmic reticulum stress[205].

4.1.1.2.1 Methionine and choline-deficient diet

Among the different models that induce NAFLD in mice, methionine, and choline-deficient diet (MCD) induce severe NASH phenotype in the shortest time compared to other dietary models, like HFD[199]. This diet induced steatosis in 2-4 weeks in mice, and if continued, can progress to fibrosis in 4-8 weeks[206]. Some studies have claimed that this diet caused mitochondrial DNA damage, induction of ROS production and apoptotic cell death, making it one of the most suitable models to study NAFLD progression[207]. Nevertheless, this model could not accurately replicate the main metabolic features found in humans, since mice fed MCD diets can lose weight, leading to cachexia. Additionally, these mice demonstrate low fasting serum insulin, leptin, glucose and TG levels, and exhibit insulin sensitive[200].

4.1.1.2.2 Choline-deficient and L-amino acid-defined diet

Another popular model for pharmacological research of NAFLD is the choline-deficient (CDD) diet. Typically, this tended to contain higher levels of fat (45-60% kcal) and this induced simple steatosis, NASH and fibrosis without the reduction in body weight found when mice are fed by CDD[188]. Thus, choline-deficient and L-amino acid-defined diet (CDAA) is widely used in order to investigate NAFLD progression. This diet incorporated sulfhydryl-containing amino acids that were less restricted in addition to providing energy[208]. Steatohepatitis with fibrosis developed after 12 weeks of feeding on this diet, which could progress to a moderate stage after 21 weeks[99]. However, although fasting serum insulin, glucose and hepatic TG levels were increased, one of the main drawbacks of this model is that obesity was not developed[181].

4.1.1.2.3 Choline-deficient, L-amino acid-defined and high-fat diet

Choline-deficient, L-amino acid-defined, high-fat diet (CDAHFD) is another model used in NAFLD/NASH studies[209]. The most used nutritional composition is based on a high-fat and choline -deficient diet, supplemented with 0.1% methionine and 45% fat[210]. It induced steatohepatitis in the first week accompanied by mitochondrial dysfunction and oxidative stress, whereas after six 6-12 weeks of feeding it could progress to fibrosis[37], confirmed by higher values of hydroxiproline, the major component of collagen which is a biomarker routinely used to estimate liver fibrosis[211]. Among all the metabolic features, there were found higher values of serum ALT, AST and hepatic TG that resemble those observed in NASH patients[212]. Nevertheless, having a normal content of methionine in the nutritional composition of the diet was vital to developing obesity in mice[213,214].

4.1.1.2.4 Choline-deficient and high-fat diet

Therefore, choline deficiency with a HFD (CDHF), together with normal content of methionine, could be one of the most effective models to investigate NAFLD progression[125,215]. Long-term studies in C57BL/6J mice have shown an increase in body weight over time compared with mice fed a control diet[216217].12 months later after the treatment with CDHF, mice developed severe steatosis together with liver ballooning, immune cell infiltration, Mallory-Denk body (MDB) formation and glucogenated nuclei, which were all features observed in humans[216217]. This was consistent with an increase in fat mass, lean mass in the liver, hepatic TG, serum and hepatic TC, serum AST, ALT although there were no changes in serum TG[216]. In addition, there was a downregulation of a large number of genes which are implicated in lipid metabolism in CDHF as well as inflammatory chemokines and kytokines[217]. Also, mitochondrial structural alterations and a decrease ATP production in mitochondria isolated from C57BL/6J mice fed by CDHF for 6 months were observed[216].

At present, histological and biochemical hepatic parameters are still the gold standard for monitoring NAFLD. Liver biopsy remains the primary diagnostic tool, despite its invasive nature, susceptibility to sampling errors, and the associated risk. Moreover, it is not practical outside specialist practice. The absence of biomarkers has hampered the diagnosis and monitoring of disease progression.

In response to the urgent need for biomarkers, our research group has developed a ^{31}P-NMR-based method to study the liver “phosphorome” through the simultaneous

identification and quantification of multiple phosphorylated small molecules (metabolites) (<~ 1500 kDa)[218]. This method provides a simplified view of metabolism with still maximal coverage of all anabolic and catabolic pathways of the liver, being a snapshot of the liver´s metabolism in disease. Accordingly, the main objective of this research is to study liver “phosphorome” in two dietary models of NASH (HFD and CDHFD) to characterize metabolic changes in each condition as well as to distinguish metabolic patterns as compared to STD group.

4.2 Methods

4.2.1 Animals and diets

8-week-old male C57BL/6J mice were subjected to a 12-hour light/dark cycle and had *ad libitum* access to various diets, including a standard chow diet (U8200G10R, SAFE), high-fat diet (HFD; D12451 45% fat, Research Diets) and choline-deficient and high-fat diet CDHFD (D05010402; 45% fat, Research Diets) for 20, 52 or 78 weeks. Body weight was monitored during the experimental phase. All animal procedures were approved by the University of Santiago de Compostela's committee (15010/14/007). Upon the conclusion of the specified durations, the animals were sacrificed by decapitation, and whole-trunk blood samples and tissues were collected. Liver and epididymal adipose tissue were weighted and frozen immediately on dry ice and kept at −80 °C until analysis. In **Table 4.1**, the number of mice used for each experimental condition was shown.

Table 4.1. Number of mice used for each experimental condition.

Weeks\Diets	STD	HFD	CDHF
20 weeks	5	5	5
52 weeks	6	9	9
78 weeks	4	4	4

4.2.2 Determination of whole body composition using MRI

Whole body composition of the subjects was quantitatively assessed using the EchoMRI Whole Body Composition Analyzer, employing nuclear magnetic resonance imaging (MRI) techniques. Prior to scanning, subjects were appropriately prepared and positioned to ensure optimal image acquisition. Post-scan, the data were systematically processed using EchoMRI's proprietary software, which generated detailed reports on various body composition metrics essential for the study's objectives.

4.2.3 Determination of serum levels of metabolites

Fresh whole-trunk blood samples were centrifuged at 6000xg for 15 min at 4ºC. The supernatant was carefully transferred into new tubes for subsequent serum assays. Concentrations of serum total cholesterol (TC) (1001093, Spinreact), triglycerides (TG) (1001310, Spinreact), non-esterified fatty acids (NEFA) (436-91995, 434-91795, WAKO), alanine aminotransferase (ALT) activity (41283, Spinreact) and aspartate aminotransferase (AST) activity (41273, Spinreact) were determined by spectrophotometry in a ThermoScientific Multiskan GO spectrophotometer.

4.2.4 Histological analysis of mouse liver tissue

For *Hematoxylin and Eosin* (H&E) Staining, liver specimens were fixed in 10% (v/v) neutral buffered formalin at RT for 24 hours and subsequently stored in 50% (v/v) ethanol until paraffinized. Tissue sections of 5 µm thickness were generated from the paraffin blocks. For staining, sections were immersed in Shandon TM Harris hematoxylin (Thermo Scientific; USA) for 5 minutes, rinsed in tap water for 5 minutes, and subjected to decolorization in 0.5% (v/v) HCl followed by a thorough rinse with tap water. Then the sections were counterstained with aqueous Eosin (Thermo Scientific; USA) for 15 minutes and washed with tap water for 3 minutes. The sections were then dehydrated with graded ethanol solutions and mounted with permanent mounting media (DPX).

Sirius Red Staining: performed to assess liver fibrosis following the protocol similarly as described for H&E staining. Tissue sections of 5 µm were obtained from paraffinized blocks and stained with a Sirius red solution (0.01% (w/v) Fast Green FCF combined with 0.1% (w/v) Sirius red in picric acid, Sigma-Aldrich; USA) for 30 minutes in each solution. Post-staining, sections underwent dehydration in 100% ethanol and were mounted using DPX mounting media.

For *F4/80 Immunohistochemical Staining* liver tissue sections were subjected to antigen retrieval with proteinase K for 15 minutes followed by peroxide blocking using 3% H_2O_2 in PBS for 10 minutes at room temperature (RT). Blocking was performed using 5% goat serum for 30 minutes at RT. Sections were incubated with the primary antibody overnight at 4ºC at 1:50 dilution of the primary antibody, and after that, they were incubated with Imppress anti-rat HRP-conjugated polymer (Vector) for 30 minutes at RT. Color development was achieved with Vector VIP chromogen (Vector). Hematoxylin was employed for counterstaining the sections.

4.2.5 Extraction method

Aliquots of the liver (the liver weight is shown in **Table 4.2**) were distributed into three different Eppendorf tubes[116]. Each liver fraction was lysed in 774 µL of ice-cold chloroform/methanol mixture (38.8/61.2 vol/vol). 254 nmol of DSS was added to monitor the extraction yield[116]. Livers were homogenized in a Precellys tissue homogenizer at 4,000 g for 2 x 30 seconds and 554 µL of a chloroform/water mixture (45.8/54.2 vol/vol) was added to the homogenate[116]. After vortexing, the solution was kept on ice for 15 minutes before being centrifugated for 15 minutes at 9,000 g, 4ºC[116]. The two obtained

phases were then carefully separated and dried in a Speed Vac for 3 hours[116]. Pellets were stored at -80 ºC for further analysis[116].

Table 4.2. Liver weights for the extraction for the different animals employed.

Diet	STD			HFD			CDHF		
Weeks	**20**	**52**	**78**	**20**	**52**	**78**	**20**	**52**	**78**
Weighted liver (mg)	267	103	200	161	116	295	203	107	335
	267	108	130	177	128	300	171	103	310
	134	105	300	140	106	280	216	111	275
	193	101	125	136	102	345	177	129	275
	204	111		182	116		113	100	
		111			111			101	
					120			99	
					99			104	
					120			98	

4.2.6 NMR spectroscopy

Liver extracts were resuspended in 300 µL solution according to the extract fraction (**Table 4.3**).

Table 4.3. Buffer or solvent, reference compound and PRE of each extract fraction.

	Hydrophilic fraction (E1)	**Hydrophobic fraction (E2)**
Buffer/Solvent	100 mM Tris-d_{11}-DCl	D_6-DMSO
Reference compound	1 mM TMP^+	4 mM TPPO
PRE	0.5 mM Gadobutrol	No needed

All NMR experiments were recorded at 298 K on a Bruker 600 MHz (12T) Avance III spectrometer equipped with a QXI (^{1}H, ^{13}C, ^{15}N, ^{31}P) or a BBO (BB,^{1}H) probehead. For each sample, three different experiments were collected (i) a 1D ^{31}P zgig spectrum with inverse gated ^{1}H decoupling (3-11.5 hours), (ii) a 1D ^{1}H p3919gp with water signals suppression using a binomial 3-9-19 pulse with echo gradient pair (7 minutes), and (iii) a 2D ^{31}P,^{1}H HSQMBC-TOCSY spectrum (5-13.5 hours)[116]. The 1D ^{31}P experiment was recorded with long interscan delays $D_1 > 3.T_{1,\,max}(^{31}P)$ for quantification, whereas the paramagnetic relaxation enhancer (gadobutrol) added only to hydrophilic fraction allowed to use a short D_1 = 1 second, whereas the hydrophobic fraction required D_1 = 5

seconds[116]. Chemical shift assignment was done using standard compounds in order to facilitate the identification of metabolites[116]. Then, assigned metabolites were quantified by referencing their ^{31}P peak integral against the internal reference compound added[116]. In some cases, we used peak deconvolution with the aim of assigning the corresponding peak in case of signal overlap[116]. Peak integration and quantification were done using TopSpin 4.0.7 (Bruker Biospin GmbH)[116].

4.2.7 Statistical analysis

Statistical analysis was performed using MetaboAnalyst (MetaboAnalyst 5.0 version) and R (4.2.2 version) softwares. Univariate and multivariate analysis were applied, and different methods were used to carry out these studies including unsupervised[219] and supervised[220] techniques.

4.3 Results and discussion

NAFLD is a spectrum of conditions characterized by excessive fat accumulation in the liver in the absence of alcohol abuse. Strikingly, the global prevalence of NAFLD patients has been on the rise[216,217]. NAFLD is classified into two categories: 1) *simple steatosis*, a benign liver condition in which only hepatic steatosis is observed, and 2) NASH, in which either necroinflammatory reactions and liver steatosis occur in addition to advanced liver fibrosis and hepatocellular carcinoma[221].

Currently, the definitive diagnosis of NASH still relies heavily on histological evaluation of the liver and serum biomarkers[222]. However, the application of single omics technologies has enabled a better understanding of the molecular profiles associated with hepatic inflammation for diagnosis NASH, as well as the discovery of novel biomarkers[223].

In this Chapter, the serum biochemical and liver histological differences between mice fed by HFD and CDHF will be evaluated. Furthermore, as a complementary technique, we proposed the use of ^{31}P-NMR as a robust, reproducible, and reliable method that can accurately distinguish between normal and NASH-affected livers. Additionally, we aimed to characterize the metabolic changes in liver phosphorome of mice fed by HFD and CDHF as compared to STD group.

4.3.1 Histological analysis

Albeit several non-invasive clinical scores have been proposed to diagnose NASH and predict fibrosis[219], histopathological evaluation of biopsy remains a golden standard NASH diagnosis[224].

In this thesis, it has analyzed specific histopathological abnormalities present in liver sections of mice fed by STD, HFD and CDHF at different ages (20,52 and 78 weeks) paying special attention to hepatocellular steatosis, liver inflammation, and the degree of fibrosis.

Initially, hepatocellular steatosis was evaluated through Hematoxylin and Eosin (H&E)-stained liver histology specimens (**Figure 4.1**). Hence, at 20 weeks, mice fed by HFD and CDHF developed macrovesicular steatosis as compared to STD, which did not develop the steatotic condition. Macrovesicular steatosis is characterized by well-defined

fat droplets occupying the hepatocyte cytoplasm. Likewise, at 52 weeks, there was an increase in steatosis severity in both HFD and CDHF groups, which had more prominent changes in those on HFD. However, mice fed by HFD did not impair steatosis at 78 weeks as compared to 52 weeks. On the contrary, steatosis in mice fed by CDHF progressed dramatically at 78 weeks as compared to 52 weeks. As expected, the mice on STD did not exhibit steatosis at any time point.

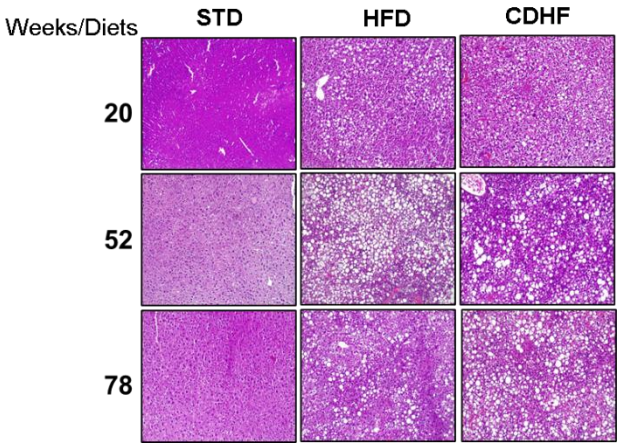

Figure 4.1. Liver histopathology of rodent NASH models. Representative hematoxylin and eosin-stained liver sections from mice fed by STD, HFD and CDHF at 20, 52 and 78 weeks for studying steatosis.

Secondly, F4/80 staining was performed to evaluate liver inflammation (**Figure 4.2**). F4/80 is a marker of macrophages/Kupffer cells, which plays a crucial role in the pathogenesis of NASH and inflammation developement[225]. At 20 weeks, no liver inflammation was observed in mice fed with any of the diets. Nevertheless, at 52 weeks, HFD exacerbated hepatic inflammation, a condition that worsened by 78 weeks. Interestingly, no inflammation was observed in the mice fed with CDHF until 78 weeks. As expected, STD did not cause hepatic inflammation in any age of mice.

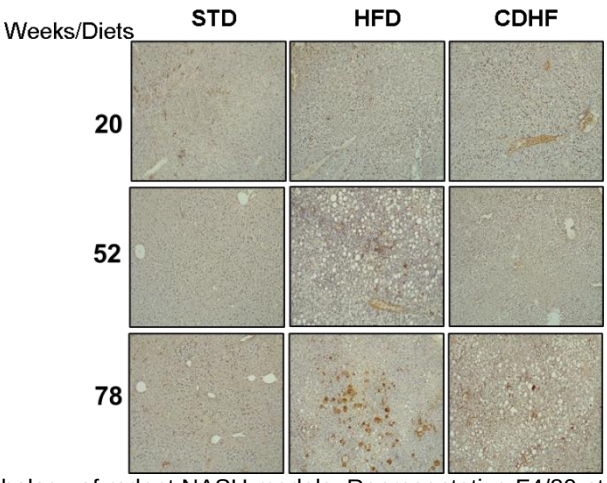

Figure 4.2. Liver histopathology of rodent NASH models. Representative F4/80-stained liver sections from mice fed by STD, HFD and CDHF at 20, 52 and 78 weeks for studying inflammation.

Thirdly, fibrosis was evaluated with Sirius Red staining (**Figure 4.3**), which characterizes fibrillar collagen deposition within the hepatic parenchyma. As proposed by several researchers, collagen subtypes I and II, both of which are fibrillar collagens, are upregulated in NASH with fibrosis[226]. Likewise, mice liver fed by HFD could develop fibrosis at 52 weeks, and worsen at 78 weeks, whereas CDHF did not develop fibrosis until 78 weeks. Likewise, STD did not develop fibrosis at any time.

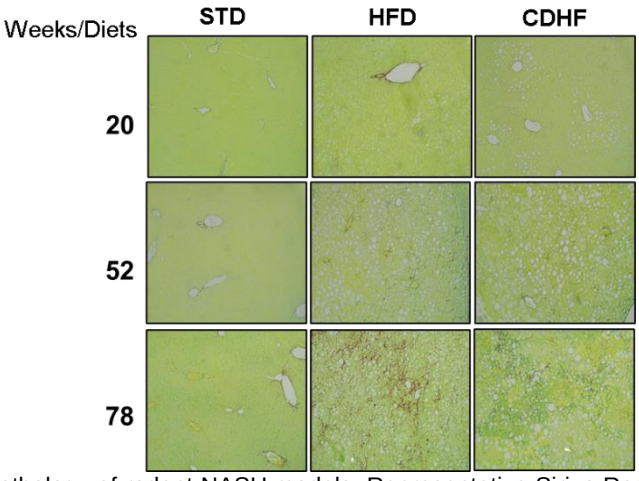

Figure 4.3. Liver histopathology of rodent NASH models. Representative Sirius Red stained liver sections from mice fed by STD, HFD and CDHF at 20, 52 and 78 weeks for studying fibrosis.

4.3.2 Biochemical analysis

Complementing the histological analysis, several biochemical markers and lipids are associated with the progression of NASH[227]. These indicators include body weight, epididymal white adipose tissue (EWAT), AST, ALT) values as well as serum lipid profile (TC, TG and NFA).

In this way, mice fed the HF gained more weight as compared to the control group. This trend became evident after 20 weeks and could be attributed to an increased energy intake. The weight gain became more pronounced at 52 weeks, and further so at 78 weeks. Nevertheless, in the CDHF animals it was observed an increase of body weight until 52 weeks, after which there was a reduction of it from 52 to 78 weeks.

After 20, 52 and 78 weeks, the weight of epididymal white adipose tissue, which is assumed to reflect the overall adiposity of the animals, was higher in mice fed with HFD or CDHF compared to STD group. In addition, an increase in liver index or liver-to-body weight *ratio* was only observed in CDHF mice compared to the STD group at 20 weeks. This indicates a possible condition of hepatomegaly[228]. These results are summarized in **Table 4.4**.

Table 4.4. Body weight, epididymal white adipose tissue (EWAT) and liver index of male CD57BL/6J mice fed by STD, HFD or CDHF for 20, 52 and 78 weeks.

	Body weight (g)			EWAT (g)			Liver Index (%)		
Week	STD	HFD	CDHF	STD	HFD	CDHF	STD	HFD	CDHF
20	26.2 ± 1.1	39.2 ± 2.0**	35.0 ± 1.7**	0.93 ± 0.1	2.7 ± 0.3**	2.3 ± 0.4*	4.4 ± 0.4	4.7 ± 0.5	6.4 ± 0.7*
52	28.3 ± 1.2	48.6 ± 2.3****	45.3 ± 3.4***	1.4 ± 0.1	3.3 ± 0.3***	2.5 ± 0.3*	5.2 ± 0.5	5.7 ± 0.6	6.3 ± 0.6
78	31.9 ± 1.9	50.3 ± 3.6**	38.8 ± 3.4	1.8 ± 0.1	3.3 ± 0.3**	2.2 ± 0.3	5.7 ± 0.9	5.9 ± 0.5	7.3 ± 1.0

Note: The data are expressed as Mean ± SEM. Groups bearing common superscripts are not significantly different. Symbols represent statistical significance: *P<0.05, **P<0.01, ***P<0.001, ****P<0.0001, all compared with STD group. EWAT, epididymal white adipose tissue. Liver index calculated as liver weight/body weight x 100%.

Moreover, serum ALT and AST levels were evaluated (**Table 4.5**). Both enzymes serve as indicators of hepatocellular injury[229]. Several previous studies demonstrated that high levels of ALT and AST are correlated with a higher risk of NASH[230]. Throughout this study, both HFD and CDHF animals exhibited increased serum AST and ALT compared to STD group at 20, 52 and 78 weeks. Moreover, both markers increased over time, reflecting a rise in liver damage in mice fed both diets over time.

Table 4.5. Serum AST and ALT levels of male CD57BL/6J mice fed by STD, HFD or CDHF for 20, 52 and 78 weeks.

	Serum AST (U/L)			Serum ALT (U/L)		
Week	STD	HFD	CDHF	STD	HFD	CDHF
20	12.8 ± 3.5	57.8 ± 4.4****	83.6 ± 8.1***	13.6 ± 3.4	40.1 ± 3.2***	59.3 ± 4.4****
52	54.3 ± 7.8	105.7 ± 10.8**	137.1 ± 12.7***	41.4 ± 10.6	65.3 ± 5.8	99.7 ± 13.7**
78	67.4 ± 5.7	166.2 ± 21.1*	171.3 ± 25.5*	58.4 ± 12.0	94.5 ± 12.7	122.5 ± 18.8

Note: The data are expressed as Mean ± SEM. Groups bearing common superscripts are not significantly different. Symbols represent statistical significance: *P<0.05, **P<0.01, ***P<0.001, ****P<0.0001, all compared with STD group. Serum ALT, serum alanine transaminases; Serum AST, serum aspartate transaminases.

In general, elevated lipid levels are closely associated with hepatic inflammation, which can be a consequence of the production of reactive oxygen species during oxidation[231]. Specifically, cholesterol, triglycerides and free fatty acids are known contributors to the pathogenesis of NASH[232]. Therefore, in this study, serum TC, TG and NFA were analyzed. Thus, it was found that both HFD and CDHF groups exhibited increased serum levels of TC, TG and NFA compared to STD group at 20 and 52 weeks. Moreover, there was a marked increase in their levels from 20 to 52 weeks (**Table 4.6**).

Table 4.6. Serum TC, TG and NFA levels of male CD57BL/6J mice fed by STD, HFD or CDHF for 20, 52 and 78 weeks.

	Serum TC (mg. dL^{-1})			**Serum TG (mg. dL^{-1})**			**Serum NFA (mg. dL^{1})**		
Week	STD	HFD	CDHF	STD	HFD	CDHF	STD	HFD	CDHF
20	82.1 ± 7.7	179.5 ± 13.3***	214.2 ± 35.4*	81.9 ± 7.7	192.8 ± 19.8**	169.7 ± 13.6**	35.0 ± 4.8	105.5 ± 11.5**	103.8 ± 15.0**
52	119.6 ± 11.8	247.7 ± 15.9****	240.8 ± 13.9****	133.1 ± 7.9	278.8 ± 14.1****	249.4 ± 20.5***	78.6 ± 6.3	128.4 ± 17.0*	157.7 ± 13.5***
78	168.8 ± 17.6	241.5 ± 31.1	227.2 ± 44.8	159.0 ± 11.9	277.9 ± 12.6***	194.9 ± 21.1	105.7 ± 13.6	146.5 ± 5.9*	114.9 ± 27.0

Note: The data are expressed as Mean ± SEM. Groups bearing common superscripts are not significantly different. Symbols represent statistical significance: *P<0.05, **P<0.01, ***P<0.001, ****P<0.0001, all compared with STD group. Serum TC, serum total cholesterol; Serum TG, serum triglycerides; Serum NFA, serum non-esterified fatty acids.

4.3.3 ^{31}P-NMR quantitative analysis of the phosphorome

In addition to using histological and biochemical markers as clinical tools to monitor the progression of NASH in mice fed by HFD and CDHF, this thesis proposes a method based on ^{31}P NMR to quantitatively analyze the subset of phosphorylated metabolites as a metabolic fingerprint of the pathology. The “phosphorome” has the potential to provide a simplified yet comprehensive perspective on the metabolic progression of this liver disease, covering the predominant anabolic and catabolic pathways.

As presented, first, a univariate analysis was conducted to explore the variable “diet” within the dataset separately. This approach allows the observation of the central tendency due to the variation of each diet (HFD and CDHF) when compared to STD group (**Figures 4.4 and 4.6**). Concentration values of all metabolites from each condition are shown in **Table 4S1-3 in Chapter 4.4**.

4.3.3.1 ^{31}P-NMR univariate analysis in liver mice fed by HFD

Liver extracts from HFD animals showed a significant decrease in Fructose 6-phosphate (F6P), Fructose 1,6-bisphosphate (FBP) and 3-phosphoglyceric acid (3PG), which are phosphorylated metabolites involved in the glycolysis pathway. Prior literature has suggested that a deficiency in FBP could be considered as an etiology of hepatic steatosis[233]. On the contrary, Phosphoenolpyruvate (PEP), the end phosphorylated product of glycolysis, was unchanged. Moreover, Glucose 6-phosphate (G6P), the first

intermediate of the glycolysis, and Glucose 1-phosphate (G1P), an intermediate metabolite involved in gluconeogenesis, remained unchanged. However, lactic acid, a by-product of pyruvate metabolism under anaerobic conditions, was significantly increased, which is strongly associated with Warburg effect[234], defined as an increase in the rate of glucose uptake and preferential production of lactate, even in the presence of oxygen, as explained in the previous Chapter.

Likewise, 6-Phosphogluconic acid (6PG), an intermediate in the oxidative phase of pentose phosphate pathway and the glycolysis pathway, increased significantly. In contrast, non-oxidative phase phosphorylated metabolites of pentose phosphate pathway (PPP), such as Sedoheptulose 7-phosphate (S7P) and Xylulose 5-phosphate (X5P), were significantly reduced in liver mice fed by HFD.

In the context of the Kennedy pathway, during cytidine diphospho (CDP) ethanolamine pathway, Phosphoethanolamine (PEA) and Glycerophosphoethanolamine (GPE) decreased, whereas Cytidine diphospho ethanolamine (CDPEA), the rate-limiting and the most regulatory step, increased. Phosphoethanolamine cytidylyltransferase (PCT) catalyzes the second step in the synthesis of Phosphatidylethanolamine (PE) from PEA to CDPEA being the inhibition of the PCT pathway for diacylglycerol utilization triggers to increase fatty acid synthesis to support the idea that the formation of TG leads to liver steatosis[235]. Likewise, all these metabolites are precursors for the synthesis of phosphatidylethanolamine (PE), the second most abundant phospholipid found in biological membranes, which increased.

Meanwhile, in CDP choline pathway, glycerophosphocholine (GPC) was increased, although Phosphocholine (PCHO) was decreased. Choline (CHO) and Cytidine diphospho choline (CDPCH), the key rate-limiting enzyme in Phosphatidylcholine synthesis, remained unvaried. All of them are precursors of the synthesis of PC, the most abundant phospholipid of the lipid droplet monolayer, which did not show any significant change in HFD mice.

The balance between PC and PE, the two main cell membrane phospholipids, have special importance. In fact, according to diverse mechanistic studies in animal models carried out, they have demonstrated that Phosphatidylethanolamine *N*-methyltransferase (PEMT), the enzyme responsible for the synthesis of PC by the methylation of PE, knockout mice lead to hepatic steatosis, steatohepatitis and death from liver failure with a reduction in hepatic PC/PE *ratio* suggesting that the lower PC/PE

ratio caused a disruption in membrane integrity and consequently, a hepatocyte damage and inflammation, similar to NASH[236]. In addition, a decrease in hepatic PC/PE *ratio* has been documented in patients clinically diagnosed with NASH[237] supposing that S-adenosylmethionine availability, the main biological methyl donor in humans that is abundant in the liver, had been limited[238]. To sum up, lower PC/PE *ratio* levels may be a good predictor of the development of NAFLD and of liver damage. Thus, in liver mice fed by HFD, they displayed a decreased PC/PE *ratio*, which may lead to a loss of membrane integrity and, consequently, a liver failure.

Another relevant outcome observed is that both liver Total cholesterol (TC) and triglycerides (TC) were increased. Cholesterol accumulation in the liver has been reported as a hepatic feature in some patients with NAFLD, promoting the necroinflammation and fibrosis typical of NASH[239]. In this way, it plays an important role in the development and progression of NASH[239]. Besides TC, evidence showed that an increased accumulation of TG in the liver with subsequent toxic effects contributed to liver damage and the changes in cholesterol and Triglycerides homeostasis associated with NAFLD a subject of an extensive investigation[240].

Nicotinamide adenine dinucleotide (NADH), a coenzyme which is involved in redox reactions in central metabolism such as glycolysis, beta-oxidation, the citric acid cycle, and oxidative phosphorylation in mitochondria, remained unchanged in HFD-fed mice. Moreover, Nicotinamide adenine dinucleotide phosphate (NADPH) levels, which are mainly produced in the oxidative phase of PPP and through folate-mediated one-carbon pathways, were significantly unalterable. Flavin adenine dinucleotide (FADH), a redox cofactor that is generated during the citric acid cycle and utilized during the last part of oxidative phosphorylation in mitochondria, had unchanged values in liver mice fed by HFD.

Adenosine 5´-diphosphoribose (ADPR) was also measured. It is a product of the activity of Poly (ADPR-ribose) polymerase (PARP), and it is involved in a large number of cellular processes[241]. In response to oxidative stress, ADPR activation begins an energy-demanding and ineffective cellular metabolic cycle, leading to mitochondrial and cellular dysfunction. Consequently, it boosts the functional impairment of the cells, culminating in cell necrosis[67]. In addition, ADPR is recognized by researchers as the “death substrate”, being one of the first identified substrates of caspases, the proteases that participate in the intracellular signaling cascade that leads to apoptosis. Moreover, there is a physiological importance of ADPR as a product of PARP in the maintenance of

genomic integrity and DNA repair[242]. Besides, it is also relevant to its ability in order to regulate transcription, being its three principal mechanisms involved in the effect of ADPR as a product of PARP on histones; secondly; the regulation of DNA methylation by ADPR; and thirdly, the participation of it in promoter-binding complexes[69]. Overall, ADPR is a vital biomarker involved in necrosis, apoptosis, DNA repair and regulation of transcription[67]. Thus, this biomolecular marker of cell apoptosis and necrosis was increased in the HFD-fed mice group, suggesting significant cell damage resulting from this diet.

On the other hand, nucleotides monophosphates, such as Adenosine 5´-monophosphate (AMP), Guanosine 5´-monophosphate (GMP) and Thymidine 5´-monophosphate (TMP) remained unaltered whereas Cytidine 5´-monophosphate (CMP) and Uridine 5´-monophosphate were decreased. These phosphorylated metabolites are interconverted into nucleotides diphosphates and triphosphates, which are involved in a plethora of energy-demanding cellular functions, such as protein and cell membrane synthesis, cell division, etc.

Finally, other nucleotides sugars have been measured, including Uridine diphospho glucuronic acid and galactose (UDPGA/UDPgal), Nucleotides diphospho glucose (NDPG), Uridine diphospho N-acethyl glucosamine (UDPNAcglu), Guanosine diphospho fucose (GDP Fuc) and Guanosine diphospho mannose (GDP Man). All these remained unchanged in the HFD-fed mice group.

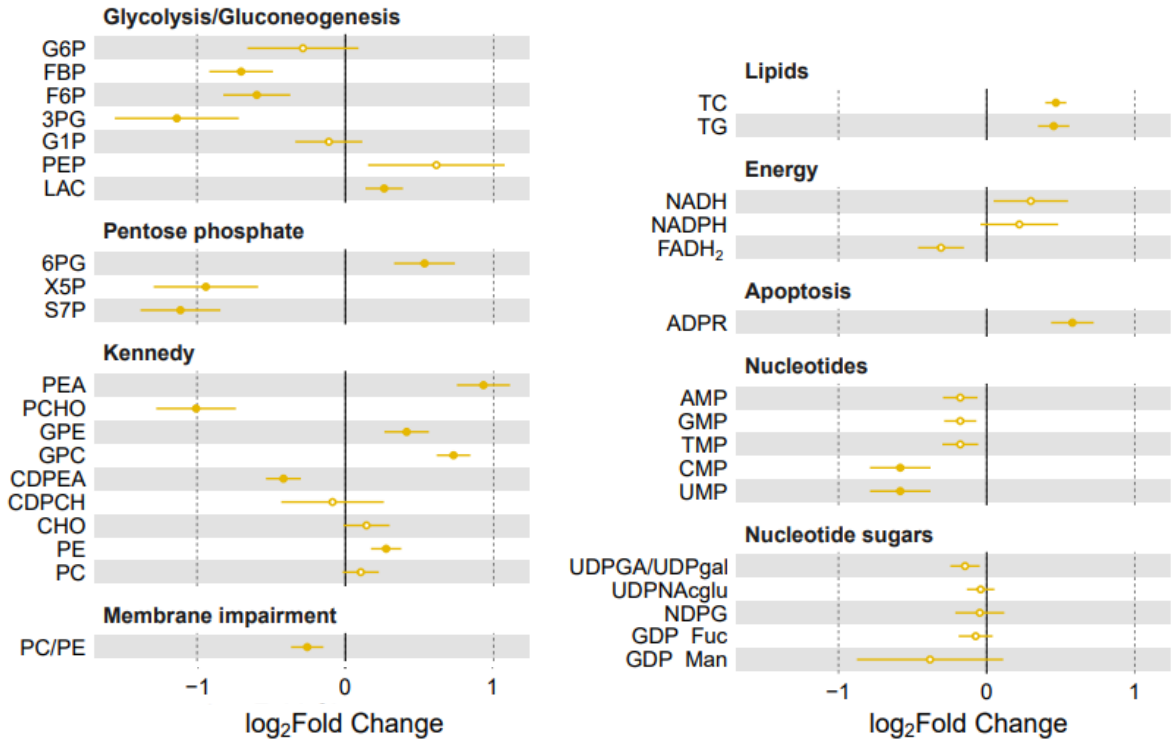

Figure 4.4. Average effect of HFD on each Metabolite, regardless of the age of mice. The horizontal axis

showed the log_2Fold Change that is on mean average increased (or decreased) when a mouse was fed by HFD. Circles represented the specific mean increase (decrease) value, whereas horizontal yellow bars were the 95% confidence interval. Statistically significant differences (*p-value* < 0.05) were represented with filled circles.

In general terms, according to the results obtained through ^{31}P-NMR univariate analysis, HFD can cause a loss of membrane integrity, cell injury and metabolic changes in glycolysis, PPP and Kennedy pathway. Next, a volcano plot has been represented (**Figure 4.5**) to summarize which phosphorylated metabolites have large fold changes and are also statistically significant, as mentioned before. The analysis performed resulted in the identification of 15 different phosphometabolites in HFD *versus* STD with satisfying values (*p-value* < 0.05, log_2 Fold Change ≥ 1 and log_2 FC ≤ -1). The most relevant results are that the phosphometabolites with the highest fold change and significant differences were PEA and GPC, which were increased, suggesting an increased turnover of phospholipids in HFD-fed mice group. Likewise, two metabolic features of NASH, TG and TC, were increased just as expected.

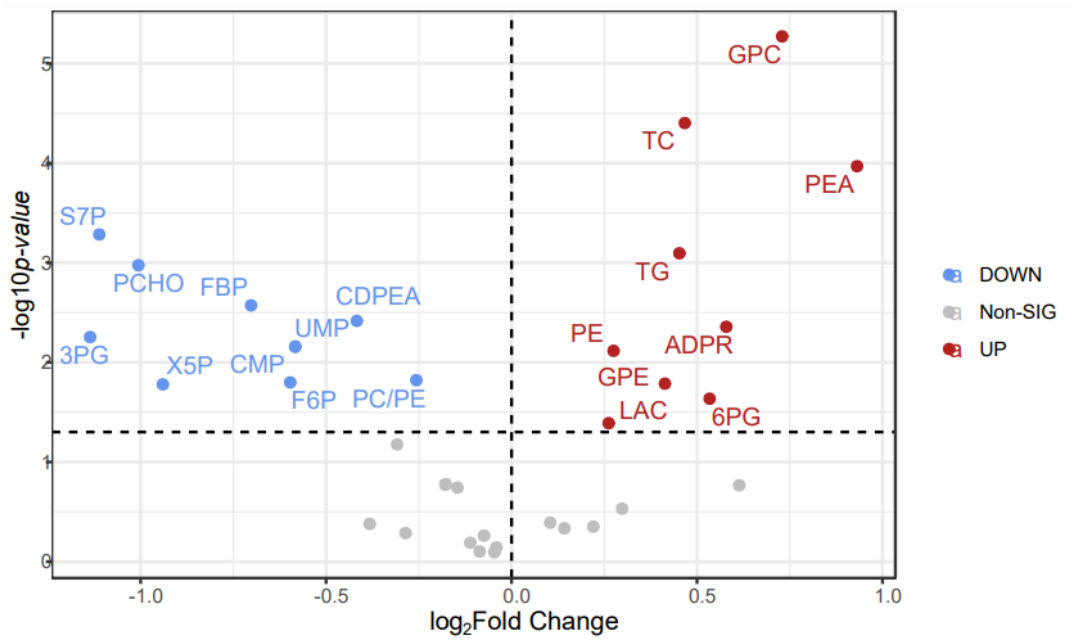

Figure 4.5. Volcano plot for HFD vs STD group, regardless of the age of mice. Untargeted analysis showing the log_2 Fold Change and *p-values* of phosphorylated metabolites differing between two groups. *P-values* are calculated from *t-test*. In blue, the metabolites that decreased significantly in liver mice fed with HFD whereas in red, those metabolites that increased significantly in liver mice fed with HFD. Significance level = 0.05.

3.3.3.2 ^{31}P-NMR univariate analysis in liver mice fed by CDHF

Mice livers fed with CDHF showed a reduction in F6P along with its downstream metabolites FBP and 3PG whereas no significant change was observed in G6P. However, an increase in hepatic PEP and LAC levels was detected in the CDHF animal group compared to the STD group. It has been reported that the accumulation of lactate, a feature of the Warburg effect, is significantly higher in fatty liver than in normal liver[243].

Likewise, S7P and X5P content decreased in the CDHF group, as was previously observed in the HFD group. Nevertheless, 6PG levels were increased, although not significantly.

Regarding the Kennedy pathway, during the CDP-ethanolamine pathway, a decrease in CDPEA was observed, despite an increase in PEA, GPE and PE. Increased levels of PE suggested that PE metabolism has been activated or PE in the membrane has been partially impaired. In the case of liver disease, the second one seems more probable, because the methylation of PE, which is stimulated by methionine is responsible for 30% of the PC synthesis in the liver. Methionine metabolism, those metabolites that have not been identified and quantified during this thesis, is typically altered in advanced liver disease and, probably, could be responsible for the abnormal levels of PE and its precursors observed. For another hand, CHO, CDPCH and PCHO were reduced showing an aberrant choline metabolism. CHO deficiency diet may have an impact on several metabolic pathways, potentially predisposing one to NAFLD. CHO deficiency as a cause of hepatic steatosis is shown in the setting of total parenteral nutrition, in which choline replacement causes a reversal of fatty infiltration[244].

As with HFD group, it was demonstrated that a reduction in the PC/PE *ratio* in liver mice fed by CDHF may be due to a decreased choline bioavailability for the CDP-choline pathway. However, it also could be because of a decreased PEMT activity or even an impaired methylation capacity. Thus, a downregulation of the PC/PE *ratio* of hepatic membranes could be a key to the changes that are seen with choline deficiency metabolism.

Likewise, as occurred with HFD, the hepatic levels of TG and TC were increased in CDHF group, being possible an increase of fatty acid uptake into the liver that could contribute to an accumulation of liver TG, which are secreted, together with cholesteryl esters in the form of VLDL particles for delivery to peripheral tissues such as skeletal

muscle, cardiac muscle and adipose tissue.

Moreover, an increase in NADH hepatic levels and a decrease in $FADH_2$ levels suggested an imbalance of tricarboxylic acid activity. At the same time, NADH over-production could increase the H^+ gradient across mitochondrial membranes and potentiate reactive oxygen species generation from the electron transport chain, damaging mitochondrial functionality. Concurrently, $FADH_2$ is directly attached to the second protein of the electron transport chain. A decrease in this metabolite could affect the electron transportation across the membrane and reduce the proton gradient. Altogether, an increase of NADPH, the product of the oxidative phase of PPP, was also observed, in line with the increase observed in 6PG, although this last metabolite was not significant.

ADPR, as discussed in the previous chapter, is a vital phosphometabolite involved in several cellular processes mainly in DNA repair as well as programmed cell death. As it occurred with mice HFD group, mice fed by CDHF have ADPR liver levels increased, suggesting apoptosis and necrosis.

Nucleotides monophosphate (AMP, GMP, TMP, UMP and CMP) were statistically significantly decreased. This effect could disrupt cellular homeostasis and affect diverse physiological processes, including carbohydrate metabolism and oxidative phosphorylation, as previously discussed in Chapter **4.3.3.1**.

UDPNAcglu is the end product of the hexosamine biosynthetic pathway and is regulated *via* F6P.Thus, it is considered an important regulator of cell signaling as it constitutes the major substrate for protein glycosylation. In this study, UDPNAcglu was decreased in liver mice fed by CDHF, suggesting a potential decrease in cell survival. On the contrary, GDP Man, which plays an important role as a donor substrate for *N-glycosylation*, remained unchanged. NDPG content, which is an important intermediate in several different metabolic pathways and biosynthetic reactions, including biosynthesis of polysaccharides, was unchanged. UDPGA/UDPgal, phosphorylated intermediate metabolites involved in the biosynthesis of ascorbic acid and the creation of polysaccharides, were reduced in CDHF group, as another nucleotide sugar, GDP Fuc.

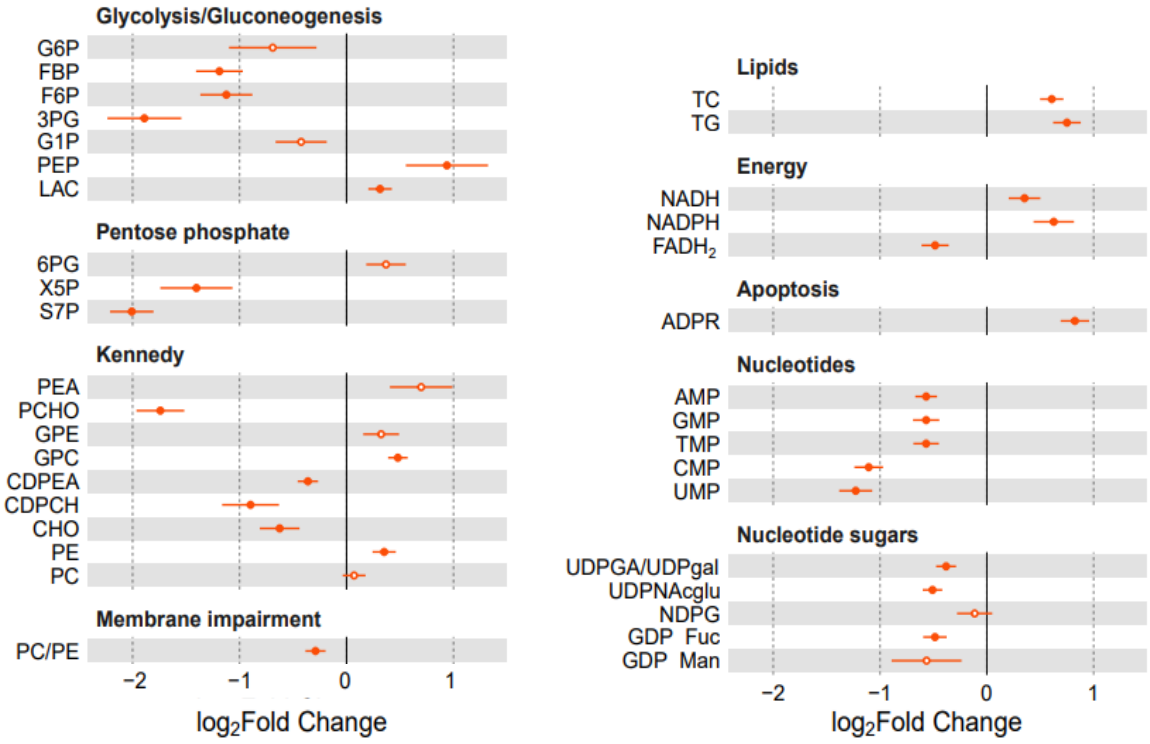

Figure 4.6. Average effect of CDHF for each Metabolite, regardless of the age of mice. The horizontal axis is the log_2Fold Change that is on mean average increased (or decreased) when a mouse is fed by CDHF. Circles were positioned in the specific mean increase (decrease) value, whereas horizontal red bars were the 95% confidence interval. Statistically significant differences (*p value* < 0.05) were represented with filled circles.

Overall, the CDHF liver animals group showed an impaired mitochondrial function with a loss of membrane integrity provoking liver damage as well as metabolic changes in glycolysis, PPP, triglycerides biosynthesis, hexosamines metabolic pathway, Kennedy pathway and nucleotides metabolism.

Figure 4.7 represents a volcano plot in which appears which phosphorylated metabolites have the biggest effect because of a comparison between CDHF and STD groups in addition to the statistical significance of its effect, summarizing the most significant data that it has discussed before. Of about 40 phosphometabolites, 18 metabolites had at least 1-Fold downregulated and significantly different whereas 7 metabolites had at least 1-Fold upregulated as well as significant differences.

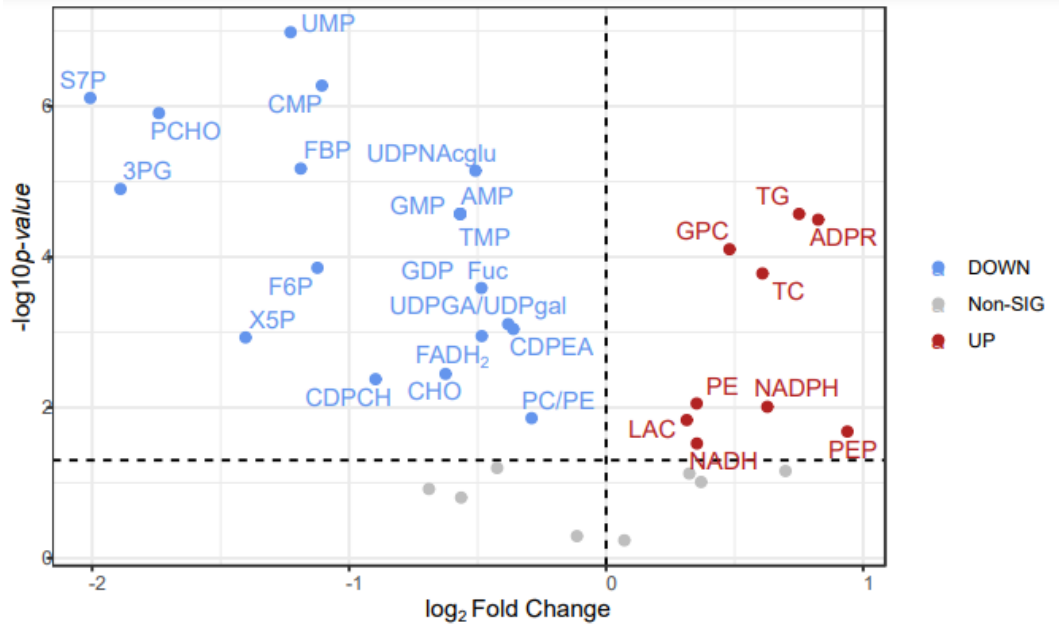

Figure 4.7. Volcano plot for CDHF vs STD group, regardless of the age of mice. Untargeted analysis showing the $\log_2$ Fold Change and *p-values* of phosphorylated metabolites differing between two groups. *P-values* were calculated from the Wilcoxon test. In blue, the metabolites that decreased significantly in liver mice fed with CDHF whereas in red, those metabolites that increased significantly in liver mice fed with CDHF. Significance level = 0.05.

3.3.3.3 ^{31}P-NMR supervised analysis in the effect of diets

In univariate analysis, it was observed that the hepatic metabolic profiles of HFD and CDHF animals groups differ from those observed in STD group, confirming this fact through the development of PLS-DA analysis. PLS-DA is a supervised analysis that forces a separation between experimental groups based in their intrinsic features, in this case, phosphorylated metabolites (**Figure 4.8**).

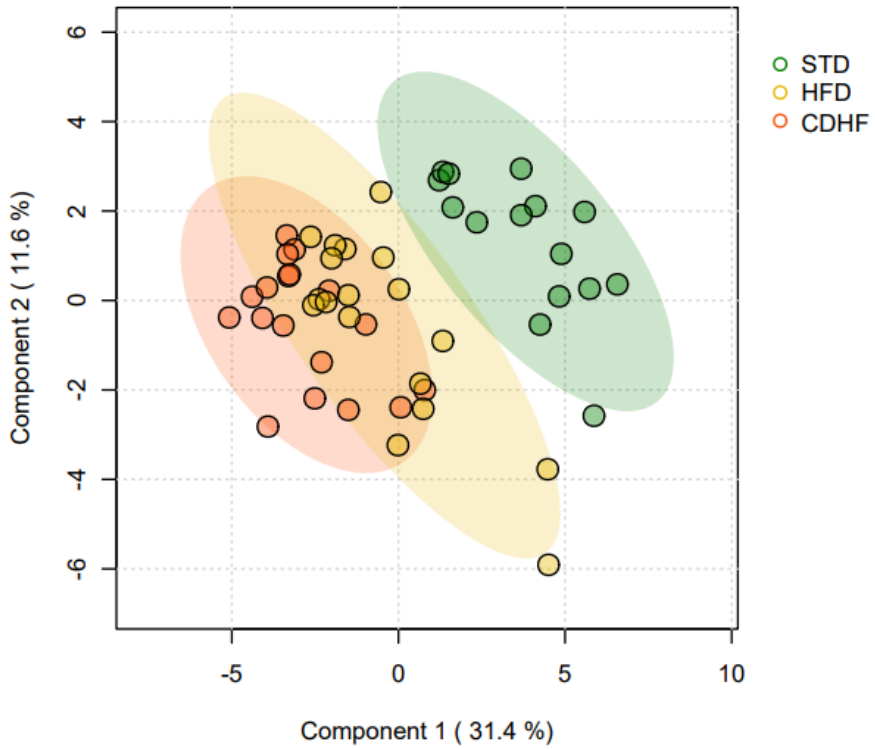

Figure 4.8. PLS-DA by a group of each diet (STD, green; HFD, yellow and CDHF, red) showing the first and the second component. Differences between STD and the other two groups of diet (HFD and CDHF) have been found although not much separation was found between HFD and CDHF with this supervised analysis.

3.3.3.4 ^{31}P-NMR supervised analysis in the effect of age

Prior studies[245,246] have demonstrated that aging promotes risk factors associated with NASH such as inflammation, diabetes, and obesity in addition to an increase in susceptibility and incidence of obesity and insulin resistance leading to liver damage and promoting the development of NASH.

Thus, a longitudinal study was carried out to determine the aging effect in the liver metabolic response in mice fed by two diets which can develop NASH[247]. To further understand the implication of aging in this study, PLS-DA was performed.

The outcome of this analysis is summarized in **Figure 4.9**. It showed the PSL-DA by group with the first and second components (**Figure 4.9**). Interestingly, there appeared to be a separation between the group of 20 weeks and the other groups. Nevertheless, a clear separation between 52 and 78 weeks of age was not observed. In any case, this plot provided information because it is possible to distinguish between the age of mice, a variable which was vital to take into consideration in the mentioned study.

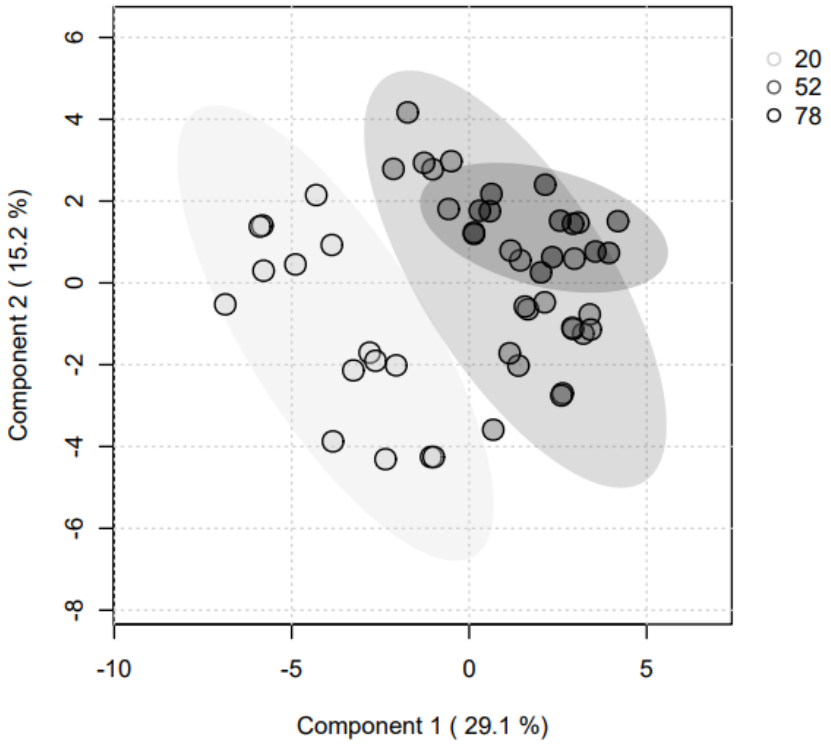

Figure 4.9. PLS-DA by a group of age (20 weeks, bright grey; 52 weeks, dark grey and 78 weeks, black) showing the first and the second component. Differences between 20 and the other two groups of age (52 and 78 weeks) have been found although no separation was found between 52 and 78 weeks with this supervised analysis.

In summary, given that both age and diet type are crucial factors to consider, the next section will attempt to establish a linear model adjusted to age and diet. This will enable us to ascertain the effect size and statistical significance for each metabolite about to each variable (diet or age).

3.3.3.5 Towards molecular discrimination of diets and age

Using the spectra database obtained from the measurement of liver samples from mice fed two different diets included in the study (HFD and CDHF) at different ages (20,52 and 78 weeks), it is attempted to build a metabolic model for differentiating the effect of diets and ages. This was done by obtaining different β coefficients for each metabolite across various ages or diets, to understand how different the age or diet is when it was compared with their respective reference (20 weeks in case of age and STD in case of diet). Additionally, it is determined if the observed differences were statistically significant. The results are summarized in the heatmap shown in **Figure 4.10**.

Firstly, based on the results obtained, either the age of mice or the type of diet which

they eat exerts different effects on each phosphorylated metabolite. Thus, it is crucial to explain each variable separately although some metabolites have a common pattern due to the variation of age as well as the type of diet that the mice are fed.

For instance, ADPR, a biomarker of apoptosis and necrosis, increased in both the CDHF and HFD groups compared to the STD group, as previously explained. However, the ADPR liver values were higher over time, as it has reported in previous research[248]. Thus, therefore, the cell damage could have been due to a high-fat content diet (both HFD and CDHF) and an increase in the age of mice.

Moreover, the PC/PE *ratio*, a marker of membrane integrity, was decreased in liver mice fed by HFD and CDHF as compared to STD group. Besides, the hepatic levels were decreased by increasing the age of the mice, especially from 20 to 52 weeks mice, suggesting that liver failure could be produced because of both variables (diet and age).

Furthermore, regarding the PPP, 6PG, a phosphometabolite involved in the oxidative phase of this metabolic pathway, was elevated in HFD mice group and increased over time. Meanwhile, non-oxidative phosphorylated metabolites, X5P and S7P, were reduced in mice fed by HFD and CDHF. Both were greatly reduced from 20 to 52 weeks of age.

Finally, in the glycolysis pathway, it was detected both, FBP and F6P in liver mice fed by HFD and CDHF. Simultaneously, all of them decreased at 52 weeks as compared to 20 weeks although FBP hepatic levels were changed in older age mice, increasing its hepatic content. Likewise, 3PG and F6P were much more reduced at 52 weeks than at 78 weeks as compared to 20 weeks age of mice. Besides, G6P was considerably reduced at 52, not increasing much more to 78 weeks.

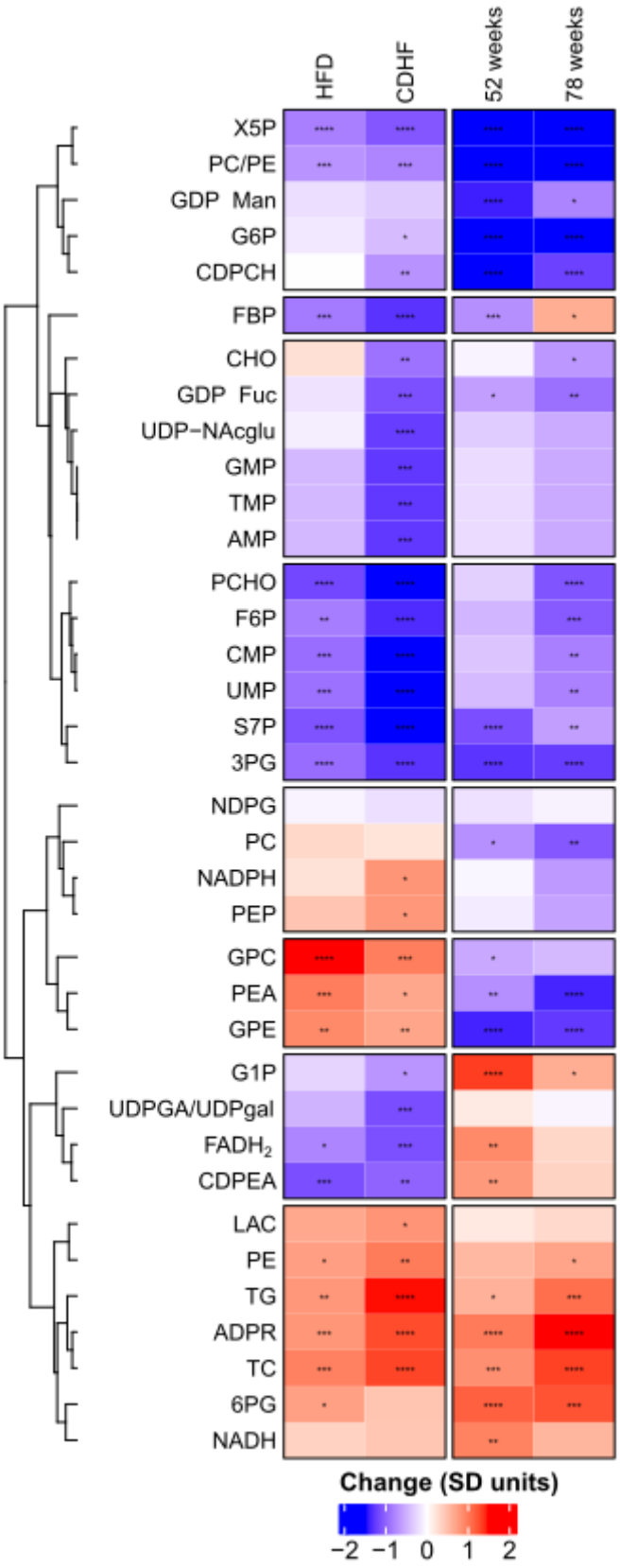

Figure 4.10. Heatmap for the different conditions of diets (HFD and CDHF) and age (52 and 78 weeks) as compared as their reference (STD in case of diet and 20 weeks in case of age). The metabolites (in the ordinate axis) have been sorted according to cluster analysis. The squares are color-coded according to the

bar legend which represented how different is (on average) the age or diet when it was compared with their reference. The differences between conditions were converted to standard deviation (SD) units in order to make the scale comparable between variables. For each condition, the statistical significance of the variation with respect to each reference was determined by the *p-value*, shown inside the squares.

3.3.3.5.1 Metabolic model for diets differentiation

Next, supervised analysis is used to evaluate how each diet (HFD and CDHF) can be differentiated from the STD group, as well as the distinguishing factors between the two diets themselves. We also sought to determine the impact of the mice´s age on these metabolic changes in liver phosphorome.

First, an Orthogonal Partial Least-Squares Discriminative Analysis (OPLS-DA) was performed. This supervised analysis was introduced as an improvement of the PLS-DA approach to discriminate two groups or more using multivariate data. Hence, we could see a clear separation between HFD and STD animals' groups (**Figure 4.11B**). Likewise, it was tested to see if this model was optimum using a Receiving Operating Characteristic (ROC) curve (**Figure 4.11A**). The best point for the balance between sensitivity and specificity was a maximum is 0.232. The Area Under the Curve of this ROC Curve (AUC = 1) indicates that our training model was explicative, and it could distinguish between the different parts of the NMR spectrum that differ between HFD and STD, bypassing the intermediate conditions. Furthermore, it also told us that our model fits well with the data from the cohort of mice we have been working with.

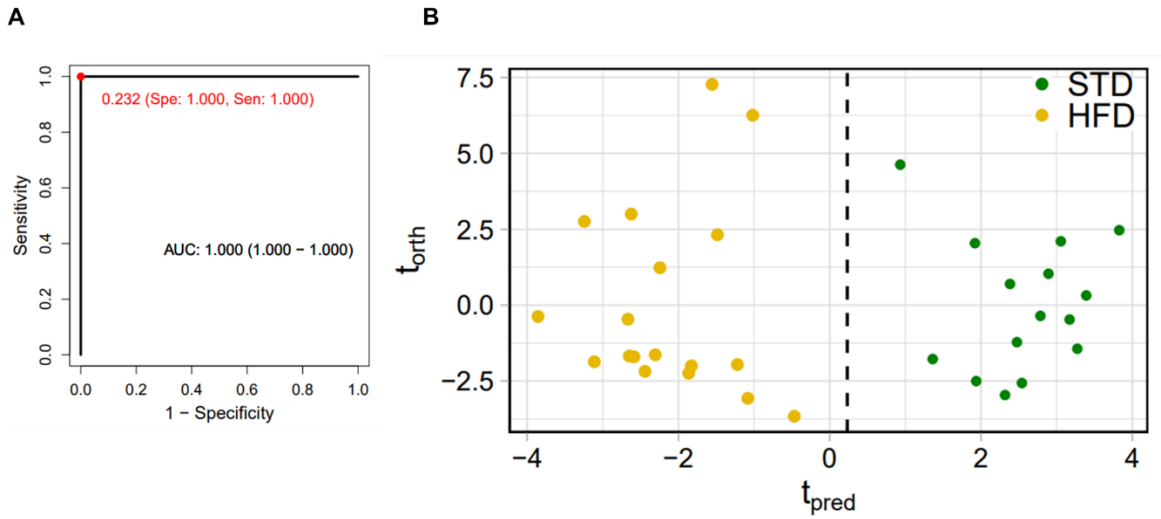

Figure 4.11. A) Receiving Operating Characteristic (ROC) curve for our training model analyzing the effect of HFD in liver mice samples. The graph showed the ROC curve and the best sensitivity-specificity point (0.232). B) OPLS-DA of liver mice fed by HFD and STD. There was a clear separation between HFD and STD.

Furthermore, **Table 4.7** summarizes the Variable Importance in Projection (VIP) score plot for the top 11 most important metabolites. The VIP is an estimation of the importance of each variable – in this case, each phosphorylated metabolite - in the projection used in OPLS-DA model. It provides a quantitative estimation of the discriminatory power of each individual phosphometabolite. The analysis identified 2 metabolites involved in CDP-ethanolamine pathway (PEA and PE), CDP-choline pathway (GPC and PCHO), lipids metabolism (TG and TC) and nucleotides metabolism (CMP and UMP), 1 metabolite involved in glycolytic pathway (3PG) as well PPP (S7P) and cell death marker (ADPR), were highly abundant metabolites in order to discriminate HFD and STD mice groups.

Table 4.7. Summary of metabolites discriminating HFD vs. STD.

Metabolite	Variable importance in this model	Up or Downregulated
GPC	76.9	Up regulated
TC	72.7	Up regulated
TG	65.7	Up regulated
PEA	60.0	Up regulated
S7P	57.5	Downregulated
PE	57.3	Up regulated
PCHO	56.6	Downregulated
ADPR	53.3	Up regulated
3PG	51.1	Downregulated
CMP	49.7	Downregulated
UMP	49.7	Downregulated

Additionally, as expected, the comparison between liver mice fed by CDHF and STD cohorts presented a high separation degree with good predictability (AUC) = 1) (**Figure 4.12**).

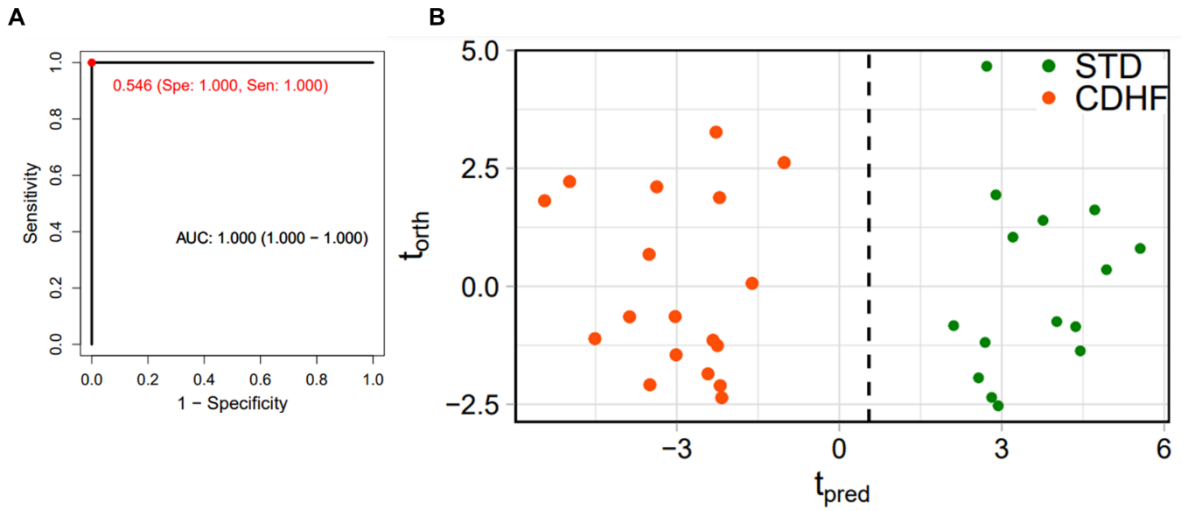

Figure 4.12. A) ROC curve for our training model analyzing the effect of CDHF in liver mice samples. The graph showed the ROC curve and the best sensitivity-specificity point (0.546). B) OPLS-DA of liver mice fed by CDHF and STD. There was a clear separation between CDHF and STD.

Moreover, the metabolites that were responsible for the differentiation pattern in the OPLS-DA plot were phosphometabolites involved in nucleotides metabolism (AMP, GMP, TMP, UMP and CMP), glycolysis (3PG, F6P and FBP), CDP choline pathway (GPC and PCHO), hexosamines (UDPNAcglu), PPP (S7P) and lipid metabolism (TG) (**Table 4.8**).

Table 4.8. Summary of metabolites discriminating CDHF vs. STD.

Metabolite	Variable importance in this model	Up or Downregulated
UMP	60.7	Downregulated
S7P	59.8	Downregulated
PCHO	56.3	Downregulated
CMP	55.8	Downregulated
AMP/GMP/TMP	54.6	Downregulated
FBP	52.9	Downregulated
3PG	51.9	Downregulated
UDPNAcglu	51.2	Downregulated
GPC	50.5	Up regulated
F6P	47.8	Downregulated
TG	47.7	Up regulated

Finally, it was confirmed that phosphoromics pattern of HFD and CDHF mice groups can be discriminated among them through OPLS-DA although in this case AUC worsens up until 0.969 (**Figure 4.13**).

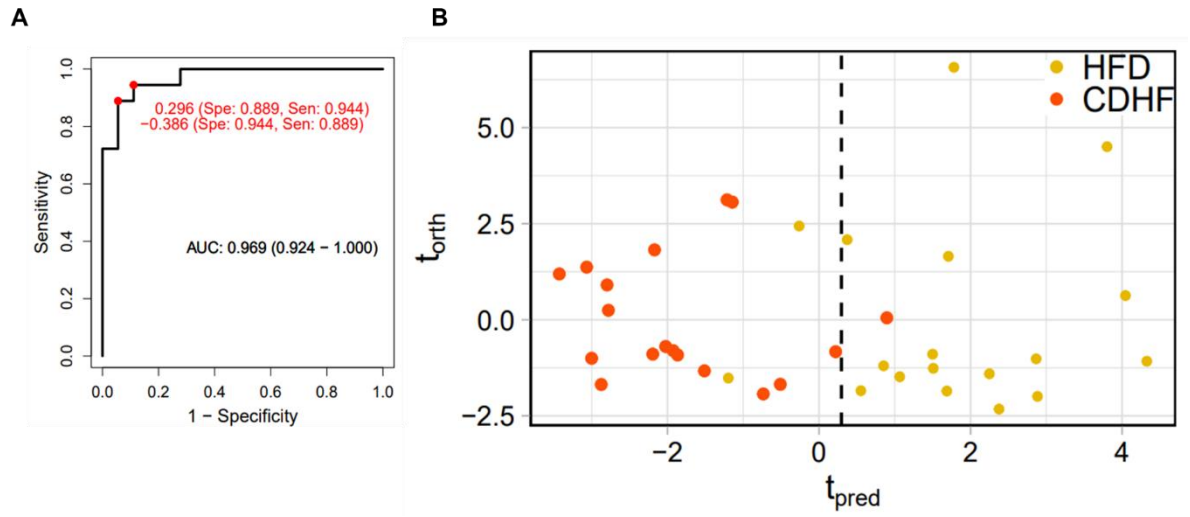

Figure 4.13. A) ROC curve for our training model analyzing the comparison between CDHF and HFD in liver mice samples. The graph showed the ROC curve and the best sensitivity-specificity point (-0.386). B) OPLS-DA of liver mice fed by CDHF and HFD. There was a separation between CDHF and HFD.

According to the variable importance values obtained, liver mice fed by HFD and CDHF could be discerned because of phosphometabolites. This covered a spectrum from nucleotides metabolism (AMP, GMP, TMP, UMP and CMP) to nucleotide sugars (UDP Fuc, UPDGA and UDPNAcglu), CHO, PCHO, a redox- active coenzyme $FADH_2$, among others (**Table 4.9**).

Table 4.9. Summary of metabolites discriminating HFD vs. CDHF.

Metabolite	Variable importance in this model	Up or Down-regulated
UDPNAcglu	84.4	Downregulated
GDP Fuc	75.2	Downregulated
CHO	71.8	Downregulated
AMP/GMP/TMP	69.7	Downregulated
UDPGA/UDPgal	66.6	Downregulated
UMP	58.4	Downregulated
$FADH_2$	55.6	Downregulated
PCHO	49.8	Downregulated
CMP	49.7	Downregulated
S7P	44.9	Downregulated
F6P	40.8	Downregulated

To sum up, the three built models, based on the phosphoromics analysis of the measured liver samples, proved to be able to distinguish liver mice fed by different types of diets with AUC values between 0.963 and 1, reflecting the importance of the type of the diet for this metabolic model, also previously evidenced.

3.3.3.5.2 Metabolic model for age differentiation

Likewise, multiple studies have evidenced a direct correlation between the severity of NASH and age[249,250]. To investigate if the observed changes in the expression of metabolites were correlated with age, different age-related OPLS-DA have been done. Thus, when it was compared two cohorts of liver samples with 20 and 52 weeks, it was observed that there was a clear separation confirmed by AUC (**Figure 4.14**).

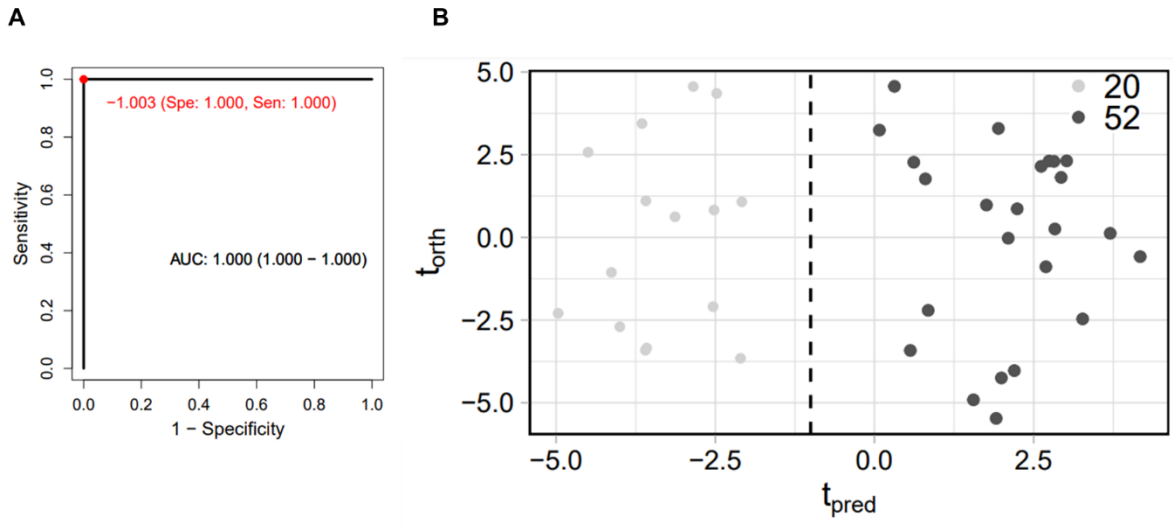

Figure 4.14. A) ROC curve for our training model analyzing the comparison between 20 week and 52 weeks in liver mice samples. The graph showed the ROC curve and the best sensitivity-specificity point (-1.003). B) OPLS-DA of liver mice fed by 20 and 52 weeks. There was a separation between 20 and 52 weeks.

Once the variable importance values obtained, the metabolites that were responsible for the differentiation pattern in the OPLS-DA plot were phosphometabolites involved in glycolysis (G6P and 3PG), PPP (X5P and 6PG), phospholipids precursors (CDPCH and GPE), gluconeogenesis (G1P), nucleotide sugars (GDP Man), lipids (TC), a biomarker of cell death (ADPR) and membrane impairment (PC/PE *ratio*) (**Table 4.10**).

Table 4.10. Summary of metabolites discriminating 52 vs. 20 weeks.

Metabolite	Variable importance in this model	Up or Down-regulated
PC/PE	71.8	Downregulated
G6P	71.1	Downregulated
X5P	68.2	Downregulated
CDPCH	67.5	Downregulated
ADPR	67.2	Up regulated
GDP Man	63.9	Downregulated
G1P	61.2	Up regulated
6PG	56.0	Up regulated
TC	55.7	Up regulated

3PG	55.6	Downregulated
GPE	55.5	Downregulated

Just, as expected, OPLS-DA and ROC curve revealed that the metabolic patterns of both set of liver mice samples from 20 and 78 weeks were different (**Figure 4.15**).

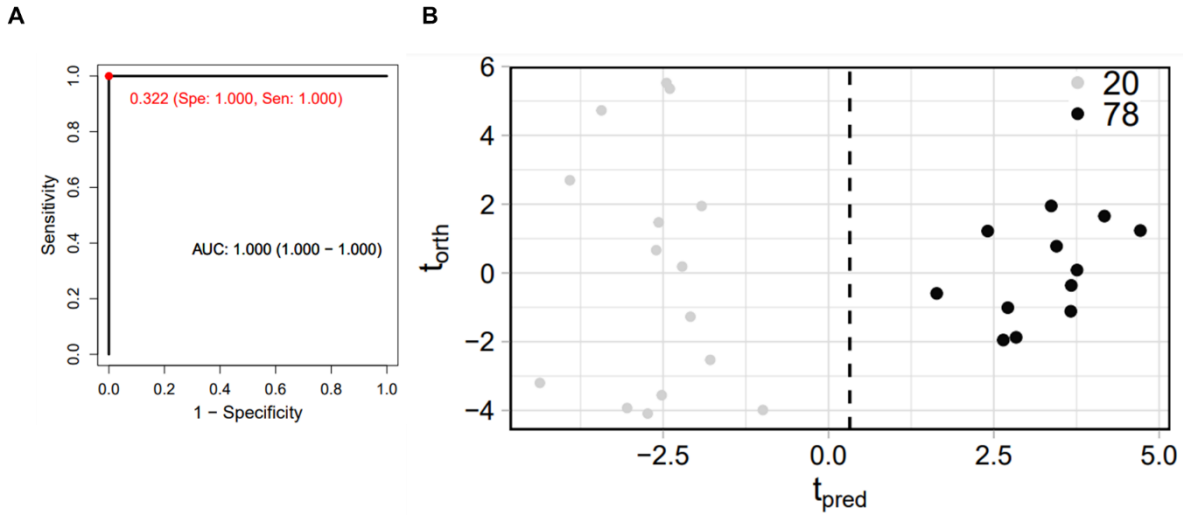

Figure 4.15. A) ROC curve for our training model analyzing the comparison between 20 week and 78 weeks in liver mice samples. The graph showed the ROC curve and the best sensitivity-specificity point (0.322). B) OPLS-DA of liver mice fed by 20 and 78 weeks. There was a separation between 20 and 78 weeks.

Thus, the metabolic profile of the liver from 20 and 78 weeks of age can be differentiated due to metabolites including those which are shown in **Table 4.11**.

Table 4.11. Summary of metabolites discriminating 78 vs. 20 weeks.

Metabolite	Variable importance in this model	Up or Downregulated
PC/PE	71.4	Downregulated
ADPR	65.1	Up regulated
X5P	63.6	Downregulated
G6P	63.3	Downregulated
6PG	62.1	Up regulated
PC	60.5	Downregulated
TC	54.8	Up regulated
PEA	52.0	Downregulated
CDPCH	50.9	Downregulated
F6P	50.2	Downregulated
TG	50.1	Up regulated

Lastly, as occurred previously, the OPLSA-DA score plots highlighted the separation between liver samples from 52 and 78 weeks of age, having been corroborated with an

AUC value of 1 (**Figure 4.16**).

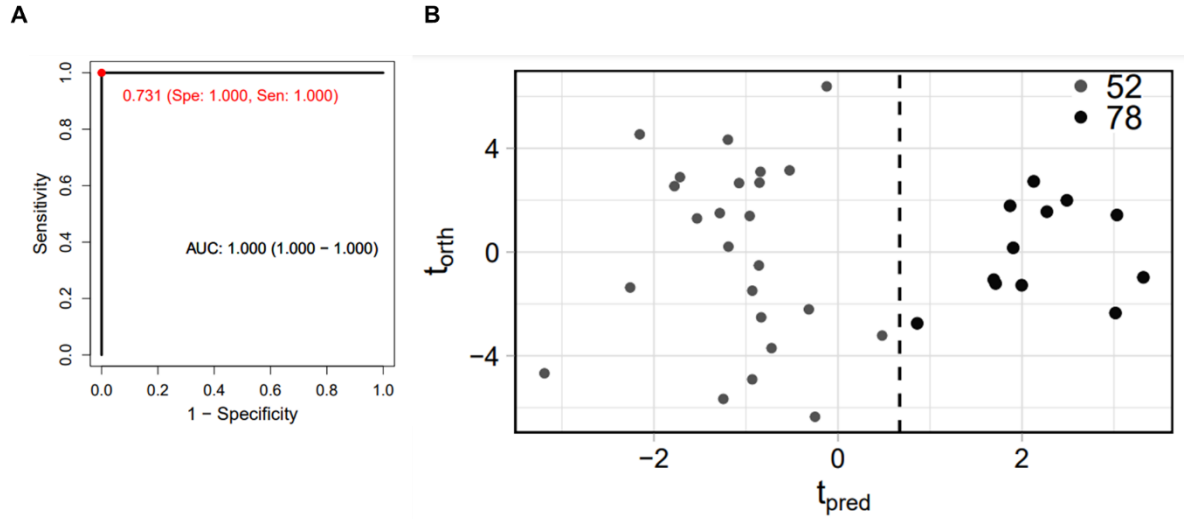

Figure 4.16. A) ROC curve for our training model analyzing the comparison between 52 week and 78 weeks in liver mice samples. The graph showed the ROC curve and the best sensitivity-specificity point (0.731). B) OPLS-DA of liver mice fed by 52 and 78 weeks. There was a separation between 52 and 78 weeks.

In addition, after doing the analysis, the most discriminant metabolites between the metabolic profile of liver mice of 52 and 78 weeks of age take part in glycolysis (FBP,PEP,G6P and F6P), phospholipids precursors (PEA, CHO and CDPCH), PPP (S7P), gluconeogenesis (G1P), nicotinamide metabolism (NADH) and nucleotide sugar (GDP Man).

Table 4.12. Summary of metabolites discriminating 78 vs. 52 weeks.

Metabolite	Variable importance in this model	Up or Down-regulated
FBP	101.1	Up regulated
S7P	85.8	Up regulated
GDP Man	84.6	Up regulated
PEA	78.6	Downregulated
CDPCH	67.8	Up regulated
CHO	66.0	Downregulated
PEP	59.0	Downregulated
G6P	50.5	Up regulated
G1P	46.5	Downregulated
NADH	46.1	Downregulated
F6P	43.8	Downregulated

Hence, these findings point toward the influence of age in the metabolic changes from liver mice samples.

In summary, ^{31}P-NMR can serve as a supplementary tool to characterize metabolic changes in mice liver fed by diets with high-fat content. It also proved that metabolic profiles obtained from ^{31}P-NMR quantitative analysis can aid in distinguishing these groups.

However, ^{31}P-NMR methods have not been systematically assessed for metabolomics application, and a robust workflow has not been established to encourage broader implementation in the field of metabolomics. Therefore, to facilitate the application of ^{31}P NMR in metabolomics, a protocol adopting ^{31}P NMR for characterizing liver samples and expanding the coverage of the metabolome will be presented in the next Chapter.

4.4 Supplementary material

Table 4S1. Quantification of the metabolites and standard deviations (STDV) for the different compounds and mouse models under consideration at 20 weeks of age.

Compound	STD	STDV	HFD	STDV	CDHF	STDV
6PG	0,071	0,009	0,060	0,012	0,049	0,009
G6P	2,416	0,476	2,359	0,192	1,559	0,295
FBP	0,228	0,040	0,169	0,023	0,113	0,014
F6P	0,314	0,045	0,248	0,038	0,207	0,046
3PG	0,439	0,065	0,288	0,083	0,137	0,042
G1P	0,132	0,005	0,106	0,009	0,070	0,008
PEP	0,010	0,002	0,006	0,000	0,008	0,002
LAC	2,286	0,250	2,532	0,347	2,512	0,495
X5P	0,664	0,127	0,447	0,028	0,331	0,031
S7P	2,263	0,289	1,159	0,134	0,317	0,011
PEA	0,081	0,014	0,191	0,017	0,219	0,049
PCHO	0,979	0,169	0,626	0,102	0,269	0,036
GPE	0,145	0,013	0,162	0,016	0,188	0,013
GPC	0,259	0,019	0,468	0,057	0,416	0,034
CDPEA	0,439	0,045	0,248	0,052	0,334	0,030
CDPCH	0,053	0,006	0,064	0,006	0,026	0,006
CHO	4,885	1,231	5,394	1,026	2,647	0,481
PE	0,603	0,070	0,740	0,028	0,656	0,028
PC	5,746	0,489	7,567	0,193	6,834	0,419
PC/PE	10,640	0,492	10,117	0,263	10,630	0,530
TC	23,605	0,441	25,988	1,279	24,642	1,445
TG	13,294	1,090	19,796	0,847	17,457	0,582
NADH	0,157	0,016	0,134	0,022	0,368	0,023
NADPH	0,063	0,002	0,158	0,023	0,093	0,007
$FADH_2$	0,421	0,009	0,372	0,037	0,483	0,032
ADPR	0,228	0,028	0,228	0,015	0,290	0,011

AMP	0,740	0,062	0,772	0,086	0,549	0,092
GMP	0,740	0,062	0,772	0,086	0,549	0,092
TMP	0,740	0,062	0,772	0,086	0,549	0,092
CMP	0,517	0,045	0,452	0,095	0,205	0,049
UMP	0,517	0,045	0,452	0,095	0,205	0,049
UDPGA/UDPglu	0,201	0,018	0,476	0,066	0,127	0,007
UDPNAcglu	0,248	0,013	0,160	0,016	0,150	0,005
NDPG	0,326	0,049	0,223	0,017	0,371	0,050
GDP Fuc	0,153	0,008	0,135	0,013	0,088	0,004
GDP Man	0,035	0,008	0,038	0,010	0,017	0,002

Table 4S2. Quantification of the metabolites and standard deviations (STDV) for the different compounds and mouse models under consideration at 52 weeks of age.

Compound	**STD**	**STDV**	**HFD**	**STDV**	**CDHF**	**STDV**
6PG	0,080	0,016	0,133	0,016	0,115	0,010
G6P	0,451	0,064	0,504	0,073	0,443	0,067
FBP	0,226	0,019	0,066	0,007	0,042	0,006
F6P	0,292	0,074	0,204	0,022	0,112	0,010
3PG	0,207	0,016	0,052	0,002	0,038	0,002
G1P	0,234	0,032	0,224	0,040	0,185	0,026
PEP	0,001	0,000	0,009	0,002	0,011	0,002
LAC	2,137	0,181	2,663	0,189	2,836	0,099
X5P	0,275	0,020	0,133	0,018	0,083	0,008
S7P	0,950	0,060	0,316	0,015	0,243	0,022
PEA	0,091	0,008	0,151	0,015	0,099	0,023
PCHO	0,988	0,095	0,389	0,063	0,232	0,019
GPE	0,092	0,007	0,118	0,011	0,111	0,008
GPC	0,270	0,015	0,366	0,034	0,344	0,020
CDPEA	0,497	0,035	0,403	0,038	0,373	0,033
CDPCH	0,021	0,001	0,017	0,004	0,013	0,004
CHO	4,388	0,424	4,818	0,542	3,258	0,196

PE	0,636	0,059	0,770	0,051	0,869	0,078
PC	5,619	0,643	5,613	0,592	5,812	0,669
PC/PE	8,800	0,394	7,147	0,456	6,620	0,285
TC	24,067	0,603	34,971	1,945	39,017	2,639
TG	14,596	1,422	19,744	1,449	28,401	2,255
NADH	0,298	0,025	0,424	0,069	0,329	0,038
NADPH	0,114	0,010	0,056	0,007	0,145	0,019
$FADH_2$	0,763	0,052	0,579	0,062	0,398	0,029
ADPR	0,290	0,015	0,428	0,048	0,500	0,028
AMP	0,852	0,044	0,639	0,077	0,475	0,046
GMP	0,852	0,044	0,639	0,077	0,475	0,046
TMP	0,852	0,044	0,639	0,077	0,475	0,046
CMP	0,527	0,056	0,263	0,034	0,221	0,025
UMP	0,527	0,056	0,263	0,034	0,186	0,019
UDPGA/UDPglu	0,199	0,013	0,169	0,014	0,143	0,009
UDPNAcglu	0,207	0,015	0,218	0,023	0,143	0,010
NDPG	0,373	0,043	0,314	0,047	0,238	0,018
GDP Fuc	0,117	0,008	0,116	0,012	0,085	0,008
GDP Man	0,014	0,001	0,004	0,001	0,008	0,002

Table 4S3. Quantification of the metabolites and standard deviations (STDV) for the different compounds and mouse models under consideration at 78 weeks of age.

Compound	**STD**	**STDV**	**HFD**	**STDV**	**CDHF**	**STDV**
6PG	0,081	0,016	0,130	0,009	0,132	0,019
G6P	0,954	0,064	0,496	0,080	0,513	0,026
FBP	0,215	0,022	0,258	0,019	0,207	0,018
F6P	0,241	0,030	0,081	0,020	0,079	0,007
3PG	0,164	0,019	0,082	0,003	0,074	0,006
G1P	0,191	0,017	0,148	0,006	0,128	0,010
PEP	0,004	0,001	0,006	0,001	0,005	0,001
LAC	2,245	0,275	2,795	0,454	2,868	0,381

X5P	0,219	0,015	0,056	0,005	0,062	0,005
S7P	1,095	0,079	0,811	0,015	0,653	0,023
PEA	0,050	0,014	0,081	0,007	0,063	0,003
PCHO	0,329	0,088	0,156	0,047	0,232	0,038
GPE	0,072	0,007	0,157	0,023	0,104	0,014
GPC	0,221	0,022	0,482	0,025	0,297	0,030
CDPEA	0,435	0,019	0,338	0,035	0,360	0,011
CDPCH	0,028	0,007	0,025	0,005	0,020	0,000
CHO	3,557	0,693	3,934	0,167	2,001	0,394
PE	0,680	0,096	0,807	0,041	0,880	0,072
PC	5,411	0,391	5,027	0,182	4,872	0,131
PC/PE	8,315	0,575	6,238	0,515	5,982	0,432
TC	25,185	2,637	39,425	2,848	47,459	5,341
TG	18,656	1,841	24,700	3,480	29,670	2,857
NADH	0,321	0,022	0,300	0,058	0,276	0,028
NADPH	0,040	0,007	0,081	0,013	0,094	0,010
$FADH_2$	0,581	0,072	0,415	0,023	0,434	0,029
ADPR	0,290	0,019	0,563	0,020	0,661	0,066
AMP	0,622	0,016	0,593	0,059	0,529	0,040
GMP	0,622	0,016	0,593	0,059	0,529	0,040
TMP	0,622	0,016	0,593	0,059	0,529	0,040
CMP	0,309	0,053	0,241	0,038	0,218	0,014
UMP	0,309	0,053	0,241	0,038	0,218	0,014
UDPGA/UDPglu	0,146	0,002	0,174	0,017	0,161	0,018
UDPNAcglu	0,190	0,009	0,175	0,009	0,173	0,022
NDPG	0,241	0,040	0,359	0,049	0,341	0,057
GDP Fuc	0,097	0,003	0,097	0,003	0,097	0,014
GDP Man	0,015	0,002	0,014	0,002	0,025	0,011

CHAPTER 5

AN ENHANCEMENT OF ^{31}P-NMR METHOD: A QUANTITATIVE ^{31}P-NMR PROTOCOL UNDER SOPs

5.1 Introduction

^{31}P, an NMR active nucleus with a nuclear spin of ½, provides relevant and interesting characteristics such as high chemical shift dispersion, 100% natural abundance as well a higher gyromagnetic ratio ensuring higher sensitivity than other active nuclei such as ^{13}C or ^{15}N. Uniquely, ^{31}P NMR specifically selects the phosphorome without signal background and spectral simplicity (mostly 1 singlet signal per metabolite). Conversely, ^{1}H-NMR encounters significant limitations due to its lack of selectivity, strong signal background (especially from water) and extreme spectral complexity despite its inherent quantification and spectral distinction of the metabolites. Therefore, ^{31}P-NMR is exceptionally suitable for metabolic studies. It broadens the coverage of the metabolome, enabling the detection of metabolites involved in critical cellular processes, such as energy metabolism and phospholipids, being a concise overview of the metabolic state. ^{31}P NMR was used in the early applications of NMR to study a wide variety of diseases[251–253], and as a tool of synthetic chemistry[254] and to research RNA and DNA structures[255,256]. Nevertheless, its application in metabolomics has been limited.

Despite these benefits, robust methodologies for integrating ^{31}P-NMR into metabolomics have been scarce. The existing challenges in applying ^{31}PNMR to metabolomics encompass critical factors like pH, the temperature dependence of chemical shift, absence of chemical shift references, chelating agent concentration, the addition of a small amount of paramagnetic gadolinium chelate[257] or the optimization of two-dimensional ^{1}H-^{31}P experiments of correlation[258], among others. Efforts have been made to establish optimal conditions for NMR sample measurement.

For instance, Bhinderwala *et.al*[259] (**Table 5.1**) used a set of standard polar phosphometabolites and phosphometabolites mixtures to optimize experimental parameters. Firstly, the coupling constants and mixing times for the 2D ^{1}H-^{31}P HSQC-TOCSY pulse sequences were evaluated to maximize the greatest number of phosphorylated metabolites which could be detected and identified. Besides, a reference library of ^{1}D ^{31}P and ^{1}H-^{31}P HSQC-TOCSY spectra with corresponding chemical assignments was standardized for 38 typical phosphorylated metabolites. Additionally, the influence of pH and temperature was analyzed according to its impact on ^{31}P chemical shifts and peak intensities. They concluded that pH 4 was optimal to collect a ^{31}P spectrum, which corroborates what they had observed before in a report on the assignment of nitrogen-containing metabolites[260]. Due to the sensitivity of chemical shift to pH, they manually verified the pH of each sample. Likewise, they collected 2D ^{1}H-^{31}P HSQC-TOCSY spectra at different temperatures suggesting that higher temperatures

could have an impact on the broadening of peaks and a loss in several ^{1}H-correlations. Consequently, they claimed that 277 K was the suitable temperature to get the best quality 2D correlation experiment. They also used 2 mM of magnesium ion (Mg^{2+}) to assist in ^{31}P chemical shift dispersion, although this was not deemed critical.

Table 5.1. One of the fewest studies[253] about SOPs established.

Parameter	Published
pH	4
Buffer	None
Salt	2 mM Mg^{2+}
Temperature	277 K
Assignment experiment	HSQC-TOCSY

On the other hand, W. Lutz *et.al*[261] undertook a review of the experimental parameters for optimizing the quality of ^{31}P-NMR spectra for phospholipids. Indeed, ^{31}P-NMR spectroscopy has been established as a convenient tool for exhaustive phospholipids analysis[262,263], although challenges have arisen due to issues with reproducibility and robustness.

For systematic optimization, they considered that extract concentration, pH value of the aqueous component of the solvent system as well as the temperature of the measurement of NMR experiment were vital. They used chemical shifts and linewidth changes generated by each of these parameters to optimize them together. Firstly, the optimal temperature range was established between 277 and 297 K. Subsequently, they optimized the extract concentration for phospholipids analysis reporting that the optimal concentration range was obtained by extracting between 100 and 1000 mg tissue. Notably, the dependence of chemical shift on extract concentration was more pronounced for samples with elevated temperatures than it was for samples with low temperatures. Finally, concerning the effect of pH changes, they emphasized the importance of maintaining the pH range close to 7 as phospholipids can be hydrolyzed.

In the context of this thesis, a ^{31}P NMR-based platform has already been introduced for the quantification of 54 phosphometabolites from liver extracts. This platform has proven valuable in monitoring the metabolic response to liver diseases and the effects of drug administration[264]. However, given the inherent limitations of existing ^{31}P-NMR methods, there is a pressing need to develop a robust, quantitative, and reproducible approach that can be widely adopted in phosphoromics.

Despite the potential of ^{31}P-NMR for phosphoromics studies, a significant gap exists in the literature; there are no comprehensive standard operating procedures (SOPs) available. Thus, the primary objective of this Chapter is to bridge this gap by developing SOPs that facilitate fine-tuning of sample measurements. These guidelines aim to enhance the existing ^{31}P-NMR methodologies and provide a reliable and reproducible framework for future phosphoromics research. By doing so, the ambition is to significantly contribute to the standardization and advancement of the phosphoromics field.

5.2 Methods

5.2.1 Chemicals

Tris(hydroxymethyl-d_3)amino-d_2-methane (449105, Tris-d_{11}), Aminoacetic acid (G7126, ≥99%, Glycine), Carbonic acid disodium salt (223530, ≥99.5%, Na_2CO_3), Sodium bicarbonate (S6014, ≥99.7%, $NaHCO_3$), Disodium hydrogen arsenate heptahydrate (A6756, ≥98%, $Na_2HAsO_4.7H_20$), Sodium acetate (S2889, ≥99%, CH_3COONa) were purchased from Sigma Aldrich (Milwaukee, WI).

Paramagnetic relaxation enhancers, 10-[(1SR,2RS)-2,3-dihydroxy-1-hydroxymethylpropyl]-1,4,7,10-tetraazacyclododecane-1,4,7-triacetic acid, gadolinium complex monohydrate (Y0001803, Gadobutrol monohydrate) and [10-(2-Hydroxypropyl)-1,4,7,10-tetraazacyclododecane-1,4,7-triacetato(3-)-N^1,N^4,N^7,N^{10},O^1,O^4,O^7,O^{10}]gadolinium complex monohydrate (1287631, Gadoteridol monohydrate) were also acquired from Sigma Aldrich (Milwaukee, WI) as well as the chelating agent, Ethylenediaminetetraacetic acid (798681, ≥97%, EDTA) and Deuterium oxide (151882, D_2O).

Dimethyl sulfoxide-d_6(151874, DMSO-d_6), Methanol-d_4(151947, CD_3OD), -d_8-Tetrahydrofuran (437727, d_8-THF), Toluene-d_8(471399), Chloroform-d(151823, $CDCl_3$), 1-Hexanol (471402, ≥99%) and Acetone (179124, ≥99.5%) were acquired by Sigma Aldrich (Milwaukee, WI).

L-α-lysophosphatidylcholine (830071, LPC) and L-α phosphatidylcholine (Egg, Chicken, 95%, 131601, PC) were supplied by Avanti (Alabaster, Alabama).

Triethylphosphine oxide(AA3039103, $OPEt_3$), Triphenylphosphine oxide (T84603, 98%, TPPO), Trimethylphosphine oxide (AA3039403, $OPMe_3$) were supplied by Thermo Fisher Scientific. Furthermore, Adenosine 5´-monophosphate disodium salt (01930, AMP), Thymidine 5´-monophosphate disodium salt hydrate (T7004, TMP), α-D-Glucose 1-phosphate dipotassium salt hydrate (G6875, G1P) and L-α-Glycerophosphorylcholine (G5291, GPC) were acquired by Sgima Aldrich (Milwaukee, WI).

5.2.2 Animals and diets

To optimize the experimental conditions of ^{31}P-NMR protocol, eight-month-old males fed by standard diet (C57BL/6J background control mice) were generated as indicated before in Chapter III. Animals were treated humanely, and all procedures followed our institution's guidelines for the use of laboratory animals. At the end of the animal

experiments, livers were collected, cryogenized in liquid nitrogen and stored at -80 ºC until further use.

It is important to note that the use of animal models in research is a critical and sensitive area that requires utmost care and ethical considerations. In our study, we placed paramount importance on ethical adherence and were committed to ensuring that all animals were treated humanely and with dignity.

We followed the principles of the 3Rs - replacement, reduction, and refinement - to limit the use of animals in experiments wherever possible. This means we sought alternatives to animals where we could, used the minimum number of animals necessary to achieve our research objectives, and improved our experimental techniques to minimize potential pain or distress for the animals involved.

All procedures involving animals were conducted according to the guidelines provided by our institution for the use of laboratory animals, with the assurance of providing the best possible care. This included taking steps to ensure their environment was well-managed and stimulating, and that their physiological and psychological well-being was prioritized. Any discomfort or pain was minimized through the appropriate use of anesthetics or analgesics.

5.2.3 Extraction method

~ 100 mg of the liver of each sample was lysed in 774 µL of a mixture of ice-cold chloroform/methanol (40/60 v/v%) and DSS 254 nmol with a tissue homogenizer (Precellys) in 2 x 30 second cycles at 6000 rpm. Subsequently, 554 µL of a mixture of chloroform/water (45/55 v/v%) was added over the homogenate. Next, the solution was left 15 min in dry ice before being centrifugated for 15 min at 14000 rpm at 4 µL. Then, the two phases obtained were separated at first and then, they were evaporated in a speedvac for approximately 3 h.

5.2.4 NMR spectroscopy

All NMR experiments were carried out in a 600 MHz Bruker Avance spectrometer equipped with BBO probehead. Different 1D ^{31}P, 2D ^{1}H-^{31}P HSQC TOCSY and Inversion recovery experiments (InvRec) to measure T_1 relaxation times were carried out. The InvRec pulse sequence comprises two RF pulses separated by a time, τ, by collecting a series of Invrec spectra with increasing values of τ, and phasing the spectra identically, the phase of each signal will invert as τ increases, from this T_1 can be calculated for each signal in the NMR spectrum.

5.2.4.1 NMR data acquisition for optimization of parameters in hydrophilic extract of 100 mg of mice liver

5.2.4.1.1 Chelator

EDTA concentration was evaluated using a hydrophilic extract liver mice sample resuspended with 1 mM of Gadoteridol, TMP^+ and $OPMe_3$ in 600 µL of 50 mM of Glycine (pH = 9.5) in H_2O. The EDTA concentrations used were 0 mM, 1 mM and 2 mM. For 1D ^{31}P experiment, it was conducted at 298 K. The spectra were acquired with 8 scans, 32 dummy scans as well as a 4 second recycle delay. They were collected with a spectral width of 102.90 ppm (25000 Hz) and each 1D ^{31}P spectra was acquired with 24576 data points.

5.2.4.1.2 Buffer

The appropriate buffer was approved by resuspending the hydrophilic extract of liver mice samples in 600 µL of different tentative buffers in H_2O: 50 mM $H_2AsO_4^-$ (pH = 2.2), 50 mM Acetate (pH =4), 50 mM $HAsO_4^{2-}$ (pH = 7), 100 mMTris-d_{11} (pH = 7), 50 mM Glycine (pH = 9.5), 50 mM CO_3^{2-}/HCO_3^-(pH = 10) and 50 mM AsO_4^{3-} (pH = 11). In addition, it was added 1 mM of $OPMe_3$, 1 mM of TMP^+, 2 mM EDTA and 1 mM Gadoteridol (Gdter). ^1D ^{31}P spectrum was taken with 24576 data points. A total of 8 scans and 32 dummy scans were collected with a 4 second interscan delay. They were acquired with a spectral width of 102.90 ppm (25000 Hz). All spectra were collected at 298 K.

5.2.4.1.3 Solvent

Regarding to the choice of suitable solvent, hydrophilic extract of liver mice samples was resuspended in 600 µL of Glycine (pH = 9.5) in D_2O or H_2O in addition to 1 mM of $OPMe_3$, 1 mM TMP^+, 2 mM EDTA and 1 mM Gdter. Each 1D ^{31}P spectrum was collected with a spectral width of 102.90 ppm (25000 Hz) centered at 0 ppm. Both of spectra were acquired with 8 scans, 32 dummy scans and a 4 second recycle delay.

5.2.4.1.4 Paramagnetic Relaxation Enhancer (PRE) type

A mixture of 1 mM of $OPEt_3$, $OPMe_3$, AMP, TMP, G1P and GPC was dissolved in 600 µL of Tris-d_{11} (pH = 7) in H_2O with the aim of choosing the suitable PRE. It was added each PRE (Gadobutrol (Gdbut) or Gdter) at different concentrations (0 mM, 0.5 mM, 1.0 mM and 1.5 mM), respectively. Each 1D ^{31}P spectrum was acquired with 32768 data points and a spectral width of 102 ppm (25000 centered at 0 ppm. A total of 8 scans and 4 dummy scans with a 4 s interscan delay were collected. Likewise, the ^{31}P NMR

measurement was carried out using a standard 90º pulse program with inverse-gated decoupling (zgig). Regarding the InvRec experiment, they were acquired with 8 scans, 16 dummy scans and ^{31}P spectral width of 10.41 ppm (6250 Hz) centered at 0 ppm. All spectra were collected at 298 K.

5.2.4.1.5 Temperature

The effect temperature was analyzed by using different hydrophilic extracts of liver mice samples resuspended in 600 µL of Glycine (pH = 9.5), with 1 mM $OPMe_3$, 1 mM TMP^+ and 2 mM EDTA at different temperatures (278 K, 288 K, 298 K and 308 K). ^{1}D ^{31}P spectrum was taken with 24576 data points. A total of 8 scans and 32 dummy scans were collected with a 4 second interscan delay. They were acquired with a spectral width of 102.90 ppm (25000 Hz).

5.2.4.1.6 Temperature and Gdter concentration dependance

With the aim of evaluating the dependence between the concentration of Gdter and temperature, different hydrophilic extract liver mice samples were resuspended in 600 µL of Glycine (pH = 9.5) in D_20 with 1 mM $OPMe_3$, 1 mM TMP^+ and 2 mM EDTA. Likewise, different concentrations of Gdter were added (0 mM, 0.5 mM and 1 mM) and 1D ^{31}P spectra were collected at different temperatures (278 K, 288 K, 298 K and 308 K). Each 1 D ^{31}P spectra was acquired 8 scans, 32 dummy scans, a 4 second interscan delay with 65536 data points. Meanwhile, each InvRec experiment was collected with 512 scans, 32 dummy scans and 24576 data points as well as ^{31}P spectral width of 85.75 ppm (20833.334) centered at 0 ppm.

5.2.4.1.7 Temperature in the 2D ^{1}H-^{31}P HSQC TOCSY

600 µL of Glycine (pH = 9.5) in D_2O was added with 1 mM $OPMe_3$, 1 mM TMP^+, 2 mM EDTA and 1 mM Gdter in hydrophilic extract of liver mice samples. 2D ^{1}H-^{31}P HSQC TOCSY spectra were acquired with a ^{1}H spectral width of 11.90 ppm (7142.85 Hz) and ^{31}P spectral width of 20 ppm (4848.72 Hz) centered at 0 ppm. The 2D spectra were acquired with 16 scans, 80 dummy scans, a 4 second interscan delay, 4096 points in the ^{1}H dimension and 380 points in the ^{31}P dimension. All spectra were collected at different temperatures (278 K, 288 K, 298 K and 308 K).

5.2.4.2 NMR data acquisition for optimization of parameters in the hydrophobic extract of 100 mg of mice liver

5.2.4.2.1 Buffer

600 µL of different solvents (d_8-Toluene, $CDCl_3$, n-Hexanol, CD_3OD, d_8-THF, Acetone and d_6-DMSO) were resuspended in lipophilic extract of liver mice with 4 mM TPPO. 1D ^{31}P was collected with 8 scans, 32 dummy scans, 5 second interscan delay and 32768 data points.

5.2.4.2.2 Temperature

The effect of the temperature was tested through several lipophilic extracts of liver mice resuspended with 600 µL of d_6-DMSO and 4 mM TPPO. 1D ^{31}P was collected with 8 scans, 32 dummy scans, 5 second interscan delay and 32768 data points. All spectra were collected at different temperatures (298 K, 303 K, 308 K, 313 K, 318 K and 323 K).

5.2.4.2.3 Effect of PRE

The effect of PRE was evaluated in a mixture of 1 mM of LPC and PC by adding 600 µL d_6-DMSO, 4 mM TPPO and different concentrations of Gdter (0 mM, 0.05 mM and 0.5 mM). 1D ^{31}P was collected with 8 scans, 4 dummy scans, 6.3 second interscan delay and 32768 data points. Each InvRec was collected with 16 scans, 8 dummy scans and 16384 data points as well as ^{31}P spectral width of 51.45 ppm (12500 Hz) centered at 0 ppm.

5.2.4.2.3 Effect of temperature in the 2D ^{1}H-^{31}P HSQC TOCSY

600 µL of d_6-DMSO was added with 4 mM TPPO in the hydrophobic extract of liver mice samples. 2D ^{1}H-^{31}P HSQC TOCSY spectra were acquired with a ^{1}H spectral width of 11.90 ppm (7142.85 Hz) and ^{31}P spectral width of 4.3 ppm (1044.62 Hz) centered at 0 ppm. The 2D spectra were acquired with 8 scans, 128 dummy scans, a 5 second interscan delay, 4096 points in the ^{1}H dimension and 320 points in the ^{31}P dimension. The spectra were collected at 310K.

5.3 Results and discussion

For the successful conduction of quantitative phosphoromics studies, samples must be meticulously prepared to avoid bias that may arise from unintentional dephosphorylation of metabolites. Additionally, phosphate ^{31}P NMR signals shift and broaden in function of diverse parameters that must be controlled. These parameters include the solvent, pH, buffer, temperature, type and concentration of paramagnetic relaxation enhancer, reference compound, and the concentration of chelator, among others.

To ensure the maximal intensity-vs-time and spectral dispersion, minimal signal linewidth and background, absolute referencing, and precise quantification of the basic 1D ^{31}P spectrum for phosphoromics, it is essential to consider several sample parameters. These considerations apply to both hydrophilic and lipophilic extracts derived from mouse liver. By adhering to these rigorous sample preparation guidelines, we can effectively increase the reliability and reproducibility of our phosphoromics studies.

5.3.1 SOPs for quantitative ^{31}P NMR analysis in the hydrophilic extract of 100 mg of mice liver

5.3.1.1 Reference compound

^{31}P frequency referencing requires a compound that can provide a sharp, distinct signal with minimal shift dependence on factors such as the solvent, pH, cations and temperature. This criterion discourages the use of phosphorous oxides due to their unpaired electron. In previous studies, TMP^+ chloride was selected, that produced sharp, invariant ^{31}P singlet signal at 22.86 ppm), well separated from most metabolites.

Nevertheless, quantitative referencing requires short T_1 for fast signal recovery. Here, T_1 of TMP^+ was long (9.2 s), requiring further testing of compounds with shorter T_1(^{31}P) for quantitative referencing. Both $OPMe_3$ and $OPEt_3$ were examined and found to have shorter T_1. Nevertheless, $OPEt_3$ generated two signals in ^{1}H (1.82 ppm (q), 1.105 ppm (t)), that could potentially overlap with metabolites present in the liver sample. Moreover, $OPMe_3$ had a smaller ^{31}P offset, minimizing possible offset effects. Hence, the optimal reference compound for quantitative ^{31}P signal integral referencing was $OPMe_3$. However, TMP^+ also remained a viable reference compound due to its minor pH dependence, as summarized in **Table 5.2**.

Table 5.2. Relevant NMR properties of TMP^+, $OPMe_3$ and $OPEt_3$.

	^1H (ppm)	^{31}P (ppm)	$T_1(^{31}P)$ (s)
TMP+	1.790	22.86	10.0
$OPMe_3$	1.586	53.10	5.4
$OPEt_3$	1.82 (q), 1.105 (t)	65.21	4.0

5.3.1.2 Chelator

The negative charge of the phosphate groups can interact with cations, especially divalent cations such as Mg^{2+} or Ca^{2+}, which play a pivotal role in many fundamental biochemical processes. For instance, it has been demonstrated that Mg^{2+} ions are responsible for modulating nucleic acid structures[265]. Moreover, they are crucial in the catalytic activity of ribozymes[266]. Meanwhile, calcium ions are associated with the interaction of phospholipid membranes with proteins, and the formation of calcium-phosphate structures is vital for bone mineralization[267]. Due to the interaction between phosphorous and cations, ^{31}P signal shifts and linewidths (chemical/conformational exchange broadening) could be affected. This issue is particularly relevant for multivalent metal cations; hence, their addition must be avoided.

To mitigate ^{31}P signal shift and broaden detrimental effects, cations present in hydrophilic extract should be neutralized by a chelating agent. According to previous research[268], EDTA is an excellent chelating agent. EDTA consists of four carboxylic acid groups and two amine groups with an unshared pair of valence electrons, allowing interaction with a single ion at a total of six positions[269]. It forms stable transition metal complexes and metal group ions chelate in solutions at different pH levels[270].

Hence, the effect of EDTA as a chelating agent was evaluated. To simplify this analysis, the four most characteristic regions of a representative ^{31}P-NMR spectrum, corresponding to a hydrophilic extract of a mouse liver sample, were analyzed. These regions included monophosphates (R´-O-P-O_2-O-R´), diphosphodiesters (H-O-PO_2-O-P´-O_2-O-R´), ortodiphosphodiesters (R-O-PO_2-O-P´-O_2-O-R) and P-β in nucleoside triphosphates (NTP). Three different concentrations of EDTA were tested: 0 mM, 1 mM and 2 mM (**Figure 5.1**). The results revealed that maximal ^{31}P signal intensities were achieved with 1 mM of EDTA, most notably in diphosphodiesters, ortophosphodiesters and P-β in NTP although it was observed in monophosphates as well. Nevertheless, particularly P-β in NTP and phosphodiesters signals still shifted slightly upon increasing the EDTA concentration to 2 mM, indicating further cation sequestration. Thus, to ensure

sufficient capacity for cation capture, for addition of 2 mM EDTA was chosen. Given those divalent cations (like Mg^{2+}, Ca^{2+}, Zn^{2+}) may also catalyze phosphoester hydrolysis, their sequestration by EDTA aids in stabilizing the phosphometabolites.

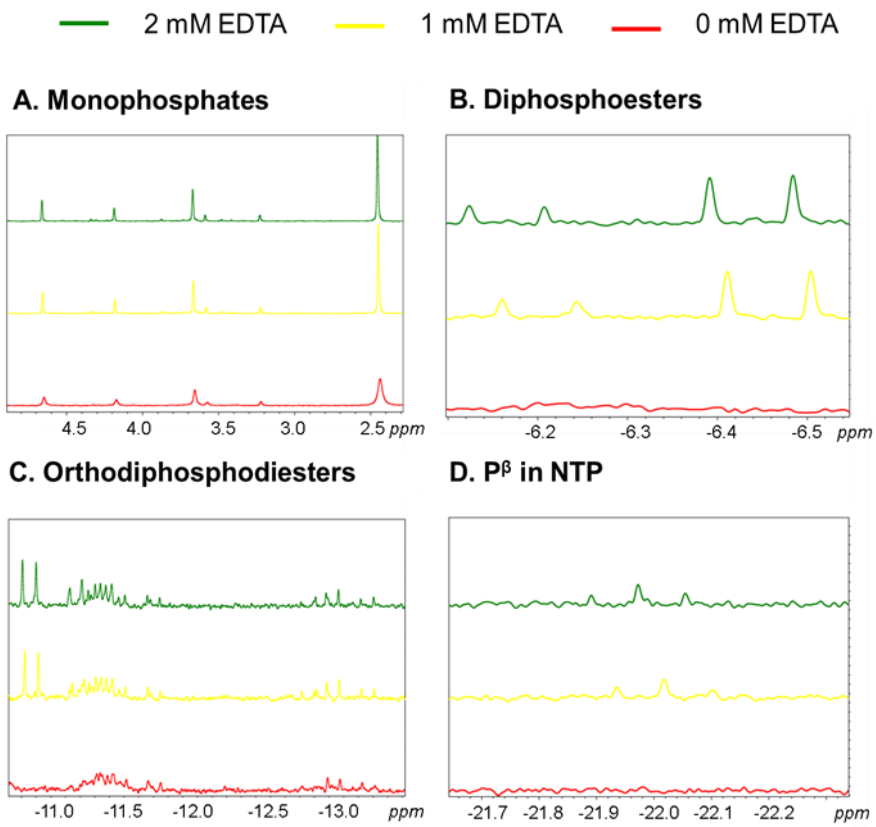

Figure 5.1. ^{31}P-NMR spectrum of mouse liver at different EDTA concentrations (from bottom to top) at the four most representative regions of ^{31}P-NMR spectra. Red: EDTA 0 mM, Yellow: 1 mM EDTA , Green: 2 mM EDTA. The most representative regions of ^{31}P-NMR spectra were shown: A) Monophosphates, B) Diphosphodiesthers, C) Orthodiphosphodiesters and D) P-β in NTP.

5.3.1.3 Buffer

The correct choice of buffer in phosphoromic studies is critical, as it should not contain phosphorous to avoid any ^{31}P signal background. Thus, phosphate buffer (PBS) is discouraged in phosphoromics studies in addition to adding an intense ^{31}P NMR background signal that obscures inherent phosphate and may bias further nearby ^{31}P signal integrals. Therefore, the effect of different buffer at different pH levels was evaluated: $H_2AsO_4^-$ (pH = 2.2), Acetate (pH =4), $HAsO_4^{2-}$ (pH = 7), Tris-d_{11} (pH = 7), Glycine (pH = 9.5), CO_3^{2-}/HCO_3^-(pH = 10) and AsO_4^{3-} (pH = 11) (**Figure 5.2**). This selection covers most of the pH range.

Overall, phosphometabolite ^{31}P signal intensities and dispersion increase with pH, favoring moderately basic conditions. Most notably, ^{31}P signals around -6.5 ppm (doublets, diphosphodiester region) and -22 ppm (triplets, from P-β in NTP) were only observed at basic pH >7. At extreme (acid or basic) pH, the stability of phosphometabolites decreased rapidly (due to fast phosphoester hydrolysis) compromising their detection and quantification. Indeed, it was observed irreversible ^{31}P NMR spectral changes (from fragmentation and signal coalescence) in arsenate buffer at both the highest (pH = 11.5) and lowest (pH = 2) buffer pH. Likewise, CO_3^{2-}/HCO_3^- buffer does not add any ^1H signals, although it is a high-conductivity and consequently, yields a 5% longer p90(^1H) reference pulse of 12.25 µs (at 50 W).

Conversely, Glycine is a low-conductivity buffer with minimal B_{RF} losses, as confirmed by its shortest ^1H pulses. Moreover, overall metabolite stability appears sufficiently high at pH 9.5. At high pH, the capacity of EDTA to complex cations is significantly increased due to its deprotonation. This, coupled with the larger OH^- concentration at high pH, reduces the concentration of free cations that might detrimentally interact with phosphate groups. Consequently, 50 mM of Glycine buffer at pH 9.5 was identified as the optimal choice.

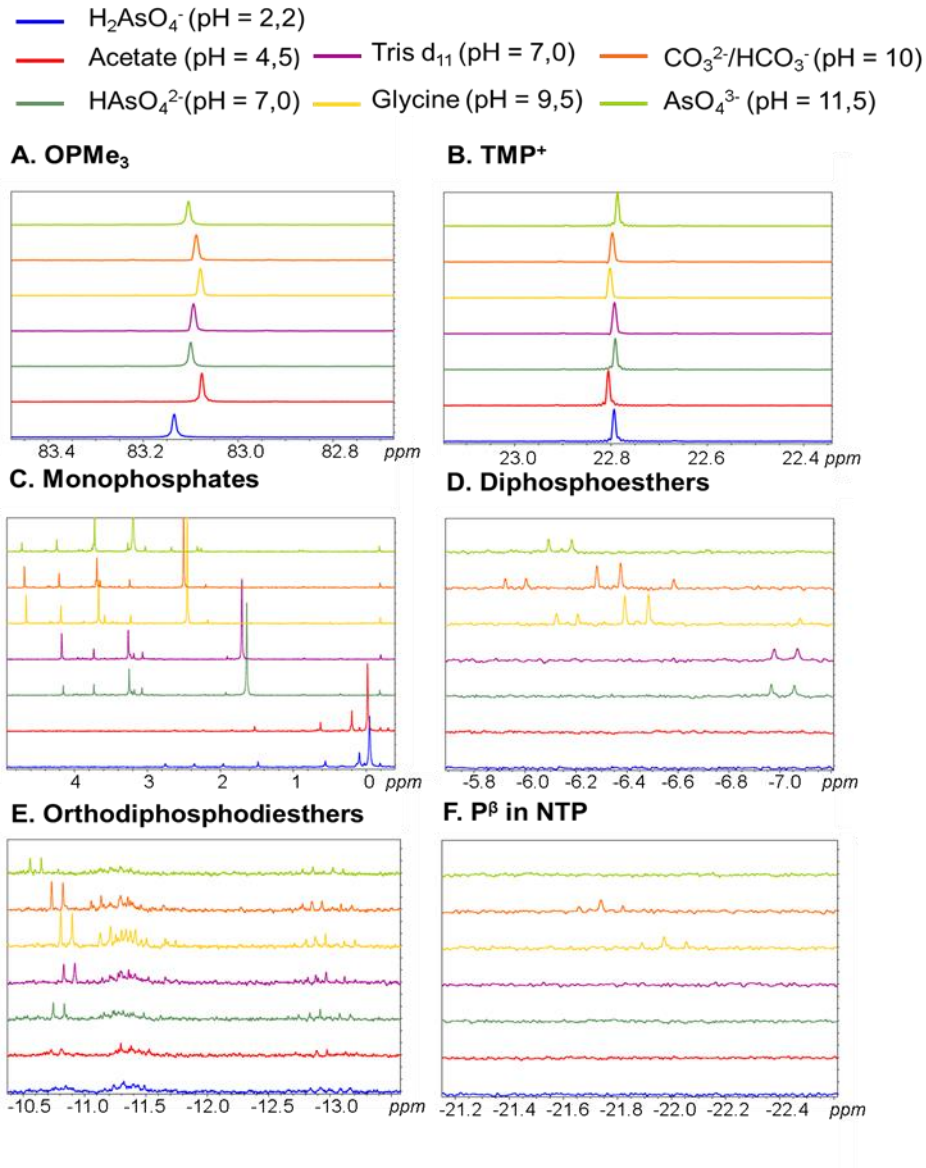

Figure 5.2. ^{31}P NMR spectrum of mouse liver in different buffers with increasing pH (from bottom to top). Blue: $H_2AsO_4^-$ pH = 2.2 (50 mM). Red: Acetate pH = 4.5 (50 mM). Dark green: $HAsO_4^{2-}$ pH = 7.0 (50 mM). Purple: Tris-d_{11} pH = 7.0 (100 mM). Yellow: Glycine pH = 9.5 (50 mM). Orange:CO_3^{2-}/HCO_3^- pH = 10 (50 mM). Bright green: AsO_4^{3-} pH = 11.5 (50 mM). The most representative regions of ^{31}P-NMR spectra were shown: A) $OPMe_3$, B) TMP^+, C) Monophosphates, D) Diphosphoesthers, E) Orthophosphodiesters and F) P-β in NTP.

Thus, with the newly optimized buffer in place, the most characteristic and resolved ^{31}P peaks were assigned similarly to the report in Chapter 3. These assignments were then used to optimize the remaining experimental conditions, as illustrated in **Figure 5.3** and **Table 5.3**.

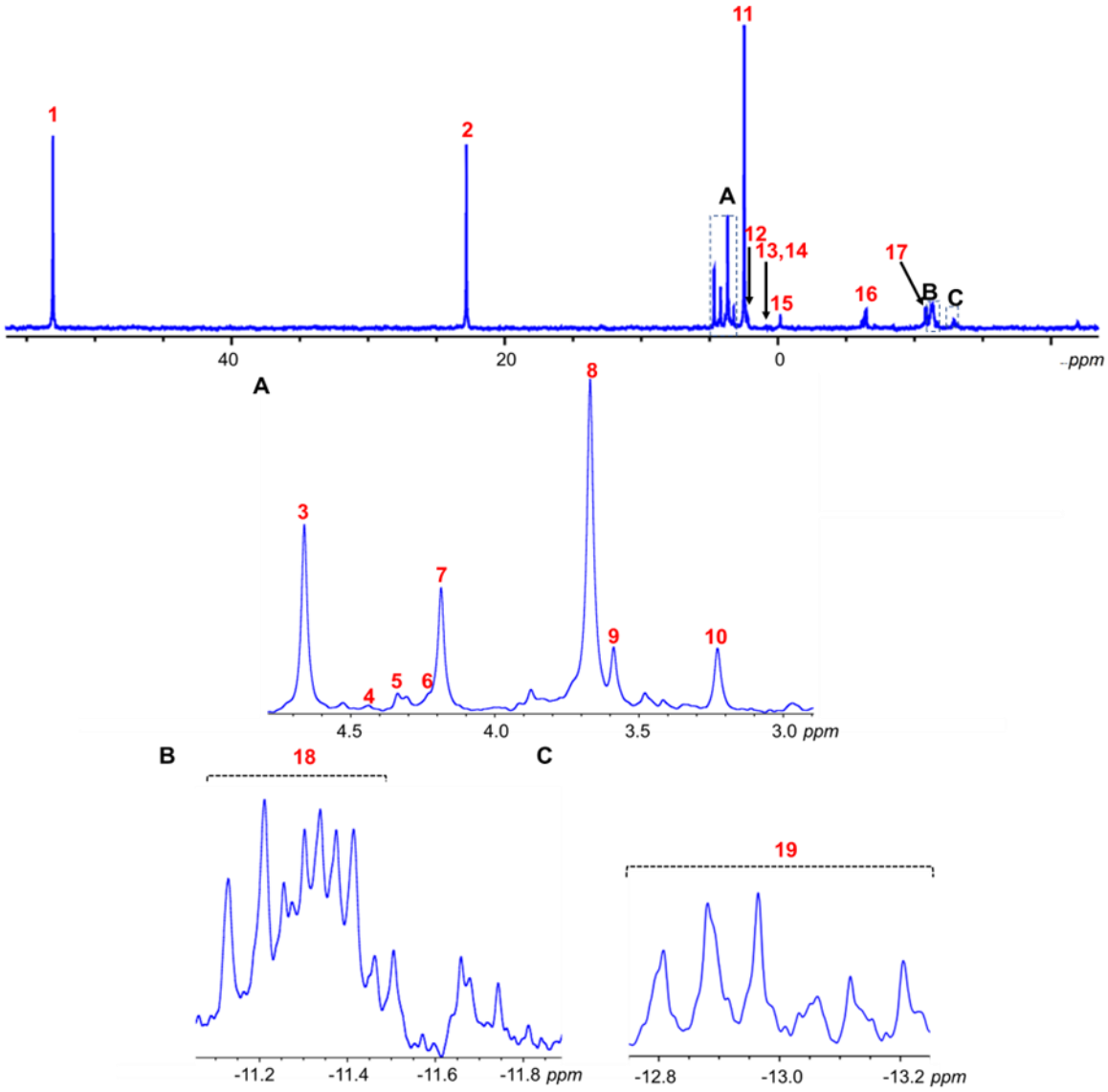

Figure 5.3. ^{31}P-NMR spectroscopy of hydrophilic mice liver extract, enlarging three spectral regions indicated with A, B and C.

Table 5.3. A total of 19 different peaks with the corresponding chemical shifts were used to enhance ^{31}P-NMR methodology protocol.

Peak	Abbreviation	Compound	Chemical shift (ppm)
1	$OPMe_3$	Trimethylphosphine oxide	53.09
2	TMP^+	Tetramethyl phosphonium chloride	22.80
3	G6P	Glucose 6-phosphate	4.66
4	6PG	6-Phosphogluconate	4.43
5	X5P	Xylulose 5-phosphate	4.34
6	FBP	Fructose 1,6-bisphosphate	4.23
7	S7P	Sedoheptulose 7-phosphate	4.19
8	NMP	Nucleoside monophosphates	3.67
9	F6P	Fructose 6-phosphate	3.59
10	PCH	Phosphocholine	3.23
11	PO_4^{3-}	Inorganic phosphate	2.46
12	G1P	Glucose 1-phosphate	2.17
13	NADPH	Nicotinamide adenine dinucleotide phosphate reduced form	0.86
14	GPE	Glycerophosphoethanolamine	0.49
15	GPC	Glycerophosphocholine	0.19
16	NDP(Pβ)	Nucleoside diphosphates (Pβ)	-6.39/-6.48
17	NDP(Pα)	Nucleoside diphosphates (Pα)	-10.80/-10.90
18	NDPS(Pα)	Nucleoside diphospho sugars (Pα)	-11.13/-11.50
19	NDPS(Pβ)	Nucleoside diphospho sugars (Pβ)	-12.71/-13.20

5.3.1.4 Solvent

Relative to H_2O, D_2O demonstrated a reduction in signal intensity for NADPH and GPE, whereas an increase in intensity signal was observed for X5P and FBP (**Table 5.4**). In general, for ^{31}P observed NMR, as primarily used in this phosphoromics approach, the use of H_2O or D_2O makes no difference according to the linewidth values obtained in each of the phosphometabolites (**Figure 5.4**). However, in pure D_2O, suppression of residual H_2O signal is unproblematic and robust (even on cryoprobes and at high B_0), facilitating any ^{1}H detected experiments (including 2D ^{1}H, ^{31}P correlation experiments required for phosphometabolite identification). Alongside, H_2O produces less sample heating and the more intense ^{2}H signal improves the lock and lock level-based shimming performance. Consequently, D_2O was preferred over H_2O as a solvent in ^{31}P-NMR methodology optimized.

Table 5.4. Intensity values of the most representative phosphometabolites in D_2O and H_2O as well as the *ratio* of the intensity values between them. There were no differences regarding the intensities between the phosphometabolites in H_2O and D_2O, except in those which have a *ratio* more or less than 1.20 or 0.80 which are marked in red.

Metabolite	Intensity (D_2O)	Intensity (H_2O)	Ratio(D_2O/H_2O)
$OPMe_3$	15033760	15185403	0,99
TMP^+	21706622	22765524	0,95
G6P	1137085	1175039	0,97
6PG	179469	157487	1,14
X5P	109808	85699	1,28
S7P	1091954	1097022	0,99
FBP	99255	82073	1,21
NMP	3038481	2801767	1,09
F6P	594038	633738	0,94
PCHO	300549	253198	1,19
PO_4^{3-}	10764526	9582230	1,12
G1P	366914	343127	1,07
NADPH	84943	110189	0,77
GPE	80411	119011	0,68
GPC	489381	470810	1,04
NDP(Pβ)	448022	431582	1,04
NDP(Pα)	441129	444447	0,99
NDPS(Pα)	154311	128148	1,20
NDPS(Pβ)	94816	100214	0,94

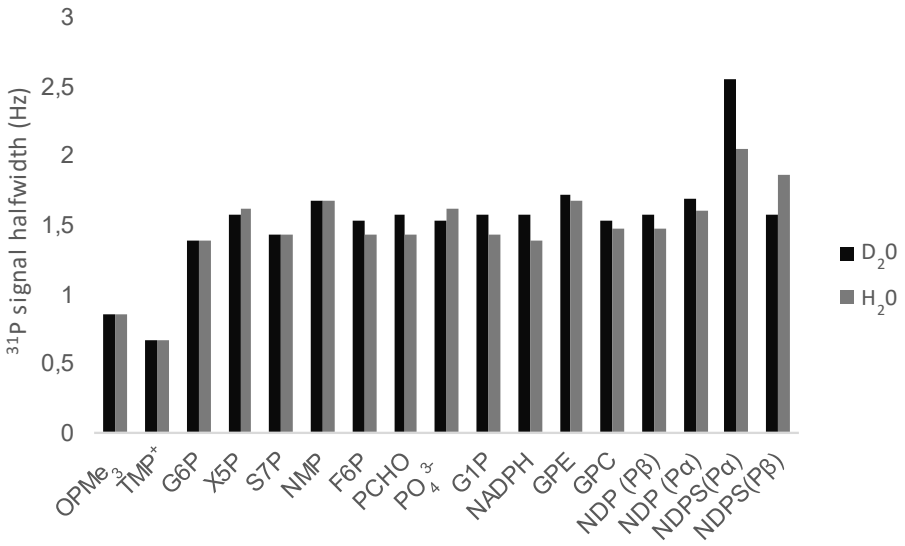

Figure 5.4. Linewidth values of the most representative phosphometabolites in D_2O and H_2O. There were no differences regarding the intensities between the phosphometabolites in H_2O and D_2O.

5.3.1.5 PRE type

The enthalpic $T_1(^{31}P)$ relaxation time limits the total interscan delay τ for exact quantification ($\tau_{quant} > 3.T_{1,max}(^{31}P)$) and maximal signal-to-noise per unit time ($SN_{max} \sim 1/\sqrt{\tau_{opt}}$ at $\tau_{opt} \sim 1.25.T_1(^{31}P)$). Hence, either significant sensitivity or experiment time can be gained by accelerating T_1 through the addition of a suitable PRE agent. However, the PRE agent must not substantially shorten T_2.

T_2, also known as spin-spin relaxation, involves the relative orientations of the spin and contributes to the broadening of spectral lines, a phenomenon that should be avoided for proper quantification of the metabolites. The definitions of T_1 and T_2 relaxation are summarized in **Table 5.5**.

Table 5.5. Definitions T_1 and T_2 relaxation

T_1 relaxation, also known as the *longitudinal relaxation time*, refers to the time for the spins to realign along the longitudinal (z)-axis. It is also termed the *spin-lattice relaxation time,* representing the duration required for the spins to dissipate the energy they absorbed from the radio frequency (RF) to the surrounding lattice, thereby recovering their equilibrium state. After the 90 º pulse, the magnetization within the x-y plane oscillates around the z-axis, with all nuclear spins rotating in phase (**Figure 5.5A**). Likewise, once have been flipped 90 º into the x-y plane, the RF pulse is turned off and consequently, the spins then revert to their lowest energy state and gradually lose their coherence (**Figure 5.5B**).

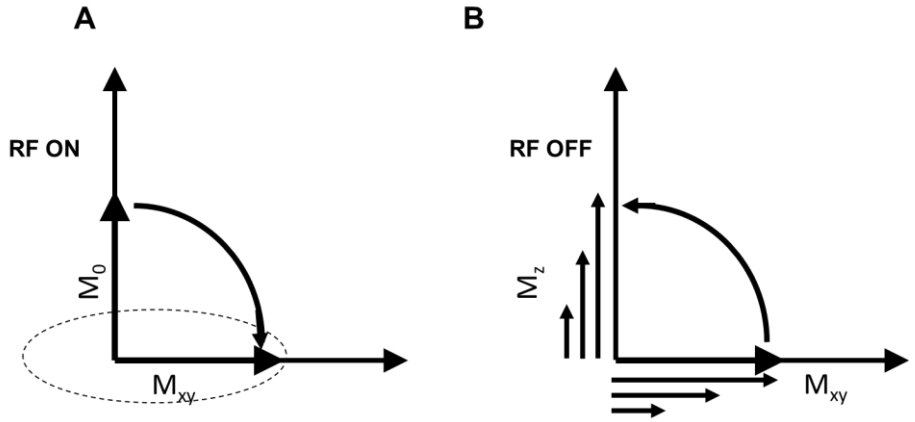

Figure 5.5. T_1 relaxation time. A) After the RF pulse, the longitudinal magnetization vector is flipped into the s-y plane. B) Once the RF is turned off, the transverse magnetization vector begins to decay while the longitudinal component begins to recover.

T_2 relaxation, also called *transverse relaxation*, quantifies the rate at which the magnetization decays within the xy plane. This process occurs concurrently, yet independently, of the recovery of longitudinal magnetization (**Figure 5.6**).

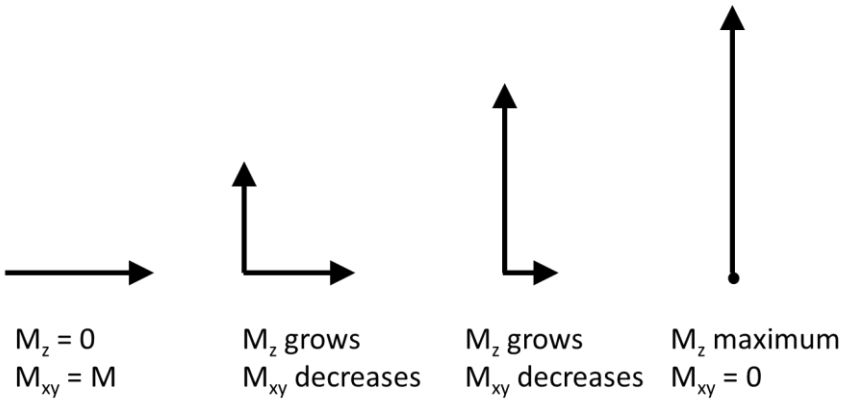

Figure 5.6. The recovery of longitudinal magnetization and the decay of transverse magnetization are independent processes of each other with the RF off.

T_2 is related to the linewidth at half-height ($\Delta\nu_{1/2}$) of the NMR signal, following the **Equation 5.1**.

$$T_2 \sim 1/\Delta\nu_{1/2}$$

Equation 5.1. T_2 or transverse relaxation is inversely proportional to the linewidth at half-height.

Reflecting on our purpose to reduce $T_1(^{31}P)$ without significantly impacting $T_2(^{31}P)$, low concentrations of stable Gd^{3+} complexes like Gdter or Gdbut were used. Previous research[271] has demonstrated that the addition of a small amount of paramagnetic gadolinium chelate could drastically reduce T_1 relaxation time of chemical compounds, thereby accelerating sample measurement time and enhancing the efficiency of quantitative-NMR.

The effects of Gdbut are notably pronounced for more polar phosphometabolites such as AMP and G1P. T_1 of these metabolites was reduced due to the addition of Gdbut compared to Gdter (**Figure 5.7**). Nevertheless, at the same time, ^{31}P signal halfwidth, the peak width at half height, was much larger in Gdbut causing signal broadening (T_2) which is undesirable (**Figure 5.8**). With the aim of reaching a compromise between T_2 and T_1, Gdter, which is less polar than Gdbut, appeared to be the preferable choice. This is due to its weaker interaction with polar phosphometabolites in addition to having a weaker spread of T_1 and line broadening, having a more homogeneous effect as PRE.

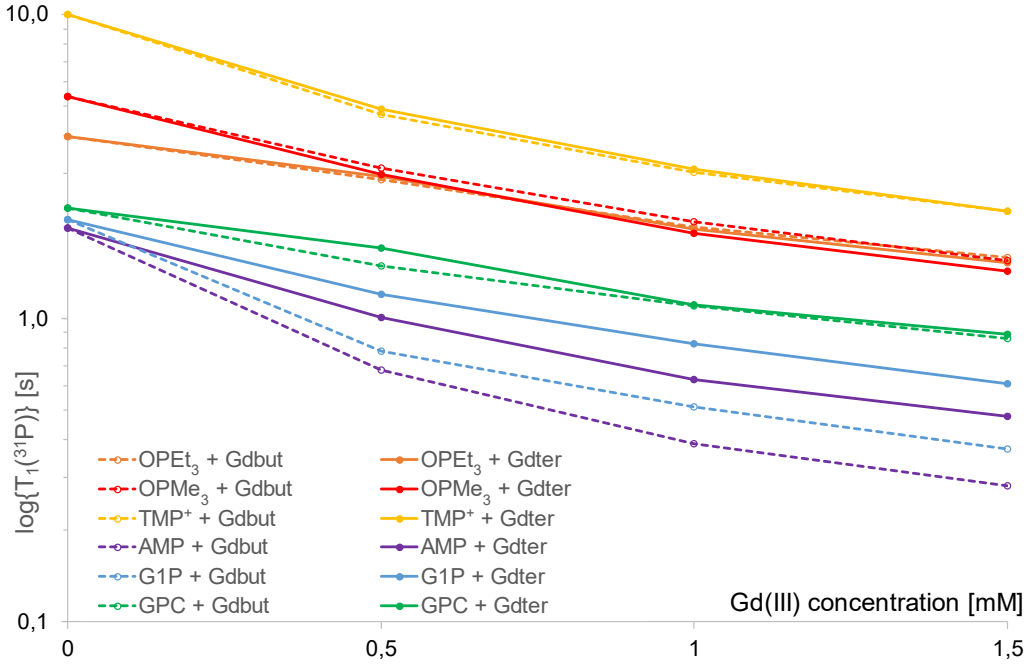

Figure 5.7. Log(T_1) of a standard mixture of phosphometabolites at different concentrations of Gdbut or Gdter (0 mM, 0.5 mM, 1 mM, 1.5 mM). It was observed that the higher concentration of the paramagnetic relaxation enhancer , the lower T_1 of each metabolite is. Abbreviations: TMP, Thymidine 5´-monophosphate; AMP, Adenosine 5´-monophosphate.

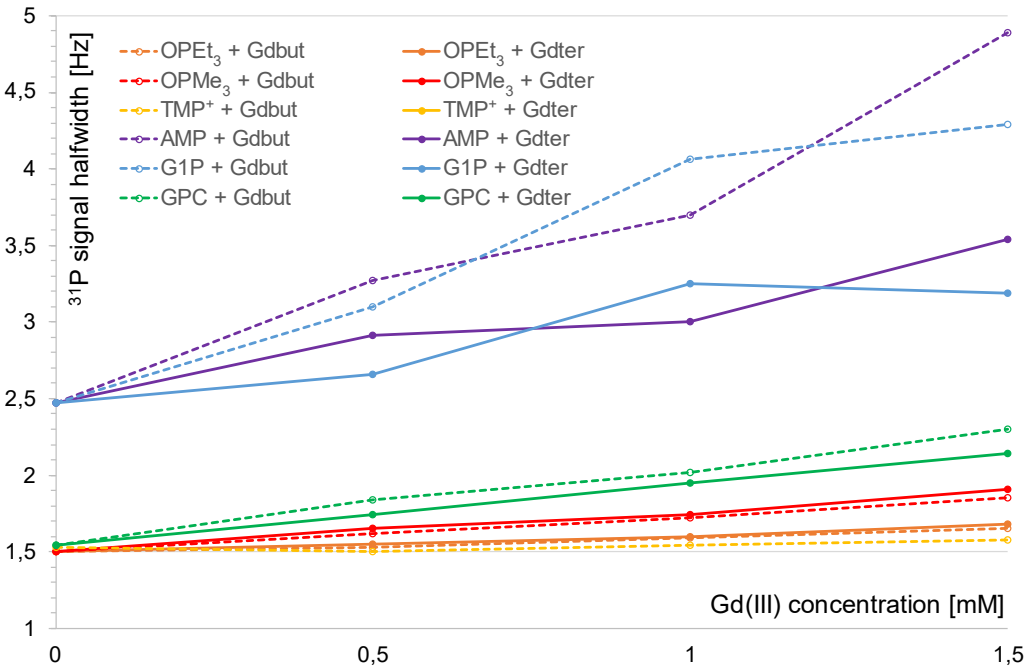

Figure 5.8. ^{31}P signal halfwidth of a standard mixture of phosphometabolites at different concentrations Gdbut or Gdter (0 mM, 0.5 mM, 1 mM, 1.5 mM). It was observed that the lower linewidths are observed in general terms in Gdter. Abbreviations: TMP, Thymidine 5´-monophosphate; AMP, Adenosine 5´-monophosphate.

5.3.1.6 Temperature

The temperature-dependent T_1 times for a mouse liver sample were recorded in a buffer composed of 50 mM of Glycine pD 9.5, with and without 2 mM of Gdter. **Tables 5.6-5.9** summarize the data, listing the ^{31}P chemical shifts vs temperature, T_1 vs temperature, halfwidth(^{31}P) vs temperature and signal intensity vs temperature.

Notably, the ^{31}P chemical shifts, T_1, halfwidth and signal intensity of phosphometabolites changed with the temperature. In fact, for all phosphometabolites, with a decrease in temperature, T_1 and halfwidth of the majority of metabolites were reduced whereas signal intensity was increased. Likewise, TMP^+ stood out as a perfect ^{31}P reference as neither its ^{31}P chemical shift nor its T_1 time depended (much) on the temperature. However, T_1 of some phosphometabolites (especially G6P, S7P or PCHO and inorganic phosphate, among others) were exceedingly long. Consequently, PRE should be added to shorten the exceptionally long T_1 to a reasonable maximum. Overall, its low temperatures produced the highest quality ^{31}P-NMR spectra. However, it was vital to evaluate the PRE effect to confirm this statement.

Table 5.6. Chemical shift of the most representative phosphorylated metabolites of a mice liver sample at different temperatures (278 K, 288 K, 298 K and 308 K) It was observed that the lower temperature, the lower T_1 of each metabolite is.

Chemical shift ^{31}P vs T(K)	**278 K**	**288 K**	**298 K**	**308 K**
$OPMe_3$	53,35	53,22	53,08	52,91
TMP^+	22,90	22,87	22,85	22,84
G6P	4,52	4,68	4,83	4,97
6PG	4,33	4,48	4,63	4,76
X5P	4,23	4,38	4,53	4,67
FBP	4,10	4,26	4,41	4,55
S7P	4,05	4,21	4,36	4,51
NMP	3,53	3,69	3,85	3,99
F6P	3,44	3,60	3,76	3,91
PCHO	3,08	3,25	3,41	3,57
PO_4^{3-}	2,28	2,45	2,60	2,75
G1P	2,08	2,22	2,35	2,47
NADPH	0,73	0,84	0,94	1,04
GPE	0,29	0,40	0,52	0,63
GPC	-0,34	-0,23	-0,12	0,00
NDP(Pβ)	-6,61	-6,42	-6,24	-6,07
NDP(Pα)	-11,03	-10,89	-10,76	-10,62

NDPS(Pα)	-11,45	-11,34	-11,22	-11,12
NDPS(Pβ)	-13,05	-12,95	-12,86	-12,76

Table 5.7. $T_1(^{31}P)$ values of the most representative phosphorylated metabolites of a mice liver sample at different temperatures (278 K, 288 K, 298 K and 308 K) It was observed that the lower temperature, the lower T_1 of each metabolite is.

T_1(31P) (ms) vs T(K)	**278 K**	**288 K**	**298 K**	**308 K**
$OPMe_3$	4000	4700	5800	6800
TMP^+	9750	9620	9870	9640
G6P	6400	12000	14750	18000
6PG	2350	5500	6000	9500
X5P	2080	3150	3500	5400
FBP	1950	3700	4200	5000
S7P	3200	4850	6100	8200
NMP	1610	2350	3020	3730
F6P	1630	2440	3120	3870
PCHO	3020	4600	6080	8000
PO_4^{3-}	8900	14200	18500	24670
G1P	2090	3100	3550	4500
NADPH	900	1350	1500	2100
GPE	1430	1550	2950	2900
GPC	1150	1850	2600	3150
NDP(Pβ)	1382,5	2025	2500	3350
NDP(Pα)	705	1025	1350	1562,5
NDPS(Pα)	447,5	622,5	850	1062,5
NDPS(Pβ)	415	575	815	925

Table 5.8. Linewidth values of the most representative phosphorylated metabolites of a mice liver sample at different temperatures (278 K, 288 K, 298 K and 308 K) It was observed that the lower temperature, the lower linewidth of each metabolite is.

Halfwidth (Hz) vs T(K)	**278 K**	**288 K**	**298 K**	**308 K**
$OPMe_3$	0,5563	0,6358	0,7947	0,9536
TMP^+	0,596	0,6755	0,8742	1,0729
G6P	1,1524	1,1921	1,2716	1,3511
6PG	1,2318	0,9934	1,2318	1,4702
X5P	1,0729	1,351	1,3113	1,2716
FBP	1,1524	1,1524	1,3908	1,6292
S7P	1,1921	1,1524	1,3908	1,6292
NMP	1,2716	1,351	1,3908	1,4306

F6P	1,2716	1,2716	1,4702	1,6688
PCHO	1,1921	1,2318	1,351	1,4702
PO_4^{3-}	0,7947	0,9537	1,1126	1,2715
G1P	1,2318	1,3113	1,2318	1,1523
NADPH	1,2318	1,3908	1,1524	0,914
GPE	1,2318	1,0729	1,4305	1,7881
GPC	1,2318	1,2716	1,4702	1,6688
NDP(Pβ)	1,3113	1,2716	1,3709	1,4702
NDP(Pα)	1,41065	1,41065	1,808	2,20535
NDPS(Pα)	1,96695	2,02655	1,7484	1,47025
NDPS(Pβ)	1,9272	1,94705	1,6292	1,31135

Table 5.9. Intensity values of the most representative phosphorylated metabolites of a mice liver sample at different temperatures (278 K, 288 K, 298 K and 308 K) It was observed that the lower temperature, the higher intensity of each metabolite is.

Intensity vs T(K)	**278 K**	**288 K**	**298 K**	**308 K**
$OPMe_3$	21349754	15764098	10461476	2918921
TMP^+	14393083	11058651	7839446	2463315
G6P	970554,4	790451,1	605693,7	199752,3
6PG	65935,44	111060,9	61989,41	37391,52
X5P	201906,6	152323	132952,8	70090,8
FBP	137066,8	164945,7	111700,2	53133,48
S7P	471354,9	412925	318211,4	124048,1
NMP	4735023	4414158	3777951	1567146
F6P	649444	623882,5	485468,7	215944
PCHO	1333874	1192055	929567,5	359927,1
PO_4^{3-}	21629724	15242957	10453235	3327601
G1P	328708,1	350045,3	253230,8	98144,99
NADPH	76674,88	92628,03	105183,9	35061,95
GPE	145029,2	156027,4	99816,25	39749,32
GPC	523361,9	499010,3	400722	184010,1
NDP(Pβ)	355590,6	347668,5	297462,8	134068,7
NDP(Pα)	327220,2	359210,5	298766,4	138883,1
NDPS(Pα)	185634,1	185099,9	163303,2	81705,07
NDPS(Pβ)	143213,9	130506,1	153044,2	73177,78

5.3.1.7 Temperature and Gdter concentration dependence

As previously discussed, achieving the appropriate balance between the amount of Gdter required and the chosen temperature is crucial. To meet this objective, three different concentrations of Gdter (0 mM, 0.5 mM and 1 mM) at four different temperatures

(278 K, 288 K, 298 K, 308 K) were tested. $T_1(^{31}P)$ and signal intensities for the most representative phosphometabolites at different experimental conditions are shown in **Figure 5S1-5S9**.

G6P showed the longest T_1 among all phosphometabolites. In the absence of Gdter, the T_1 of G6P was prohibitively long. It shortens significantly at 0.5 mM Gdter, but it remained above 2 s at all temperatures. Finally, at 1 mM Gdter and lower temperature, the time limiting T_1 of G6P was acceptably short (< 1.5 s) (**Table 5.10)**.

Table 5.10. T_1 values of Glucose 6-phosphate (G6P), the phosphometabolite that takes the longest T_1 to be fully relaxed, at different concentrations of Gdter (0 mM, 0.5 mM and 1 mM) and temperatures (278 K, 288 K, 298 K and 308 K).

Maximal $T_1(^{31}P)$ (ms) vs T (K) G6P	0 mM Gdter	0.5 mM Gdter	1 mM Gdter
278	6400	1935	1170
288	12000	2340	1340
298	14750	2850	1590
308	18000	3000	1750

Conversely, the NDPS(P-β) region presented the shortest T_1, although a longer T_1 would have been prepared, given that a significant amount of time was misspend due to the long d_1 dictated by the maximal T_1 of G6P. Consequently, a lesser amount of Gdter and a higher temperature were deemed preferable.

Overall, the amount of Gdter required decreases with decreasing temperature, as the natural T_1 is generally shortest at low temperatures (**Table 5.11**). In addition, T_1 was reduced at increasing Gdter concentration (**Table 5.11**). Therefore, taking into consideration only this parameter, the temperature chosen and the Gdter amount would be 278 K and 1 mM, respectively.

Table 5.11. $T_1(^{31}P)$ average values of the most representative phosphometabolites identified and quantified, at different concentrations of Gdter (0, 0.5 and 1 mM) and temperatures (278 K, 288 K, 298 K and 308 K).

Average $T_1(^{31}P)$ (ms) vs T (K)	0 mM Gdter	0.5 mM Gdter	1 mM Gdter
278	1691	930	634
288	2749	1169	776
298	3424	1383	911
308	4398	1533	1031

Unfortunately, as it has been explained before, together with a decrease of T_1, shortened transverse relaxation or T_2 can cause dramatic line broadening in ^{31}P signal of the metabolites at the highest Gdter amount and temperature. One way to indirectly examine T_2 was via signal intensity (**Table 5.12**). It was noted that maximal intensity was reached

around 278 K without Gdter. Nevertheless, if the desired effect of T_1 (reduced at a higher Gdter amount) and the undesirable effect of T_2 (reduced causing line broadening) were balanced, an intermediate compromise could be reached. This led to the conclusion that an optimal scenario involved 0.5 mM Gdter at a temperature of 288 K.

Table 5.12. Intensity (^{31}P) average values of the most representative phosphometabolites identified and quantified, at different concentrations of Gdter (0 mM, 0.5 mM and 1 mM) and temperatures (278 K, 288 K, 298 K and 308 K).

Average intensity (^{31}P) vs T (K)	0 mM Gdter	0.5 mM Gdter	1 mM Gdter
278	560186	469870	381061
288	527564	493480	406864
298	437310	462185	394713
308	441122	433323	357843

4.3.1.8 D_1 for quantitative ^{31}P NMR

D_1 is the delay time before the excitation pulse is applied and it is referred to as the "relaxation delay", in other words, the total amount of time it is given nuclear spins to fully relax before being pulsed again. Therefore, it was a limiting parameter for quantitative ^{31}P-NMR analysis that it was vital to optimize, being the total interscan delay for exact quantification $d_1 > 3.T_{1,max}$ (^{31}P) and maximal signal-to-noise ($SN_{max} \sim 1/\sqrt{d_1}$ at $d_1 = 1.25.T_1(^{31}P)$).

Thus, considering that the optimized amount of Gdter was 0.5 mM at 288 K, for ≥ 95% recovery of the slowest relaxing species such as G6P and the reference for quantification, $OPMe_3$, the required relaxation delay should be D_1 = 7.0 s (**Table 5.13**).

D_1 (s) for >95% ^{31}P recovery	0 mM Gdter	0.5 mM Gdter	1 mM Gdter
278	19.2	5.8	3.5
288	35.9	7.0	4.0
298	44.2	8.5	4.8
308	53.9	9.0	5.2

Table 5.13. Interscan delay assuming 5% error from residual saturation having been optimized taking into consideration the slowest relaxing species, G6P.

Likewise, some simulations have been done to assess the final D_1 for quantitative ^{31}P NMR analysis. Hence, a simulation for the slowest (G6P) and fastest (NDPS (P-β)) relaxing species found under standard conditions (600 MHz, 288 K, 0.5 mM Gdter, 2 mM EDTA, 50 mM Glycine buffer pD 9.5) assuming a minimal single-scan signal-to-noise (SN_0 = 1.1 or 2) and six hours of total experiment time (**Figure 5.9**).

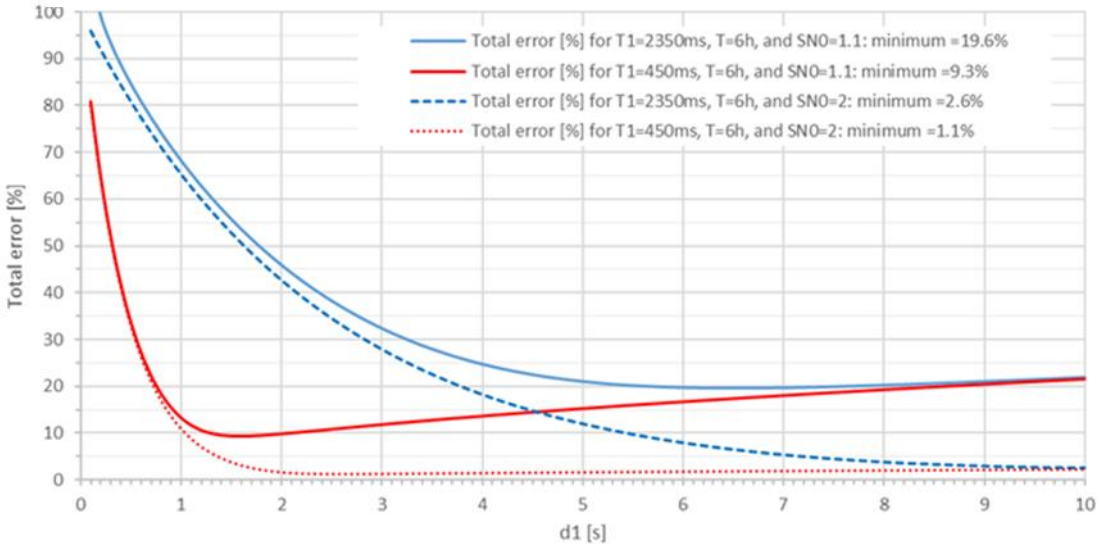

Figure 5.9. Simulation of the total quantification error vs. D_1 from slowest and fastest relaxing species at standard conditions (600 MHz, 288 K, 0.5 mM Gdter, 2mM EDTA, 50 mM Glycine (pH = 9.5), with a minimal single-scan signal-to-noise SN_0 = 1.1 or 2 at 6 hours of total experiment time).

Under these conditions of signal-to-noise, if the slowest relaxing species (G6P) had the lower SN_0, there was no time misspend for the slowest species when it was pulsed at D_1 = 7s, being the quantification error marginal and unchanged.

However, if the fastest relaxing species had the lower SN_0, a large amount of time is misspend then for this species and consequently, its quantification error increased massively. In this situation, D_1 should be shortened. Given that most of the time, the signal intensity of NDPS-Pβ was lower than G6P one, d_1 was shortened to 6 seconds.

5.3.1.9 Temperature in the 2D ^{1}H,^{31}P HSQMBC-TOCSY

Organic phosphate groups exhibit low ^{31}P signal dispersion due to their similar local chemical environment. Therefore, they require correlation with neighboring stable protons for spectral separation and molecular assignment. For this reason, 2D ^{1}H,^{31}P HSQMBC-TOCSY have been optimized. However, accelerated T_2(^{1}H,^{31}P) due to the effect of Gdter at 288 K, caused line broadening, especially in ^{1}H. These hampers efficient ^{1}H,^{31}P coherence transfer. Consequently, this 2D ^{31}P-NMR experiment lost long-range correlations which are critical for metabolite recognition and assignment. Under these conditions, its sensitivity was reduced, especially losing ^{1}H-^{31}P correlations for NDPS region.

By increasing the temperature, a significant reduction in ^{1}H relaxation was observed, leading to an improvement in ^{1}H-^{31}P correlations for NDPS region (**Figure 5.10**).

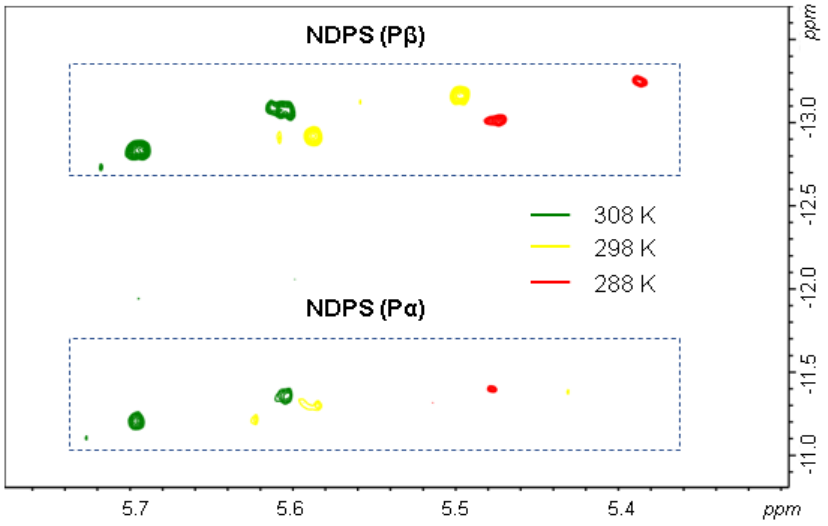

Figure 5.10. NDPS(P-α) and NDPS(P-β) regions of different 2D ^{1}H,^{31}P HSQMBC-TOCSY at different temperatures, observing the best ^{1}H-^{31}P correlation at the highest temperature (308K).

This substantial increase in sensitivity for 2D ^{1}H,^{31}P HSQMBC-TOCSY is not only observable in the NDPs region but also in monophosphates such as GPC, GPE or NADPH. Therefore, it is advised that ^{1}H,^{31}P HSQMBC-TOCSY experiments should be conducted at 308 K (**Figure 5.11**).

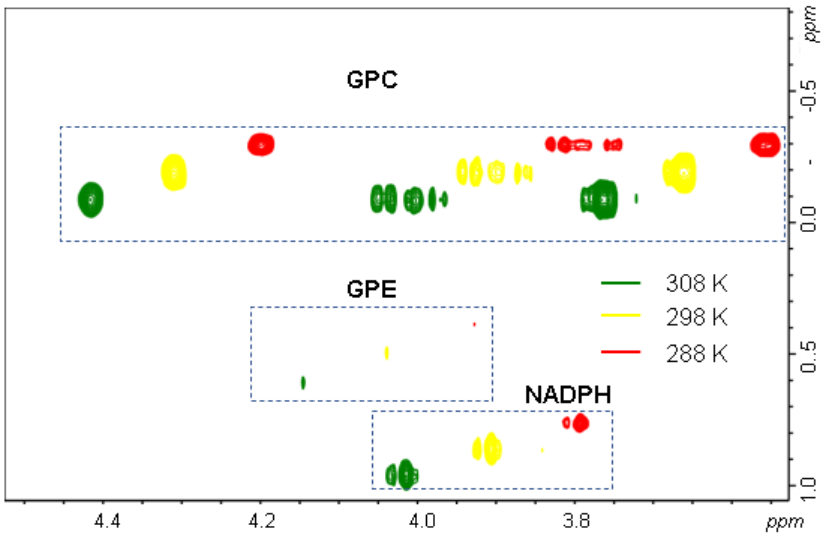

Figure 5.11. Monophosphates (GPC,GPE or NADPH) of different 2D ^{1}H,^{31}P HSQMBC-TOCSY at different temperatures, observing the best ^{1}H-^{31}P correlation at the highest temperature (308K).

5.3.1.10 SOPs proposed in hydrophilic extract of liver mice for quantitative ^{31}P-NMR analysis

In summary, **Table 5.14** shows the optimal parameters for quantitative ^{31}P-NMR analysis.

Table 5.14. SOPs proposed for quantitative ^{31}P-NMR analysis.

Parameter	Proposed
Chelator	EDTA 2 Mm
Buffer and pH	Glycine pH = 9.5
Solvent	D2O
PRE agent	Gdter 0.5 mM
Temperature	288 K
Interscan d_1	6 s
Assignment experiment	HSQMBC-TOCSY at 308 K

Once have improved the ^{31}P NMR methodology for phosphoromics studies, **Figure 5.12** and **Table 5.15** shows the assignment of the resolved ^{31}P peaks of hydrophilic extract of mice liver as it has presented in Chapter III.

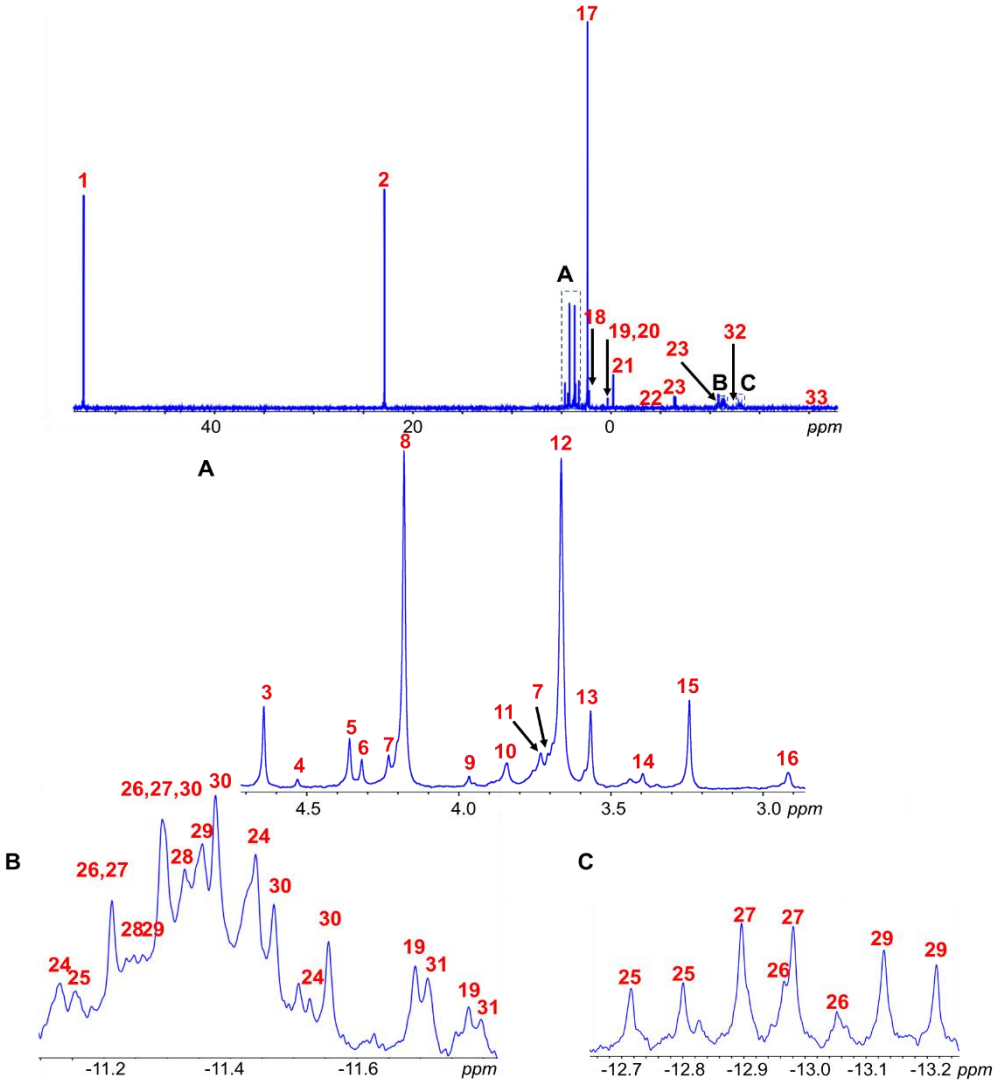

Figure 5.12. ^{31}P-NMR spectroscopy of hydrophilic mice liver extract. 30 phosphometabolites could be identified and quantified.

Table 5.15. ^{31}P-NMR spectroscopy of hydrophilic mice liver extract. 30 phosphometabolites could be identified and quantified.

Peak	Abbreviation	Compound	Chemical shift (ppm)
1	$OPMe_3$	Trimethylphosphine oxide	53.22
2	TMP^+	Tetramethyl phosphonium chloride	22.87
3	G6P	Glucose 6-phosphate	4.62
4	6PG	6-Phosphogluconate	4.50
5	X5P	Xylulose 5-phosphate	4.34
6	Unknown	Unknown	4.30
7	FBP	Fructose 1,6-bisphosphate	4.21, 3.69
8	S7P	Sedoheptulose 7-phosphate	4.17
9	Unknown	Unknown	3.93
10	PEA	Phosphoethanolamine	3.73
11	CMP/UMP/TMP	Cytidine 5´-monophosphate/ Uridine 5´-monophosphate/ Thymidine 5´-monophosphate	3.82
12	AMP/GMP	Adenosine 5´-monophosphate/ Guanosine 5´-monophosphate	3.64
13	F6P	Fructose 6-phosphate	3.55
14	E4P	Erythrose 4-phosphate	3.38
15	PCHO	Phosphocholine	3.23
16	3PG	3-Phosphoglyceric acid	2.91
17	PO_4^{3-}	Inorganic phosphate	2.31
18	G1P	Glucose 1-phosphate	2.19
19	NADPH	Nicotinamide adenine dinucleotide phosphate	0.84, -11.70, -11.78
20	GPE	Glycerophosphoethanolamine	0.32
21	GPC	Glycerophosphocholine	-0.22
22	PCr	Phosphocreatine	-4.72
23	NDP	Nucleoside diphosphates	-6.43, -6.52, -10.81, -10.91
24	ADPR	Adenosine 5´-diphosphoribose	-11.15, -11.44, -11.52
25	UDPGA/UDPgal	Uridine diphosphoglucuronic acid/ Uridine diphosphogalactose	-11.17, -12.72, -12.80
26	GDPF	Guanosine diphosphofucose	-11.22, -11.30, -12.97, -13.05
27	NDPG	Nucleoside diphosphoglucose	-11.22, -11.30, -12.90, -12.98
28	$FADH_2$	Flavin adenine dinucleotide	-11.24, -11.33
29	UDPNAcglu/UDPNAcgal	Uridine diphospho N-acethylglucosamine/ Uridine diphospho N-acethylgalactosamine	-11.26, -11.34, -13.13, -13.21
30	CDPE	Cytidine diphosphoethanolamine	-11.30, -11.38, -11.47, -11.56
31	NADH	Nicotinamide adenine dinucleotide	-11.71, -11.80
32	CDPCH	Cytidine diphosphocholine	-12.21,-12.31
33	NTP	Nucleoside triphosphates	-21.86, -21.96, -22

5.3.2 SOPs for quantitative ^{31}P NMR analysis in the hydrophobic extract of 100 mg of mice liver

5.3.2.1 Reference compound

Previously, we selected TPPO, which consistently produces a sharp singlet signal at 25.59 ppm, which is well separated from most of the metabolites. For effective quantitative referencing, a short $T_1(^{31}P)$ is needed for fast signal recovery. In this context, $T_1(^{31}P)$ of TPPO proved optimal (1.3 s at 298 K).

5.3.2.2 Buffer

A set of different buffers (d_8-Toluene, $CDCl_3$, n-Hexanol, CD_3OD, d_8-THF, Acetone and d_6-DMSO) were tested. It was observed that the ^{31}P signal dispersion and intensity roughly increase with solvents dipolar moment μ (**Figure 5.13 and Table 5.16**). Likewise, organic solvents with low μ may form inverse micelles, such as d_8-Toluene, $CDCl_3$ or d_8-THF. In addition, TPPO, the reference compound, remained stable at different buffers. Therefore, the optimal solvent, because of its signal intensity and especially good signal dispersion, was d_6-DMSO (**Figure 5.13**).

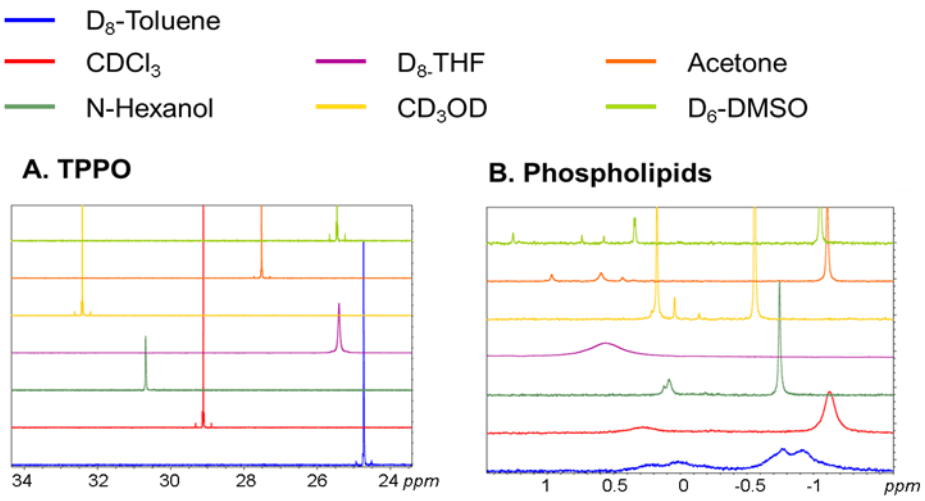

Figure 5.13. ^{31}P-NMR spectrum of lipophilic extract of mouse liver in different buffers with increasing μ(from bottom to top). Blue: d_8-Toluene. Red: $CDCl_3$. Dark green: N-Hexanol. Purple: d_8-THF. Yellow:: CD_3OD. Orange: Acetone. Bright green: DMSO-d_6. The most representative regions of ^{31}P NMR spectra were shown: A) TPPO, B) Phospholipids.

Table 5.16. Dipolar moment (μ) of the solvents tested in the lipophilic extract of liver mice sample.

Solvent	Dipolar moment (μ) (D)
D_6-DMSO	3.96
Acetone	2.91
CD_3OD	1.69
D_8-THF	1.63
N-Hexanol	1.60
$CDCl_3$	1.15
D_8-Toluene	0.36

Thus, taking into consideration the optimized buffer, the ^{31}P resolved peaks were assigned in the same way as had been reported previously, being used for optimization of the rest experimental conditions (**Figure 5.14** and **Table 5.17**).

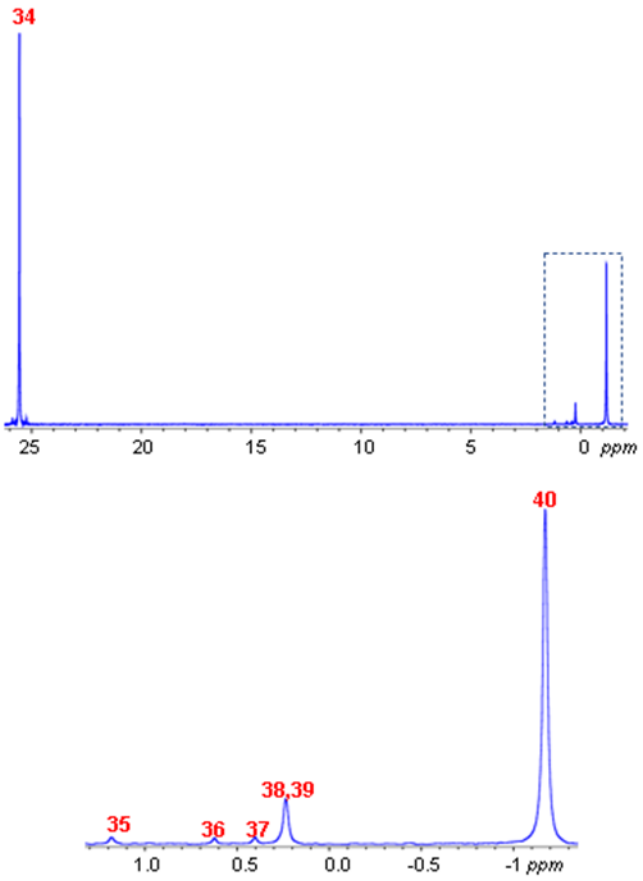

Figure 5.14. ^{31}P-NMR spectroscopy of hydrophobic mice liver extract.

Table 5.17. ^{31}P-NMR spectroscopy of lipophilic mice liver extract. About 7 phosphometabolites are identified and quantified.

Peak	Abbreviation	Compound	Chemical shift (ppm)
34	TPPO	Triphenylphosphine oxide	25.56
35	LPE	Lysophosphatidylethanolamine	1.18
36	SPM	Sphingomyelin	0.62
37	LPC	Lysophosphatidylcholine	0.40
38	CL	Cardiolipin	0.26
39	PE	Phosphatidylethanolamine	0.24
40	PC	Phosphatidylcholine	-1.17

5.3.2.3 Effect of PRE

The effect of Gdter on a mixture of 4 mM TPPO, 1 mM LPC and PC in d_6-DMSO at 298 K was tested. Even at a low concentration of 0.05 mM, Gdter had a deleterious effect on ^{31}P halfwidth (T_2) causing line-broadening for LPC and PC. Therefore, this data demonstrated that there was no need for adding any PRE.In fact, the additon of Gdter at a concentration as low as 0.05 mM, was detrimental, causing severe broadening of ^{31}P signals (**Table 5.18**).

Table 5.18. ^{31}P halfwidth and T_1(^{31}P) of a mixture sample of TPPO, LPC and PC in d_6-DMSO at 298 K with and without Gdter.

	Without Gdter		Gdter (0.05 m)	
Metabolite	**^{31}P halfwidth (Hz)**	**T_1 (^{31}P) (s)**	**^{31}P halfwidth (Hz)**	**T_1 (^{31}P)**
TPPO	1.06	1.30	1.62	-*
LPC	1.36	0.69	-*	-*
PC	1.62	0.45	-*	-*

*A very extreme line broadening prevented its measurement.

5.3.2.4 Temperature

Concerning the impact of the temperature on the lipophilic extract of mouse liver, the highest intensity peak of the phospholipids (except TPPO) was found at T = 310 K (**Table 5.19**). This temperature was deemed appropriate to balance T_2 and T_1, considering that the phospholipids exhibited T_1 values below 1 second (**Table 5.20**).

Table 5.19. ^{31}P-NMR average intensity values of the phosphorylated metabolites identified at the lipophilic mice liver extract at 298 K, 303 K, 308 K, 313 K, 318 K and 323 K.

Average intensity (^{31}P) vs T (K)	298	303	308	313	318	323
TPPO	**41269944**	39412002	39627285	38405570	37129557	35927564
PC	10034108	10172560	**10233958**	10016171	9851112	9615314
PE	1483123	1516250	1544404	**1576896**	1568555	1538730
CL	1336916	1391850	**1428592**	1427569	1394438	1416263
LPC	186426	182080	171672	**189719**	164217	175805
SPM	238794	272297	275348	**289810**	284807	272381
LPE	444583	473391	**470563**	429756	438495	377591

5.3.2.5 D_1 for quantitative ^{31}P NMR

Under these experimental conditions (in d_6-DMSO at 310 K), T_1 of each phosphometabolite (including TPPO) was measured (**Table 5.20**).

Table 5.20. $T_1(^{31}P)$ of the phosphometabolites measured in d_6-DMSO at 310 K.

Metabolite	$T_1(^{31}P)$ (s)
TPPO	1.71
LPE	0.45
SPM	0.35
LPC	0.95
CL	0.74
PE	0.73
PC	0.60

Assuming that the total interscan delay for exact quantification $D_1 > 3.T_{1,max}$ (^{31}P) and the $T_{1,max}(^{31}P)$ is from the reference compound (1.71 s), it was suggested a minimal interscan delay D_1 = 5 seconds.

5.3.2.6 Temperature in the 2D ^{1}H,^{31}P HSQMBC-TOCSY

Finally, the molecular assignment could be confirmed by looking at 2D ^{1}H,^{31}P HSQMBC-TOCSY at 310 K, having sufficient sensitivity to assign and identify the aforementioned phospholipids (**Figure 5.15**).

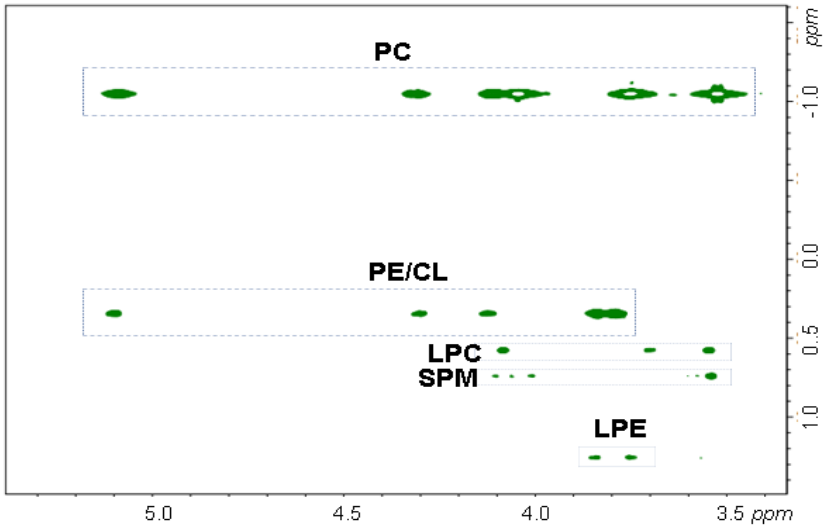

Figure 5.15. Phospholipids of 2D $^{1}H,^{31}P$ HSQMBC-TOCSY at 308 K.

5.3.2.7 SOPs proposed in hydrophobic extract of liver mice for quantitative ^{31}P-NMR analysis

In summary, **Table 5.21** shows the optimal parameters for quantitative ^{31}P-NMR analysis in the lipophilic extract of 100 mg of mice liver sample.

Table 5.21. SOPs proposed for quantitative ^{31}P-NMR analysis.

Parameter	Proposed
solvent	D_6-DMSO
PRE agent	No needed
Temperature	310 K
Interscan d_1	5 s
Assignment experiment	HSQMBC-TOCSY at 310 K

In summary, ^{31}P-NMR offers several benefits to the metabolomics field by expanding the coverage of the metabolome, and it allows to detection of metabolites that come from critical cellular processes, such as energy metabolism and cell signaling. Furthermore, it requires minimal instrument time due to its higher sensitivity in addition to avoiding expensive isotope labeling costs found with ^{13}C and ^{15}N-RMN, being particularly valuable for studies involving animals or even human clinical samples where it is prohibitive the use of isotope labeling. Despite the advantages of ^{31}P NMR, there are also notable challenges such as minimal ^{31}P chemical shift dispersion requires 2D NMR experiments for obtaining reliable metabolite identification. Furthermore, ^{31}P-NMR has also many low stabilities of phosphorylated metabolites, therefore, they could hydrolyze and consequently, it can give a false view of the true biological distribution. Hence, to

preserve phosphorylated metabolites, chloroform/methanol extraction solvent and cell lysing techniques are required. Despite some of these challenges, ^{31}P NMR could be applied as a routine component of a metabolomics study providing valuable information and novel insights that are not obtained by other analytical techniques.

5.4 Supplementary material

Table 5S1. $T_1(^{31}P)$ values of the most representative phosphorylated metabolites of a liver mice sample at different concentrations of Gdter (0, 0.5 and 1 mM) at 278 K. It was observed that the higher concentration of Gdter, the lower T_1 of each metabolite is.

T_1(ms) vs Conc. Gdter(mM)	**0 mM**	**0.5 mM**	**1 mM**
$OPMe_3$	4000	1990	1320
TMP^+	9750	3580	2155
G6P	6400	1935	1170
6PG	2350	1700	740
X5P	2080	1000	690
FBP	1950	1100	900
S7P	3200	1240	905
NMP	1630	780	560
F6P	3020	855	695
PCHO	8900	1040	740
PO_4^{3-}	2090	1225	700
G1P	900	1300	690
NADPH	1430	1130	630
GPE	1150	750	580
GPC	1385	970	720
NDP(Pβ)	1045	847,5	665
NDP(Pα)	575	652,5	385
NDPS(Pα)	432,5	462,5	365
NDPS(Pβ)	380	342,5	340

Table 5S2. $T_1(^{31}P)$ values of the most representative phosphorylated metabolites of a liver mice sample at different concentrations of Gdter (0, 0.5 and 1 mM) at 288 K. It was observed that the higher concentration of Gdter, the lower T_1 of each metabolite is.

T_1(ms) vs Conc. Gdter(mM)	**0 mM**	**0.5 mM**	**1 mM**
$OPMe_3$	4700	2470	1575
TMP^+	9620	4150	2530
G6P	12000	2340	1340
6PG	5500	1900	1000
X5P	3150	1700	1000
FBP	3700	1100	1000
S7P	4850	1310	1060

NMP	2440	950	650
F6P	4600	1070	805
PCHO	14200	1220	850
PO_4^{3-}	3100	1450	735
G1P	1350	1350	780
NADPH	1550	1325	830
GPE	1850	1250	710
GPC	2100	1300	855
NDP(Pβ)	1500	1115	745
NDP(Pα)	800	895	505
NDPS(Pα)	622,5	610	442,5
NDPS(Pβ)	510	507,5	437,5

Table 5S3. $T_1(^{31}P)$ values of the most representative phosphorylated metabolites of a liver mice sample at different concentrations of Gdter (0, 0.5 and 1 mM) at 298 K. It was observed that the higher concentration of Gdter, the lower T_1 of each metabolite is.

T_1(ms) vs Conc. Gdter(mM)	**0 mM**	**0.5 mM**	**1 mM**
$OPMe_3$	5800	2920	1935
TMP^+	9870	4630	2900
G6P	14750	2850	1590
6PG	6000	2200	1200
X5P	3500	1850	1100
FBP	4200	1620	1220
S7P	6100	1340	1250
NMP	3120	880	720
F6P	6080	1210	880
PCHO	18500	1500	860
PO_4^{3-}	3550	1720	690
G1P	1500	1400	900
NADPH	2950	1410	1100
GPE	2600	1200	1100
GPC	2600	1500	1100
NDP(Pβ)	1900	1445	935
NDP(Pα)	1075	1180	635
NDPS(Pα)	850	832,5	575
NDPS(Pβ)	710	667,5	520

Table 5S4. $T_1(^{31}P)$ values of the most representative phosphorylated metabolites of a liver mice sample at different concentrations of Gdter (0, 0.5 and 1 mM) at 308 K. It was observed that the higher concentration of Gdter, the lower T_1 of each metabolite is.

T_1(ms) vs Conc. Gdter(mM)	**0 mM**	**0.5 mM**	**1 mM**
$OPMe_3$	5800	2920	1935
TMP^+	9870	4630	2900
G6P	14750	2850	1590
6PG	6000	2200	1200
X5P	3500	1850	1100
FBP	4200	1620	1220
S7P	6100	1340	1250
NMP	3120	880	720
F6P	6080	1210	880
PCHO	18500	1500	860
PO_4^{3-}	3550	1720	690
G1P	1500	1400	900
NADPH	2950	1410	1100
GPE	2600	1200	1100
GPC	2600	1500	1100
NDP(Pβ)	1900	1445	935
NDP(Pα)	1075	1180	635
NDPS(Pα)	850	832,5	575
NDPS(Pβ)	710	667,5	520

Table 5S5. Intensity values of the most representative phosphorylated metabolites of a liver mice sample at different concentrations of Gdter (0, 0.5 and 1 mM) at 278 K. It was observed that the higher concentration of Gdter, the lower intensity of each metabolite is.

Intensity vs Conc. Gdter(mM)	**0 mM**	**0.5 mM**	**1 mM**
$OPMe_3$	21349754	15643578	12849291
TMP^+	14393083	19559523	16207558
G6P	970554,4	948831	775296
6PG	65935,44	84580	68726
X5P	201906,6	149488	132842
FBP	137066,8	64300	104566
S7P	471354,9	127545	369174
NMP	649444	90769	2762380
F6P	1333874	3740946	476064
PCHO	21629724	577448	823748

PO_4^{3-}	328708	1105646	10711903
G1P	76675	17051833	188131
NADPH	145029	278839	77153
GPE	523362	97910	94576
GPC	347572	114211	371716
NDP(Pβ)	339711	385701	254661
NDP(Pα)	262443	284174	217556
NDPS(Pα)	153601	216593	119882
NDPS(Pβ)	125699	130708	96323

Table 5S6. Intensity values of the most representative phosphorylated metabolites of a liver mice sample at different concentrations of Gdter (0, 0.5 and 1 mM) at 288 K. It was observed that the higher concentration of Gdter, the lower intensity of each metabolite is.

Intensity vs Conc. Gdter(mM)	**0 mM**	**0.5 mM**	**1 mM**
$OPMe_3$	15764098	14959305	11595151
TMP^+	11058651	17978523	15458037
G6P	790451	966504	766764
6PG	111061	99227	68846
X5P	152323	165850	129925
FBP	164946	114453	96103
S7P	412925	99648	308699
NMP	623883	152903	3052261
F6P	1192055	3892125	492659
PCHO	15242957	610330	810677
PO_4^{3-}	350045	1053626	10198879
G1P	92628	15818801	251805
NADPH	156027	305542	88857
GPE	499010	118495	89795
GPC	335451	128706	381631
NDP(Pβ)	363639	382110	275774
NDP(Pα)	257877	331772	252276
NDPS(Pα)	178643	248387	152969
NDPS(Pβ)	111872	176902	118605

Table 5S7. Intensity values of the most representative phosphorylated metabolites of a liver mice sample at different concentrations of Gdter (0, 0.5 and 1 mM) at 298 K. It was observed that the higher concentration of Gdter, the lower intensity of each metabolite is.

Intensity vs Conc. Gdter(mM)	**0 mM**	**0.5 mM**	**1 mM**
$OPMe_3$	10461476	14226990	9887822
TMP^+	7839446	16468025	15478360
G6P	605694	845779	717848
6PG	61989	76999	70804
X5P	132953	134492	132606
FBP	111700	107805	91649
S7P	318211	113461	311446
NMP	4854689	112942	2996699
F6P	929567	3655861	500232
PCHO	10453235	578530	703279
PO_4^{3-}	253231	983879	8036024
G1P	105184	13229728	223332
NADPH	99816	257688	89591
GPE	400722	109473	74296
GPC	289840	111815	346489
NDP(Pβ)	318041	374882	279467
NDP(Pα)	214409	325970	265802
NDPS(Pα)	159442	239200	146580
NDPS(Pβ)	153131	176573	126143

Table 5S8. Intensity values of the most representative phosphorylated metabolites of a liver mice sample at different concentrations of Gdter (0, 0.5 and 1 mM) at 308 K. It was observed that the higher concentration of Gdter, the lower intensity of each metabolite is.

Intensity vs Conc. Gdter(mM)	**0 mM**	**0.5 mM**	**1 mM**
$OPMe_3$	2918921	10848643	8202910
TMP^+	2463315	14591885	15101258
G6P	199752	731602	609719
6PG	37391	93453	75699
X5P	70091	160714	146249
FBP	53133	92355	99859
S7P	124048	331826	276944,9
NMP	1567146	3536266	2717303

F6P	215944	570246	427742
PCHO	359927	791110	558624
PO_4^{3-}	3327601	9688548	5703510
G1P	98145	220459	199355
NADPH	35062	72328	98393
GPE	39749	112239	77852
GPC	184010	373438	254703
NDP(Pβ)	134069	315330	269361
NDP(Pα)	138883	313918	266736
NDPS(Pα)	81705	172499	136900
NDPS(Pβ)	73178	174717	134208

CHAPTER 6
CONCLUSIONS

- A minimum of 20 mg and optimal 100 mg of mice liver extract was optimal to obtain a reliable ^{31}P-NMR quantitative analysis.

- The protocol extraction implied the separation into hydrophilic and hydrophobic fractions with an optimized stoichiometry of extract solvent (55:20:20 (w/w/w of chloroform: methanol: water) according to the ternary phase diagram.

- On average, ^{31}P-NMR extraction had good reproducibility with a good yield.

- For quantitative analysis, in the case of hydrophilic fraction, a commercial contrast agent induces fast relaxation of the signal. Meanwhile, an internal reference that produces a defined peak separated from the rest of the phosphometabolites present in the biological samples was included in both extracted fractions.

- ^{31}P peaks were assigned by comparison of a database of ^{31}P chemical shifts obtained from more than 80 phosphometabolites. In addition, 2D ^{1}H,^{31}P-COLOC, 2D ^{1}H,^{31}P HSQMBC-TOCSY and spiking over the sample the tentative phosphometabolite were used to confirm their assignment.

- This technique has been applied to define the metabolic landscape in livers from a mouse model of the rare disease disorder (CEP) as well as two well-known murine models of NASH; one genetic (MAT1A-KO) and other dietary (CDHF), reporting alterations in the concentrations of phosphometabolites that were readouts of the balance between glycolysis, gluconeogenesis, PPP, the TCA cycle, oxidative phosphorylation, phospholipids metabolism and apoptosis.

- It was proved that the treatment with the repurposed drug CPX improved the phosphoromics profile of CEP mice, as observed by the normalization of liver histology.

- In response to the urgent need for biomarkers for monitoring the progression of NAFLD, ^{31}P NMR method was used to observe metabolic changes and distinguish unique metabolic profiles from two dietary models of NASH (HFD and CDHF) at three different ages (20,52 and 78 weeks).

- In HFD animals' group, the liver phosphoromics profile showed a loss of membrane integrity, cell injury as well as metabolic changes in glycolysis, PPP and phospholipids precursors and lipids metabolism.

- Meantime, in CDHF liver animals group, an impaired mitochondrial function with a loss of membrane integrity provoking liver damage as well as metabolic changes in glycolysis, PPP, hexosamines metabolic pathway, nucleotides and phospholipids metabolism were observed.

- Multivariate analysis demonstrated metabolic differences due to the age of the mice as well as the diet fed by them.

- A promising training model was developed to differentiate liver phosphoromics profile obtained by NMR from mice fed with different diets that could develop NASH.

- A robust quantitative ^{31}P-NMR-based method protocol was optimized to apply it in the metabolomics field under SOPs.

- For the hydrophilic fraction, this protocol involved the use of chelating agent (EDTA, 2 mM), $OPMe_3$ (1 mM) and TMP^+ (1 mM) as internal references, a suitable PRE (Gdter) with 0.5 mM at temperature 288 K, 50 mM Glycine buffer at pH 9.5 as buffer, D_2O as solvent, D_1 of 6 seconds and 2D ^{1}H,^{31}P HSQMBC-TOCSY optimized at 308 K.

- Concurrently, the hydrophobic fraction implied the presence of TPPO (4 mM) as an internal reference, d_6-DMSO as a solvent, the optimal temperature at 310 K, D_1 of 5 seconds with the absence of PRE.

- Overall, the ^{31}P-NMR-based platform provided the absolute concentration of up to 54 phosphorylated metabolites separated into two phases being a snapshot of the organ´s metabolism in health, disease, and response to treatment, which could correlate with liver histology and providing mechanistic information.

SUMMARY

Phosphoromics is a branch of metabolomics whose aim is to study metabolism using phosphorous and phosphorylated metabolites as biomarkers. Likewise, phosphorous is a chemical element essential for life. Phosphorous corresponds to 1% of all human body mass, being the sixth most abundant element behind oxygen (65%), carbon (18.5%), hydrogen (9.5%), nitrogen (3.2%) and calcium (1.5%). 85% of all the phosphorous present in the human body is deposited in bones and teeth. The rest is part of soft tissues and extracellular fluids. The average concentration of phosphorous in the blood is 0.4 g/L (1% of all phosphorous) where it can be present in two forms: in the form of inorganic phosphate (30 %) and the form of organic phosphate forming part of other molecules (70%). The daily intake of phosphorus is 1-3 g in the form of phospholipids, nucleic acids and inorganic phosphate being excreted in the same quantity, but mainly in the form of inorganic phosphate through the urinary tract.

Phosphorous is a particularly interesting nucleus to be studied by NMR. The ^{31}P isotope has a natural abundance of 100% and it has a relatively high gyromagnetic constant (40.4% concerning ^{1}H). Due to its electronic density, it has a greater range of chemical shift values, allowing a greater dispersion in the signals, therefore, it can avoid overlapping. Its nuclear spin is ½, consequently, it makes the spectra easier to interpret. ^{31}P-NMR nucleus responds in an independent way to the NMR experiment, making ^{31}P-NMR a suitable methodology for analyzing biochemical systems in which phosphorous is a key component of many relevant biological compounds (DNA, RNA or ATP).

Nevertheless, one of the main downsides is the relative sensitivity of ^{31}P, so it is advisable to use concentrated samples and a specific probe for the detection of this nucleus. Even so, in 1974 this kind of resonance was used for the to observe the phosphorous content in tissues and since then, it has not stopped being used.

Likewise, phosphoromics has been presented in the previous literature as an excellent reporter of the phenotypic state of an individual because there are about 1500 phosphorylated compounds that are widely distributed in the most important metabolic pathways of the organism:

- Carbohydrate metabolism: glycolysis, gluconeogenesis, pentose phosphate and galactose metabolism.
- Lipid metabolism: biosynthesis of TG, PC and PE as well as sphingosine breakdown.
- Energetic metabolism: ATP, GTP, ADPR, NADPH, $FADH_2$, as energy carriers.

- Nucleoside metabolism: synthesis and degradation of purines and pyrimidines.
- Metabolism of amino acids: metabolism of serine and threonine, biosynthesis and recycling methionine, synthesis of arginine and proline, urea and creatine cycle.
- Metabolism of glycans: Biosynthesis of *N*- and *O*-glycans.
- Metabolism of cofactors and vitamins: Biosynthesis of coenzyme A and tetrahydrobiopterin.
- Biosynthesis of terpenoids and polyketides: Biosynthesis of C5 and C10-C20 isoprenoids.

Particularly, the liver is a tissue that arouses interest due to the presence of a large number of phosphorylated compounds. In the 1980s, the phospholipids and nucleoside metabolism of the liver were evaluated for the first time by ^{31}P-NMR. Since then, it has tried to implement this spectroscopic technique in the diagnosis of different liver diseases either *in vitr*o or *in vivo.*

Likewise, ^{31}P-NMR is suited to detect, identify, and quantify a wide range of phosphorylated metabolites being the metabolic profile observed a metabolic state of the organism. Subject to a pathological or physiological state of an individual, the metabolic profile can be altered, monitoring the changes in each metabolic pathway. Due to the technical limitations, the vast majority of the studies carried out in ^{31}P-NMR either *in vivo* or *in vitro* have been limited to a set of a small number of phosphorylated biomarkers involved in phospholipids and energy metabolism.

Hence, the main objective of this thesis has been to promote phosphoromics as an analytical method in extracts of biological samples, overcoming some limitations that were necessary to take into consideration, such as lack of standardization in the extraction method, the lack of internal references to standardize chemical shifts, the lack of spectral resolution and sensitivity, erroneous assignment of metabolites and quantification of metabolites.

Thus, Chapter 3 presented a robust method for the characterization and quantification of the phosphorome composition from mouse liver samples being the approach followed by the direct observation and quantification of the phosphorous signals that come from liver phosphometabolites. To that end, some experimental aspects of the procedure included sample preparation were optimized. Firstly, it was determined that the detection limit was around 30 pmol of ^{31}P-compound per milligram of liver with a signal-to-noise *ratio* of 4. Therefore, a minimum of 20 mg and an optimal 100 mg of extract of liver was desired to obtain reliable quantitative analysis by this methodology although in case it is

used a more sensitivity probe (i.e., heteronuclear detection cryoprobe), an amount of liver less than 10 mg could be used with the significant improvement in its sensitivity. Regarding metabolic extraction, it was crucial to involve one with the subsequent separation into the hydrophilic and the hydrophobic fractions. Since the reported ternary mixtures of chloroform: methanol cannot be used due to the release of water molecules compromising phase separation, the ternary phase diagram was evaluated identifying an optimal stoichiometry at 55:25:20 (w/w/w of chloroform: methanol: water). The extraction protocol optimized provided excellent reproducibility with a good yield (69% ± 5%) determined with DSS, an added reference compound.

For quantitative analysis, one of the main criteria is that ^{31}P-NMR signal intensity must be proportional to its concentration for each metabolite. Thus, the hydrophilic extract was doped with a commercial contrast agent inducing fast relaxation of the signal (Gdbut) as well as an internal reference (TMP+) producing sharp, invariant ^{31}P single signal (22.86 ppm) and separated from most of the phosphometabolites in Tris-d_{11} (pD = 7.0) in D_2O. Concurrently, this approach was not applied to the hydrophobic extract because of its limited solubility and longer recover times were used instead. Therefore, TPPO, which generates a defined singlet signal of ^{31}P (25.58 ppm), was added in d_6-DMSO, which was used as a solvent over a hydrophobic fraction. ^{31}P resolved peaks were assigned through the comparison of a database of ^{31}P chemical shifts obtained for more than 80 phosphometabolites. Likewise, the assignments of peaks were corroborated by heteronuclear 2D ^{1}H,^{31}P-COLOC correlation spectra of the ^{31}P(-O-C-)$^{1}H_n$ moieties presented in the phosphorylated metabolites. In addition, in several cases, it was necessary to spike the sample with a suspect phosphometabolite in order to confirm its assignment. On the whole, the ^{31}P-NMR platform contained 54 phosphorylated metabolites covering central metabolism (glycolysis, PPP and the TCA cycle), glycogenesis, phospholipids, nucleotides and nicotinamide metabolism.

As a proof of concept, it was elucidated the phosphorome from a mouse model of an autosomal recessive disorder congenital erythropoietic porphyria (CEP), suffering patients with CEP a deficient biosynthesis of the heme prosthetic group, resulted in steatohepatitis that can progress to fibrosis, and finally, in liver failure. The ^{31}P-NMR analysis of CEP provided alterations in the activities of glycolysis, glycogenesis, PPP, oxidative phosphorylation, phospholipids metabolism and apoptosis. However, the phosphoromics profile of CEP mice liver enhanced after the treatment with the repurposed drug CPX, which could be correlated with the improvement of the liver histology. Likewise, phosphoromics profile of two well-known murine models of NASH, one genetic, MAT1A-KO mice and the other dietary, CDHF diet, were analyzed,

correlating the metabolic alterations observed with the main histological features such as steatosis, apoptosis and fibrosis. Thus, the ^{31}P pattern of MAT1A-KO mice liver showed alterations in glycolysis, oxidative phosphorylation, PPP, apoptosis and phospholipids metabolism. For another hand, the phosphoromics profile observed in mice fed with a CDHF diet was different from those in MAT1A-KO, especially in glycogenesis and glycolysis although it remained a remarkable change in phospholipids metabolism, as it was observed in MAT1A-KO mice.

During Chapter 4, ^{31}P-NMR method was applied to the study of the progression of NAFLD. NAFLD is the leading cause of chronic liver disease in Western countries, being currently one of the most common causes of liver disease. NAFLD global prevalence is about 25% and this term is used to refer to several disorders including steatosis, NASH, fibrosis, cirrhosis and HCC. NASH is the advanced form of NAFLD, and it is characterized by the presence of steatosis together with inflammation, ballooning with or without liver fibrosis.

Regarding NAFLD diagnosis, histological from liver biopsies and blood test of liver enzymes remains the gold standard for monitoring NAFLD. Nevertheless, liver biopsies present some drawbacks because it is a very invasive technique as well and the results depend on the liver portion taken in the biopsy, which sometimes does not reflect the status of the entire organ. Therefore, the absence of biomarkers has hampered the diagnosis and monitoring of this liver disease progression.

In response to the need for biomarkers for the diagnosis and monitoring of NAFLD, it was applied ^{31}P-NMR-base method to study liver phosphorome in two dietary models of NASH (HFD and CDHF) at three different ages (20,52 and 78 weeks) to characterize metabolic changes in each condition as well as to distinguish unique metabolic patterns as compared to control groups.

In general, HFD can cause a loss of membrane integrity and consequently liver failure, by reducing PC/PE *ratio* which has been demonstrated to be a good predictor of the development of NAFLD and liver damage. Furthermore, apoptosis has been shown through the elevation of ADPR, a vital biomarker involved in several cellular processes such as necrosis, apoptosis, DNA repair and regulation of transcription. Moreover, changes in oxidative phosphorylation, phospholipids precursors metabolism, lipids metabolism, glycolysis and PPP were observed.

Meantime, CDHF liver animals phosphoromics profile showed an impaired mitochondrial function with an elevation of NADH and $FADH_2$, which are electron carriers during the process of cellular respiration. Likewise, increased levels of PE and its precursors (PEA

and GPE) suggested that PE metabolism has been activated or PE activity has been partially impaired. In addition, CHO deficiency caused an aberrant impact on choline metabolism, potentially predisposing one to NAFLD. As with HFD group, it has observed a reduction in the PC/PE ratio suggesting a dysregulation of membrane integrity due to the changes observed in the CHO and ethanolamine metabolism. Moreover, elevated levels of hepatic ADPR claimed apoptosis and necrosis. In addition, the reduction of UDPNAcglu, the end product of hexosamine biosynthetic pathway can be due to a potential decrease in cell survival. Besides, changes in glycolysis, PPP and nucleotide metabolism were observed provoking alterations in carbohydrate metabolism.

Likewise, as demonstrated by univariate analysis, a clear separation was observed between the metabolic profiles of liver mice fed by HFD and CDHF concerning STD by supervised analysis.

For another hand, previous studies have claimed that aging promotes risk factors associated with NASH such as inflammation, diabetes, and obesity, therefore, it is vital to understand the implications of aging in this study. Thus, PLS-DA showed that there was a clear separation between the group of 20 weeks and the other groups, not observing significant changes between the 52- and 78-week group, considering aging was a necessary variable to take into consideration in this research.

In addition, multivariate analyses were performed such as OPLS-DA, where it saw that there was a clear separation between liver phosphoromics profiles of mice fed with HFD and CDHF compared to ones with STD as well as between HFD and CDHF. On the other hand, it was verified the predictive capacity of this model indicated the results obtained that this training model has good explanatory power, being able to differentiate hepatic phosphoromics profile obtained by NMR from mice fed with different diets that can develop NASH. Also, by each OPLS-DA, the most ten discriminating metabolites were determined by VIP score estimation. Although preliminary, these results are very promising as they suggest that if it is increased the number of samples analyzed, it is possible to distinguish the different phenotypes and create an algorithm that in the future helps to determine the status of liver metabolism of the mice whether they are fed with a different diet that can develop NASH.

^{31}P-NMR methodology has not been optimized for metabolomics purposes, and there is not a robust workflow established to implement it in the metabolomics field. Thus, during Chapter 5, with the sole purpose of facilitating the application of ^{31}P NMR in metabolomics, a protocol under SOPs, either for hydrophilic or hydrophobic fraction

measurement, was developed as well as to facilitate fine-tuning of sample measurements.

Firstly, for hydrophilic fraction, it concluded that the optimal reference compound for quantitative ^{31}P-NMR analysis was $OPMe_3$ due to the shorter T_1, which is required for quantitative referencing although TMP^+ also remained as a second reference compound because of a minor pH dependence.

Secondly, due to the interaction of the phosphate groups and cations, causing chemical or conformational exchange broadening, EDTA was used as a chelating agent, ensuring that 2 mM EDTA had sufficient capacity for divalent cations captures, and consequently for stabilizing the phosphorylated metabolites.

Thirdly, 50 mM Glycine buffer at pH 9.5 was the optimal choice because of its low-conductivity buffer in addition to the high stability of the phosphometabolites at pH 9.5. Furthermore, the capacity of EDTA to complex cations divalent was significantly increased because of its deprotonation with the use of this buffer.

Next, D_2O was preferred over H_2O because the suppression of residual H_2O signal is unproblematic and robust, allowing it to facilitate the measurement of any 1D ^{1}H experiment.

Alongside, enthalpic T_1 relaxation time limits the total interscan delay τ for exact quantification ($\tau_{quant} > 3.T_{1,max}$) and maximal signal-to-noise per unit time ($SN_{max} \sim 1/\sqrt{\tau_{opt}}$ at $\tau_{opt} \sim 1.25.T_1$). Thus, sensitivity is gained by accelerating T_1 with a PRE agent but without shortening T_2, showing that Gdter was preferable over Gdbut because Gdbut provoked shorter T_1 but also shorter T_2, which is undesirable, causing line broadening.

Overall, low temperatures produced the highest quality ^{31}P-NMR spectra, accelerating T_1 but not shortening halfwidth and increasing signal intensity of the phosphorylated metabolites although the presence of PRE was needed because of extremely long T_1 of some phosphometabolites such as G6P, S7P, PCHO and PO_4^{3-}.

Thus, the balance between the chosen temperature and the amount of Gdter required was crucial, determining that the optimal scenario implies 0.5 mM Gdter at temperature 288 K, taking into consideration that the desired T_1 (reduced at higher Gdter amount) and the undesirable effect of T_2 (reduced causing line broadening) must be balanced.

D_1, a limiting parameter for quantitative ^{31}P-NMR analysis, should be at 7.0 seconds considering that more than 95% of the phosphometabolites were fully relaxed including the slowest relaxing species such as G6P and the reference for quantification ($OPMe_3$).

However, after some simulations, given the vast majority of the time, the signal intensity of the fastest relaxing species (NDPS-Pβ) was lower and, consequently, had a lower SN_0 as compared to the slowest relaxing species (G6P), a large amount of time was miss pended for NDPS-Pβ, increasing quantification error and, therefore, D_1 was shortened to 6 seconds.

Finally, regarding hydrophilic extract, the temperature at 2D $^{1}H,^{31}P$ HSQMBC-TOCSY was optimized for molecular assignments purposes, showing that increasing the temperature, with Gdter 0.5 mM, a significant reduction in ^{1}H relaxation was observed, and consequently, ^{1}H-^{31}P correlation for some resonances were enhanced, especially for NDPS region, concluding that this 2D experiment should be conducted at 308 K.

Concurrently, for the hydrophobic fraction, TPPO was the optimal reference compound for quantitative ^{31}P-NMR analysis due to its short T_1, being a fast signal recovery.

For another hand, d_6-DMSO was suitable due to its signal intensity and good signal dispersion. It has a higher dipolar moment μ (3.96 D), having seen a correlation between each chemical parameter and the ^{31}P signal dispersion and intensity.

Likewise, the effect of Gdter was evaluated over a phospholipid mixture, in which the addition of Gdter at a low concentration of 0.05 mM caused severe broadening of ^{31}P-signals, therefore PRE addition was avoided.

Meantime, the impact of the temperature in the lipophilic extract of mouse liver was analyzed being the highest intensity peak of the phospholipids found at T = 310 K.

Finally, assuming that the total interscan delay for exact quantification $D_1 > 3.T_{1,max}$ (^{31}P) and the $T_{1,max}$(^{31}P) is from the reference compound (1.71 s), the D_1 suggested was 5 seconds.

To sum up, the liver phosphorome provides a snapshot of the organ´s metabolism in order to unravel the metabolic phenotype of liver injury and to identify the mechanism of drug action, having developed under strict SOPs for the extraction of metabolites, the assignment of metabolites by ^{31}P-NMR and their quantification using a standard reference in combination with relaxation accelerating paramagnetic compound and chelating agent in addition to being optimized the suitable temperature as well as buffer or solvent. This methodology could be applied to different disease models, cell lines, different tissues (heart, brain, pancreas, among others) or different biological systems including humans. In the future, it could also automate the measurement, processing, and analysis of the samples, using advanced computing techniques (*deep learning*) for the integration of the database in the pathways of metabolism.

RESUMEN

La fosforómica es una rama de la metabolómica cuyo objetivo es estudiar el metabolismo utilizando fósforo y metabolitos fosforilados como biomarcadores. Asimismo, el fósforo es un elemento químico imprescindible para la vida. El fósforo corresponde al 1 % de toda la masa corporal humana, siendo el sexto elemento más abundante detrás del oxígeno (65 %), el carbono (18,5 %), el hidrógeno (9,5 %), el nitrógeno (3,2 %) y el calcio (1,5 %). El 85% de todo el fósforo presente en el cuerpo humano se deposita en huesos y dientes. El resto forma parte de tejidos blandos y fluidos extracelulares. La concentración media de fósforo en sangre es de 0,4 g/L (1 % de todo el fósforo) donde puede estar presente en dos formas: en forma de fosfato inorgánico (30 %) y en forma de fosfato orgánico formando parte de otras moléculas (70%). La ingesta diaria de fósforo es de 1-3 g en forma de fosfolípidos, ácidos nucleicos y fosfato inorgánico siendo la excreción en la misma cantidad, pero principalmente en forma de fosfato inorgánico a través del tracto urinario.

Asimismo, el fósforo es un núcleo particularmente interesante para ser estudiado por Resonancia Magnética Nuclear (RMN). El isótopo ^{31}P tiene una abundancia natural del 100% y tiene un constante giro magnética relativamente alta (40,4% con respecto al ^{1}H). Debido a su densidad electrónica, tiene un mayor rango de valores de desplazamiento químico, lo que permite una mayor dispersión en las señales, por lo tanto, puede evitar la superposición. Su espín nuclear es ½, por lo que facilita la interpretación de los espectros. El núcleo de ^{31}P-RMN responde de forma independiente al experimento de RMN, lo que convierte a ^{31}P-RMN en una metodología adecuada para analizar sistemas bioquímicos en los que el fósforo es un componente clave de muchos compuestos biológicos relevantes (ADN, ARN o ATP).

No obstante, uno de los principales inconvenientes es la relativa sensibilidad del ^{31}P, por lo que es recomendable utilizar muestras concentradas y con una sonda específica para la detección de este núcleo. Aun así, en 1974 se utilizó este tipo de resonancia para observar el contenido de fósforo en los tejidos y desde entonces no ha dejado de utilizarse.

Asimismo, la fosforómica ha sido presentada en la literatura previa como un excelente reportero del estado fenotípico de un individuo debido a que existen alrededor de 1500 compuestos fosforilados que se encuentran ampliamente distribuidos en las vías metabólicas más importantes del organismo:

-Metabolismo de los hidratos de carbono: glucólisis, gluconeogénesis, metabolismo de las pentosas fosfato y de la galactosa.

- Metabolismo de los lípidos: biosíntesis de TG, PC y PE, así como descomposición de la esfingosina.

-Metabolismo energético: ATP, GTP, ADPR, NADPH, $FADH_2$, como transportadores de energía.

- Metabolismo de nucleósidos: síntesis y degradación de purinas y pirimidinas.

- Metabolismo de los aminoácidos: metabolismo de la serina y treonina, biosíntesis y reciclado de metionina, síntesis de arginina y prolina, ciclo de urea y creatina.

- Metabolismo de los glicanos: biosíntesis de N- y O-glicanos.

-Metabolismo de cofactores y vitaminas: biosíntesis de coenzima A y tetrahidrobiopterina.

- Biosíntesis de terpenoides y policétidos: biosíntesis de isoprenoides C5 y C10-C20.

En particular, el hígado es un tejido que despertó interés por la presencia de una gran cantidad de compuestos fosforilados. En la década de 1980, el metabolismo hepático de fosfolípidos y nucleósidos se evaluó por primera vez mediante ^{31}P-RMN. Desde entonces se ha intentado implementar esta técnica espectroscópica en el diagnóstico de diferentes enfermedades hepáticas ya sea *in vitro* o *in vivo*.

Asimismo, la ^{31}P-RMN es adecuada para detectar, identificar y cuantificar una amplia gama de metabolitos fosforilados siendo el perfil metabólico observado un estado metabólico del organismo. Sujeto a un estado patológico o fisiológico de un individuo, se puede alterar el perfil metabólico, monitoreando los cambios en cada ruta metabólica. Debido a las limitaciones técnicas mencionadas anteriormente, la gran mayoría de los estudios realizados en ^{31}P-RMN tanto *in vivo* como *in vitro* se han limitado a un conjunto de un pequeño número de biomarcadores fosforilados implicados en fosfolípidos y metabolismo energético.

Por tanto, el objetivo principal de esta tesis ha sido promover la fosforómica como método analítico en extractos de muestras biológicas, superando algunas limitaciones que era necesario tener en cuenta, como la falta de estandarización en el método de extracción, la falta de referencias internas para estandarizar

desplazamientos químicos, falta de resolución espectral y sensibilidad, asignación errónea de metabolitos y cuantificación de metabolitos.

Así, durante el Capítulo 3, se presenta un método robusto para la caracterización y cuantificación de la composición de fósforo de muestras de hígado de ratón, siendo el enfoque seguido la observación directa y la cuantificación de las señales de fósforo que provienen de los fosfometabolitos hepáticos. Para ello, se optimizaron algunos aspectos experimentales en el procedimiento incluyendo la preparación de muestras. En primer lugar, se determinó que el límite de detección era de alrededor de 30 pmol de compuesto ^{31}P por miligramo de hígado con una relación señal-ruido de 4. Por lo tanto, se deseaba un mínimo de 20 mg y un óptimo de 100 mg de extracto de hígado con el objetivo de obtener un análisis cuantitativo fiable mediante esta metodología, aunque en caso de que se utilice una sonda de mayor sensibilidad (es decir, una sonda de detección heteronuclear), se podría utilizar una cantidad de hígado inferior a 10 mg con una mejora significativa en su sensibilidad. En cuanto a la extracción metabólica, era crucial involucrar una con la posterior separación en la fracción hidrofílica e hidrofóbica. Dado que las mezclas ternarias de cloroformo: metanol reportadas no pueden ser utilizadas debido a la liberación de moléculas de agua que comprometen la separación de fases, se evaluó el diagrama de fases ternario identificando una estequiometría óptima a 55:25:20 (p/p/p de cloroformo: metanol: agua). El protocolo de extracción optimizado proporcionó una excelente reproducibilidad con buenos rendimientos (69% ± 5%) determinados con DSS, un compuesto de referencia añadido.

Para el análisis cuantitativo, uno de los principales criterios es que la intensidad de la señal de ^{31}P-RMN debe ser proporcional a su concentración para cada metabolito. Por lo tanto, el extracto hidrofílico se dopó con un agente de contraste comercial que inducía una relajación rápida de la señal (Gadobutrol (*Gdbut*, siglas en inglés)), así como con una referencia interna, Cloruro de tetrametilfosfonio (*TMP*$^{+}$, siglas en inglés), que producía una señal única nítida e invariable de ^{31}P (22,86 ppm) y se separaba de la mayoría de los fosfometabolitos en Tris-d_{11} (pD = 7,0) en D_2O. Al mismo tiempo, este enfoque no se aplicó al extracto hidrofóbico debido a su solubilidad limitada y en su lugar se usaron tiempos de recuperación más largos. Por lo tanto, se añadió Óxido de trifenilfosfina (*TPPO*, siglas en inglés), que genera una señal de singlete definida de ^{31}P (25,58 ppm), en d_6-DMSO, que se usó éste último como disolvente sobre la fracción hidrofóbica. Los picos resueltos de ^{31}P se asignaron mediante la comparación de una base de datos de desplazamiento químico de 31P

obtenido para más de 80 fosfometabolitos. Asimismo, las asignaciones de picos fueron corroboradas por espectros de correlación heteronuclear 2D ^{1}H,^{31}P-COLOC de los restos $^{31}P(-O-C-)^{1}H_n$ presentados en los metabolitos fosforilados. Además, en varios casos fue necesario añadir a la muestra un estándar de un fosfometabolito sospechoso para confirmar su asignación. En total, la plataforma ^{31}P-RMN contenía 54 metabolitos fosforilados que abarcaban el metabolismo central (glucólisis, PPP y el ciclo TCA), la glucogénesis, los fosfolípidos, los nucleótidos y el metabolismo de la nicotinamida.

Como prueba de concepto, se elucidó el fosforoma a partir de un modelo murino de un trastorno autosómico recesivo llamado porfiria eritropoyética congénita (*CEP*, siglas en inglés), que sufre pacientes con *CEP* una biosíntesis deficiente del grupo protésico hemo, resultando en esteatohepatitis que puede progresar a fibrosis, y finalmente, a insuficiencia hepática. El análisis de ^{31}P-RMN de *CEP* proporcionó alteraciones en las actividades de glucólisis, glucogénesis, la ruta de la pentosa fosfato, fosforilación oxidativa, metabolismo de fosfolípidos y apoptosis. Sin embargo, el perfil fosforómico del hígado de los ratones *CEP* mejoró después del tratamiento con el fármaco reutilizado Ciclopirox (CPX), lo que podría correlacionarse con la mejora de la histología del hígado. Asimismo, también se analizó el perfil fosforómico de dos modelos murinos bien conocidos de *NASH* (siglas en inglés), uno genético, ratones MAT1A-knockout (*MAT1A-KO*, siglas en inglés) y otro dietético, dieta deficiente en colina y rica en grasas (*CDHF*, siglas en inglés), correlacionando las alteraciones metabólicas observadas con las principales características histológicas como esteatosis, apoptosis y fibrosis. Así, el patrón ^{31}P del hígado de ratones MAT1A-KO mostró alteraciones en la glucólisis, fosforilación oxidativa, la ruta de la pentosa fosfato, apoptosis y metabolismo de fosfolípidos. Por otro lado, el perfil fosforómico observado en los ratones alimentados con una dieta CDHF fue diferente al de MAT1A-KO, especialmente en la glucogénesis y glucólisis, aunque se mantuvo un cambio notable en el metabolismo de los fosfolípidos, tal y como se observó en los ratones MAT1A-KO.

Durante el Capítulo 4, se aplicó el método ^{31}P-RMN al estudio de la progresión de la enfermedad del hígado graso no alcohólico (*NAFLD,* siglas en inglés). *NAFLD* es la principal causa de enfermedad hepática crónica en los países occidentales, siendo actualmente una de las causas más comunes de enfermedad hepática. La prevalencia mundial de *NAFLD* es de alrededor del 25 % y este término se utiliza para referirse a varios trastornos, como esteatosis, esteatosis hepática no alcohólica

(*NASH*, siglas en inglés), fibrosis, cirrosis y carcinoma hepatocelular. *NASH* es la forma avanzada de *NAFLD* y se caracteriza por la presencia de esteatosis junto con inflamación con o sin fibrosis hepática.

En cuanto al diagnóstico de *NAFLD*, la histología a partir de biopsias hepáticas y análisis de sangre de enzimas hepáticas siguen siendo el estándar de oro para el seguimiento de *NAFLD*. Sin embargo, las biopsias de hígado presentan algunos inconvenientes debido a que es una técnica muy invasiva y los resultados dependen de la porción de hígado tomada en la biopsia, que a veces no refleja el estado de todo el órgano. Por tanto, la ausencia de biomarcadores ha dificultado el diagnóstico y seguimiento de la progresión de esta enfermedad hepática.

En respuesta a la necesidad de biomarcadores para el diagnóstico y seguimiento de *NAFLD*, se aplicó el método basado en ^{31}P-RMN para estudiar el fósforo hepático en dos modelos dietéticos de NASH, una dieta rica en grasas y una dieta deficiente en colina y rica en grasas (*HFD* y *CDHF*, siglas en inglés) a tres edades diferentes (20, 52 y 78 semanas) para caracterizar los cambios metabólicos en cada condición, así como para distinguir patrones metabólicos únicos en comparación con los grupos de control.

En general, se observó que *HFD* puede causar una pérdida de la integridad de la membrana y, en consecuencia, una insuficiencia hepática, al reducir la relación Fosfatidilcolina y Fosfatidiletanolamina (*PC/PE*, siglas en inglés), que ha demostrado ser un buen predictor del desarrollo de *NAFLD* y de daño hepático. Además, se ha demostrado la apoptosis a través de la elevación de la Adenosina 5´difosforibosa (*ADPR*, siglas en inglés), un biomarcador vital implicado en varios procesos celulares como la necrosis, la apoptosis, la reparación del ADN y la regulación de la transcripción. Además, se observaron cambios en la fosforilación oxidativa, el metabolismo de los precursores de los fosfolípidos, lípidos, la glucólisis y la ruta de la pentosa fosfato.

Mientras tanto, el perfil fosforómico de animales hepáticos *CDHF* mostró una función mitocondrial alterada con una elevación de *NADH* y *$FADH_2$*, que son transportadores de electrones durante el proceso de respiración celular. Asimismo, los niveles elevados de fosfatidiletanolamina (*PE*, siglas en inglés) y sus precursores (fosfoetanolamina y glicerofosfoetanolamina (*PEA* y *GPE*, siglas en inglés)) sugirieron que el metabolismo de la *PE* se ha activado o que la actividad de la *PE* se

ha alterado parcialmente. Además, la deficiencia de colina (*CHO*, siglas en inglés) causó un impacto aberrante en el metabolismo de la colina, predisponiéndolo potencialmente a la *NAFLD*. Al igual que con el grupo *HFD*, se ha observado una reducción en la relación *PC/PE* que sugiere una desregulación de la integridad de la membrana debido a los cambios observados en el metabolismo de *CHO* y etanolamina. Además, los niveles elevados de *ADPR* hepática provocaron apoptosis y necrosis. Además, la reducción de UDP-N-acetil glucosamina (*UDPNAcglu*, siglas en inglés), el producto final de la vía biosintética de hexosamina, puede deberse a una disminución potencial de la supervivencia celular. Además, se observaron cambios en el metabolismo de la glucólisis, la ruta de la pentosa fosfato y nucleótidos, lo que provocó alteraciones en el metabolismo de los carbohidratos.

Asimismo, como se ha demostrado mediante análisis univariante, se observó una clara separación entre los perfiles metabólicos de hígado de ratones alimentados con *HFD* y *CDHF* con respecto a una dieta estándar (*STD*, siglas en inglés) mediante análisis supervisado.

Por otro lado, estudios previos han afirmado que el envejecimiento promueve factores de riesgo asociados con *NASH* como la inflamación, la diabetes y la obesidad, por lo que es vital comprender la implicación del envejecimiento en este estudio. Así, el Análisis Discriminante Mínimos Cuadrados Parciales (*PLS-DA*, siglas en inglés) mostró que hubo una clara separación entre el grupo de 20 semanas y los demás grupos, no observándose cambios significativos entre el grupo de 52 y 78 semanas, considerando que el envejecimiento era una variable necesaria a tener en cuenta en esta investigación.

Además, se realizaron análisis multivariados como *OPLS-DA*, donde se vio que había una clara separación entre los perfiles de fosforómica del hígado de ratones alimentados con *HFD* y *CDHF* en comparación con los que tenían *STD*, así como entre *HFD* y *CDHF*. Por otra parte, se comprobó la capacidad predictiva de este modelo indicando los resultados obtenidos que este modelo de entrenamiento tiene un buen poder explicativo, siendo capaz de diferenciar el perfil de fosforómica hepática obtenido por RMN de ratones alimentados con diferentes dietas que pueden desarrollar NAFLD. Además, por cada *OPLS-DA*, la mayoría de los diez metabolitos discriminantes se determinaron mediante la estimación de la puntuación VIP. Aunque preliminares, estos resultados son muy prometedores ya que sugieren que, si se aumenta el número de muestras analizadas, es posible distinguir los diferentes

fenotipos y crear un algoritmo que en el futuro ayude a determinar el estado del metabolismo hepático de los ratones, pudiendo ser alimentados con una dieta diferente que puede desarrollar *NAFLD*.

La metodología de ^{31}P-RMN no se ha optimizado para fines de metabolómica y no se ha establecido un flujo de trabajo sólido para implementarla en el campo de la metabolómica. Así, durante el Capítulo 5, con el único propósito de facilitar la aplicación de ^{31}P NMR en metabolómica, se desarrolló un protocolo bajo Procedimientos Operativos Estándar (*SOP* ,siglas en inglés), ya sea para la medición de la fracción hidrofílica o hidrofóbica, así como para facilitar el ajuste fino de las medidas de la muestra.

En primer lugar, para la fracción hidrófila, concluyó que el compuesto de referencia óptimo para el análisis cuantitativo de ^{31}P-RMN era Óxido de trimetilfosfina (*$OPMe_3$*, siglas en inglés) debido al T_1 más corto, que se requiere para la referenciación cuantitativa, aunque *TMP^+* también se mantuvo como segundo compuesto de referencia debido a una menor dependencia del pH.

En segundo lugar, debido a la interacción de los grupos fosfato y los cationes, que provocan la ampliación del intercambio químico o conformacional, se utilizó EDTA como agente quelante, asegurando que EDTA 2 mM tuviera la capacidad suficiente para capturar cationes divalentes y, en consecuencia, para estabilizar los metabolitos fosforilados.

En tercer lugar, el tampón de glicina 50 mM a pH 9,5 fue la elección óptima debido a su tampón de baja conductividad además de la alta estabilidad de los fosfometabolitos a pH 9,5. Además, la capacidad del EDTA para complejar cationes divalentes aumentó significativamente debido a su desprotonación con el uso de este tampón.

A continuación, se prefirió D_2O sobre H_2O porque la supresión de la señal residual de H_2O no presenta problemas y es robusta, lo que permite facilitar la medición de cualquier experimento 1D ^{1}H.

Además, el tiempo de relajación entálpica T_1 limita el retraso total entre escaneos τ para la cuantificación exacta ($\tau quant > 3.T_{1,max}$) y la relación señal/ruido máxima por unidad de tiempo ($SNmax \sim 1/\sqrt{\tau opt}$ at $\tau opt \sim 1.25.T_1$). Por lo tanto, la sensibilidad se

gana acelerando T_1 con un agente paramagnético de mejora de la relajación (*PRE*, siglas en inglés) pero sin acortar T_2, lo que demuestra que Gadoteridol (*Gdter*, siglas en inglés) era preferible a *Gdbut* porque *Gdbut* provocaba T_1 más corto pero también T_2 más corto, lo cual es indeseable, provocando el ensanchamiento de la línea.

En general, las bajas temperaturas produjeron espectros de ^{31}P-NMR de la más alta calidad, acelerando T_1 pero no acortando la mitad del ancho y aumentando la intensidad de la señal de los metabolitos fosforilados, aunque se necesitaba la presencia de un agente *PRE* debido a T_1 extremadamente largo de algunos fosfometabolitos como Glucosa 6-fosfato, Sedoheptulosa 7-fosfato, Fosfocolina y Fosfato inorgánico (*G6P*, *S7P*, *PCHO* y PO_4^{3-}, siglas en inglés).

Así, el balance entre la temperatura elegida y la cantidad de *Gdter* requerida fue crucial, determinando que el escenario óptimo implica 0.5 mM *Gdter* a una temperatura de 288 K, considerando que el deseado de T_1 (reducido a mayor cantidad de *Gdter*) y el indeseable el efecto de T_2 (reducción que causa el ensanchamiento de la línea) debe equilibrarse.
D_1, un parámetro limitante para el análisis cuantitativo de ^{31}P-RMN, debe estar en 7,0 segundos si se considera que más del 95 % de los fosfometabolitos se relajaron por completo, incluidas las especies que se relajan más lentamente, como G6P y la referencia para la cuantificación ($OPMe_3$). Sin embargo, después de algunas simulaciones, dada la gran mayoría del tiempo, la intensidad de la señal de la especie de relajación más rápida Nucleótido difosfoazúcar en posición β en el fósforo (*NDPS-Pβ*, siglas en inglés) fue menor y, en consecuencia, tuvo el SN0 más bajo en comparación con la especie de relajación más lenta (*G6P*), lo que aumentó el error de cuantificación y, por lo tanto, D_1 se acortó a 6 segundos.

Finalmente, en cuanto al extracto hidrofílico, se optimizó la temperatura a 2D ^{1}H,^{31}P HSQMBC-TOCSY para propósitos de asignaciones moleculares, demostrando que al aumentar la temperatura, con *Gdter* 0.5 mM, se observó una reducción significativa en la relajación ^{1}H y, en consecuencia, mejoró la ^{1}H- Correlación ^{31}P para algunas resonancias, especialmente para la región *NDPS*, concluyendo que este experimento 2D debería realizarse a 308 K.

Al mismo tiempo, para la fracción hidrofóbica, *TPPO* fue el compuesto de referencia óptimo para el análisis cuantitativo de ^{31}P-NMR debido a su corto T_1, siendo una recuperación de señal rápida. Por otro lado, d_6-DMSO fue el adecuado debido a su

intensidad de señal y buena dispersión de señal. Tiene un momento dipolar μ mayor (3,96 D), habiéndose observado una correlación entre cada parámetro químico y la dispersión e intensidad de la señal de ^{31}P.Asimismo, se evaluó el efecto de *Gdter* sobre una mezcla de fosfolípidos, en la que la adición de *Gdter* a una concentración baja de 0,05 mM provocó un ensanchamiento severo de las señales de ^{31}P, por lo que se evitó la adición de *PRE*.

Mientras tanto, se analizó el impacto de la temperatura en el extracto lipofílico de hígado de ratón, encontrándose el pico de mayor intensidad de los fosfolípidos a T = 310 K.
Finalmente, suponiendo que el retraso total entre *scans* para la cuantificación exacta $D_1 > 3.T_{1,max}$ (^{31}P) y el $T_{1,max}$(^{31}P) es del compuesto de referencia (1,71 s), el D_1 sugerido fue de 5 segundos.

En resumen, el fósforo hepático proporciona una instantánea del metabolismo del órgano para desentrañar el fenotipo metabólico de la lesión hepática e identificar el mecanismo de acción del fármaco, habiéndose desarrollado el método bajo estrictos *SOP* para la extracción de metabolitos, la asignación de metabolitos por ^{31}P -RMN y su cuantificación utilizando una referencia estándar en combinación con un compuesto paramagnético acelerador de la relajación así como un agente quelante además de optimizar la temperatura adecuada y el tampón o disolvente. Esta metodología podría aplicarse a diferentes modelos de enfermedades, líneas celulares, diferentes tejidos (corazón, cerebro, páncreas, entre otros) o diferentes sistemas biológicos incluidos los humanos. En el futuro, también se podría pretender automatizar la medición, el procesamiento y el análisis de las muestras, utilizando técnicas informáticas avanzadas para la integración de la base de datos en las rutas del metabolismo.

REFERENCES

1. Araújo, A. M., Carvalho, M., Carvalho, F., Bastos, M. de L. & Guedes de Pinho, P. Metabolomic approaches in the discovery of potential urinary biomarkers of drug-induced liver injury (DILI). *Critical Reviews in Toxicology* vol. 47 633–649 Preprint at https://doi.org/10.1080/10408444.2017.1309638 (2017).
2. Horgan, R. P. & Kenny, L. C. 'Omic' technologies: genomics, transcriptomics, proteomics and metabolomics. *The Obstetrician & Gynaecologist* **13**, 189–195 (2011).
3. Kell, D. B. & Oliver, S. G. Here is the evidence, now what is the hypothesis? The complementary roles of inductive and hypothesis-driven science in the post-genomic era. *BioEssays* vol. 26 99–105 Preprint at https://doi.org/10.1002/bies.10385 (2004).
4. Shannon, P. *et al.* Cytoscape: A software Environment for integrated models of biomolecular interaction networks. *Genome Res* **13**, 2498–2504 (2003).
5. Zhou, G. & Xia, J. Using OmicsNet for Network Integration and 3D Visualization. *Curr Protoc Bioinformatics* **65**, (2019).
6. Rohart, F., Gautier, B., Singh, A. & Lê Cao, K. A. mixOmics: An R package for 'omics feature selection and multiple data integration. *PLoS Comput Biol* **13**, (2017).
7. Hernandez-Ferrer, C., Ruiz-Arenas, C., Beltran-Gomila, A. & González, J. R. MultiDataSet: An R package for encapsulating multiple data sets with application to omic data integration. *BMC Bioinformatics* **18**, (2017).
8. Thum, K. E. *et al.* An integrated genetic, genomic and systems approach defines gene networks regulated by the interaction of light and carbon signaling pathways in Arabidopsis. *BMC Syst Biol* **2**, (2008).
9. Haukaas, T. H., Euceda, L. R., Giskeødegård, G. F. & Bathen, T. F. Metabolic portraits of breast cancer by HR MAS MR spectroscopy of intact tissue samples. *Metabolites* vol. 7 Preprint at https://doi.org/10.3390/metabo7020018 (2017).
10. Aretz, I. & Meierhofer, D. Advantages and pitfalls of mass spectrometry based metabolome profiling in systems biology. *International Journal of Molecular Sciences* vol. 17 Preprint at https://doi.org/10.3390/ijms17050632 (2016).
11. Chaleckis, R., Meister, I., Zhang, P. & Wheelock, C. E. Challenges, progress and promises of metabolite annotation for LC–MS-based metabolomics. *Current Opinion in Biotechnology* vol. 55 44–50 Preprint at https://doi.org/10.1016/j.copbio.2018.07.010 (2019).

12. Fiehn, O. *Metabolomics-the link between genotypes and phenotypes*. *Plant Molecular Biology* vol. 48 (2002).
13. Viant, M. R., Kurland, I. J., Jones, M. R. & Dunn, W. B. How close are we to complete annotation of metabolomes? *Current Opinion in Chemical Biology* vol. 36 64–69 Preprint at https://doi.org/10.1016/j.cbpa.2017.01.001 (2017).
14. Fiehn, O. Combining genomics, metabolome analysis, and biochemical modelling to understand metabolic networks. *Comparative and Functional Genomics* vol. 2 155–168 Preprint at https://doi.org/10.1002/cfg.82 (2001).
15. Ren, S., Hinzman, A. A., Kang, E. L., Szczesniak, R. D. & Lu, L. J. Computational and statistical analysis of metabolomics data. *Metabolomics* vol. 11 1492–1513 Preprint at https://doi.org/10.1007/s11306-015-0823-6 (2015).
16. Bujak, R., Struck-Lewicka, W., Markuszewski, M. J. & Kaliszan, R. Metabolomics for laboratory diagnostics. *Journal of Pharmaceutical and Biomedical Analysis* vol. 113 108–120 Preprint at https://doi.org/10.1016/j.jpba.2014.12.017 (2015).
17. Goodacre, R., Vaidyanathan, S., Dunn, W. B., Harrigan, G. G. & Kell, D. B. Metabolomics by numbers: Acquiring and understanding global metabolite data. *Trends in Biotechnology* vol. 22 245–252 Preprint at https://doi.org/10.1016/j.tibtech.2004.03.007 (2004).
18. Dunn, W. B. & Ellis, D. I. Metabolomics: Current analytical platforms and methodologies. *TrAC - Trends in Analytical Chemistry* **24**, 285–294 (2005).
19. Nicholson, J. K., Lindon, J. C. & Holmes, E. *understanding the metabolic responses of living systems to pathophysiological stimuli via multivariate statistical analysis of biological NMR spectroscopic data*. www.taylorandfrancis.com}.
20. Nicholson, J. K., Lindon, J. C. & Holmes, E. *understanding the metabolic responses of living systems to pathophysiological stimuli via multivariate statistical analysis of biological NMR spectroscopic data*. www.taylorandfrancis.com}.
21. Allen, J. *et al. High-throughput classification of yeast mutants for functional genomics using metabolic footprinting*. *NATURE BIOTECHNOLOGY 1 Institute of Biological Sciences* vol. 21 http://mips.gsf.de/proj/yeast/CYGD/db/index.html (2003).
22. Kell, D. B. *et al.* Metabolic footprinting and systems biology: The medium is the message. *Nature Reviews Microbiology* vol. 3 557–565 Preprint at https://doi.org/10.1038/nrmicro1177 (2005).
23. Becker, S., Kortz, L., Helmschrodt, C., Thiery, J. & Ceglarek, U. LC-MS-based metabolomics in the clinical laboratory. *Journal of Chromatography B: Analytical Technologies in the Biomedical and Life Sciences* vols 883–884 68–75 Preprint at https://doi.org/10.1016/j.jchromb.2011.10.018 (2012).

24. Califf, R. M. Biomarker definitions and their applications. *Exp Biol Med* **243**, 213–221 (2018).
25. Beger, R. A Review of Applications of Metabolomics in Cancer. *Metabolites* **3**, 552–574 (2013).
26. Barnes, S. *et al.* Training in metabolomics research. I. Designing the experiment, collecting and extracting samples and generating metabolomics data. *Journal of Mass Spectrometry* 461–475 (2016) doi:10.1002/jms.3782.
27. Ferreira, J. A. & Zwinderman, A. Approximate sample size calculations with microarray data: An illustration. *Stat Appl Genet Mol Biol* **5**, (2006).
28. Blaise, B. J. Data-driven sample size determination for metabolic phenotyping studies. *Anal Chem* **85**, 8943–8950 (2013).
29. Liang, Y. J., Wang, H. P., Yang, L., Li, W. & Wu, Y. J. Metabonomic responses in rat urine following subacute exposure to propoxur. *Int J Toxicol* **31**, 287–293 (2012).
30. Boudonck, K. J. *et al.* Discovery of Metabolomics Biomarkers for Early Detection of Nephrotoxicity. *Toxicol Pathol* **37**, 280–292 (2009).
31. Kim, H. J. *et al.* LC-MS-based metabolomic analysis of serum and livers from red ginseng-fed rats. *J Ginseng Res* **37**, 371–378 (2013).
32. Dunn, W. B. & Ellis, D. I. Metabolomics: Current analytical platforms and methodologies. *TrAC - Trends in Analytical Chemistry* **24**, 285–294 (2005).
33. Dunn, W. B. *et al.* Procedures for large-scale metabolic profiling of serum and plasma using gas chromatography and liquid chromatography coupled to mass spectrometry. *Nat Protoc* **6**, 1060–1083 (2011).
34. Want, E. J. *et al.* Global metabolic profiling of animal and human tissues via UPLC-MS. *Nat Protoc* **8**, 17–32 (2013).
35. Naz, S., García, A. & Barbas, C. Multiplatform analytical methodology for metabolic fingerprinting of lung tissue. *Anal Chem* **85**, 10941–10948 (2013).
36. Kapoore, R. V. & Vaidyanathan, S. Towards quantitative mass spectrometry-based metabolomics in microbial and mammalian systems. *Philosophical Transactions of the Royal Society A: Mathematical, Physical and Engineering Sciences* vol. 374 Preprint at https://doi.org/10.1098/rsta.2015.0363 (2016).
37. Larive, C. K., Barding, G. A. & Dinges, M. M. NMR spectroscopy for metabolomics and metabolic profiling. *Analytical Chemistry* vol. 87 133–146 Preprint at https://doi.org/10.1021/ac504075g (2015).
38. Nagana Gowda, G. A. & Raftery, D. Recent advances in NMR-based metabolomics. *Analytical Chemistry* vol. 89 490–510 Preprint at https://doi.org/10.1021/acs.analchem.6b04420 (2017).

39. Cui, L., Lu, H. & Lee, Y. H. Challenges and emergent solutions for LC-MS/MS based untargeted metabolomics in diseases. *Mass Spectrometry Reviews* vol. 37 772–792 Preprint at https://doi.org/10.1002/mas.21562 (2018).
40. Saigusa, D. *et al.* Establishment of protocols for global metabolomics by LC-MS for biomarker discovery. *PLoS One* **11**, (2016).
41. Emwas, A. H. M. The strengths and weaknesses of NMR spectroscopy and mass spectrometry with particular focus on metabolomics research. *Methods in Molecular Biology* **1277**, 161–193 (2015).
42. Amiel, A. *et al.* Proton NMR enables the absolute quantification of aqueous metabolites and lipid classes in unique mouse liver samples. *Metabolites* **10**, (2020).
43. Hao, J., Astle, W., De iorio, M. & Ebbels, T. M. D. Batman-an R package for the automated quantification of metabolites from nuclear magnetic resonance spectra using a bayesian model. *Bioinformatics* **28**, 2088–2090 (2012).
44. Ravanbakhsh, S. *et al.* Accurate, fully-automated NMR spectral profiling for metabolomics. *PLoS One* **10**, (2015).
45. Giraudeau, P., Silvestre, V. & Akoka, S. Optimizing water suppression for quantitative NMR-based metabolomics: a tutorial review. *Metabolomics* vol. 11 1041–1055 Preprint at https://doi.org/10.1007/s11306-015-0794-7 (2015).
46. Gu~ron, M., Plateau+, P. & Decorps, M. *SOLVENT SIGNAL SUPPRESSION IN NMR*. *Pmgress ia NMR Spectroscopy* vol. 23 (1991).
47. Emwas, A. H. *et al.* Nmr spectroscopy for metabolomics research. *Metabolites* vol. 9 Preprint at https://doi.org/10.3390/metabo9070123 (2019).
48. Cloarec, O. *et al.* Statistical total correlation spectroscopy: An exploratory approach for latent biomarker identification from metabolic 1H NMR data sets. *Anal Chem* **77**, 1282–1289 (2005).
49. Fonville, J. M. *et al.* Evaluation of full-resolution J-resolved1H NMR projections of biofluids for metabonomics information retrieval and biomarker identification. *Anal Chem* **82**, 1811–1821 (2010).
50. Maclean, H., Fellow, C. & Williams, O. T. *ON THE NATURE OF THE SO-CALLED FAT OF TISSUES AND ORGANS*.
51. Iles, R. A. *et al. Effects of fructose on the energy metabolism and acid-base status of the perfused starved-rat liver A 31phosphorus nuclear magnetic resonance study*. *Biochem. J* vol. 192 (1980).
52. Iles, R. A., Stevens, A. N., Griffithst, J. R. & Morrist, P. G. *41 Printed in Great Britain*. *Biochem. J* vol. 229 (1985).
53. Khan, S. A., Cox, I. J., Hamilton, G., Thomas, H. C. & Taylor-Robinson, S. D. In

vivo and in vitro nuclear magnetic resonance spectroscopy as a tool for investigating hepatobiliary disease: A Review of 1H and 31P MRS applications. *Liver International* vol. 25 273–281 Preprint at https://doi.org/10.1111/j.1478-3231.2005.01090.x (2005).

54. Setiawan, V. W. *et al.* Prevalence of chronic liver disease and cirrhosis by underlying cause in understudied ethnic groups: The multiethnic cohort. *Hepatology* **64**, 1969–1977 (2016).
55. Suzuki, A. & Diehl, A. M. Nonalcoholic Steatohepatitis. *Annual Review of Medicine* vol. 68 85–98 Preprint at https://doi.org/10.1146/annurev-med-051215-031109 (2017).
56. Cassidy, S. & Syed, B. A. Nonalcoholic steatohepatitis (NASH) drugs market. doi:10.1038/nrd2016.188.
57. Mayo, R. *et al.* Metabolomic-Based Noninvasive Serum Test to Diagnose Nonalcoholic Steatohepatitis: Results From Discovery and Validation Cohorts. (2018) doi:10.1002/hep4.1188/full.
58. Younossi, Z. M. Non-alcoholic fatty liver disease – A global public health perspective. *Journal of Hepatology* vol. 70 531–544 Preprint at https://doi.org/10.1016/j.jhep.2018.10.033 (2019).
59. Noren, B. *et al.* Separation of advanced from mild fibrosis in diffuse liver disease using 31P magnetic resonance spectroscopy. *Eur J Radiol* **66**, 313–320 (2008).
60. Sevastianova, K. *et al.* Nonalcoholic fatty liver disease: Detection of elevated nicotinamide adenine dinucleotide phosphate with in vivo 3.0-T31P MR spectroscopy with proton decoupling. *Radiology* **256**, 466–473 (2010).
61. Traussnigg, S. *et al.* Ultra-high-field magnetic resonance spectroscopy in non-alcoholic fatty liver disease: Novel mechanistic and diagnostic insights of energy metabolism in non-alcoholic steatohepatitis and advanced fibrosis. *Liver International* **37**, 1544–1553 (2017).
62. Rijpma, A., van der Graaf, M., Meulenbroek, O., Olde Rikkert, M. G. M. & Heerschap, A. Altered brain high-energy phosphate metabolism in mild Alzheimer's disease: A 3-dimensional 31P MR spectroscopic imaging study. *Neuroimage Clin* **18**, 254–261 (2018).
63. Hull, W. E., Lutz, N. W., Franks, S. E., Frank, M. H. & Pomer, S. Investigation of multidrug resistance in cultured human renal cell carcinoma cells by 31P-NMR spectroscopy and treatment survival assays. *Magnetic Resonance Materials in Physics, Biology and Medicine* **18**, 144–161 (2005).
64. Jung, W.-I. *et al. P NMR Spectroscopy Detects Metabolic Abnormalities in Asymptomatic Patients With Hypertrophic Cardiomyopathy*.

http://circ.ahajournals.org/ (1998).

65. Merchant, T. E., De Graaf, P. W., Minsky, B. D., Obertopt, H. & Gloneks, T. *Esophageal Cancer Phospholipid Characterization by 31P NMR*. *NMR IN BIOMEDICINE* vol. 6 (1993).
66. Kaplan, O., Van Zijl, P. C. M. & Cohen, J. S. *BIOCHEMICAL AND BIOPHYSICAL RESEARCH COMMUNICATIONS*. vol. 169 (1990).
67. Sukumaran, D. K. *et al.* Standard operating procedure formetabonomics studies of blood serum and plasma samples using a 1H-NMR micro-flow probe. *Magnetic Resonance in Chemistry* **47**, (2009).
68. Sumner, L. W. *et al.* Proposed minimum reporting standards for chemical analysis: Chemical Analysis Working Group (CAWG) Metabolomics Standards Initiative (MSI). *Metabolomics* **3**, 211–221 (2007).
69. Lutz, N. W. & Cozzone, P. J. Principles of multiparametric optimization for phospholipidomics by 31P NMR spectroscopy. *Biophysical Reviews* vol. 5 295–304 Preprint at https://doi.org/10.1007/s12551-013-0105-3 (2013).
70. Scholarship@western, S., Sharma, H. A. & Bartha, R. *Multiparametric Imaging and MR Image Texture Analysis in Brain Tumors*. https://ir.lib.uwo.ca/etdhttps://ir.lib.uwo.ca/etd/1967 (2014).
71. Hoch, J. C. *et al.* Biological Magnetic Resonance Data Bank. *Nucleic Acids Res* **51**, D368–D376 (2023).
72. Wishart, D. S. *et al.* HMDB 5.0: The Human Metabolome Database for 2022. *Nucleic Acids Res* **50**, D622–D631 (2022).
73. Ludwig, C. *et al.* Birmingham Metabolite Library: A publicly accessible database of 1-D 1H and 2-D 1H J-resolved NMR spectra of authentic metabolite standards (BML-NMR). *Metabolomics* **8**, 8–18 (2012).
74. Bingol, K., Zhang, F., Bruschweiler-Li, L. & Brüschweiler, R. TOCCATA: A customized carbon total correlation spectroscopy NMR metabolomics database. *Anal Chem* **84**, 9395–9401 (2012).
75. Brennan, L. NMR-based metabolomics: From sample preparation to applications in nutrition research. *Progress in Nuclear Magnetic Resonance Spectroscopy* vol. 83 42–49 Preprint at https://doi.org/10.1016/j.pnmrs.2014.09.001 (2014).
76. Barker, M. & Rayens, W. Partial least squares for discrimination. *J Chemom* **17**, 166–173 (2003).
77. Gromski, P. S. *et al.* A tutorial review: Metabolomics and partial least squares-discriminant analysis - a marriage of convenience or a shotgun wedding. *Analytica Chimica Acta* vol. 879 10–23 Preprint at https://doi.org/10.1016/j.aca.2015.02.012 (2015).

78. Du, J. *et al.* KEGG-PATH: Kyoto encyclopedia of genes and genomes-based pathway analysis using a path analysis model. *Mol Biosyst* **10**, 2441–2447 (2014).
79. Frolkis, A. *et al.* SMPDB: The small molecule pathway database. *Nucleic Acids Res* **38**, (2009).
80. Caspi, R. *et al.* The MetaCyc database of metabolic pathways and enzymes-a 2019 update. *Nucleic Acids Res* **48**, D455–D453 (2020).
81. Slenter, D. N. *et al.* WikiPathways: A multifaceted pathway database bridging metabolomics to other omics research. *Nucleic Acids Res* **46**, D661–D667 (2018).
82. Wishart, D. S. Metabolomics: applications to food science and nutrition research. *Trends Food Sci Technol* **19**, 482–493 (2008).
83. Wishart, D. S. *et al.* HMDB 4.0: The human metabolome database for 2018. *Nucleic Acids Res* **46**, D608–D617 (2018).
84. Wishart, D. S. Proteomics and the Human Metabolome Project. *Expert Rev Proteomics* **4**, 333–335 (2007).
85. Wishart, D. S. *et al.* HMDB: A knowledgebase for the human metabolome. *Nucleic Acids Res* **37**, 603–610 (2009).
86. Wishart, D. S. *et al.* HMDB 3.0-The Human Metabolome Database in 2013. *Nucleic Acids Res* **41**, 1–7 (2013).
87. Dias, D. A. *et al.* Current and future perspectives on the structural identification of small molecules in biological systems. *Metabolites* **6**, (2016).
88. Jeffryes, J. G. *et al.* MINEs: Open access databases of computationally predicted enzyme promiscuity products for untargeted metabolomics. *J Cheminform* **7**, 1–8 (2015).
89. Allen, F., Pon, A., Wilson, M., Greiner, R. & Wishart, D. CFM-ID: A web server for annotation, spectrum prediction and metabolite identification from tandem mass spectra. *Nucleic Acids Res* **42**, 94–99 (2014).
90. Gao, J., Ellis, L. B. M. & Wackett, L. P. The University of Minnesota Biocatalysis/Biodegradation Database: Improving public access. *Nucleic Acids Res* **38**, 1–4 (2009).
91. Walsh, C. T., Tu, B. P. & Tang, Y. Eight Kinetically Stable but Thermodynamically Activated Molecules that Power Cell Metabolism. *Chem Rev* **118**, 1460–1494 (2018).
92. Pietrocola, F., Galluzzi, L., Bravo-San Pedro, J. M., Madeo, F. & Kroemer, G. Acetyl coenzyme A: A central metabolite and second messenger. *Cell Metab* **21**, 805–821 (2015).
93. Cantó, C., Menzies, K. J. & Auwerx, J. NAD+ Metabolism and the Control of Energy Homeostasis: A Balancing Act between Mitochondria and the Nucleus.

Cell Metab **22**, 31–53 (2015).

94. Walsh, C. T., Tu, B. P. & Tang, Y. Eight Kinetically Stable but Thermodynamically Activated Molecules that Power Cell Metabolism. *Chemical Reviews* vol. 118 1460–1494 Preprint at https://doi.org/10.1021/acs.chemrev.7b00510 (2018).
95. Westheimer, F. H. Nature Chose Phosphates The Role of Phosphates The Importance of Being Ionized. *Science* **235**, 1173–1178 (1987).
96. Van Der Donk, W. A. Introduction: Unusual Enzymology in Natural Product Synthesis. *Chem Rev* **117**, 5223–5225 (2017).
97. Chang, M. Metabolic Signature of Hepatic Fibrosis : 1–20 (2019).
98. Ã, Q. M. A. & Goldin, R. D. <Iep0087-0001.Pdf>. 1–16 (2006).
99. Farrell, G. *et al.* Mouse Models of Nonalcoholic Steatohepatitis: Toward Optimization of Their Relevance to Human Nonalcoholic Steatohepatitis. *Hepatology* **69**, 2241–2257 (2019).
100. Haczeyni, F. *et al.* Mouse models of non-alcoholic steatohepatitis: A reflection on recent literature. *Journal of Gastroenterology and Hepatology (Australia)* **33**, 1312–1320 (2018).
101. Kilkenny, C., Browne, W. J., Cuthill, I. C., Emerson, M. & Altman, D. G. Improving bioscience research reporting: The arrive guidelines for reporting animal research. *PLoS Biol* **8**, 6–11 (2010).
102. du Sert, N. P. *et al. Reporting animal research: Explanation and elaboration for the arrive guidelines 2.0*. *PLoS Biology* vol. 18 (2020).
103. du Sert, N. P. *et al.* The arrive guidelines 2.0: Updated guidelines for reporting animal research. *PLoS Biol* **18**, 1–12 (2020).
104. Weltman, M. D., Farrell, G. C. & Liddle, C. Increased Hepatocyte. 1645–1653 (1996).
105. Reid, D. T. & Eksteen, B. Murine models provide insight to the development of non-alcoholic fatty liver disease. *Nutr Res Rev* **28**, 133–142 (2015).
106. Alonso, C. *et al.* Metabolomic Identification of Subtypes of Nonalcoholic Steatohepatitis. *Gastroenterology* **152**, 1449-1461.e7 (2017).
107. Fernández-Ramos, D. *et al.* Arachidyl amido cholanoic acid improves liver glucose and lipid homeostasis in nonalcoholic steatohepatitis via AMPK and mTOR regulation. *World J Gastroenterol* **26**, 5101–5117 (2020).
108. Witze, E. S., Old, W. M., Resing, K. A. & Ahn, N. G. <Nature Methods 2007 Witze.pdf>. **4**, (2007).
109. Kumar, G. S., Page, R. & Peti, W. *Preparation of Phosphorylated Proteins for NMR Spectroscopy*. *Methods in Enzymology* vol. 614 (Elsevier Inc., 2019).
110. Emwas, A. H. *et al.* Nmr spectroscopy for metabolomics research. *Metabolites* **9**,

(2019).

111. Bell, J. D. *et al.* A 31P and 1H-NMR investigation in vitro of normal and abnormal human liver. *BBA - Molecular Basis of Disease* **1225**, 71–77 (1993).
112. Harvey, P. J., Gready, J. E., Hickey, H. M., Le Couteur, D. G. & McLean, A. J. 31P and 1H NMR spectroscopic studies of liver extracts of carbon tetrachloride-treated rats. *NMR Biomed* **12**, 395–401 (1999).
113. Jeon, M. J. *et al.* High resolution in vivo 31P-MRS of the liver: Potential advantages in the assessment of non-alcoholic fatty liver disease. *Acta radiol* **56**, 1051–1060 (2015).
114. Information From Combined 1H And 3IP NMR Studies Of Cell Extracts : Differences In Metabolism Between Drug-Sensitive And MCF-7 Human Breast Cancer Cells Ofer Kaplan , Peter C . M . van Zijl , and Jack S . Cohen Medicine Branch , NCI , National Institutes . **169**, 383–390 (1990).
115. Ruiz-Cabello, J. & Cohen, J. S. Phospholipid metabolites as indicators of cancer cell function. *NMR Biomed* **5**, 226–233 (1992).
116. Bernardo-Seisdedos, G. *et al.* Metabolic Landscape of the Mouse Liver by Quantitative 31P Nuclear Magnetic Resonance Analysis of the Phosphorome. *Hepatology* **74**, 148–163 (2021).
117. Dsnick, R. J. & Astrin, K. H. Congenital erythropoietic porphyria: Advances in pathogenesis and treatment. *Br J Haematol* **117**, 779–795 (2002).
118. Dailey, H. A. & Meissner, P. N. Erythroid heme biosynthesis and its disorders. *Cold Spring Harb Perspect Med* **3**, (2013).
119. Urquiza, P. *et al.* Repurposing ciclopirox as a pharmacological chaperone in a model of congenital erythropoietic porphyria. *Sci Transl Med* **10**, (2018).
120. Lu, S. C. *et al.* Methionine adenosyltransferase 1A knockout mice are predisposed to liver injury and exhibit increased expression of genes involved. *Pnas* **98**, 5560–5565 (2011).
121. CATONI, G. L. S-Adenosylmethionine; a new intermediate formed enzymatically from L-methionine and adenosinetriphosphate. *J Biol Chem* **204**, 403–416 (1953).
122. Chiba, T., Suzuki, S., Sato, Y., Itoh, T. & Umegaki, K. Evaluation of methionine content in a high-fat and choline-deficient diet on body weight gain and the development of non-alcoholic steatohepatitis in mice. *PLoS One* **11**, (2016).
123. Ikawa-Yoshida, A. *et al.* Hepatocellular carcinoma in a mouse model fed a choline-deficient, L-amino acid-defined, high-fat diet. *Int J Exp Pathol* **98**, 221–233 (2017).
124. Fondevila, M. F. *et al.* The L-α-Lysophosphatidylinositol/G Protein–Coupled Receptor 55 System Induces the Development of Nonalcoholic Steatosis and Steatohepatitis. *Hepatology* **73**, 606–624 (2021).

125. Wolf, M. J. *et al.* Metabolic activation of intrahepatic CD8+ T cells and NKT cells causes nonalcoholic steatohepatitis and liver cancer via cross-talk with hepatocytes. *Cancer Cell* **26**, 549–564 (2014).
126. Kleiner, D. E. *et al.* Design and validation of a histological scoring system for nonalcoholic fatty liver disease. *Hepatology* **41**, 1313–1321 (2005).
127. Bligh, E.G. and Dyer, W. J. Canadian Journal of Biochemistry and Physiology. *Can J Biochem Physiol* **37**, (1959).
128. Nagana Gowda, G. A. & Raftery, D. Analysis of Coenzymes and Antioxidants in Tissue and Blood Using 1D 1H NMR Spectroscopy. in *Methods in Molecular Biology* vol. 2037 97–110 (Humana Press Inc., 2019).
129. Metabolomics, N., Honrao, C., Teissier, N., Zhang, B. & Powers, R. Gadolinium-Based Paramagnetic Relaxation Enhancement. (2021).
130. Bock, F. J. & Chang, P. New directions in poly(ADP-ribose) polymerase biology. *FEBS Journal* **283**, 4017–4031 (2016).
131. van der Veen, J. N. *et al.* The critical role of phosphatidylcholine and phosphatidylethanolamine metabolism in health and disease. *Biochim Biophys Acta Biomembr* **1859**, 1558–1572 (2017).
132. DeLong, C. J., Shen, Y. J., Thomas, M. J. & Cui, Z. Molecular distinction of phosphatidylcholine synthesis between the CDP- choline pathway and phosphatidylethanolamine methylation pathway. *Journal of Biological Chemistry* **274**, 29683–29688 (1999).
133. Li, Z. *et al.* The ratio of phosphatidylcholine to phosphatidylethanolamine influences membrane integrity and steatohepatitis. *Cell Metab* **3**, 321–331 (2006).
134. Ren, M., Phoon, C. K. L. & Schlame, M. Metabolism and function of mitochondrial cardiolipin. *Prog Lipid Res* **55**, 1–16 (2014).
135. Houtkooper, R. H. & Vaz, F. M. Cardiolipin, the heart of mitochondrial metabolism. *Cellular and Molecular Life Sciences* **65**, 2493–2506 (2008).
136. Romeo, B. Y. G. & Levin, E. Y. Cosynthetase in human congenital erythropoietic porphyria * by giovanni romeo. *Cellulose* 856–863 (1969).
137. Erwin, A. L. & Desnick, R. J. Congenital erythropoietic porphyria: Recent advances. *Mol Genet Metab* **128**, 288–297 (2019).
138. Bickers, D. R. & Frank, J. The Porphyrias : Introduction. 1–59 (2023).
139. Bishop, D. F., Tchaikovskii, V., Hoffbrand, A. V., Fraser, M. E. & Margolis, S. X-linked sideroblastic anemia due to carboxyl-terminal ALAS2 mutations that cause loss of binding to the β-subunit of succinyl-CoA synthetase (SUCLA2). *Journal of Biological Chemistry* **287**, 28943–28955 (2012).
140. Di Pierro, E., Brancaleoni, V. & Granata, F. Advances in understanding the

pathogenesis of congenital erythropoietic porphyria. *Br J Haematol* **173**, 365–379 (2016).

141. Desnick, R. J., Glass, I. A., Xu, W., Solis, C. & Astrin, K. H. Molecular genetics of congenital erythropoietic porphyria. *Semin Liver Dis* **18**, 77–84 (1998).
142. Sachar, M., Anderson, K. E. & Ma, X. Protoporphyrin IX: The good, the bad, and the ugly. *Journal of Pharmacology and Experimental Therapeutics* **356**, 267–275 (2016).
143. Lee, W. H., Tai, W. C. & Wu, P. Y. Congenital erythropoietic porphyria. *Dermatologica Sinica* **30**, 62–65 (2012).
144. Blouin, J. M. *et al.* Therapeutic potential of proteasome inhibitors in congenital erythropoietic porphyria. *Proc Natl Acad Sci U S A* **110**, 18238–18243 (2013).
145. Bishop, D. F., Clavero, S., Mohandas, N. & Desnick, R. J. Congenital erythropoietic porphyria: Characterization of murine models of the severe common (C73R/C73R) and later-onset genotypes. *Molecular Medicine* **17**, 748–756 (2011).
146. Ph, D. Erythropoietic. (1967).
147. Content, P. & Marrow, B. in the Various Forms of Porphyria. (2015).
148. Studies in Congenital Porphyria. **47**, 87–92 (1950).
149. Venkatesh, K. V, Darunte, L. & Bhat, P. J. Encyclopedia of Systems Biology. *Encyclopedia of Systems Biology* (2013) doi:10.1007/978-1-4419-9863-7.
150. Warburg, O. O n the origin. *Science (1979)* **123**, 309–314 (1956).
151. Chacko, B. *et al.* Feasibility of cellular bioenergetics as a biomarker in porphyria patients. *Mol Genet Metab Rep* **19**, 100451 (2019).
152. Lee, J. C. *et al.* The iron chelator, Dp44mT, effectively inhibits human oral squamous cell carcinoma cell growth in vitro and in vivo. *Int J Mol Sci* **17**, 1–13 (2016).
153. Pourcelot, E. *et al.* Iron for proliferation of cell lines and hematopoietic progenitors: Nailing down the intracellular functional iron concentration. *Biochim Biophys Acta Mol Cell Res* **1853**, 1596–1605 (2015).
154. Lloyd, R. V., Hanna, P. M. & Mason, R. P. The origin of the hydroxyl radical oxygenin the fenton reaction. *Free Radic Biol Med* **22**, 885–888 (1997).
155. Mello-Filho, A. C. & Meneghini, R. Iron is the intracellular metal involved in the production of DNA damage by oxygen radicals. *Mutation Research - Fundamental and Molecular Mechanisms of Mutagenesis* **251**, 109–113 (1991).
156. Sengupta, A., Hon, T. & Zhang, L. Heme deficiency suppresses the expression of key neuronal genes and causes neuronal cell death. *Molecular Brain Research* **137**, 23–30 (2005).

157. Perraud, A. L. *et al.* Accumulation of free ADP-ribose from mitochondria mediates oxidative stress-induced gating of TRPM2 cation channels. *Journal of Biological Chemistry* **280**, 6138–6148 (2005).
158. Kakisaka, K. *et al.* Mechanisms of lysophosphatidylcholine-induced hepatocyte lipoapoptosis. *Am J Physiol Gastrointest Liver Physiol* **302**, 77–84 (2012).
159. Puri, P. *et al.* A lipidomic analysis of nonalcoholic fatty liver disease. *Hepatology* **46**, 1081–1090 (2007).
160. Lu, Y. W. & Claypool, S. M. Disorders of phospholipid metabolism: An emerging class of mitochondrial disease due to defects in nuclear genes. *Front Genet* **6**, 1–28 (2015).
161. Alonso, C., Noureddin, M., Lu, S. C. & Mato, J. M. Biomarkers and subtypes of deranged lipid metabolism in nonalcoholic fatty liver disease. *World J Gastroenterol* **25**, 3009–3020 (2019).
162. Liberti, M. V. & Locasale, J. W. The Warburg Effect: How Does it Benefit Cancer Cells? *Trends Biochem Sci* **41**, 211–218 (2016).
163. Fortian, A. *et al.* Uroporphyrinogen III synthase mutations related to congenital erythropoietic porphyria identify a key helix for protein stability. *Biochemistry* **48**, 454–461 (2009).
164. Blouin, J. M. *et al.* Missense UROS mutations causing congenital erythropoietic porphyria reduce UROS homeostasis that can be rescued by proteasome inhibition. *Hum Mol Genet* **26**, 1565–1576 (2017).
165. Fortian, A., González, E., Castaño, D., Falcon-Perez, J. M. & Millet, O. Intracellular rescue of the uroporphyrinogen III synthase activity in enzymes carrying the hotspot mutation C73R. *Journal of Biological Chemistry* **286**, 13127–13133 (2011).
166. Kotb, M. *et al.* Consensus nomenclature for the mammalian methionine adenosyltransferase genes and gene products. *Trends Genet* **13**, 51–52 (1997).
167. Gil, B. *et al.* Differential expression pattern of S-adenosylmethionine synthetase isoenzymes during rat liver development. *Hepatology* **24**, 876–881 (1996).
168. Mato, J. M. & Lu, S. C. Role of S-adenosyl-L-methionine in liver health and injury. *Hepatology* **45**, 1306–1312 (2007).
169. Cano, A. *et al.* Methionine adenosyltransferase 1A gene deletion disrupts hepatic very low-density lipoprotein assembly in mice. *Hepatology* **54**, 1975–1986 (2011).
170. Kim, S. H. *et al.* Comparative study of fatty liver induced by methionine and choline-deficiency in C57BL/6N mice originating from three different sources. *Lab Anim Res* **33**, 157 (2017).
171. Varela-Rey, M. *et al.* Non-alcoholic steatohepatitis and animal models:

Understanding the human disease. *International Journal of Biochemistry and Cell Biology* **41**, 969–976 (2009).

172. Kanuri, G. & Bergheim, I. In vitro and in vivo models of non-alcoholic fatty liver disease (NAFLD). *Int J Mol Sci* **14**, 11963–11980 (2013).
173. Ueland, P. M. Choline and betaine in health and disease. *J Inherit Metab Dis* **34**, 3–15 (2011).
174. Sayiner, M., Koenig, A., Henry, L. & Younossi, Z. M. Epidemiology of Nonalcoholic Fatty Liver Disease and Nonalcoholic Steatohepatitis in the United States and the Rest of the World. *Clin Liver Dis* **20**, 205–214 (2016).
175. Marchesini, G. & Marzocchi, R. Metabolic Syndrome and NASH. *Clin Liver Dis* **11**, 105–117 (2007).
176. Lim, H. Bin, Kim, D. Y. & Kim, J. Y. Reply. *Retina* **38**, e31–e33 (2018).
177. Targher, G., Corey, K. E., Byrne, C. D. & Roden, M. The complex link between NAFLD and type 2 diabetes mellitus — mechanisms and treatments. *Nat Rev Gastroenterol Hepatol* **18**, 599–612 (2021).
178. Chatrath, H., Vuppalanchi, R. & Chalasani, N. Dyslipidemia in patients with nonalcoholic fatty liver disease. *Semin Liver Dis* **32**, 22–29 (2012).
179. Powell, E. E., Wong, V. W. S. & Rinella, M. Non-alcoholic fatty liver disease. *The Lancet* **397**, 2212–2224 (2021).
180. Wu, W. *et al.* Worldwide long-term trends in the incidence of nonalcoholic fatty liver disease during 1990–2019: A joinpoint and age-period-cohort analysis. *Front Cardiovasc Med* **9**, (2022).
181. Liu, J. *et al.* Estimating global prevalence, incidence, and outcomes of non-alcoholic fatty liver disease from 2000 to 2021: systematic review and meta-analysis. *Chin Med J (Engl)* **135**, 1682–1691 (2022).
182. Lazarus, J. V. *et al.* The global NAFLD policy review and preparedness index: Are countries ready to address this silent public health challenge? *J Hepatol* **76**, 771–780 (2022).
183. Ge, X., Zheng, L., Wang, M., Du, Y. & Jiang, J. Prevalence trends in non-alcoholic fatty liver disease at the global, regional and national levels, 1990-2017: a population-based observational study. *BMJ Open* **10**, e036663 (2020).
184. Kwak, M. S. & Kim, D. Non-alcoholic fatty liver disease and lifestyle modifications, focusing on physical activity. *Korean Journal of Internal Medicine* **33**, 64–74 (2018).
185. Zelber-Sagi, S., Godos, J. & Salomone, F. Lifestyle changes for the treatment of nonalcoholic fatty liver disease: A review of observational studies and intervention trials. *Therap Adv Gastroenterol* **9**, 392–407 (2016).

186. Takahashi, Y., Soejima, Y. & Fukusato, T. Animal models of nonalcoholic fatty liver disease/ nonalcoholic steatohepatitis. *World J Gastroenterol* **18**, 2300–2308 (2012).
187. Nakamura, A. & Terauchi, Y. Lessons from mouse models of high-fat diet-induced NAFLD. *Int J Mol Sci* **14**, 21240–21257 (2013).
188. Radhakrishnan, S., Ke, J. & Pellizzon, M. Diets for Non-Alcoholic Fatty Liver Disease 2019 -. (2019).
189. Speakman, J. R. Use of high-fat diets to study rodent obesity as a model of human obesity. *Int J Obes* **43**, 1491–1492 (2019).
190. Kirpich, I. A. *et al.* Integrated hepatic transcriptome and proteome analysis of mice with high-fat diet-induced nonalcoholic fatty liver disease. *Journal of Nutritional Biochemistry* **22**, 38–45 (2011).
191. Flores-Costa, R. *et al.* The soluble guanylate cyclase stimulator IW-1973 prevents inflammation and fibrosis in experimental non-alcoholic steatohepatitis. *Br J Pharmacol* **175**, 953–967 (2018).
192. Xu, X., So, J. S., Park, J. G. & Lee, A. H. Transcriptional control of hepatic lipid metabolism by SREBP and ChREBP. *Semin Liver Dis* **33**, 301–311 (2013).
193. Todisco, S. *et al.* PPAR Alpha as a Metabolic Modulator of the Liver: Role in the Pathogenesis of Nonalcoholic Steatohepatitis (NASH). *Biology (Basel)* **11**, (2022).
194. Kawasaki, Y. *et al.* Renal expression of alpha-smooth muscle actin and c-Met in children with Henoch-Schönlein purpura nephritis. *Pediatric Nephrology* **23**, 913–919 (2008).
195. Eccleston, H. B. *et al.* Chronic exposure to a high-fat diet induces hepatic steatosis, impairs nitric oxide bioavailability, and modifies the mitochondrial proteome in mice. *Antioxid Redox Signal* **15**, 447–459 (2011).
196. Abdelmegeed, M. A. *et al.* Critical role of cytochrome P450 2E1 (CYP2E1) in the development of high fat-induced non-alcoholic steatohepatitis. *J Hepatol* **57**, 860–866 (2012).
197. Mantena, S. K. *et al.* High fat diet induces dysregulation of hepatic oxygen gradients and mitochondrial function in vivo. *Biochemical Journal* **417**, 183–193 (2009).
198. Gallou-kabani, C. *et al.* C57BL / 6J and A / J Mice Fed a High-Fat Diet Delineate Components of Metabolic Syndrome. *Obesity* **15**, (2007).
199. Sundaresan, S., Vijayagopal, P., Mills, N., Imrhan, V. & Prasad, C. A mouse model for nonalcoholic steatohepatitis. *Journal of Nutritional Biochemistry* **22**, 979–984 (2011).
200. Farrell, G. C. *et al.* Strain dependence of diet-induced NASH and liver fibrosis in

obese mice is linked to diabetes and inflammatory phenotype. *Liver International* **34**, 1084–1093 (2014).

201. van der Heijden, R. A. *et al.* High-fat diet induced obesity primes inflammation in adipose tissue prior to liver in C57BL/6j mice. *Aging* **7**, 256–268 (2015).
202. Isokuortti, E. *et al.* Use of HOMA-IR to diagnose non-alcoholic fatty liver disease: a population-based and inter-laboratory study. *Diabetologia* **60**, 1873–1882 (2017).
203. Kirovski, G. *et al.* Elevated systemic monocyte chemoattractrant protein-1 in hepatic steatosis without significant hepatic inflammation. *Exp Mol Pathol* **91**, 780–783 (2011).
204. Sherriff, J. L., O'Sullivan, T. A., Properzi, C., Oddo, J. L. & Adams, L. A. Choline, its potential role in nonalcoholic fatty liver disease, and the case for human and bacterial genes. *Advances in Nutrition* **7**, 5–13 (2016).
205. Corbin, K. D. & Zeisel, S. H. Choline metabolism provides novel insights into nonalcoholic fatty liver disease and its progression. *Curr Opin Gastroenterol* **28**, 159–165 (2012).
206. Pellizzon, M. A. & Ricci, M. R. *Nutriphenomics in rodent models: Impact of dietary choices on toxicological biomarkers*. *Biomarkers in Toxicology* (Elsevier Inc., 2014). doi:10.1016/B978-0-12-404630-6.00036-1.
207. Ariz, U., Mato, J. M., Lu, S. C. & Martínez Chantar, M. L. Nonalcoholic steatohepatitis, animal models, and biomarkers: what is new? *Methods Mol Biol* **593**, 109–136 (2010).
208. Nakae, D. *et al.* Comparative changes in the liver of female Fischer-344 rats after short- term feeding of a semipurified or a semisynthetic L-amino acid-defined choline-deficient diet. *Toxicol Pathol* **23**, 583–590 (1995).
209. Matsumoto, M. *et al.* An improved mouse model that rapidly develops fibrosis in non-alcoholic steatohepatitis. *Int J Exp Pathol* **94**, 93–103 (2013).
210. Ulmasov, B. *et al.* An Inhibitor of Arginine-Glycine-Aspartate-Binding Integrins Reverses Fibrosis in a Mouse Model of Nonalcoholic Steatohepatitis. *Hepatol Commun* **3**, 246–261 (2019).
211. Pellicano, A. J., Spahn, K., Zhou, P., Goldberg, I. D. & Narayan, P. Collagen characterization in a model of nonalcoholic steatohepatitis with fibrosis; a call for development of targeted therapeutics. *Molecules* **26**, (2021).
212. Gallego-Durán, R. *et al.* Metabolic characterization of two different non-alcoholic fatty liver disease pre-clinical mouse models. *Revista Espanola de Enfermedades Digestivas* **111**, 301–307 (2019).
213. Suzuki-Kemuriyama, N. *et al. Nonobese mice with nonalcoholic steatohepatitis*

fed on a choline-deficient, l-amino acid-defined, high-fat diet exhibit alterations in signaling pathways. *FEBS Open Bio* vol. 11 (2021).

214. Sugasawa, T. *et al.* One week of cdahfd induces steatohepatitis and mitochondrial dysfunction with oxidative stress in liver. *Int J Mol Sci* **22**, 1–19 (2021).
215. Raubenheimer, P. J., Nyirenda, M. J. & Walker, B. R. A choline-deficient diet exacerbates fatty liver but attenuates insulin resistance and glucose intolerance in mice fed a high-fat diet. *Diabetes* **55**, 2015–2020 (2006).
216. Raubenheimer, P. J., Nyirenda, M. J. & Walker, B. R. A choline-deficient diet exacerbates fatty liver but attenuates insulin resistance and glucose intolerance in mice fed a high-fat diet. *Diabetes* **55**, 2015–2020 (2006).
217. Wolf, M. J. *et al.* Metabolic activation of intrahepatic CD8+ T cells and NKT cells causes nonalcoholic steatohepatitis and liver cancer via cross-talk with hepatocytes. *Cancer Cell* **26**, 549–564 (2014).
218. Bernardo-Seisdedos, G. *et al.* Metabolic Landscape of the Mouse Liver by Quantitative 31P Nuclear Magnetic Resonance Analysis of the Phosphorome. *Hepatology* **74**, 148–163 (2021).
219. Ringnér, M. *What is principal component analysis? NATURE BIOTECHNOLOGY* vol. 26 http://www.nature.com/naturebiotechnology (2008).
220. Triba, M. N. *et al.* PLS/OPLS models in metabolomics: The impact of permutation of dataset rows on the K-fold cross-validation quality parameters. *Molecular BioSystems* vol. 11 13–19 Preprint at https://doi.org/10.1039/c4mb00414k (2015).
221. Takahashi, Y. & Fukusato, T. Histopathology of nonalcoholic fatty liver disease/nonalcoholic steatohepatitis. *World J Gastroenterol* **20**, 15539–15548 (2014).
222. Contreras, D., González-Rocha, A., Clark, P., Barquera, S. & Denova-Gutiérrez, E. Diagnostic accuracy of blood biomarkers and non-invasive scores for the diagnosis of NAFLD and NASH: Systematic review and meta-analysis. *Ann Hepatol* **28**, (2023).
223. Niu, L. *et al.* Defining NASH from a multi-omics systems biology perspective. *Journal of Clinical Medicine* vol. 10 Preprint at https://doi.org/10.3390/jcm10204673 (2021).
224. Brown, G. T. & Kleiner, D. E. Histopathology of nonalcoholic fatty liver disease and nonalcoholic steatohepatitis. *Metabolism: Clinical and Experimental* vol. 65 1080–1086 Preprint at https://doi.org/10.1016/j.metabol.2015.11.008 (2016).
225. Wang, T. & Ma, C. The hepatic macrophage pool in NASH. *Cellular and Molecular Immunology* vol. 18 2059–2060 Preprint at https://doi.org/10.1038/s41423-021-00690-z (2021).

226. Pellicano, A. J., Spahn, K., Zhou, P., Goldberg, I. D. & Narayan, P. Collagen characterization in a model of nonalcoholic steatohepatitis with fibrosis; a call for development of targeted therapeutics. *Molecules* **26**, (2021).
227. Poynard, T. *et al.* Diagnostic value of biochemical markers (Nash Test) for the prediction of non alcoholo steato hepatitis in patients with non-alcoholic fatty liver disease. *BMC Gastroenterol* **6**, (2006).
228. Reid, A. E. Nonalcoholic steatohepatitis. *Gastroenterology* **121**, 710–723 (2001).
229. Giannini, E. G., Testa, R. & Savarino, V. Liver enzyme alteration: A guide for clinicians. *CMAJ. Canadian Medical Association Journal* vol. 172 367–379 Preprint at https://doi.org/10.1503/cmaj.1040752 (2005).
230. Khosravi, S. *et al.* Non-alcoholic fatty liver disease and correlation of serum alanin ami-notransferase level with histopathologic findings. *Official Monthly Journal of the Baqiyatallah Research Center for Gastroenterology and Liver Diseases* **11**, 452–458 (2011).
231. Chen, Z., Tian, R., She, Z., Cai, J. & Li, H. Role of oxidative stress in the pathogenesis of nonalcoholic fatty liver disease. *Free Radical Biology and Medicine* vol. 152 116–141 Preprint at https://doi.org/10.1016/j.freeradbiomed.2020.02.025 (2020).
232. Walenbergh, S. M. A. & Shiri-Sverdlov, R. Cholesterol is a significant risk factor for non-alcoholic steatohepatitis. *Expert Review of Gastroenterology and Hepatology* vol. 9 1343–1346 Preprint at https://doi.org/10.1586/17474124.2015.1092382 (2015).
233. Gorce, M. *et al.* Fructose-1,6-bisphosphatase deficiency causes fatty liver disease and requires long-term hepatic follow-up. *J Inherit Metab Dis* **45**, 215–222 (2022).
234. Heiden, M. G. V., Cantley, L. C. & Thompson, C. B. Understanding the warburg effect: The metabolic requirements of cell proliferation. *Science* vol. 324 1029–1033 Preprint at https://doi.org/10.1126/science.1160809 (2009).
235. Leonardi, R., Frank, M. W., Jackson, P. D., Rock, C. O. & Jackowski, S. Elimination of the CDP-ethanolamine pathway disrupts hepatic lipid homeostasis. *Journal of Biological Chemistry* **284**, 27077–27089 (2009).
236. Ling, J., Chaba, T., Zhu, L. F., Jacobs, R. L. & Vance, D. E. Hepatic ratio of phosphatidylcholine to phosphatidylethanolamine predicts survival after partial hepatectomy in mice. *Hepatology* **55**, 1094–1102 (2012).
237. Li, Z. *et al.* The ratio of phosphatidylcholine to phosphatidylethanolamine influences membrane integrity and steatohepatitis. *Cell Metab* **3**, 321–331 (2006).
238. Lu, S. C. & Mato, J. M. Liver Health, Injury, and Cancer. *Physiol Rev* **92**, 1515–1542 (2012).

239. Horn, C. L., Morales, A. L., Savard, C., Farrell, G. C. & Ioannou, G. N. Role of Cholesterol-Associated Steatohepatitis in the Development of NASH. *Hepatology Communications* vol. 6 12–35 Preprint at https://doi.org/10.1002/hep4.1801 (2022).
240. Chiappini, F., Desterke, C., Bertrand-Michel, J., Guettier, C. & Le Naour, F. Hepatic and serum lipid signatures specific to nonalcoholic steatohepatitis in murine models. *Sci Rep* **6**, (2016).
241. Jagtap, P. & Szabo, C. Poly(ADP-ribose) polymerase and the therapeutic effects of its inhibitors. *Nature Reviews Drug Discovery* vol. 4 421–440 Preprint at https://doi.org/10.1038/nrd1718 (2005).
242. Amé, J. C., Spenlehauer, C. & De Murcia, G. The PARP superfamily. *BioEssays* vol. 26 882–893 Preprint at https://doi.org/10.1002/bies.20085 (2004).
243. Liu, J. *et al.* Geranylgeranyl diphosphate synthase (GGPPS) regulates non-alcoholic fatty liver disease (NAFLD)–fibrosis progression by determining hepatic glucose/fatty acid preference under high-fat diet conditions. *Journal of Pathology* **246**, 277–288 (2018).
244. Sherriff, J. L., O'Sullivan, T. A., Properzi, C., Oddo, J. L. & Adams, L. A. Choline, its potential role in nonalcoholic fatty liver disease, and the case for human and bacterial genes. *Advances in Nutrition* vol. 7 5–13 Preprint at https://doi.org/10.3945/an.114.007955 (2016).
245. Barzilai, N. & Ferrucci, L. Insulin resistance and aging: A cause or a protective response? *Journals of Gerontology - Series A Biological Sciences and Medical Sciences* vol. 67 1329–1331 Preprint at https://doi.org/10.1093/gerona/gls145 (2012).
246. Sheedfar, F., Biase, S. Di, Koonen, D. & Vinciguerra, M. Liver diseases and aging: Friends or foes? *Aging Cell* vol. 12 950–954 Preprint at https://doi.org/10.1111/acel.12128 (2013).
247. Sheedfar, F., Biase, S. Di, Koonen, D. & Vinciguerra, M. Liver diseases and aging: Friends or foes? *Aging Cell* vol. 12 950–954 Preprint at https://doi.org/10.1111/acel.12128 (2013).
248. Beneke, S. & Bürkle, A. Survey and summary: Poly(ADP-ribosyl)ation in mammalian ageing. *Nucleic Acids Res* **35**, 7456–7465 (2007).
249. Sheedfar, F., Biase, S. Di, Koonen, D. & Vinciguerra, M. Liver diseases and aging: Friends or foes? *Aging Cell* vol. 12 950–954 Preprint at https://doi.org/10.1111/acel.12128 (2013).
250. Alqahtani, S. A. & Schattenberg, J. M. Nafld in the elderly. *Clinical Interventions in Aging* vol. 16 1633–1649 Preprint at https://doi.org/10.2147/CIA.S295524

(2021).

251. Hull, W. E., Lutz, N. W., Franks, S. E., Frank, M. H. & Pomer, S. Investigation of multidrug resistance in cultured human renal cell carcinoma cells by 31P-NMR spectroscopy and treatment survival assays. *Magnetic Resonance Materials in Physics, Biology and Medicine* **18**, 144–161 (2005).
252. Fernando, H. *et al.* 1H and 31P NMR lipidome of ethanol-induced fatty liver. *Alcohol Clin Exp Res* **34**, 1937–1947 (2010).
253. Tolman, C. J., Kanodia, S., Roberts, M. F. & Daniels, L. *31 P-NMR spectra of methanogens: 2,3-cyclopyrophosphoglycerate is detectable only in methanobacteria strains*. *Biochimica et Biophysica Acta* vol. 886 (1986).
254. Kühl, O. *Phosphorus-31 NMR spectroscopy : a concise introduction for the synthetic organic and organometallic chemist*. (Springer, 2008).
255. Kellogg, G. W. *Two-and three-dimensional 31p-driven NMR procedures for complete assignment of backbone resonances in oligodeoxyribonucleotides*. *Journal of Biomolecular NMR* vol. 3 (1993).
256. Abi-Ghanem, J., Heddi, B., Foloppe, N. & Hartmann, B. DNA structures from phosphate chemical shifts. *Nucleic Acids Res* **38**, 1119–1128 (2009).
257. Mulder, F. A. A., Tenori, L. & Luchinat, C. Fast and Quantitative NMR Metabolite Analysis Afforded by a Paramagnetic Co-Solute. *Angewandte Chemie - International Edition* **58**, 15283–15286 (2019).
258. Cox, N., Millard, P., Charlier, C. & Lippens, G. Improved NMR Detection of Phospho-Metabolites in a Complex Mixture. *Anal Chem* **93**, 4818–4824 (2021).
259. Bhinderwala, F. *et al.* Phosphorus NMR and Its Application to Metabolomics. *Anal Chem* **92**, 9536–9545 (2020).
260. Bhinderwala, F. *et al.* Expanding the Coverage of the Metabolome with Nitrogen-Based NMR. *Anal Chem* **90**, 4521–4528 (2018).
261. Lutz, N. W. & Cozzone, P. J. Principles of multiparametric optimization for phospholipidomics by 31P NMR spectroscopy. *Biophysical Reviews* vol. 5 295–304 Preprint at https://doi.org/10.1007/s12551-013-0105-3 (2013).
262. Schröter, J., Popkova, Y., Süß, R. & Schiller, J. Combined use of MALDI-TOF mass spectrometry and 31P NMR spectroscopy for analysis of phospholipids. *Methods in Molecular Biology* **1609**, 107–122 (2017).
263. Furse, S. *et al.* A pipeline for making 31 P NMR accessible for small-and large-scale lipidomics studies. doi:10.1007/s00216-021-03430-4/Published.
264. Bernardo-Seisdedos, G. *et al.* Metabolic Landscape of the Mouse Liver by Quantitative 31P Nuclear Magnetic Resonance Analysis of the Phosphorome. *Hepatology* **74**, 148–163 (2021).

265. Draper, D. E., Grilley, D. & Soto, A. M. Ions and RNA folding. *Annual Review of Biophysics and Biomolecular Structure* vol. 34 221–243 Preprint at https://doi.org/10.1146/annurev.biophys.34.040204.144511 (2005).
266. *Metal ions in ribozyme folding and catalysis Hanna and Doudna 167*.
267. Brini, M., Ottolini, D., Calì, T. & Carafoli, E. Calcium in health and disease. *Met Ions Life Sci* **13**, 81–137 (2013).
268. Mathuthu, E., Janse Van Rensburg, A., Plessis, D. Du & Mason, S. *EDTA as a chelating agent in quantitative 1 H-NMR of biologically important ions*. https://orcid.org/0000-0002-2945-5768.
269. Mohammadi, Z., Shalavi, S. & Jafarzadeh, H. Ethylenediaminetetraacetic acid in endodontics. *Eur J Dent* **7**, (2013).
270. Panda, S. K. & Chaudhuri, S. Chelating ligand-mediated synthesis of hollow ZnS microspheres and its optical properties. *J Colloid Interface Sci* **313**, 338–344 (2007).
271. Mulder, F. A. A., Tenori, L. & Luchinat, C. Fast and Quantitative NMR Metabolite Analysis Afforded by a Paramagnetic Co-Solute. *Angewandte Chemie - International Edition* **58**, 15283–15286 (2019).

PUBLICATIONS

- Bilbao, J., Bernardo-Seisdedos, G., Fernández-Ramos, D., Lopitz-Otsoa, F., Gutiérrez de Juan, V., Bizkarguenaga, M., Mateos, B., F.Fondevila, M., Abril-Fornaguera, J., Diercks, T., C Lu, S., Nogueiras, R., Mato, J.M., Millet, O. Metabolic landscape of the mouse liver by quantitative ^{31}P-NMR analysis of the phosphorome*. Hepatology* (2020) doi:10.1002/hep.316.

- Férnandez-Ramos,D., Lopitz-Otsoa,F., Delacruz-Villar,L., Bilbao,J., Pagano,M., Mosca,L., Bizkarguenaga,M., Serrano-Macía,M., Azkargorta,M., Iruarrizaga-Lejarreta,M., Sot,J., Tsvirkun,D., Martijn van Liempd,S., Goni,F., Alonso,C., Martínez-Chantar,M.L., Elortza,F., Hawardeny,L., C.Lu,S., Mato,J.M. World Journal of Gastroenterology (2020) doi: 10.3748/WJG.V26.I34.5101.

- Gonzalez-Rellan,M.J., Fondevila,M.F., Fernandez,U., Rodríguez,A., Varela-Rey,M., Veyrat-Durebex,C., Seoane,S., Bernardo,G., Lopitz-Otsoa,F., Férnandez-Ramos,D., Bilbao,J., Iglesias,C., Novoa,E., Ameneiro,C., Senra,A., Beiroa,D., Cuñarro,J., Chantada-Vazquez,M., Garcia-Vence,M., Bravo,S.B., Da Silva Lima,N., Porteiro,B., Carneiro,C., Vidal,A., Tovar,s., D.Muller,T., Ferno,J., Guallar,D., Fidalgo,M., Sabio, G., Herzig,S., Ho Yang,W., Won Cho,J., Martinez-Chantar,M.L., Perez-Fernandez,R., López,M., Dieguez,C., Mato,J.M., Coppari,R., Woodhoo,A., Fruhbeck,G., Nogueiras,R. Nature communications vol. 12,1 5068. 20 Aug. 2021, doi:10.1038/s41467-021-25390-0.

- Capelo-Diz, A., Lachiondo-Ortega,S., Fernández-Ramos,D., Cañas-Martín,J., Goikoetxea-Usandizaga,N., Serrano-Maciá,M., González-Rellan,M.J., Mosca,L., Blazquez-Vicens,J., Tinahones-Ruano,A., Fondevila,M., Buyan,M., Delgado,T., Gutierrez de Juan,V., Ayuso-García,P., Sánchez-Rueda,A., Velasco-Avilés,S., Hernández-Susavila,H., Riobello-Suárez,C., Dziechciarz,B., Montiel-Duarte,C., Lopitz-Otsoa,F., Bizkarguenaga,M., Bilbao,J., Bernardo-Seisdedos, G., Senra, A., Soriano-Navarro,M., Millet,O., Díaz-Lagares,A., Crujeiras,A., Bao-Caamano,A., Cabrera,D., Van Liempd,S., Tamayo-Carro,M., Borzacchiello,L., Gomez-Santos,B., Buqué, X., Sáenz de Urturi,D., González-Romeiro,F., Simon,J., Rodríguez-Agudo,R., Ruiz,A., Matute,C., Beiroa,D., Falcon-Perez,J.M., Aspichueta,P., Rodriguez-Cuesta,J., Porcelli,M., Pajares,M.A., Ameneiro,C., Fidalgo,M., Aransay,A., Lama-Díaz,T., Blanco,M., López,M., Villa-

Bellosta,R., Muller,T., Nogueiras,R., Woodhoo,A., Martínez-Chantar,M.L., Varela-Rey,M. Cell metabolism vol. 35,8 (2023): 1373-1389. e8. doi:10.1016/j.cmet.2023.07.002.

FIGURE LIST

TABLE LIST

Table 5S6. Intensity values of the most representative phosphorylated metabolites of a liver mice sample at different concentrations of Gdter (0, 0.5 and 1 mM) at 288 K. It was observed that the higher concentration of Gdter, the lower intensity of each metabolite is.

Table 5S7. Intensity values of the most representative phosphorylated metabolites of a liver mice sample at different concentrations of Gdter (0, 0.5 and 1 mM) at 298 K. It was observed that the higher concentration of Gdter, the lower intensity of each metabolite is.

Table 5S8. Intensity values of the most representative phosphorylated metabolites of a liver mice sample at different concentrations of Gdter (0, 0.5 and 1 mM) at 308 K. It was observed that the higher concentration of Gdter, the lower intensity of each metabolite is.

EQUATION LIST

Equation 1.1. Nuclear energetic transitions where is equivalent to Larmor frequency (v) and Planck´s constant (h = $6.626.10^{-34}$. J.s)

Equation 1.2. Chemical shifts in ppm. Derived by subtracting the resonance frequency from a reference molecule (such as tetrametylsilane (TMS) or a comparable compound) and normalizing the result by the spectrometer's frequency.

Equation 4.1. T_2 or transverse relaxation is inversely proportional to the linewidth at half-height.